National Technical University
of Athens

School of Electrical and
Computer Engineering

Study and Simulation of the Radiation background of the ATLAS Experiment at CERN using the Monte Carlo method

A Diploma Thesis
By

Maria Lymperaiou

Supervisor: Evangelos Gazis

March, 2017

ΕΘΝΙΚΟ ΜΕΤΣΟΒΙΟ ΠΟΛΥΤΕΧΝΕΙΟ

ΣΧΟΛΗ ΗΛΕΚΤΡΟΛΟΓΩΝ ΜΗΧΑΝΙΚΩΝ
ΚΑΙ ΜΗΧΑΝΙΚΩΝ ΥΠΟΛΟΓΙΣΤΩΝ

Μελετη και Προσομοιωση του υποβαθρου ακτινοβολιας για το πειραμα ATLAS στο CERN χρησιμοποιωντας τη μεθοδο Monte Carlo

---

ΔΙΠΛΩΜΑΤΙΚΗ ΕΡΓΑΣΙΑ
ΤΗΣ

Μαρίας Λυμπεραίου

ΕΠΙΒΛΕΠΩΝ: Ευάγγελος Γαζής

ΜΑΡΤΙΟΣ, 2017

ΕΘΝΙΚΟ ΜΕΤΣΟΒΙΟ ΠΟΛΥΤΕΧΝΕΙΟ

ΣΧΟΛΗ ΗΛΕΚΤΡΟΛΟΓΩΝ ΜΗΧΑΝΙΚΩΝ
ΚΑΙ ΜΗΧΑΝΙΚΩΝ ΥΠΟΛΟΓΙΣΤΩΝ

Μελέτη και Προσομοίωση του υποβάθρου ακτινοβολίας για το πείραμα ATLAS στο CERN χρησιμοποιώντας τη μέθοδο Monte Carlo

---

ΔΙΠΛΩΜΑΤΙΚΗ ΕΡΓΑΣΙΑ
ΤΗΣ

Μαρίας Λυμπεραίου

ΕΠΙΒΛΕΠΩΝ: Ευάγγελος Γαζής

Εγκρίθηκε από την τριμελή εξεταστική επιτροπή την 27η Μαρτίου 2017.

(Υπογραφή)	(Υπογραφή)	(Υπογραφή)
....	....	....
Ευάγγελος Γαζής Καθηγητής Ε.Μ.Π	Ηλίας Γλύτσης Καθηγητής Ε.Μ.Π	Ιωάννης Ξανθάκης Καθηγητής Ε.Μ.Π

(Υπογραφή)

....

Λυμπεραίου Μαρία

Διπλωματούχος Ηλεκτρολόγος Μηχανικός και Μηχανικός Υπολογιστών Ε.Μ.Π

Λυμπεραίου Μαρία, 27/3/2017

I. ΠΕΡΙΛΗΨΗ

Ο ATLAS είναι ένας από τους δύο ανιχνευτές γενικού σκοπού στο Μεγάλο Επιταχυντή Αδρονίων (LHC) στο CERN. Διερευνεί ένα ευρύ πεδίο φυσικής, από την αναζήτηση του μποζονίου Higgs μέχρι την ύπαρξη επιπλέον διαστάσεων και σωματιδίων που μπορούν να δημιουργήσουν σκοτεινή ύλη. Ο ανιχνευτής ATLAS αποτελείται από ομοαξονικούς κυλίνδρους αυξανόμενης ακτίνας περί το σημείο αλληλεπίδρασης όπου οι δέσμες πρωτονίων από τον LHC συγκρούονται. Μπορεί να χωριστεί σε τέσσερα κύρια κομμάτια: ο Εσωτερικός Ανιχνευτής, η εσώτερη διάταξη, ανιχνεύει την κίνηση φορτισμένων σωματιδίων, καθώς αυτά απομακρύνονται από το σημείο αλληλεπίδρασης. Οι καταγραφόμενες τροχιές που ανιχνεύονται από τις αλληλεπιδράσεις σωματιδίων-ανιχνευτή ως ένα πλήθος διακριτών σημείων αποτελούν το πρώτο βήμα στην αναγνώριση μέχρι πρότινος άγνωστων σωματιδίων. Τα θερμιδόμετρα μετρούν την ενέργεια ουδέτερων και φορτισμένων σωματιδίων αλληλεπιδρώντας με αυτά, με αποτέλεσμα τη δημιουργία καταιγισμό δευτερευόντων σωματιδίων. Το φασματόμετρο μιονίων, το εξώτερο τμήμα του ανιχνευτή, πραγματοποιεί επιπλέον μετρήσεις πολύ διαπεραστικών μιονίων, τα οποία είναι ικανά να διαπεράσουν τα εσώτερα στρώματα χωρίς αλληλεπίδραση. Τέλος, το σύστημα μαγνητών καμπυλώνει φορτισμένα σωματίδια στον Εσωτερικό ανιχνευτή και στο Φασματόμετρο μιονίων˙ η κατεύθυνση κίνησής τους και ο βαθμός καμπύλωσης υποδεικνύουν το φορτίο και την ορμή του αντίστοιχα.

Ο ανιχνευτής δημιουργεί δυσκόλως διαχειρίσιμα σε όγκο ακατέργαστα δεδομένα: περίπου 25 megabytes ανά γεγονός, πολλαπλασιαζόμενα επί 40 εκατομμύρια διασταυρώσεις δεσμών ανά δευτερόλεπτα στο κέντρο του ανιχνευτή, παράγοντας συνολικά 1 petabyte ακατέργαστων δεδομένων ανά δευτερόλεπτο. Έτσι, χρειάζεται ένα σύστημα σκανδαλισμού ώστε να επιλέγει εν δυνάμει ενδιαφέροντα γεγονότα προς αποθήκευση σε πραγματικό χρόνο έτσι ώστε να ελαχιστοποιείται η επίδραση διεργασιών υποβάθρου. Το σύστημα σκανδαλισμού του ATLAS χρησιμοποιεί απλές πληροφορίες για την αναγνώριση των πιο ενδιαφερόντων γεγονότων τα οποία διατηρούνται για περαιτέρω ανάλυση. Το σύστημα απόκτησης δεδομένων λαμβάνει και αποθηκεύει τα δεδομένα του γεγονότος από τα ειδικά ηλεκτρονικά ανάγνωσης των ανιχνευτών. Το υπολογιστικό πλέγμα χρησιμοποιείται εκτεταμένα για την ανακατασκευή γεγονότων, επιτρέποντας την παράλληλη επεξεργασία σε δίκτυα υπολογιστών σε όλο τον κόσμο.

Ένα μεγάλο πρόβλημα στον ανιχνευτή ATLAS είναι το μεγάλο υπόβαθρο ακτινοβολίας προερχόμενο από τις συγκρούσεις στο σημείο αλληλεπίδρασης. Αυτό το υπόβαθρο προκαλεί διάφορα προβλήματα, όπως βλάβη στους ανιχνευτές πυριτίου και στα ηλεκτρονικά ανάγνωσης, γήρανση των υποανιχνευτών, εναποθέσεις ακτινοβολίας που αλλοιώνουν τα ηλεκτρονικά σήματα ή καταστρέφουν τα εξαρτήματα, και σήματα υποβάθρου που προκαλούν εσφαλμένους και τυχαίους σκανδαλισμούς. Για τον περιορισμό των συνεπειών αυτών, ο ATLAS χρησιμοποιεί σχεδόν 3000 τόνους θωράκισης σε πολυστρωματικό σχεδιασμό, εκμεταλλευόμενος τις απορροφητικές ικανότητες διαφορετικών υλικών.

Στο πρώτο κεφάλαιο παρουσιάζεται μια εισαγωγή στους σκοπούς και τις φυσικές μελέτες του LHC. Το δεύτερο κεφάλαιο περιγράφει τις διαδικασίες που αφορούν τις αλληλεπιδράσεις των διαφόρων σωματιδίων με την ύλη, οι οποίες μπορεί να οδηγήσουν στη δημιουργία νέων σωματιδίων. Μια ανάλυση της διάταξης του LHC διεξάγεται στο τρίτο κεφάλαιο και μια περιγραφή της οργανολογίας και της επεξεργασίας δεδομένων του ανιχνευτή ATLAS ακολουθεί στο τέταρτο κεφάλαιο. Το κεφάλαιο 5 παρουσιάζει το λογισμικό MCNP, βασισμένο στη μέθοδο Monte Carlo, το οποίο χρησιμοποιείται στη σχεδίαση και την προσομοίωση των διαφόρων υποανιχνευτών του πειράματος. Η περιγραφή του υποβάθρου ακτινοβολίας και των περιοχών θωράκισης για την περικοπή των συνεπειών της ακτινοβολίας στους υποανιχνευτές και στο σύστημα σκανδαλισμού αναλύονται στο Κεφάλαιο 6. Το τελευταίο κεφάλαιο περιέχει τη μεθοδολογία της προσομοίωσης και τα αποτελέσματα για τους υποανιχνευτές του ATLAS. Κάποιες επιπρόσθετες προσομοιώσεις απλών γεωμετριών, καθώς και ο MCNP κώδικας για τον ανιχνευτή ATLAS συμπεριλαμβάνονται στα παραρτήματα.

ΛΕΞΕΙΣ ΚΛΕΙΔΙΑ: ανιχνευτής ATLAS, LHC, εσωτερικός ανιχνευτής, θερμιδόμετρο, φασματόμετρο μιονίων, σύστημα σκανδαλισμού, υπόβαθρο ακτινοβολίας, θωράκιση, επιδράσεις ακτινοβολίας, μέθοδος Monte Carlo, λογισμικό MCNP.

II. ABSTRACT

ATLAS is one of two general-purpose detectors at the Large Hadron Collider (LHC) at CERN. It investigates a wide range of physics, from the search for the Higgs boson to extra dimensions and particles that could make up dark matter. The ATLAS detector consists of a series of ever-larger concentric cylinders around the interaction point where the proton beams from the LHC collide. It can be divided into four major sections: The Inner Detector, the innermost component, tracks the motion of charged particles as they move away from the interaction point. The tracks measured by recording particle/detector interactions at a multitude of discrete points, form the first step in identifying the unknown particles. The calorimeters measure the energy of both neutral and charged particles by interacting with them, resulting in creating cascades of secondary particles. The Muon Spectrometer, the outermost component of the detector, makes additional measurements of highly penetrating muons, which are capable of passing through the inner layers without interaction. Finally, the magnet systems bend charged particles in the Inner Detector and the Muon Spectrometer; their direction of motion and degree of curvature become indicative of their charge and momentum, respectively.

The detector generates unmanageably large amounts of raw data: about 25 megabytes per event, multiplied by 40 million beam crossings per second in the center of the detector, producing a total of 1 petabyte of raw data per second. Thus, a trigger system is needed in order to select potentially interesting events for storage in real-time, so as to avoid being overwhelmed by background processes. The ATLAS trigger system uses simple information to identify the most interesting events to retain for detailed analysis. The data acquisition system receives and buffers the event data from the detector-specific readout electronics. Grid computing is being extensively used for event reconstruction, allowing the parallel use of computer networks throughout the world.

A major problem at the ATLAS detector is the huge radiation background, coming from the collisions at the interaction point. This background causes several problems such as radiation damage to silicon detectors and readout electronics, ageing of the subdetectors, radiation deposits that disrupt electronic signals or destroy components, and background signals resulting in spurious and random triggers. For the limitation of these consequences, ATLAS uses almost 3000 tonnes of shielding in a multilayer design, taking advantage of the absorbing capacities of different materials.

In the first chapter an introduction on the purposes and the physics studies of the LHC is presented. The second chapter describes the processes regarding the interactions of the various particles with matter, which may lead to the creation of new particles. An analysis of the LHC machine is carried out in the third chapter and a description of the ATLAS detector instrumentation and data processing follows in the fourth chapter. Chapter 5 presents the MCNP software, based on the Monte Carlo method, which is used for the design and the simulation of the various subdetectors of the experiment. The description of the radiation background and the shielding regions needed to curb the radiation effects in the subdetectors and the trigger system are analyzed in Chapter 6. The last chapter contains the methodology of the simulation and the results for the ATLAS subdetectors. Some additional simulations of simple geometries, as well as the MCNP code for the ATLAS detector are included in the appendices.

KEYWORDS: ATLAS detector, LHC, inner detector, calorimeter, muon spectrometer, trigger system, radiation background, shielding, radiation impact, Monte Carlo method, MCNP software.

III. ΕΥΧΑΡΙΣΤΙΕΣ

Αρχικά, θα ήθελα να ευχαριστήσω τον επιβλέποντά μου, Ευάγγελο Γαζή, που με εμπιστεύθηκε στην ανάθεση αυτής της εργασίας. Η βοήθεια που μου προσέφερε, η εμπιστοσύνη του και η συνεχής υποστήριξή του με βοήθησαν σε πολύ μεγάλο βαθμό καθ' όλη τη διάρκεια της εκπόνησης αυτής της εργασίας, ακόμα και στα σημεία εκείνα που πίστευα ότι δε θα τα καταφέρω.

Ιδιαίτερη ευγνωμοσύνη οφείλω στη Βιολέτα Γκίκα, χωρίς τη συνδρομή της οποίας θα ήταν πολύ δύσκολη η εξοικείωσή μου με τον κώδικα και το περιβάλλον του λογισμικού που χρησιμοποιήσαμε. Η άμεση βοήθειά της, οι συμβουλές και η επιβράβευση που μου προσέφερε συνέβαλαν απεριόριστα στην ολοκλήρωση αυτού του έργου. Στο θέμα του λογισμικού θα ήθελα επίσης να ευχαριστήσω τη Δώρα Βασιλοπούλου, η οποία με τις γνώσεις και την εμπειρία της συνέβαλε στην επίλυση πολλών αποριών οι οποίες με εμπόδιζαν να συνεχίσω.

Τέλος, αξίζει να ευχαριστήσω τους ανθρώπους εκείνους που με τον δικό τους τρόπο με εμψύχωσαν και με στήριξαν κατά την εκπόνηση αυτής της εργασίας. Στο πλευρό μου στάθηκε ιδιαίτερα η Μαρία με την οποία δουλέψαμε μαζί πάνω στον κώδικα που χρησιμοποιήθηκε στην εργασία αυτή και περάσαμε πολλές ώρες προσπαθώντας να καταλήξουμε στο καλύτερο δυνατό αποτέλεσμα. Επιπλέον, οφείλω ένα ευχαριστώ στο Σταμάτη που με βοήθησε σε πολύ μεγάλο βαθμό και με υποστήριξε απεριόριστα όλο αυτό το διάστημα.

IV. ΕΚΤΕΤΑΜΕΝΗ ΠΕΡΙΛΗΨΗ

1. ΕΡΕΥΝΕΣ ΣΤΟΝ ΕΠΙΤΑΧΥΝΤΗ LHC

Το Καθιερωμένο Πρότυπο της σωματιδιακής φυσικής περιγράφει όλα τα γνωστά στοιχειώδη σωματίδια και τις μεταξύ τους αλληλεπιδράσεις μέσω τριών αλληλεπιδράσεων: του ηλεκτρομαγνητισμού, της ασθενούς πυρηνικής και της ισχυρής πυρηνικής αλληλεπίδρασης. Σύμφωνα με το Καθιερωμένο Πρότυπο υπάρχουν τρία είδη στοιχειωδών σωματιδίων: λεπτόνια, κουάρκ και φορείς αλληλεπιδράσεων (μποζόνια βαθμίδας). Κάθε σωματίδιο διαθέτει ένα αντίστοιχο αντισωματίδιο. Τα λεπτόνια και τα κουάρκ ανήκουν στα φερμιόνια, έχοντας ημιακέραιο σπιν, και υπακούουν στη στατιστική Fermi – Dirac. Τα λεπτόνια διαθέτουν ακέραιο ηλεκτρικό φορτίο και διαχωρίζονται σε τρεις γενιές, καθεμία από τις οποίες απαρτίζεται από ένα λεπτόνιο (e, μ και τ) με μοναδική διαφορά την αυξανόμενη μάζα, μαζί με ένα αντίστοιχο νετρίνο (ν_e, ν_μ και ν_τ). Τα κουάρκ διαθέτουν κλασματικό ηλεκτρικό φορτίο (+2|e|/3 ή −|e|/3). Υπάρχουν έξι ‘γεύσεις’ κουάρκ και επίσης διαχωρίζονται σε τρεις γενιές. Ακόμη τα κουάρκ αποτελούνται από ένα εκ των τριών δυνατών ‘χρωμάτων’ (κόκκινο, μπλε ή πράσινο), ενώ τα αντι – κουάρκ από αντι – ‘χρώματα’. Η ισχυρή πυρηνική αλληλεπίδραση μέσω ανταλλαγής γλουονίων ενώνει τα κουάρκ με αποτέλεσμα το σχηματισμό αδρονίων, τα οποία διαχωρίζονται σε μεσόνια και βαρυόνια. Οι φορείς αλληλεπιδράσεων μεταξύ των φερμιονίων είναι σωματίδια ακεραίου σπιν που υπακούουν στη στατιστική BoseEinstein. Η ηλεκτρομαγνητική δύναμη, την οποία περιγράφει η κβαντική ηλεκτροδυναμική, διαδίδεται μέσω των φωτονίων μεταξύ ηλεκτρικά φορτισμένων σωματιδίων. Η ασθενής αλληλεπίδραση, περιγραφόμενη από την ηλεκτροασθενή θεωρία, διαδίδεται μέσω μεγάλης μάζας μποζόνια βαθμίδας με σπιν 1 ($W^{\pm}$ και Z). Η ισχυρή αλληλεπίδραση περιγράφεται από τη κβαντική ηλεκτροδυναμική και διαδίδεται μέσω οκτώ άμαζων γλουονίων.

1.1. ΤΟ ΜΠΟΖΟΝΙΟ HIGGS ΚΑΙ ΑΛΛΕΣ ΕΡΕΥΝΕΣ ΣΤΟΝ LHC

Ο τρόπος με τον οποίο τα σωματίδια αποκτούν μάζα περιγράφεται από το μηχανισμό Brout – Englert – Higgs, ο οποίος προϋποθέτει την ύπαρξη ενός μποζονίου με μηδενικό σπιν. Το μποζόνιο Higgs παρατηρήθηκε στα πειράματα ATLAS και CMS με μάζα 126 GeV/c^2 και χρόνο ζωής 1.6×10^{-22} s. Το μποζόνιο Higgs μπορεί να παραχθεί με τέσσερις τρόπους:

- Σύντηξη γλουονίων: $gg \rightarrow H$
- Σύντηξη μποζονίου φορέα (VBF): $q\bar{q} \rightarrow q\bar{q}H$
- Συνδεδεμένη παραγωγή με μποζόνια φορέα (Higgs Strahlung): $q\bar{q} \rightarrow WH$ ή $q\bar{q} \rightarrow ZH$

- Συνδεδεμένη παραγωγή με βαρέα κουάρκ : $q\bar{q} \rightarrow Q\bar{Q}H$ ή $gg \rightarrow Q\bar{Q}H$

Πιθανές διασπάσεις για το Higgs:

- ζεύγος φερμιονίου – αντιφερμιονίου
- ζεύγος βαρέων μποζονίων βαθμίδας
- ζεύγος γλουονίων (αντίστροφη διαδικασία της σύντηξης γλουονίων)
- ζεύγος φωτονίων

Επιπλέον έρευνες πραγματοποιούνται στον LHC. Μία από αυτές είναι η μελέτη της υπερσυμμετρίας (SUSY), η οποία πιθανολογείται ότι μπορεί να οδηγήσει στην ενοποίηση των θεμελιωδών δυνάμεων. Σύμφωνα με τη θεωρία αυτή, κάθε σωματίδιο διαθέτει ένα βαρύτερο υπερσυμμετρικό ταίρι, με το οποίο διαφέρει ως προς το σπιν κατά ½, με αποτέλεσμα τα φερμιόνια να μετατρέπονται σε μποζόνια και αντίστροφα. Εάν η θεωρία είναι σωστή, κάποια από τα ελαφρύτερα υπερσυμμετρικά σωματίδια πρέπει να παρατηρηθούν στον LHC. Ακόμη, μελετάται η ασυμετρία ύλης – αντιύλης στο σύμπαν. Κατά τη μεγάλη έκρηξη, ίσες ποσότητες ύλης και αντιύλης θεωρείται ότι είχαν δημιουργηθεί. Παρόλα αυτά, οτιδήποτε στο σύμπαν αποτελείται σχεδόν αποκλειστικά από ύλη, συνεπώς μια από τις μεγαλύτερες προκλήσεις είναι να ανακαλυφθεί η αιτία της ασυμμετρίας αυτής. Τέλος, μελετάται μια ιδιαίτερη μορφή της ύλης, το πλάσμα κουάρκ – γλουονίων. Λίγο μετά τη μεγάλη έκρηξη, το σύμπαν κατακλύστηκε από ένα πολύ ζεστό πυκνό μίγμα ποικίλων σωματιδίων που κινούνταν κοντά στην ταχύτητα του φωτός. Το μίγμα αυτό αποτελούνταν κατά κύριο λόγο από κουάρκ και γλουόνια ασθενώς συνδεδεμένα μεταξύ τους. Για την αναπαραγωγή των συνθηκών που επικρατούσαν στο πρώιμο σύμπαν ο LHC πραγματοποιεί μετωπικές συγκρούσεις μεταξύ βαρέων ιόντων.

2. ΑΛΛΗΛΕΠΙΔΡΑΣΗ ΑΚΤΙΝΟΒΟΛΙΑΣ ΜΕ ΤΗΝ ΥΛΗ

Η λειτουργία κάθε ανιχνευτικού συστήματος βασίζεται στην αλληλεπίδραση των διερχόμενων σωματιδίων με το υλικό του ανιχνευτή. Το προϊόν της αλληλεπίδρασης μετατρέπεται σε ηλεκτρικό σήμα. Η αλληλεπίδραση βαρέων φορτισμένων σωματιδίων με την ύλη πραγματοποιείται μέσω της δύναμης Coulomb κυρίως με τα περιφερειακά ηλεκτρόνια και σε μικρότερο βαθμό με τον πυρήνα του ατόμου. Η απώλεια ενέργειας εντός του υλικού είναι ένα στατιστικό φαινόμενο που ακολουθεί την κατανομή Landau. Οι επιμέρους μηχανισμοί απώλειας ενέργειας περιλαμβάνουν:

- Διέγερση: ένα ατομικό ηλεκτρόνιο αποκτά ενέργεια ικανή για τη μετάβασή του σε μια ανώτερη ενεργειακή στάθμη.

- Ιονισμός: παρόμοια με τη διέγερση, ένα ηλεκτρόνιο αποκτά ενέργεια ικανή να του επιτρέψει να εγκαταλείψει το άτομο στο οποίο προηγουμένως ήταν δέσμιο, με αποτέλεσμα τη δημιουργία ενός ζεύγους θετικού ιόντως και ελεύθερου ηλεκτρονίου.

- Ακτινοβολία Cherenkov: συμμετέχει λιγότερο στην απώλεια ενέργειας, όμως είναι μεγάλης σημασίας για τον καθορισμό της τροχιάς ενός φορτισμένου σωματιδίου. Εκπέμπεται όταν ένα φορτισμένο σωματίδιο περνά μέσα από ένα διηλεκτρικό μέσο με ταχύτητα μεγαλύτερη της φασικής ταχύτητας του φωτός στο μέσο αυτό. Το φορτισμένο σωματίδιο σε τροχιά εκπέμπει σφαιρικά ηλεκτρομαγνητικά κύματα μέσω της δημιουργίας ηλεκτρικών διπόλων κατά τη διέλευση του σωματιδίου.

- Ακτινοβολία μετάβασης: εκπέμπεται όταν ένα σωματίδιο διασχίζει τη διαχωριστική επιφάνεια δύο μέσων με διαφορετικές διηλεκτρικές ιδιότητες. Η αλλαγή της διηλεκτρικής σταθεράς κατά μήκος της τροχιάς του σωματιδίου προκαλεί ασυνέχεια του ηλεκτρικού πεδίου στη διαχωριστική επιφάνεια.

Τα ταχέα ηλεκτρόνια υπόκεινται σε μικρότερη απώλεια ενέργειας και η τροχιά τους είναι τυχαία και μη γραμμική όταν διέρχονται μέσα από απορροφητικά υλικά. Οι κύριοι μηχανισμοί απώλειας ενέργειας είναι:

- Σκέδαση με περιφερειακά ηλεκτρόνια: λόγω της αλληλεπίδρασης Coulomb, φαινόμενα διέγερσης και ιονισμού λαμβάνουν χώρα, με αποτέλεσμα απώλεια ενέργειας και απόκλιση από την αρχική τροχιά. Εάν η αρχική ενέργεια του αρχικού ηλεκτρονίου είναι αρκετά μεγάλη, μπορούν να προκληθούν δευτερεύοντες ιονισμοί.

- Ακτινοβολία πέδησης (bremsstrahlung): αποτελεί ηλεκτρομαγνητική ακτινοβολία παραγόμενη από την επιβράδυνση ενός φορτισμένου σωματιδίου (ηλεκτρόνιο) όταν εκτρέπεται λόγω ενός άλλου φορτισμένου σωματιδίου (ατομικός πυρήνας). Λόγω της διατήρησης της ενέργειας, η κινητική ενέργεια που χάνεται μετατρέπεται σε ένα φωτόνιο.

- Σκεδάσεις Moller και Bhabha: εμπεριέχουν αλληλεπιδράσεις μεταξύ προσπιπτόντων ηλεκτρονίων ή ποζιτρονίων με ατομικά ηλεκτρόνια. Στην κβαντική χρωμοδυναμική, η σκέδαση Moller περιγράφει την άπωση δύο ηλεκτρονίων, ενώ η σκέδαση Bhabha περιγράφει την έλξη μεταξύ ηλεκτρονίου και ποζιτρονίου.

Οι μηχανισμοί αλληλεπίδρασης των φωτονίων οδηγούν στη μεταφορά ενέργειας φωτονίου, μερικής ή ολικής, στα ατομικά ηλεκτρόνια του μέσου, η οποία εμφανίζεται ως κινητική ενέργεια. Οι μηχανισμοί αλληλεπίδρασης είναι:

- Σύμφωνη σκέδαση (Rayleigh): το εισερχόμενο φωτόνιο απορροφάται και επανεκπέμπεται αμέσως χωρίς απώλεια ενέργειας, παρά μόνο αλλαγή κατεύθυνσης.

- Ασύμφωνη σκέδαση (Φωτοηλεκτρικό φαινόμενο): αφορά την αλληλεπίδραση φωτονίων ενέργειας συνήθως μικρότερης του 1 MeV με ατομικά ηλεκτρόνια. Η ενέργεια του απορροφώμενου φωτονίου πρέπει να είναι μεγαλύτερη της ενέργειας σύνδεσης των ηλεκτρονίων. Δημιουργείται ένα εξαγόμενο φωτοηλεκτρόνιο και ένα ιονισμένο άτομο στον απορροφητή, το οποίο έχει ένα κενό στις στοιβάδες του.

- Σκέδαση Compton: περιγράφει την ανελαστική σκέδαση ενός φωτονίου σε γωνία θ από ένα ατομικό ηλεκτρόνιο συνήθως ασθενώς συνδεδεμένο στο άτομο. Ένα ποσό κινητικής ενέργειας φωτονίου μεταβιβάζεται στο ηλεκτρόνιο, το οποίο μετά τη σκέδαση κινείται υπό γωνία φ σε σχέση με τον αρχικό άξονα του φωτονίου.

- Δίδυμη γένεση: ένα φωτόνιο μετατρέπεται σε ζεύγος ηλεκτρονίου – ποζιτρονίου. Απαιτείται μια ελάχιστη ενέργεια, ίση με το διπλάσιο της μάζας ηρεμίας του ηλεκτρονίου (1.02 MeV), ενώ πιθανή περίσσεια ενέργειας διανέμεται ισόποσα στα επιμέρους σωματίδια με τη μορφή κινητικής ενέργειας. Μετά τη δίδυμη γένεση, το ποζιτρόνιο χάνει ενέργεια και εξαϋλώνεται αφού προσεγγίσει ένα ηλεκτρόνιο.

Τα νετρόνια, ως αφόρτιστα σωματίδια, δε μπορούν να καμφθούν ή να επιταχυνθούν από μαγνητικό πεδίο, και επίσης είναι αδύνατη η ανίχνευσή τους μέσω ιονισμού των υλικών μέσα από τα οποία διέρχονται. Η πιθανότητα αλληλεπίδρασής του είναι μικρή κι έτσι μπορούν να ταξιδεύουν μακριά μέσα στην ύλη. Οι κύριοι τρόποι αλληλεπίδρασής τους με την ύλη είναι:

- Ελαστική σκέδαση νετρονίου – πυρήνα: είναι ο κυριότερος μηχανισμός απώλειας ενέργειας για νετρόνια ενέργειας της τάξεως των MeV. Η ενέργεια και η ορμή στο σύστημα νετρονίου – πυρήνα διατηρείται.
- Ανελαστική σκέδαση νετρονίου – πυρήνα: το νετρόνιο απορροφάται από τον πυρήνα και τον διεγείρει. Ο νέος πυρήνας αποδιεγείρεται με την εκπομπή ενός νετρονίου χαμηλής ενέργειας συνοδευόμενο από φωτόνια.
- Μη ελαστική σκέδαση: όπως στην ανελαστική σκέδαση, όμως αντί για νετρόνιο εκπέμπεται ένα σωμάτιο άλφα.
- Απορρόφηση με εκπομπή γ: το νετρόνιο ενσωματώνεται στον πυρήνα δημιουργώντας ισότοπο σε διεγερμένη κατάσταση, το οποίο αποδιεγείρεται με εκπομπή φωτονίων.
- Απορρόφηση με εκπομπή φορτισμένων σωματιδίων: ο σύνθετος πυρήνας αποδιεγείρεται με εκπομπή πρωτονίου, δευτερίου ή σωματίου άλφα.
- Απορρόφηση με εκπομπή νετρονίων: για υψηλής ενέργειας προσπίπτοντα νετρόνια, η αποδιέγερση του σύνθετου πυρήνα επιτυγχάνεται με την εκπομπή δύο ή τριών νετρονίων.

- Πυρηνική σχάση: η απορρόφηση νετρονίου οδηγεί τον πυρήνα σε ασταθή κατάσταση με αποτέλεσμα την παραγωγή ενός θυγατρικού πυρήνα μαζί με άλλα θραύσματα.
- Σχηματισμός αδρονικών πιδάκων: νετρόνια ενέργειας άνω των 100 MeV συγκρούονται με πυρήνα – στόχο με αποτέλεσμα τη θραύση του.

Ένας ακόμη μηχανισμός αλληλεπίδρασης είναι οι καταιγισμοί. Κατά τη διάρκεια ενός ηλεκτρομαγνητικού καταιγισμού ένα φωτόνιο με ενέργεια μεγαλύτερη ενός κρίσιμου ορίου παράγει ένα ζεύγος e^+e^- μέσω δίδυμης γένεσης, το οποίο μπορεί να παράξει εκ νέου φωτόνια μέσω ακτινοβολίας πέδησης, αν υπάρχει ικανή ενέργεια. Τα νέα αυτά φωτόνια μπορούν να παράξουν ξανά ζεύγη e^+e^- και η διαδικασία παραγωγή σωματιδίων σταματά όταν η ενέργεια πέσει κάτω από ένα κρίσιμο κατώφλι. Ένας αδρονικός καταιγισμός πραγματοποιείται μέσω της ισχυρής αλληλεπίδρασης ενός αδρονίου με τον πυρήνα των ατόμων ενός υλικού. ως αποτέλεσμα παράγονται φορτισμένα και μη πιόνια, νουκλεόνια (p,n), strange μεσόνια, βαρυόνια και φωτόνια.

3. ΤΟ ΠΕΙΡΑΜΑ ATLAS ΣΤΟΝ ΕΠΙΤΑΧΥΝΤΗ LHC ΣΤΟ CERN

3.1. Ο ΜΕΓΑΛΟΣ ΕΠΙΤΑΧΥΝΤΗΣ ΑΔΡΟΝΙΩΝ (LHC)

Ο Μεγάλος Επιταχυντής Αδρονίων είναι ο μεγαλύτερος και ισχυρότερος επιταχυντής σωματιδίων παγκοσμίως, καθώς επίσης και το μεγαλύτερο τεχνολογικό επίτευγμα στο πεδίο της φυσικής υψηλών ενεργειών και της τεχνολογίας επιταχυντών. Ο επιταχυντής είναι τοποθετημένος μέσα σε μία υπόγεια σήραγγα, με περίμετρο 26.7 km, διάμετρο 3.8 m και βάθος 50 – 175 m στα γαλλοελβετικά σύνορα.

Μία σημαντική παράμετρος για έναν επιταχυντή είναι η φωτεινότητα (L), καθορίζοντας τον αριθμό συγκρούσεων που μπορούν να παραχθούν ανά cm^2 και ανά δευτερόλεπτο, και εξαρτάται από τις παραμέτρους της δέσμης. Κατά την ονομαστική περίοδο λειτουργίας, η φωτεινότητα του LHC είναι $L = 10^{34}\ cm^{-2}\ s^{-1}$.

Οι αδρονικοί επιταχυντές παρουσιάζουν ποικίλα πλεονεκτήματα, όπως η δυνατότητα διεξαγωγής μελετών σε μεγάλο ενεργειακό φάσμα, ενώ οι επιταχυντές ηλεκτρονίου – ποζιτρονίου δε μπορούν να ανταποκριθούν στις απαιτήσεις του LHC, παρά τη δυνατότητα μετρήσεων ακριβείας, λόγω της εκπομπής ακτινοβολίας σύγχροτρου. Οι κύριοι στόχοι του LHC είναι η επιτάχυνση πρωτονίων και βαρέων ιόντων.

Πρωτού εισέλθουν τα σωματίδια της δέσμης στον τελικό δακτύλιο επιταχύνονται σταδιακά μέχρις ότου να αποκτήσουν την επιθυμητή ενέργεια. Ως πρώτο βήμα, τα πρωτόνια προερχόμενα από άτομα υδρογόνου τα οποία έχουν απογυμνωθεί από τα ηλεκτρόνιά τους, εισέρχονται σε ένα γραμμικό επιταχυντή (LINAC2). Εξερχόμενα από αυτόν, τα πρωτόνια έχουν αποκτήσει ενέργεια 50 MeV και κατευθύνονται προς τον Proton Synchrotron Booster (PSB), όπου επιταχύνονται στα 1.4 GeV. Από εκεί εισάγονται στο Proton Synchrotron (PS) αποκτώντας ενέργεια 26 GeV και στη συνέχεια στο Super Proton Synchrotron (SPS), εντός του οποίου φτάνουν στα 450 GeV. Τέλος, καταλήγουν στον LHC, επιτυγχάνοντας την τελική ενέργεια των 7 TeV ανά δέσμη. Για σύντομες χρονικές περιόδους το πρόγραμμα του LHC περιλαμβάνει συγκρούσεις βαρέων ιόντων για τη μελέτη του πλάσματος κουάρκ – γλουονίων. Στην περίπτωση αυτή, ιόντα μολύβδου επιταχύνονται στο γραμμικό επιταχυντή LINAC3 και έπειτα τροφοδοτούνται στο LEIR, όπου τα ιόντα αποθηκεύονται και ψύχονται.

Οι συγκρούσεις πραγματοποιούνται με τη διασταύρωση σε τέσσερα σημεία δύο δεσμών πρωτονίων, οι οποίες κινούνται σε αντίθετες κατευθύνσεις. Οι δέσμες δεν είναι συνεχείς, αλλά σε διακριτά πακέτα που περιέχουν $1.15\text{x}10^{11}$ πρωτόνια, ώστε οι συγκρούσεις πραγματοποιούνται σε διακεκριμένα χρονικά διαστήματα (25 ns). Ο ολικός αριθμός γεγονότων που προέρχονται από ανελαστικές συγκρούσεις στην ονομαστική φωτεινότητα ανέρχεται στα 600 εκατομμύρια ανά δευτερόλεπτο.

Για να επιτευχθεί η επιτάχυνση των πρωτονίων σε υψηλές ενέργειες απαιτείται κατάλληλος εξοπλισμός. Συγκεκριμένα, η επιτάχυνση φορτισμένων σωματιδίων γίνεται με τη βοήθεια ηλεκτρομαγνητικών κοιλοτήτων, δηλαδή ηλεκτρομαγνητικών κλωβών που περιέχουν ηλεκτρομαγνητικό πεδίο, το οποίο δημιουργείται με γεννήτρια. Κάθε κοιλότητα στον LHC ταλαντώνεται στα 400 MHz.

Οι υπεραγώγιμοι μαγνήτες αποτελούν τις πιο εξελιγμένες τεχνολογικές κατασκευές στον επιταχυντή LHC. Μια βασική δομή του επιταχυντή είναι το μαγνητικό δίπολο, με σκοπό να εξαναγκάσει τις δέσμες σε κυκλική τροχιά. Ο τοροειδής σωλήνας κενού του διπόλου που εμπεριέχει τη δέσμη τοποθετείται στον χώρο μεταξύ των πόλων, οι οποίοι δεν είναι παράλληλοι μεταξύ τους, αλλά εμφανίζουν κάποια κλίση ώστε το παραγόμενο πεδίο να μειώνεται με την αύξηση της ακτίνας. Μια παράλληλη βασική μονάδα του επιταχυντή LHC είναι τα υπεραγώγιμα μαγνητικά τετράπολα, τα οποία λειτουργούν ως συγκεντρωτικός φακός ώστε οι δέσμες να συναντώνται κεντρικά, αυξάνοντας την πιθανότητα αλληλεπίδρασης.

Το βασικό σύστημα για την λειτουργία του υπεραγώγιμου επιταχυντή LHC είναι το σύστημα ψύξης (Cryogenesis) που τροφοδοτεί όλα τα μαγνητικά στοιχεία του LHC. Όλα τα υπεραγώγιμα καλώδια NbTi των μαγνητών βρίσκονται σε θερμοκρασία 1,8°K χρησιμοποιώντας υπέρρευστο υγρό ήλιο ως μέσο ψύξης. Οι αγωγοί αυτοί πρέπει να παραμείνουν σε υπεραγώγιμη κατάσταση ακόμα και όταν το διερχόμενο ρεύμα μεταβάλλεται. Η διατήρηση αυτή είναι βασική λόγω του ισχυρού μαγνητικού πεδίου.

Στα 4 σημεία διασταύρωσης των δεσμών έχουν τοποθετηθεί ανιχνευτές. Ο ATLAS (A Toroidal LHC ApparatuS) και ο CMS (Compact Muon Solenoid) είναι γενικού σκοπού ανιχνευτές για την μεγάλου φάσματος έρευνα. Το πείραμα ATLAS περιγράφεται στη συνέχεια. Το CMS αποτελείται από ανιχνευτή 12000 τόνων, βασισμένο σε έναν υψηλού πεδίου συμβατικό μαγνήτη. Το πείραμα ALICE experiment (A Large Ion Collider Experiment) ειδικεύεται σε μελέτες φυσικής βαρέων ιόντων και του πλάσματος κουάρκ – γλουονίων. Το πείραμα LHCb εστιάζει σε μελέτες για τις ιδιότητες των b κουάρκ και στοχεύει σε μετρήσεις σχετικές με την παραβίαση της CP συμμετρίας.

3.2. ΤΟ ΠΕΙΡΑΜΑ ATLAS

Ο ανιχνευτής ATLAS αποτελεί τη μεγαλύτερη ανιχνευτική συσκευή στο πρόγραμμα του LHC. Σκοπός του είναι η λήψη μετρήσεων σχετικά με τον τύπο τις τροχιές και τις ενέργειες των σωματιδίων που παράγονται κατά τις συγκρούσεις. Λόγω των συνθηκών στον LHC, οι ανιχνευτές πρέπει να έχουν γρήγορα και ανθεκτικά στην ακτινοβολία ηλεκτρονικά, ικανοποιητική διακριτική ικανότητα αναφορικά με την ορμή φορτισμένων σωματιδίων και αποδοτική ανακατασκευή τροχιών, θερμιδόμετρα ικανά για τη μέτρηση και την αναγνώριση φωτονίων και ηλεκτρονίων, σύστημα μιονίων ικανό στην αναγνώριση ορμής και ικανότητα ακριβούς αναγνώρισης του φορτίου των μιονίων, και πολύ αποδοτικό σύστημα σκανδαλισμού.

Ο ATLAS είναι κυλινδρικός, αποτελούμενος από ομοαξονικούς κυλίνδρους αυξανόμενης ακτίνας, με μήκος 46 m, ύψος 25 m και βάρος 7000 τόνους. Είναι συμμετρικός ως προς το σημείο αλληλεπίδρασης (IP) και διαχωρίζεται στο κυλινδρικό τμήμα και σε σημεία κυκλικών δίσκων (end – caps). Αναλυτικά, ο ATLAS απαρτίζεται από τα συστήματα που περιγράφονται ακολούθως.

Το σύστημα συντεταγμένων του ATLAS υπαγορεύει ότι ο z άξονας είναι συνευθειακός της δέσμης, ο x κατευθύνεται προς το κέντρο του LHC ενώ ο y προς τα επάνω, r είναι η αξονική απόσταση από τον άξονα της δέσμης, ενώ η γωνία φ ορίζεται ως η αζιμουθιακή και θ η πολική.

Ο σωλήνας της δέσμης χωρίζεται σε 5 περιοχές με διαφορά στο μήκος, στο πάχος και στο υλικό του τοιχώματος, και ουσιαστικά αποτελεί το συνδετικό στοιχείο μεταξύ του ATLAS και του LHC.

Το εσώτερο ανιχνευτικό στρώμα είναι ο εσωτερικός ανιχνευτής (ID). Κύριος σκοπός του είναι η αναγνώριση του είδους των σωματιδίων και την ορμή τους, εξετάζοντας την αλληλεπίδρασή τους με το υλικό του ανιχνευτή σε διάφορα σημεία, αναγνωρίζοντας το μονοπάτι που σχηματίζουν κατά τη διέλευσή τους. Ο εσωτερικός ανιχνευτής περιβάλλεται από ημιαγώγιμο μαγνήτη 2T στο κέντρο του, ο οποίος καμπυλώνει τις τροχιές των σωματιδίων, αποκαλύπτοντας το φορτίο τους ανάλογα με την κατεύθυνση της καμπύλωσης, και την ορμή ανάλογα το βαθμό της καμπύλωσης. Τα συστήματα του εσωτερικού ανιχνευτή βασίζονται σε ανιχνευτές μικροταινίας πυριτίου. Τρία διαφορετικά στρώματα σε αυξανόμενη ακτίνα μπορούν να αναγνωριστούν: ο ανιχνευτής pixel, ο ημιαγώγιμος ανιχνευτής τροχιών και ο ανιχνευτής ακτινοβολίας μετάβασης. Οι συγκρούσεις που ανιχνεύονται στα επιμέρους τμήματα συνδυάζονται για την ανακατασκευή τροχιών.

Το θερμιδόμετρο του ATLAS αποτελείται από το ηλεκτρομαγνητικό και το αδρονικό θερμιδόμετρο, τα οποία είναι τοποθετημένα έξω από το σωληνοειδή μαγνήτη μεταξύ του εσωτερικού ανιχνευτή και του φασματόμετρου μιονίων. Τα θερμιδόμετρα καλούνται να μετρήσουν την ενέργεια και τη θέση ηλεκτρονίων και φωτονίων με δειγματοληψία της εναποτιθέμενης ενέργειας, να αναγνωρίσουν σωματίδια, να υπολογίσουν την ελλείπουσα εγκάρσια ορμή ενός γεγονότος, όπως επίσης και την ενέργεια και κατεύθυνση πιδάκων. Επιπλέον, συνεισφέρουν στην επιλογή γεγονότων για το σύστημα σκανδαλισμού. Λόγω του τεράστιου πλήθους συγκρούσεων ανά διασταύρωση δέσμης στην ονομαστική φωτεινότητα του LHC, παρατηρείται χωρική και χρονική συσσώρευση (pileup), συνεπώς τα θερμιδόμετρα πρέπει να χαρακτηρίζονται από υψηλή απόκριση ανίχνευσης και λεπτομερή διακριτική ικανότητα. Όσον αφορά το ηλεκτρομαγνητικό θερμιδόμετρο, ο ρόλος του είναι να απορροφά την ενέργεια σωματιδίων τα οποία αλληλεπιδρούν ηλεκτρομαγνητικά με αυτό. Το ενεργό υλικό του είναι υγρό Αργό, ενώ το απορροφητικό Μόλυβδος. Ο Μόλυβδος προκαλεί καταιγισμούς σωματιδίων έτσι ώστε τα σωματίδια καθώς αλληλεπιδρούν με το υγρό Αργό να προκαλούν ιονισμό ηλεκτρονίων. Το αδρονικό θερμιδόμετρο απορροφά την ενέργεια σωματιδίων που διαπερνούν το ηλεκτρομαγνητικό χωρίς ισχυρή αλληλεπίδραση (κυρίως αδρόνια).

Το φασματόμετρο μιονίων αποτελεί το εξώτερο τμήμα του ανιχνευτή, σχεδιασμένο για την ακριβή μέτρηση της ορμής των μιονίων, τα οποία διαπερνούν τα προηγούμενα τμήματα, για το λόγο αυτό και είναι μεγαλύτερο σε μέγεθος. Οι τροχιές των μιονίων καμπυλώνονται τεχνητά με τη χρήση μαγνητικού πεδίου με σκοπό τη μέτρηση της ορμής τους˙ όσο μεγαλύτερη είναι η ορμή ενός μιονίου, η τροχιά του θα καμπυλώνεται λιγότερο. Τέσσερις διαφορετικές τεχνολογίες απαρτίζουν το φασματόμετρο, συγκεκριμένα δύο υποανιχνευτές, τα MDT και τα CSC, και δύο τεχνολογίες σκανδαλισμού, τα RPC και τα TGC. Στα MDT η διέλευση ενός μιονίου προκαλεί ιονισμένα ηλεκτρόνια να κατευθυνθούν προς το θετικό ηλεκτρόδιο, ενώ θετικά ιόντα ολισθαίνουν προς το αρνητικό ηλεκτρόδιο. Στα CSC η ακρίβεια των συντεταγμένων ενός διερχόμενου μιονίου επιτυγχάνεται μετρώντας το εναποτιθέμενο φορτίο στις βαθμονομημένες καθοδικές λωρίδες που διαθέτουν με το σχηματισμό ‘χιονοστιβάδας’ στο ανοδικό καλώδιο. Το σύστημα σκανδαλισμού μιονίων επιλέγει μιόνια υψηλής ορμή. Μια καλή προσέγγιση για την εύρεση τροχιάς ενός μιονίου είναι με χρήση της sagitta, η οποία ορίζεται ως η μέγιστη απόκλιση της κυκλικής τροχιάς από την ευθεία γραμμή. Η ανακατασκευή τροχιάς είναι εφικτή όταν κάθε μιόνιο εντός συγκεκριμένου εύρους ψευδωκύτητας διασχίζει τουλάχιστον 3 ανιχνευτικούς σταθμούς.

Ο ανιχνευτής LUCID, ένας από τους εμπρόσθιους ανιχνευτές, είναι ο κύριος μετρητής φωτεινότητας του ATLAS και ανιχνεύει μη ελαστικές σκεδάσεις στην πρόσθια περιοχή. Ο δεύτερος πρόσθιος ανιχνευτής, ο ALFA, συμμετέχει επίσης στη μέτρηση φωτεινότητας. Το τρίτο πρόσθιο σύστημα, το θερμιδόμετρο μηδενικού βαθμού, παίζει κυρίαρχο ρόλο στον προσδιορισμό της κεντρικότητας σύγκρουσης βαρέων ιόντων.

Το σύστημα σκανδαλισμού καλείται να επεξεργαστεί και να αποθηκεύσει δεδομένα, η ποσότητα των οποίων όμως καλείται να μειωθεί κατά περίπου 10^7 σε σχέση με τα δεδομένα που παράγονται σε κάθε σύγκρουση. Το σύστημα σκανδαλισμού του ATLAS αποτελείται από τρία επίπεδα, με κάθε υψηλότερο επίπεδο να χρησιμοποιεί τις πληροφορίες για αποφάσεις που πάρθηκαν στο προηγούμενο επίπεδο, εισάγοντας κάποια επιπλέον κριτήρια επιλογής. Απαρτίζεται συνολικά από τον κεντρικό επεξεργαστή σκανδαλισμού (CTP), ο οποίος τροφοδοτείται από σήματα που προέρχονται από το υλικό του σκανδαλισμού των θερμιδόμετρων (L1 Calo) και του συστήματος μιονίων (L1 Muon). Το πρώτο επίπεδο είναι βασισμένο στο υλικό (hardware) με χρήση επεξεργαστών και βασίζεται σε λογική σωλήνωσης, δίνοντας τη δυνατότητα λήψης απόφασης εντός του χρόνου απόκρισης του ανιχνευτή και επιτρέποντας παραλληλοποίηση των λειτουργιών με χρήση διαφορετικών επεξεργαστών. Η απόφαση μπορεί να ληφθεί μέσα σε 2.5 μs. Το δεύτερο επίπεδο είναι βασισμένο στο λογισμικό (software) και χρησιμοποιεί προγράμματα που τρέχουν σε διαφορετικούς υπολογιστές με διαφορετικούς επεξεργαστές το καθένα. Η πλήρης υπολογιστική ισχύς βασίζεται σε πολύπλοκους αλγορίθμους σκανδαλισμού μειώνοντας τη συχνότητα σκανδαλισμού με αντίστοιχο μέσο χρόνο επεξεργασίας 40 ms. Το τρίτο επίπεδο είναι επίσης βασισμένο στο λογισμικό με μέσο χρόνο επεξεργασίας στα 4 δευτερόλεπτα.

Τα δεδομένα αφού περάσουν από το σύστημα σκανδαλισμού οδηγούνται για επεξεργασία. Ο τεράστιος όγκος δεδομένων καθιστά αδύνατη τη διαχείριση εντός των εγκαταστάσεων του CERN και για το λόγο αυτό έχει αναπτυχθεί παγκόσμιο υπολογιστικό πλέγμα, το οποίο διανέμει τα δεδομένα σε τέσσερα επίπεδα (Tiers). Κάθε επίπεδο αποτελείται από πολλαπλά κέντρα και παρέχει διαφορετικές υπηρεσίες. Το Tier 0 παρέχει λιγότερο από το 20% της συνολικής χωρητικότητας του υπολογιστικού πλέγματος, διατηρεί backup αντίγραφα και πραγματοποιεί τα πρώτα στάδια ανακατασκευής των αρχικών δεδομένων. Το Tier 1 διατηρεί ένα δεύτερο αντίγραφο των αρχικών αλλά και των ανακατασκευασμένων δεδομένων και διανέμει τα δεδομένα στο επόμενο επίπεδο. Το Tier 2 διαθέτει πάνω από 160 κέντρα παγκοσμίως αφιερωμένα στην προσομοίωση και ανάλυση από πλευράς χρήστη. Τα μικρότερα κέντρα του Tier 3 προσφέρουν τοπική πρόσβαση σε μεμονωμένους επιστήμονες.

4. ΠΡΟΣΟΜΟΙΩΣΕΙΣ ΜΕ ΤΗ ΜΕΘΟΔΟ MONTE CARLO ΚΑΙ ΣΥΜΠΕΡΑΣΜΑΤΑ

Αρχικά, πραγματοποιήθηκαν μερικές δοκιμές με χρήση απλών γεωμετριών ώστε να προσδιοριστούν οι διάφορες παράμετροι που πιθανόν να επηρεάσουν τα τελικά αποτελέσματα σε μεγαλύτερες και πιο περίπλοκες γεωμετρίες, όπως αυτή του ανιχνευτή ATLAS.

Οι προσομοιώσεις σε αρχικό επίπεδο εκτελέσθηκαν με τη χρήση ενός απλού κυλίνδρου με διαστάσεις όμοιες με αυτές του ανιχνευτή ATLAS (50 m μήκος κατά τον x άξονα και ακτίνα 12.5 m), ενώ ως πηγή τοποθετήθηκε στο κέντρο της διάταξης (0,0,0) κοβάλτιο – 60, το οποίο σε επίπεδο κώδικα MCNP περιγράφεται από την εκπομπή δύο φωτονίων με κορυφές στα 1.173 MeV και 1.332 MeV. Ο κύλινδρος αυτός περιέχει αέρα, ενώ η προσομοίωση έτρεξε για 1 λεπτό. Όπως ήταν αναμενόμενο, η ροή φωτονίων στις κάθετες πλευρές ήταν σχεδόν ίση, με πιθανές αποκλίσεις να οφείλονται στην τυχαιότητα που εισάγει η εφαρμογή της μεθόδου Monte Carlo. Με βάση τον κύλινδρο αυτό, επιπλέον δοκιμές πραγματοποιήθηκαν, με αλλαγή της κατανομής της πηγής, του αριθμού εκπεμπόμενων φωτονίων και της ενέργειας των φωτονίων αυτών, όπως επίσης και αλλαγή των περιεχομένων υλικών. Βάσει των παραπάνω παρατηρήθηκαν τα ακόλουθα:

- Η ροή σε επιφάνεια για κύλινδρο που περιέχει αέρα εξαρτάται έντονα από τον αριθμό των εκπεμπόμενων σωματιδίων, αφού η έξοδος του MCNP δίνει ως αποτέλεσμα ροή ανά σωματίδιο πηγής. Αντιθέτως, η ενέργεια των σωματιδίων πηγής δεν επηρεάζει ιδιαίτερα τη ροή, μονάχα μετατοπίζει το φάσμα της ροής.
- Τα πηγαία σωματίδια μεγαλύτερης ενέργειας διαμορφώνουν λιγότερο καμπύλες τροχιές με αποτέλεσμα να φτάνουν πιο μακριά, όπως μπορεί να διαπιστωθεί με τη χρήση του γραφικού περιβάλλοντος του MCNP (Vised).
- Ο αριθμός των πηγών επίσης επηρεάζει έντονα τη ροή, αφού παράγονται περισσότερα πηγαία σωματίδια. Η μετατόπιση της πηγής είναι δυνατό να επηρεάσει μόνο τις επιφάνειες στις οποίες πλησιάζει επιφέροντας μεγαλύτερη ροή, ή αυτές από τις οποίες απομακρύνεται, με αποτέλεσμα μικρότερη ροή.
- Σε υλικά πέραν του αέρα, η αύξηση της ενέργειας πηγής επηρεάζει την επαγόμενη ροή με αύξοντα τρόπο.

Η προσομοίωση συνεχίστηκε με σχεδιασμό του ανιχνευτή ATLAS χρησιμοποιώντας κυλινδρικές δομές, με διαστάσεις και υλικά που επιλέχθηκαν μετά από ενδελεχή αναζήτηση στην υπάρχουσα βιβλιογραφία και προσαρμογή των πραγματικών δεδομένων σύμφωνα με τους περιορισμούς του MCNP. Αρχικά, σχεδιάστηκαν οι πέντε περιοχές του σωλήνα της δέσμης συμμετρικά ως προς το σημείο αλληλεπίδρασης, το οποίο αποτελεί το κέντρο της γεωμετρίας και σημείο συμμετρίας. Στη συνέχεια, γύρω από το σωλήνα τοποθετούνται σε αυξανόμενη απόσταση και ακτίνα οι υπόλοιπες υποπεριοχές του ATLAS: ο εσωτερικός ανιχνευτής, τα θερμιδόμετρα, το σύστημα μιονίων, οι υπεραγώγιμοι μαγνήτες και οι περιοχές θωράκισης. Η γεωμετρία αυτή περιβάλλεται από ορθογώνιο παραλληλεπίπεδο που αντιπροσωπεύει τις διαστάσεις της κοιλότητας εντός της οποίας έχει τοποθετηθεί ο ανιχνευτής.

Μετά το σχεδιασμό του ανιχνευτή δοκιμάζονται διάφορες πηγές οι οποίες να μπορούν να δώσουν ικανοποιητικές τιμές του υποβάθρου σε συγκεκριμένες επιφάνειες και συγκρινόμενες με επίσημες μετρήσεις να αποκλίνουν όσο το δυνατόν λιγότερο. Για το λόγο αυτό δοκιμάστηκε τόσο σημειακή πηγή όσο και κυλινδρική κατά μήκος του σωλήνα της δέσμης. Η ενέργεια των πηγαίων φωτονίων τέθηκε στα 100 MeV, καθώς αυτή αποτελεί μια σχετικά υψηλή ενέργεια για φωτόνια υποβάθρου ώστε να μην έχουμε απώλεια πληροφορίας. Επιπλέον, τα 100 MeV αποτελούν το ανώτατο όριο ενέργειας που επιτρέπει το MCNP χωρίς εξειδικευμένες χειροκίνητες τροποποιήσεις των φυσικών χαρακτηριστικών του προβλήματος. Οι δοκιμές στο γραφικό περιβάλλον έδειξαν ότι τα σωματίδια δυσκολεύονται να φτάσουν σε μακρινές περιοχές του ανιχνευτή λόγω απόστασης και απορροφητικότητας των παρεμβαλλόμενων υλικών. Για λεπτομερείς μετρήσεις τοποθετήθηκαν αισθητήρες σε διάφορες περιοχές του ανιχνευτή η οποίες έχουν μελετηθεί διεξοδικά σε προηγούμενες προσομοιώσεις. Κάθε κελί της γεωμετρίας μπορεί να προσδίδει διαφορετική ‘βαρύτητα’ (importance) στα σωματίδια που εισέρχονται σε αυτό˙ σε περιοχές που η ανίχνευσή τους καθίσταται δύσκολη, η πιθανότητα επιβίωσής τους μπορεί να αυξηθεί με αύξηση του importance, όπως και προτείνεται στο εγχειρίδιο του MCNP. Η προσομοίωση αυτή έτρεξε για 24 ώρες, χρόνος αρκετός ώστε να μειωθεί σημαντικά το στατιστικό σφάλμα των μετρήσεων και τα αποτελέσματα να είναι αξιόπιστα, ενώ το importance θεωρήθηκε σε κάθε κελί ίσο με το 1 (αναλογική προσομοίωση). Οι μετρήσεις παρατηρήθηκαν ότι ήταν αρκετά κοντά σε αυτές των προηγούμενων μελετών, με ανεκτές αποκλίσεις. Συνεπώς, εν συνεχεία πάρθηκαν μετρήσεις και σε άλλα σημεία της γεωμετρίας, συγκεκριμένα στα διάφορα κελιά των υποανιχνευτικών συστημάτων, των μαγνητών και των περιοχών θωράκισης. Η ροή μειωνόταν σταδιακά προχωρώντας προς εξώτερα σημεία, ενώ σε διάφορα σημεία της θωράκισης μηδενιζόταν, γεγονός που επιβεβαιώνει ότι οι μετρήσεις ροών στα κελιά είναι λογικές. Δοκιμάστηκε ακόμα, για λόγους πληρότητας, και η μη αναλογική προσομοίωση. Πρώτα, μετά από μια σύντομη δοκιμή πάρθηκαν οι μετρήσεις πληθυσμού φωτονίων σε κάθε κελί. Με βάση της τιμές αυτές υπολογίστηκε ο λόγος πληθυσμών κάθε εσωτερικής περιοχής σε σχέση με μια γειτονική πιο εξωτερική, δίνοντας μια τιμή, με στρογγυλοποίηση της οποίας λαμβάνουμε το νέο importance. Η προσομοίωση αυτή έτρεξε επίσης για 24 ώρες. Τα αποτελέσματα των ροών φωτονίων στις περισσότερες επιφάνειες ήταν βελτιωμένο σε σχέση με την αναλογική προσομοίωση, όμως σε κάποιες περιπτώσεις παρουσίασε μεγάλες αποκλίσεις. Ακολούθως, πάρθηκαν μετρήσεις σε κελιά όπως και στην αναλογική προσομοίωση, παρουσιάζοντας πολύ μικρές αποκλίσεις από την αναλογική. Πιθανόν, ένας βελτιωμένος τρόπος υπολογισμού του importance για τα κελιά, λαμβάνοντας υπ’ όψιν περισσότερα γειτονικά κελιά και όχι μόνο ένα, να έδινε ακριβέστερες μετρήσεις.

Επιπλέον βελτιώσεις θα μπορούσαν να παρατηρηθούν με μια ακριβέστερη προσέγγιση της γεωμετρίας του ανιχνευτή και με εκτέλεση της προσομοίωσης για περισσότερο χρόνο. Ο περιορισμός στη σύνθεση μιγμάτων και κραμάτων από το MCNP υπήρξε ένας επιπλέον λόγος αποκλίσεων από άλλες προσομοιώσεις. Παρόλα αυτά, τα σφάλματα δεν είναι πολύ μεγάλα και ως μελλοντική έρευνα θα μπορούσαν να ελαχιστοποιηθούν με δοκιμές στη μεταβολή διαφόρων παραμέτρων της προσομοίωσης.

V. CONTENTS

1. INTRODUCTION

1.1. THE STANDARD MODEL

The Standard Model of particle physics (SM) describes all of the known fundamental particles, along with their interactions, via three out of the four interactions of nature: electromagnetism, the weak interaction and the strong interaction. Gravity is not yet included in the Standard Model as it plays no significant role at the energy scale of particle physics.

According to the Standard Model, there are three kinds of elementary particles: leptons, quarks and the force mediators (gauge bosons). An antiparticle corresponds to each of the elementary particles. Leptons and quarks are fermions, having a spin of ½ , and they obey the Fermi – Dirac statistics, so the Pauli exclusion principle does not allow the occupation of any single quantum state by more than one particle of a given type.

The leptons carry integral electric charge and are divided into three generations, each composed by the charged lepton (e, μ and τ) differing only in mass (mass is increasing in every generation with respect to the previous one) and its neutrino partner (ν_e, ν_μ and ν_τ respectively). [1]

Generation	*Lepton*	*Mass (MeV)*	*Charge*
I	e	0.511	-1
	ν_e	$< 0.26 \cdot 10^{-3}$	0
II	μ	105.69	-1
	ν_μ	< 0.19	0
III	τ	1776.99	-1
	ν_τ	< 18.2	0

Table 1.1: Generations of Leptons. [1]

The quarks carry fractional electric charges, +2|e|/3 or −|e|/3. There are six flavours of quarks divided into three generations of increasing mass. Quarks can carry one of three possible ‘colours’ (red, blue or green), while anti – quarks carry anti – colors, and they are grouped by the strong force, via gluon exchange, in order to form hadrons. The hadrons are categorized into two families, mesons and baryons. Mesons are composed of a quark–antiquark pair with integer spin, while baryons are composed of a triplet of quarks with half-integer spin. [2]

Generation	***Quark***	***Mass (GeV)***	***Charge***
I	Up (u)	$< 2.3 \cdot 10^{-3}$	+2/3
	Down (d)	$4.8 \cdot 10^{-3}$	-1/3
II	Charm (c)	1.275 ± 0.025	+2/3
	Strange (s)	$(95 \pm 5) \cdot 10^{-3}$	-1/3
III	Top (t)	173.2 ± 0.7	+2/3
	Bottom (b)	4.18 ± 0.03	-1/3

Table 1.2: Generations of quarks. [1]

The mediators of the interactions between fermions are integer spin particles that obey to Bose-Einstein statistics, which allows the occupation of a single quantum state by a large number of identical particles. The electromagnetic force, described by Quantum Electrodynamics (QED), is carried by spin-1 photons and acts between electrically charged particles. The weak interaction, described by the Electroweak Theory (EWT), is responsible for nuclear β-decays, and absorption and emission of neutrinos, and has three massive gauge bosons with spin 1, $W^{\pm}$ and Z. The gauge bosons of the strong interaction, described by Quantum Chromodynamics (QCD), are the eight massless, spin-1 gluons (g). The graviton (G), a purely theoretical spin-2 boson, is considered to be the gauge boson for gravity. [2]

Boson	***Mass (GeV)***	***Charge***	***Interaction***
G	$< 7 \cdot 10^{-41}$	0	gravitational
γ	0	0	electromagnetic
$W^{\pm}$	80.4	±1	weak
Z	91.2	0	weak
g	0	0	strong

Table 1.3: Six bosons for the four fundamental forces. [1]

1.2. LHC PHYSICS

The study of nature is based on the production and screening of rare procedures, the presence of which can be more frequent if higher energies are provided. By producing more collisions, more interesting facts that might give confirmation on theoretical studies can occur.

The Large Hadron Collider (LHC) has been designed in order to answer essential questions of the Standard Model that are described below.

1.2.1. THE HIGGS BOSON

The mechanism that describes how the particles gain mass has been incorporated in the SM via the the Brout – Englert – Higgs mechanism. This mechanism requires the existence of a spin zero boson, the Higgs boson, which has been observed by the ATLAS and CMS experiments. For a Higgs boson with a mass of 126 GeV/c^2 the SM predicts a mean life time of about 1.6×10^{-22} s. [3]

At the LHC, the Higgs boson can be produced in the following ways: [1],[4],[5],[6]

- Gluon fusion: gg → H

Gluon fusion is the dominant production mode. If the collided particles are hadrons such as the proton or antiproton then it is most likely that two of the gluons binding the hadron together collide. The easiest way to produce a Higgs particle is if the two gluons combine to form a loop of virtual quarks. this process is more likely for heavy particles, since the coupling of particles to the Higgs boson is proportional to their mass.

- Vector boson fusion (VBF): $q\bar{q}\rightarrow q\bar{q}H$

VBF is the next more important production mode. When two fermions or antifermions collide, they exchange a virtual W or Z boson, which emits a Higgs boson. The colliding fermions do not need to be the same type.

- Associated production with vector bosons (Higgs Strahlung): $q\bar{q}\rightarrow WH$ or $q\bar{q}\rightarrow ZH$

If an elementary fermion collides with an anti-fermion the two can merge to form a virtual W or Z boson, which, if it carries sufficient energy, can then emit a Higgs boson. At the LHC this process is only the third largest, because the LHC collides protons with protons.

- Associated production with heavy quarks: $q\bar{q}\rightarrow Q\bar{Q}H$ or gg → $Q\bar{Q}H$

The final process that is commonly considered is by far the least. It involves two colliding gluons, which each decay into a heavy quark–antiquark pair. A quark and antiquark from each pair can then combine to form a Higgs particle.

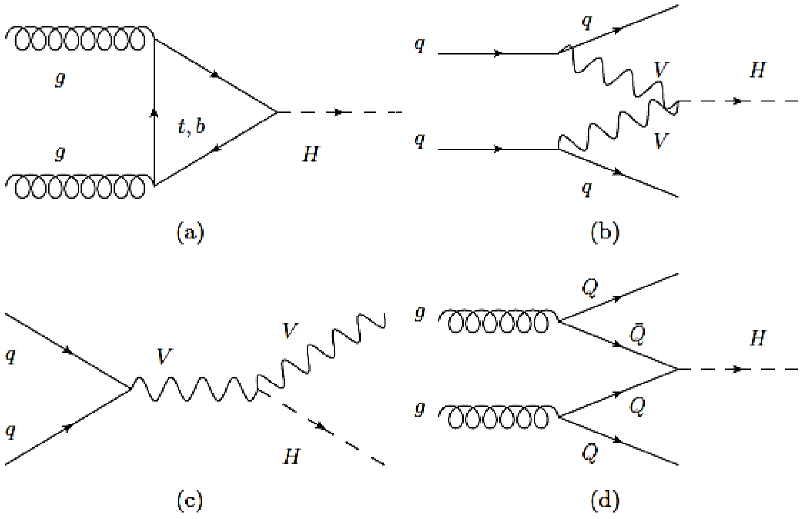

(a) (b)

(c) (d)

Figure 1.1 : Main production mechanisms of the Standard Model Higgs at LHC: (a) gluon – gluon fusion (b) vector boson fusion (c) associated production with W/Z and (d) associated production with heavy quarks. [1]

The Higgs decays in different modes and the branching ratio of each depends on the Higgs mass. The decay modes can be divided into the decays to fermions and the decays to bosons.

A possible Higgs decay is by splitting into a fermion–antifermion pair. Higgs is more likely to decay into heavy fermions than light fermions, because the mass of a fermion is proportional to the strength of its interaction with the Higgs. In the low mass region, where $m_H \leq$ 130 GeV, the most common but not easily accessible decay is into a bottom–antibottom quark pair (56.1%), while the second most common fermion decay (6%) at that mass is a tau–antitau pair, $qqH \rightarrow \tau^+\tau^-$. The taus can subsequently decay into pairs of leptons, hadrons or mixed.

Higgs also can split into a pair of massive gauge bosons. For $m_H >$ 130 GeV, the most possible Higgs decay is into a pair of W bosons (23.1%). The W bosons can subsequently decay either into a quark and an antiquark or into a charged lepton and a neutrino. However, the W bosons decays into quarks are difficult to distinguish from the background, and the decays into leptons cannot be fully reconstructed, because neutrinos are impossible to detect in particle collision experiments. A cleaner signal is given by decay into a pair of Z-bosons (2.9%), if each of the bosons subsequently decays into a pair of easy detectable charged leptons (electrons or muons).

Massless gauge bosons, photons or gluons, do not couple directly to the Higgs boson but through loops involving massive charged and/or colored particles which couple to the Higgs boson. The most common such process is the decay into a pair of gluons through a loop of virtual heavy quarks. This process, which is the reverse of the gluon fusion process, happens approximately 8.5% of the time. Much rarer is the decay into a pair of photons mediated by a loop of W bosons or heavy quarks, which happens only twice for every thousand decays. However, this process is very relevant for experimental searches for the Higgs boson, because the energy and momentum of the photons can be measured very precisely, giving an accurate reconstruction of the mass of the decaying particle. [5],[6]

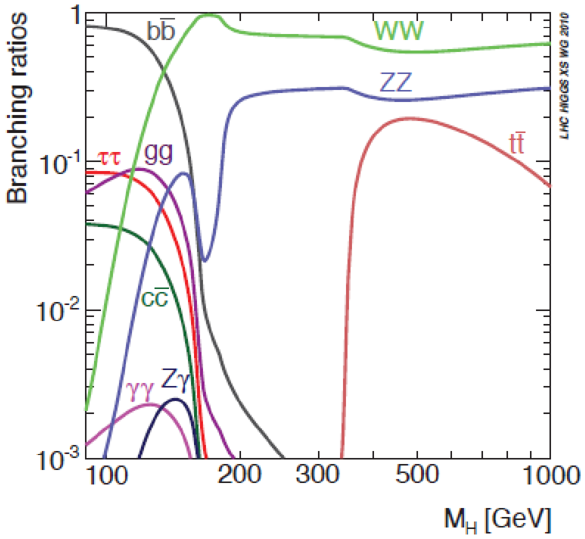

Figure 1.2: The branching ratios of the SM Higgs as a function of its mass. [1]

1.2.2. SUPERSYMMETRY

According to Supersymmetry Theory (SUSY), which may can lead to the unification of the fundamental forces, every particle has its heavier symmetric pair. The particles differ from their respective supersymmetric ones as to the spin by ½, resulting in tranforming the fermions of the Standard Model into supersymmetry bosons and vice versa. If supersymmetric particles were included in the Standard Model, the interactions of its three forces – electromagnetism and the strong and weak nuclear forces – could have the exact same strength at very high energies, as in the early universe. If this theory is correct, some of the lightest supersymmetric particles may be observed at LHC. [7],[52]

1.2.3. THE MATTER-ANTIMATTER ASYMMETRY PROBLEM (CP VIOLATION)

The Big Bang should have created equal amounts of matter and antimatter in the early universe. Nevetheless, everything in universe from the smallest life forms on Earth to the largest stellar objects, is made almost entirely of matter. Comparatively, there is not much antimatter to be found, so one of the greatest challenges in physics is to figure out the reason of the asymmetry between matter and antimatter. [51]

1.2.4. STUDY OF QUARK – GLUON PLASMA

For a few millionths of a second, shortly after the Big Bang, the universe was filled with an astonishingly hot, dense soup made of all kinds of particles moving at near the speed of light. This mixture was dominated by quarks and by gluons, that normally “glue” quarks together. In those first moments of extreme temperature, however, quarks and gluons were bound only weakly, free to move on their own in the so called quark-gluon plasma. To recreate conditions similar to those of the primordial universe, powerful accelerators like LHC make head-on collisions between massive ions, such as gold or lead nuclei. In these heavy-ion collisions the hundreds of protons and neutrons in two such nuclei smash into one another at energies of upwards of a few trillion electronvolts each. [50]

2. INTERACTIONS OF PARTICLES WITH MATTER

The operation of every detection system relies on radiation interactions with the detection medium [9] and the product of this interaction transforms into an electric signal. The interaction process depends on the type and the energy of the incident particles. Radiation can be separated into radiation of charged particles that continuously interact with the electrons of the medium via Coulomb force and particles without charge. The first category includes the radiation of heavy charged particles and accelerated electrons, while the second includes neutrons, X-rays and gamma rays.

2.1. INTERACTION OF HEAVY CHARGED PARTICLES

The interaction of heavy charged particles mainly with the negative charge of the electrons of the absorber and lesser with the atomic nucleus occurs through electromagnetic interactions (Coulomb force). The distance between the atoms and the particle orbit determines whether the impulse on the electrons due to Coulomb interaction forces these electrons to transition from their initial state to a higher bound energy state (*excitation*) or in the continuum where they are no longer bound (*ionization*). Further energy loss mechanisms are nuclear interactions, braking radiation, Cherenkov radiation and transition radiation. As a result of these mechanisms the passing particle decelerates and is finally absorbed by the material. [9]

Consider a particle of mass M moving with velocity v and an immobilized free electron of mass m_e at rest, v_1 the particle velocity after the percussion and v_2 the electron velocity. The kinetic energy and momentum of the system are maintained, so: [8]

$$\mathrm{M}v^2 = \mathrm{M}v_1^2 + \mathrm{M}v_2^2 \qquad \textbf{(1)}$$

$$Mv = Mv_1 + m_e v_2 \qquad \textbf{(2)}$$

Based on these expressions the final velocities are:

$$v_2 = \frac{Mv - Mv_1}{m_e} \quad \textbf{(3)} \qquad \text{and} \qquad v_1 = \frac{(M - m_e)v}{M + m_e} \quad \textbf{(4)}$$

Figure 2.1: Before and after collision [9]

After the collision, the particles are moving along the initial line of the incident charged particle. By using the relation (4) the maximum transferred energy is:

$$Q_{\max} = \frac{1}{2} M v^2 - \frac{1}{2} M v_1^2 = \frac{4 M m_e E}{(M + m_e)^2} \qquad \textbf{(5)}$$

Proton kinetic energy (MeV)	***Q_{max} (MeV)***	***Maximum percentage energy transfer (MeV)***
0.1	0.00022	0.22
1	0.0022	0.22
10	0.0219	0.22
100	0.229	0.23
1000	3.33	0.33
10000	136	1.4
100000	$1.06 \cdot 10^4$	10.6
1000000	$5.38 \cdot 10^5$	53.8
10000000	$9.21 \cdot 10^6$	92.1

Table 2.1: Maximum possible energy transfer during proton – electron collision. [8]

In the case of non – relativistic energies, it is apparent that the maximum energy the charged particles losses in every interaction is small comparing to its initial energy, so it needs many interactions until it yields all of its energy and then stop. Each of these interactions will not contribute significantly to change the direction of the charged particle, which interacts simultaneously with many electrons. These electrons push the particle in a different direction each, so eventually the particle trajectory is almost a straight line. In the case of relativistic energies for the charged particle (mass M) of momentum $M\beta\gamma c$, the maximum transferred energy is:

$$Q_{max} = \frac{2\gamma^2 m_e v^2}{1 + \frac{2\gamma m_e}{M} + \frac{m_e^2}{M^2}}$$

$\gamma = 1 / \sqrt{1 - \beta^2}$, $\beta = {}^{v}\!/_{c}$ and c the speed of light. [11]

2.1.1. STOPPING POWER DUE TO COULOMB INTERACTIONS

The mean rate of energy loss of heavy charged particles via Coulomb interactions per unit length, called stopping power, is given by the Bethe – Bloch equation:

$$S = -\frac{dE}{dx} = 2\pi N_a r_e^2 m_e c^2 \rho \frac{Z}{A}\frac{z^2}{\beta^2}[\frac{1}{2}\ln\frac{2m_e c^2\beta^2\gamma^2 Q_{\max}}{I^2} - 2\beta^2 - \delta - 2\frac{c}{z}]$$

$$2\pi N_\alpha r_e^2 m_e c^2 = 0.1535\ \text{MeV}\cdot\text{cm}^2/\text{g}$$

N_A Avogadro’s number = $6.022 \cdot 10^{23}$ mol^{-1}

electron radius $r_e = 2.817 \cdot 10^{-13}$ cm

m_e electron mass, $m_e c^2$ = 0:510998918MeV

I mean excitation energy (eV)

A atomic mass of absorber (g·mol^{-1})

Z atomic number of absorber

Q_{max} maximum transferred energy

ρ density of the absorber

z charge of incident particle in units of electron charge

$\beta = {}^{v}\!/_{c}$, v velocity of incident particle

$\gamma = 1 / \sqrt{1-\beta^2}$

δ density effect correction to ionization energy loss

C shell correction factor

The mean ionization energy is calculated using semi-empirical formula derived from experimental measurements:

$$\frac{I}{Z} = 12 + \frac{7}{Z}eV \qquad \text{and} \qquad \frac{I}{Z} = 9.76 + 58.8Z^{-1.19}eV$$

The density correction factor δ is considerable in high energies for X = $\log_{10}(\beta\gamma)$ is given by the following expression:

$$\delta = \begin{cases} 0 & X < X_0 \\ 4.6052X + C_0 + a(X_1 - X)^m & X_0 < X < X_1 \\ 4.6052 + C_0 & X > X_1 \end{cases}$$

The parameters C_0, X_0, X_1, α and m are depending on the absorber.

The shell correction factor C is significant in low energies, in cases that the velocity of the incident particle is lower than the speed of bounded electrons, so that they cannot be considered as immobilized in comparison to the incident particle. Considering $\eta = \beta\gamma \geq 0.1$ an empirical formula for C is:

$$C(I,\eta) = (0.422377\,\eta^{-2} + 0.0304043\,\eta^{-4} - 0.00038106\,\eta^{-6}) \cdot 10^{-6}\, I^2$$

$$+ (3.85019\,\eta^{-2} - 0.1667989\,\eta^{-4} + 0.00157955\,\eta^{-6}) \cdot 10^{-9}\, I^3.$$ [10]

The Bethe – Bloch equation for materials of intermediate Z and $0.1 < \beta\gamma < 1000$ gives accurate results. For non – relativistic particles with the same charge in the same material the stopping power varies inversely with the particle energy. For different charged particles moving with the same speed into the same material the energy loss is defined mainly from the factor z^2. The Bethe – Bloch equation diverges for low energies of charged particles because the charge exchange between the particle and the absorber becomes more important, as the positive charged particles are taking in electrons decreasing the stopping power until they become neutral. [10],[11]

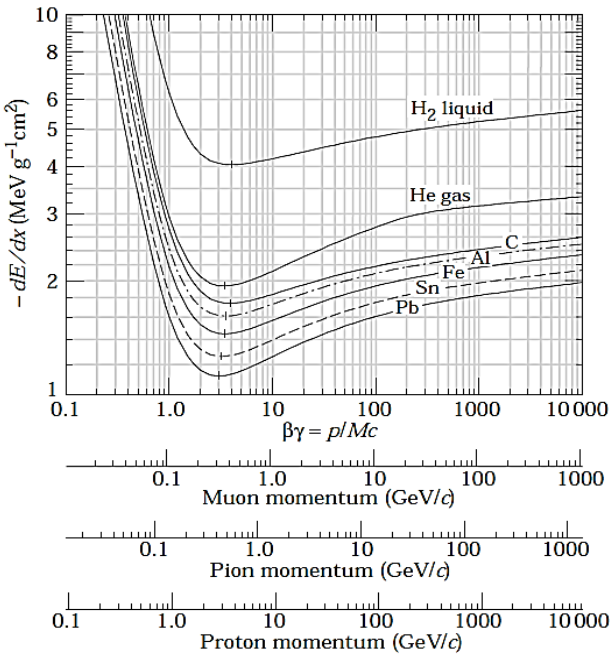

Figure 2.2: Measurement of stopping power in liquid (bubble chamber) hydrogen, gaseous helium, carbon, aluminum, iron, tin, and lead (radiative effects, relevant for muons and pions, are not included, but they are becoming significant for muons in iron for $\beta\gamma > 1000$, and at lower momenta for muons in higher-Z absorbers). Except in hydrogen, particles with the same velocity have similar rates of energy loss in different materials, although there is a slow decrease in the rate of energy loss with increasing Z. [11]

2.1.2. ENERGY LOSS

Most of the relativistic particles (muons, cosmic rays) have mean rates of energy loss near the minimum possible value and so they are called minimum ionizing particles – MIPs.

The particles may simply penetrate the material. Thus, low energy loss occurs for small values of absorption thickness, allowing all the particles of the initial beam to reach the detector. This will apply until the length that the absorption thickness is equal to the shortest orbit and if this length increases, a large decrease of the detected particles is observed. The maximum distance which the particles of a particular energy can penetrate within a material is called particle range for this material and this particle energy. The mean range R of particles of given energy E_0 represents the value of the thickness in which the number of the detected particles is equal to half of the emitted particles and it can be found by the integration of dE / dx :

$$R = \int_{E_0}^{0} \left(\frac{dE}{dx}\right)^{-1} dE$$

The value of the thickness that no particle is detected is called projected range R_e. [9]

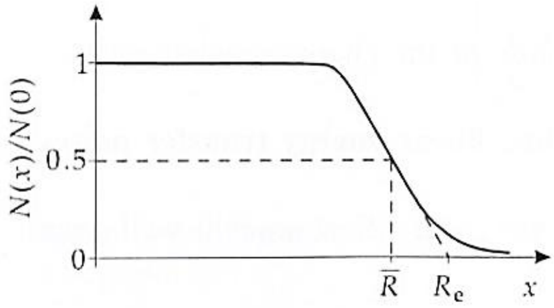

Figure 2.3: Number of particles in a material as a function of thickness x. [9]

The energy loss of a charged particle within a material is a statistical phenomenon in which the width of the energy distribution is a measure of energy dispersion (Energy Struggling). The amount of the transferred energy to any collision is following the Landau distribution:

$$f(\lambda) = \frac{1}{\sqrt{2\pi}} e^{-\frac{(\lambda + e^{-\lambda})}{2}}$$

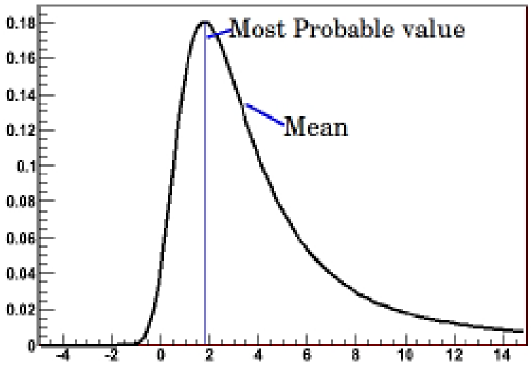

Figure 2.4: Landau distribution. The distribution shows a tail in the high energy loss region, due to rare energetic δ electrons. [10]

The parameter λ expresses the divergence from the most possible value:

$$\lambda = \frac{\Delta E - \Delta E_p}{\xi}$$

ΔE real energy loss at a layer of thickness x,
ΔE_p the most probable energy loss at a layer of thickness x,
and the mean energy loss $\xi = 2\pi N_A r_e^2 m_e c^2 z^2 \frac{Z}{A}\frac{1}{\beta^2}\rho x = kx\rho$, ρ density (g/cm^3) and x thickness of the absorber (cm).

The general formula for the most probable energy loss:

$$\Delta E_p = \xi\{\ln(\frac{2m_e c^2\gamma^2\beta^2}{I}) + \ln\frac{\xi}{I} + 0.2 - \beta^2 - \delta(\beta\gamma)\}$$

Experimentally the actual energy loss distribution is often broader than expected by Landau distribution. The most probable loss ΔE_p increases in a first approximation as x(α + lnx), and the ratio $w/\Delta E_p$ decreases with increasing x (where w is the full width at half maximum). By increasing the density of the absorber the energy loss distribution approaches Gauss distribution.

For thin absorbers the deposited energy can be given by this expression:

$$\Delta E = -\overline{(\frac{dE}{dx})}x$$

$\overline{(\frac{dE}{dx})}$ the mean value of the stopping power within the absorber. [11]

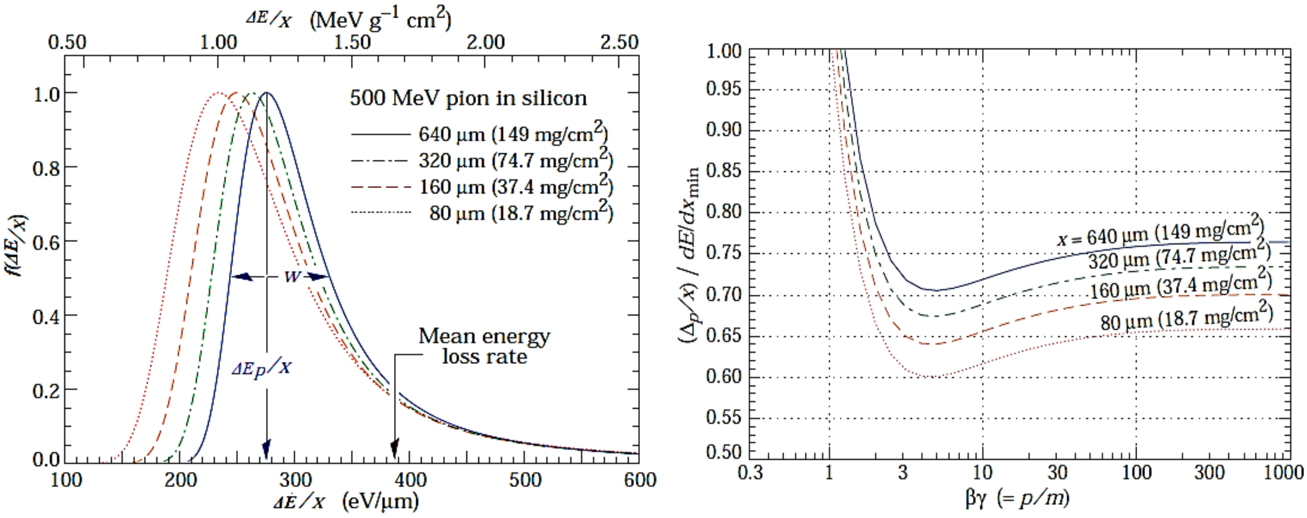

Figure 2.5: Left: Straggling functions in silicon for 500 MeV pions, normalized to unity at the most probable value $\Delta E_p/x$. Right: Most probable energy loss in silicon, scaled to the mean loss of a minimum ionizing particle, 388 eV/µm (1.66 MeV g^{-1} cm^2). [11]

In a compound of various elements i the energy loss is:

$$\frac{dE}{dx} = \sum_i f_i [\frac{dE}{dx}]_i$$

f_i the fragment of the i – th element and $[\frac{dE}{dx}]_i$ the mean energy loss of this element. [11]

2.1.3. EXCITATION

During excitation an atomic electron acquires an energy which brings the atom to an elevated (excited) state.

$$X + p \rightarrow X^* + p$$

The atom eventually returns to its stable state, usually accompanied with photon emission. A molecule may have many characteristic ways of excitation. [12],[15]

2.1.4. IONIZATION

An ionization takes place when an electron-ion pair is created. For this to happen, the energy of the passing particle should be above a threshold equal to the ionization potential of the medium. When the ionization is caused by the incident particle itself, it is called primary ionization. If the electron of the pair gains energy above the threshold it ionizes further, and produces secondary ionization. If the atoms are very closely to a charged passing particle trajectory, there is the possibility that the emitted electron has enough energy to cause further secondary ionizations after the detachment from the atom. Through these electrons of limited range (δ rays), the kinetic energy of the charged particle is transferred indirectly to the atomic electrons. The ion pairs tend to form clusters around the particle trajectory. Ionizations may continue until the threshold for ionizing reactions is reached. The number of primary produced ionization pairs is roughly linearly increasing with the atomic number following Poissonian distribution. The probability of having k pairs in one event with n the average number of primary interactions is:

$$P_k^n = \frac{n^k}{k!} e^{-n}$$

The total number of pairs produced as the sum of primary and secondary ionizations is given by:

$$n_T = \frac{\Delta E}{W_i}$$

ΔE is the energy lost and W_i the effective energy for the creation of one electron-ion pair. [12],[15]

2.1.5. CHERENKOV RADIATION

The Cherenkov radiation emission hardly contributes to energy loss, but it is of outmost importance as it is used to determine the parameters of the orbit of a charged particle. It is emitted when a charged particle is passing through a dielectric medium at a speed greater than the phase velocity of light in this medium:

$$v = \beta c \geq v_\varphi \Rightarrow \frac{v}{c} \geq \frac{v_\varphi}{c} \Rightarrow \beta \geq \frac{1}{n}$$

n = n(λ) the index of refraction for this element and 1/n the threshold velocity for the production of Cherenkov radiation.

The charged particle in orbit within the dielectric medium creates spherical electromagnetic waves as follows: The molecular dipoles of the dielectric material orientate when the charged particle is passing by, and after it has elapsed they redirect, resulting in an amount of excess polarization energy that is emitted in the form of a spherical electromagnetic pulse. As the particle moves it produces consecutive pulses along its path. The reinforcing contribution of these waves creates an electromagnetic wave front, the light cone of Cherenkov radiation, with the symmetry axis of the particle trajectory.

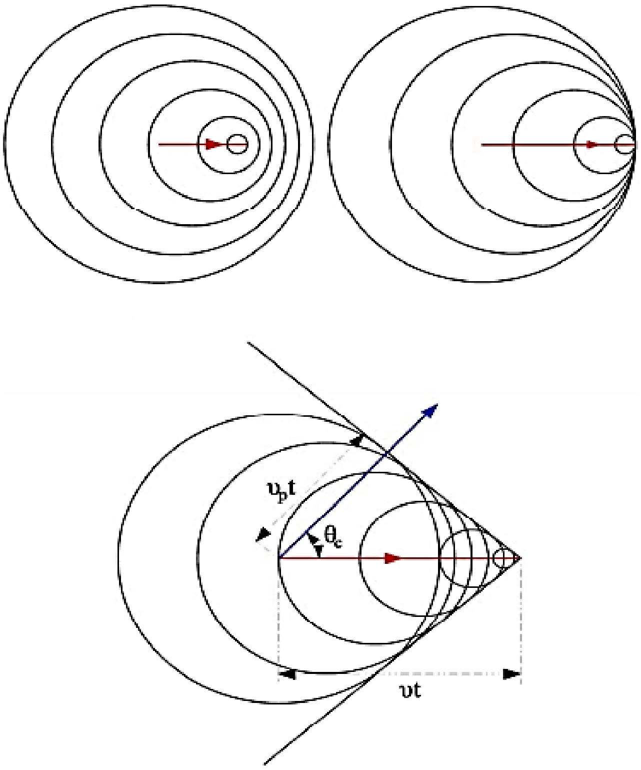

Figure 2.6: On the top left: production of spherical waves from particles with velocity less than c, wherein successive pulses do not contribute anywhere. On the top right: at a speed equal to c, when the contribution consists in the point of the particle. In the figure below, the contribution of the waves in a cone during the emission of Cherenkov radiation for velocity greater than c. The radiation front is a coherent surface. [59]

When two particles are close to one another, at a distance less than one wavelength, the electromagnetic fields may contribute reinforcingly, affecting Cherenkov radiation emission.

The angle θ_c of Cherenkov radiation according to the direction of the particle is given by the following relation:

$\cos\theta_c = 1/n\beta$ ή $\tan\theta_c = \sqrt{n^2\beta^2 - 1} \approx \sqrt{2(1-{}^{1}\!/_{n\beta})}$ for small angles θ_c.

The number of the emitted Cherenkov photons per unit track length and per unit wavelength for particle of charge ze is:

$$\frac{d^2N}{dxd\lambda} = \frac{2\pi\alpha z^2}{\lambda^2}(1-\frac{1}{\beta^2 n^2(\lambda)})$$

$\alpha = {}^{1}\!/_{137.036}$ the fine structure constant.

For a narrow range of frequencies [f_1, f_2] in which the dependence of the refractive index from the frequency and wavelength can be omitted, the relation for the energy loss per unit length is:

$$\frac{dE}{dx}=\frac{z^2e^2M}{2\hbar^2}\{\frac{(hf_1)^2-(hf_2)^2}{Mc^2}\}(1-\frac{1}{n^2\beta^2})_{av}$$

This relation suggests reliance on velocity:

$$\frac{dE}{dx}\propto N_\gamma \propto 1-\frac{1}{\beta^2n^2}=1-\frac{1}{n^2}\{1+\frac{M^2}{p^2}\}$$

Therefore, the number of photons decreases with the square of the mass for a given momentum. Based on this conclusion it is possible to separate two relativistic particles of same momentum and different mass, since the heavier and therefore slower particle will emit less Cherenkov light. [11],[16],[59]

2.1.6. TRANSITION RADIATION

The transition radiation is emitted when a charged particle penetrates the interface of two media with different electrical properties. The change of the dielectric constant of the media along the particle path causes discontinuity of the electric field at the interface. The usual case concerns an electron that crosses the interface between vacuum (ε=1) and a conductor (ε→∞). This problem can be overcome by replacing the conductor with the positive particle - 'image' of the incident, to eventually transform into the problem of the conflict of two charged particles. [20]

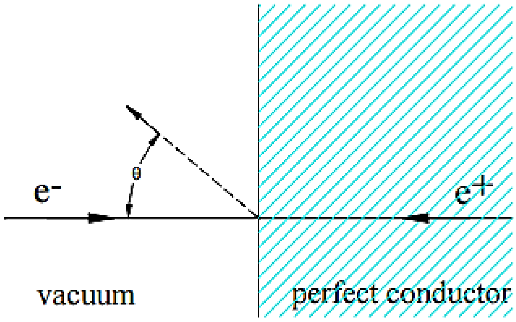

Figure 2.7: The radiation is produced by the sudden change in velocity due to the collision of the particle with its oppositely charged image and is indicated by a dotted line. [20]

2.2. INTERACTIONS OF FAST ELECTRONS

The electrons e^- and positrons e^+ are very similar, with slight variations in their interactions with matter. When a positron loses all its energy, it tends to approach an electron, targeting the production of two photons of the same energy which are traveling in opposite directions through the process of pair production. The electrons when they lose all their energy are converted into atomic electrons due to the absence of positrons in matter. Consequently, referring to energy loss of electrons the mechanisms in fact concern energy loss of both electrons and positrons.

Compared to heavy particles, fast electrons have less energy loss and their trajectory is random and nonlinear while passing through absorbing materials. [9]

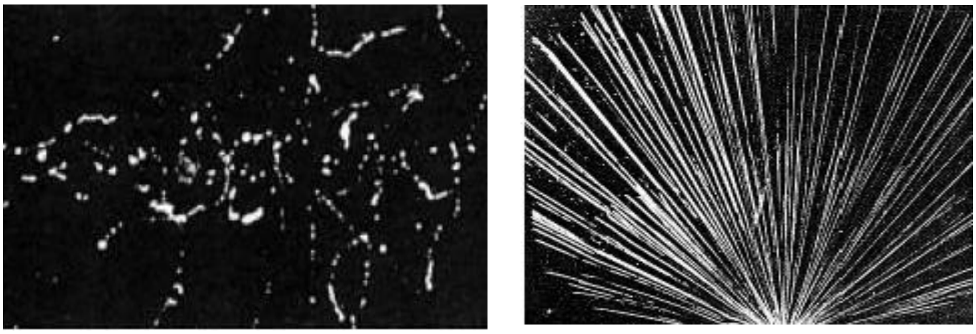

Figure 2.8: Left: Electron trajectories and Right: alpha trajectories in a Cloud Chamber.[10]

The electrons as they pass through a material lose their energy mainly either via inelastic scattering with regional electrons or via braking radiation (Bremsstrahlung).

2.2.1. SCATTERING WITH REGIONAL ELECTRONS

During the inelastic scattering of electrons excitation and ionization phenomena due to Coulomb field are noted, resulting in energy loss and deviation from their initial trajectory. If the initial energy of the initial electron is large enough, then the resulting electron by ionization may have sufficient energy to induce secondary ionization. The electrons that cause secondary ionization are called delta particles. Due to the low mass of the electrons can be considered to remain after the collision without deflected, and in addition, the maximum allowable transfer kinetic energy because of identical particles is $E_{\kappa_{max}}=E_{\kappa}^{e}/2$. These two factors require the adjustment of the Bethe - Bloch equation for the energy loss per unit length, with $\beta \equiv v / c$:

$$-(\frac{dE}{dx})_c = \frac{2\pi NZe^4}{m_e v^2}(\ln\frac{m_e v^2 E}{2I^2(1-\beta^2)}) - (\ln 2)(2\sqrt{1-\beta^2} - 1 + \beta^2) + (1-\beta^2) + \frac{1}{8}(1-\sqrt{1-\beta^2})^2$$

2.2.2. BRAKING RADIATION (BREMSSTRAHLUNG)

During the inelastic collisions with the nuclei, electrons lose their energy due to braking radiation (Bremsstrahlung radiation). Bremsstrahlung is electromagnetic radiation produced by the deceleration of a charged particle (electron) when deflected by another charged particle (atomic nucleus). Due to energy conservation the lost kinetic energy of the moving particle loses kinetic energy is converted into a photon.

The energy loss via Bremsstrahlung is given by the relation:

$$-(\frac{dE}{dx})_r = \frac{NEZ(Z+1)e^4}{137 m_e^2 c^4}(4\ln\frac{2E}{m_e c^2} - \frac{4}{3})$$

For very energetic electrons and absorbents of large atomic numbers energy losses due to radiation are important. For typical electron energies, photons created by Bremsstrahlung are quite weak and reabsorbed within a short distance from the point of creation.

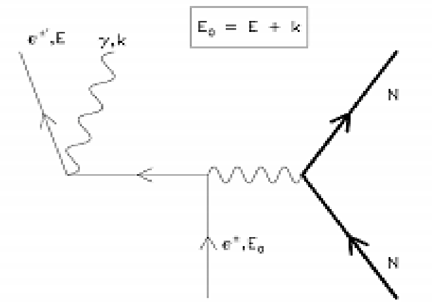

Figure 2.9: Bremsstrahlung [13]

From the energy loss relation:

$$-\frac{dE}{dx} \propto E \Rightarrow \frac{dE}{dx} = -\frac{1}{X_0}dx \Rightarrow E = E_0 e^{-x/X_0}$$

where X_0 is a constant called radiation length.

The physical meaning of the radiation length is the mean distance at which a high-energy electron reaches 1/e of its initial energy due to Bremsstrahlung and it is approximated by (Dahl):

$$X_0 = \frac{716 g cm^{-1} A}{Z(Z+1)\ln(287/\sqrt{Z})}$$

In the case of compounds radiation length is expressed as follows:

$$\frac{1}{X_0} = \sum {}^{w_i}\!/_{X_i}$$

w_i fraction by weight and X_i radiation length of the i – th element. [11],[13]

2.2.3. MOLLER AND BHABHA SCATTERING

Moller and Bhabha involve interactions between incident electrons or positrons with atomic electrons. In particular, during Moller scattering two electrons enter, exchange a photon and leave ($e^- + e^- \rightarrow e^- + e^-$).

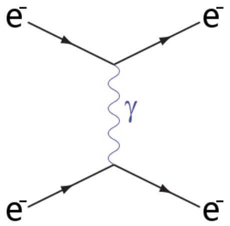

Figure 2.10: Moller scattering. In quantum chromodynamics (QCD), Moller scattering represents the repulsion of the two electrons. [13]

Bhabha scattering involves the interaction between an electron and a positron ($e^+ + e^- \rightarrow e^+ + e^-$). In this case there is an extra interaction channel which contributes to the cross section because of the possible annihilation and recreation of the electron – positron pair. [13]

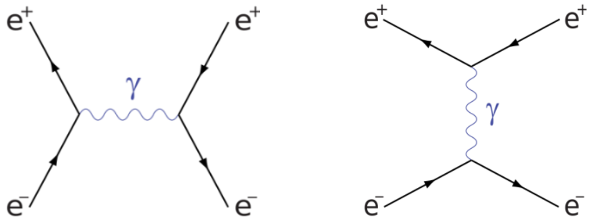

Figure 2.11: Bhabha scattering. Left: Feynman diagram for annihilation. Right: Feynman diagram for scattering. Bhabha scattering represents the traction between an electron and a positron. [13]

2.2.4. TOTAL ENERGY LOSS

The total energy loss of the electron per unit length is given by adding up the contributions of the mechanisms above:

$$\left(\frac{dE}{dx}\right)_{total} = \sum_j \left(\frac{dE}{dx}\right)_j$$

where j each of the mechanisms.

The energy loss is inversely proportional to the energy in the case of excitation and ionization, and proportional in the case of braking radiation. The point at which the two actions are equalized is called critical energy and depends mainly on the type of material. Approximately the critical energy of solid and gas is given by the following equations:

$$E_{critical}^{solid} = \frac{610(MeV)}{Z+1.24}$$

$$E_{critical}^{gas} = \frac{710(MeV)}{Z+0.92}$$

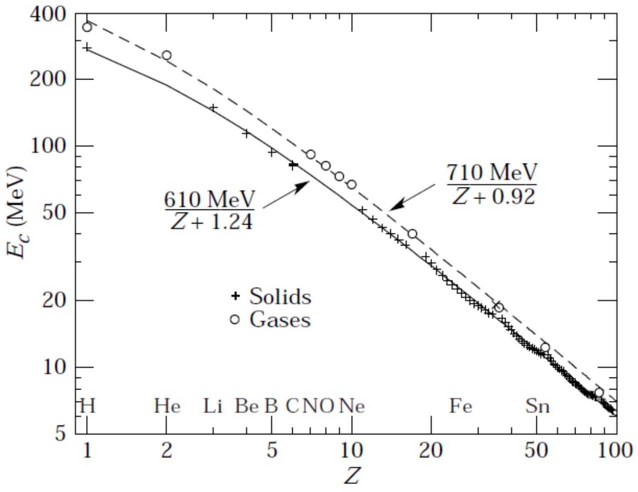

Figure 2.12: Critical energies as a function of Z, both for liquids and for solids. [11]

For speeds near the speed of light in vacuum and absorber with atomic number Z, an accurate approximation of the loss ratio is: [11]

$$\frac{\left(\frac{dE}{dx}\right)_c}{\left(\frac{dE}{dx}\right)_r} \approx \frac{Z \cdot E(MeV)}{700}$$

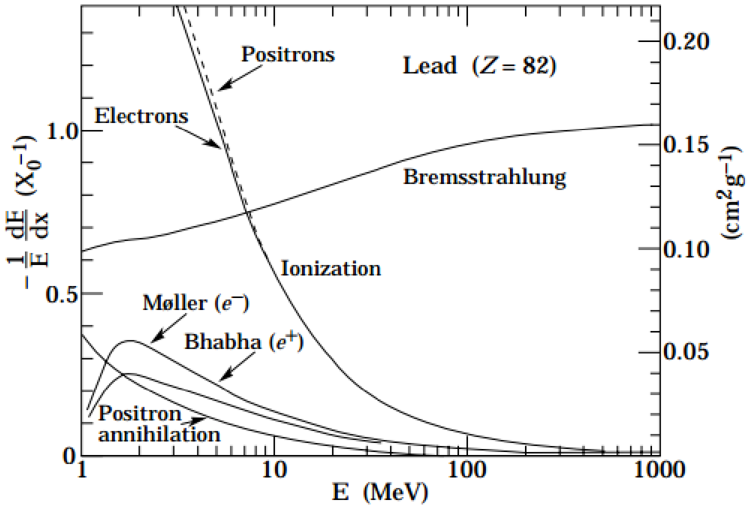

Figure 2.13: Fractional energy loss per radiation length as a function of the e^- / e^+ energy in lead. [11]

2.2.5. ELECTRON RANGE

Fast electrons, as they pass through an absorber are subjected to scatterings with the material, so some of them eventually fail to reach the detector, even if the absorber is not very thick. The range is greater for electrons that have undergone fewer scatterings. In the case of backscaterring, the electron exits from the entry point, resulting in full energy deposition therein. [9]

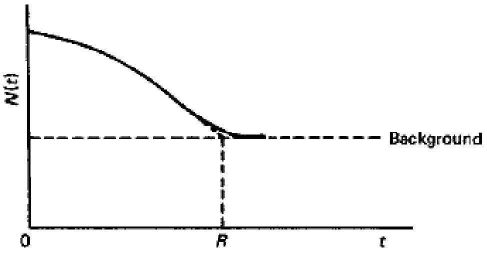

Figure 2.14: The number of electrons that manage to reach the detector after passing through the absorber is reduced and so it reaches quickly the number of background electrons. [9]

2.3. PHOTON INTERACTIONS

The main mechanisms of interaction of photons with matter are coherent scattering, photoelectric effect, Compton scattering and pair production. These processes lead to a transfer of photon energy, partial or total, to the atomic electrons of the medium, which appears as kinetic energy.

Assuming parallel beam consisting of mono – energetic photons of initial intensity I_0 that impinges perpendicularly on plate absorber with thickness x, the intensity of the output beam is exponentially reduced, and is given by:

$$I(x) = I_0\, e^{-\mu x}$$

where $\mu = \mu(\text{Coherent}) + \mu(\text{Photo}) + \mu(\text{Compton}) + \mu(\text{Pair})$ the total linear attenuation coefficient, which expresses the overall probability of a photon detachment from the beam per unit length, with the individual terms of the sum to represent the probability coefficient per unit length for each of the three processes (partial linear coefficients). Furthermore, σ is the total cross section per atom and N the atomic density. The total linear attenuation coefficient depends on the photon energy of the beam. [9],[10],[11]

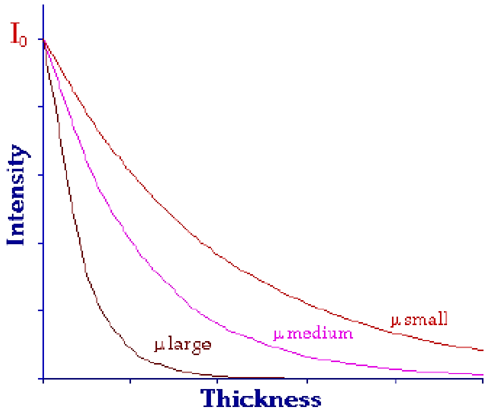

Figure 2.15: Attenuation of the intensity of the passing beam depending on the thickness of the material. [9]

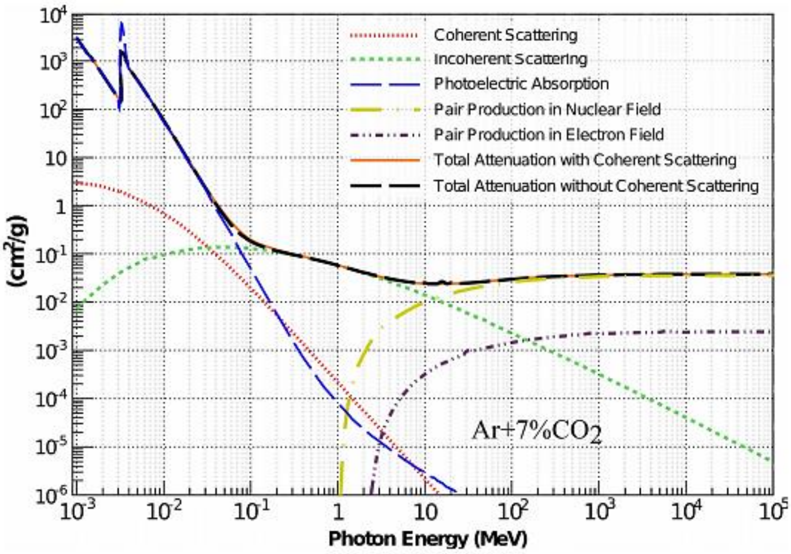

Figure 2.16: Mass attenuation coefficients $\frac{N_A}{A}\sum_i \sigma_i$ (σ_i the atomic cross section for each process and A the atomic weight) for a gas mixture of Ar+7%CO_2. (XCOM database) [45]

Additionally, $\mu = 1/\lambda$, where λ is the mean free path within the absorber:

$$\lambda = \frac{\int_0^\infty x\cdot e^{-\mu x}dx}{\int_0^\infty e^{-\mu x}dx}$$

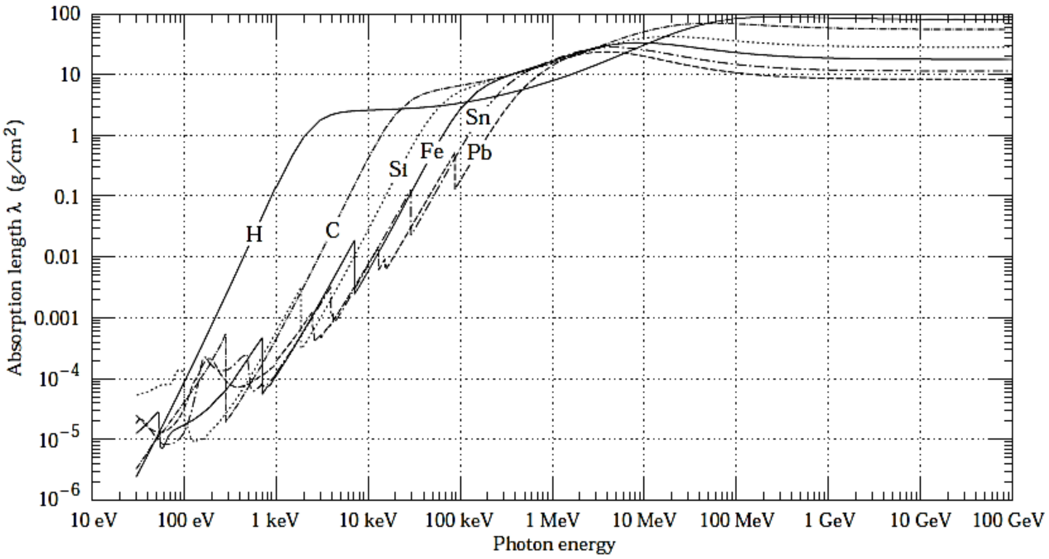

Figure 2.17: The mean free path λ for various adsorbents as a function of photon energy. The remaining intensity I after passing through a material of thickness x is $I(x) = I_0\, e^{-x/\lambda}$. [11]

2.3.1. Coherent scattering – Rayleigh

In coherent scattering the incident photon is absorbed and re-emitted immediately without energy loss, only change of direction. This kind of scattering is possible at very low energies and specifically for the cross section the following expression applies:

$$\sigma_{coh} \propto \frac{Z^2}{E_\gamma}$$

E_γ photon energy. The cross section σ_{coh} increases for $E_\gamma < 0.1$ MeV and $Z > 80$. [13]

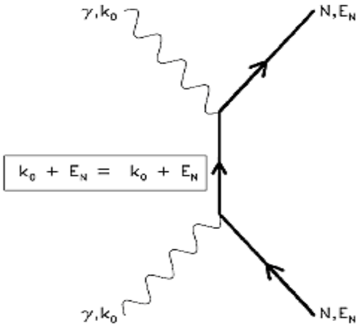

Figure 2.18: Raylight scattering [13]

2.3.2. Incoherent scattering - Photoelectric effect

This mechanism includes the interaction of photons with energy usually less than 1 MeV with the atomic electrons. The peak at 0.1 MeV in the cross sections diagram is due to the coincidence with the binding energy of the K - electron layer. A photo - electron absorbs all the energy of the photon acquiring kinetic energy:

$$E_K = E_\gamma - E_j$$

where $E_\gamma = hf$ is the photon energy and E_j the binding energy of the atom into a layer. Apparently, the energy of the absorbed photon must be greater than the electron binding energy. Apart from the exported photo – electron, an ionized atom is created in the absorber, which has a vacancy amongst its layers. The vacancy is replenished either by rearranging the electron layers of the atom or by capturing a free electron.

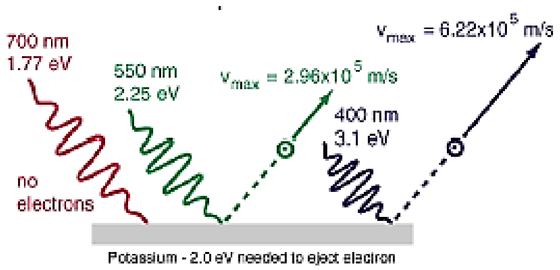

Figure 2.19: Representation of the photoelectric phenomenon [2]

By increasing the energy of the incident photon the likelihood of the phenomenon gets weaker. In the case of photon energy similar to the electron binding energy of a shell, the electron detachment is most likely to occur in this cell, and less likely in shells of lower energy. The cross section of the photoelectric phenomenon can be estimated as:

$$\sigma_{photo} = Z^5 \alpha^4 \left(\frac{m_e c^2}{E_\gamma}\right)^{3.5} \propto \frac{Z^5}{E_\gamma^{3.5}}$$

which tends to increase for $E_\gamma < 1\ MeV$.

The rearrangement of electrons in order to fill the gap because of the detachable electron is accomplished either via X-ray emission or via Auger phenomenon. The atomic number of the element and the sublayer in which the rearrangement happens determine which of the two phenomena will occur.

In the case of X-ray emission (X-ray fluorescence) the electron rearrangements are followed by photon emission in the X – ray region. Photon energy is equal to the energy difference between the layers the electron moved.

In the Auger effect filling a hole from the extraction of an electron in the inner layer of the atom is accompanied by an electron emission from the same atom. When an electron of the inner layer is detached, then an electron from a higher energy level can fill the hole, resulting in excess energy. This energy is sometimes released by the emission of a photon, but sometimes, it is transferred to another electron (Auger electron), which leaves the atom. In light elements decay through Auger phenomenon is more likely. The new holes are covered from electron transitions from upper cells until the ionized atom results in a situation where further transitions cannot take place. In many cases the combination of the two phenomena is possible. [10],[13]

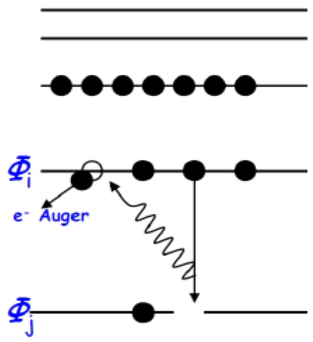

Figure 2.20: Auger phenomenon [2]

2.3.3. COMPTON SCATTERING

The Compton scattering occurs in energies similar to the electron rest energy, and describes the inelastic scattering of a photon at an angle θ of an atomic electron, usually weakly linked to the atom. A portion of the kinetic energy of the photon is transferred to the electron, which after scattering moves in a direction of an angle φ compared with the initial axis of the photon. The energy of the scattered electron has a wide range, because any scattering angle is possible. [10],[13]

For the cross section of Compton scattering:

$$\sigma_{compton} \propto \frac{Z}{E_\gamma}$$

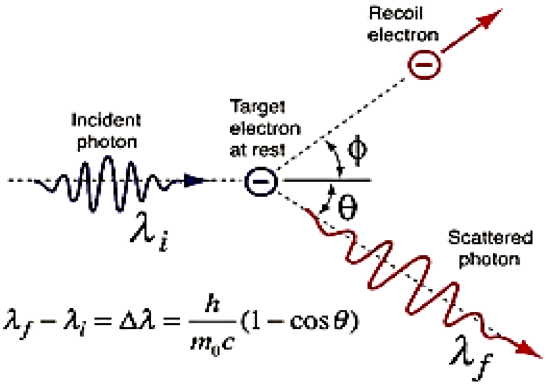

Figure 2.21: Compton scattering representation [2]

By applying the conservation laws of energy and momentum for the Compton scattering to the following conclusions are resulted:

- Wavelength shift of the scattered photon by the amount:

$$E_\tau = \frac{E_\alpha}{(A+1)^2}(\cos\theta_s + \sqrt{A^2 - \sin^2\theta_s})^2$$

$m_e c^2$ electron rest energy, λ_τ the wavelength after scattering and λ_α the wavelength before scattering. The frequency of the scattered electron only depends on the scattering angle. [2],[10]

- Energy of the scattered photon:

$$E_\gamma^\tau = hf_\tau = \frac{E_\gamma^\alpha}{1+\alpha(1-\cos\theta)}$$

$$\text{where } \alpha = \frac{hf_\alpha}{m_e c^2}$$

- Kinetic energy of recoil electron:

$$E_{\kappa} = E_{\gamma}^{\alpha}\frac{\alpha(1-\cos\theta)}{1+\alpha(1-\cos\theta)}$$

For angle θ = 180° the kinetic energy gets maximum, while for θ = 0° minimizes.

- Relation of φ and θ angles:

$$\cot\varphi = \frac{(1-\cos\theta)(1+\alpha)}{\sin\theta}$$

- Differential cross section of photons scattered per electron for Compton scattering, (cm^{-2}/electron) by Klein and Nishina:

$$\frac{d\sigma}{d\Omega} = \frac{e^4}{2m_e^2c^4}[\frac{1}{1+a(1-\cos\theta}]^2[1+\cos^2\theta+\frac{\alpha^2(1-\cos\theta)^2}{1+\alpha(1-\cos\theta)}]d\Omega$$

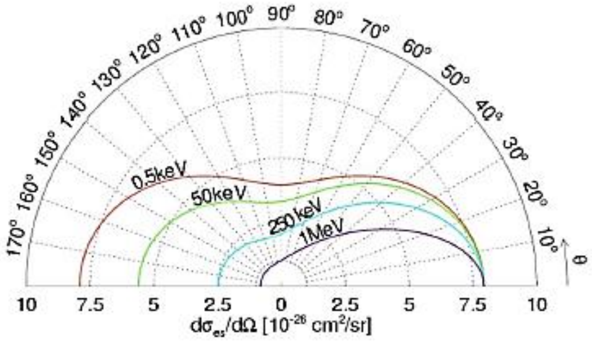

Figure 2.22: Angular distribution of the scattered photons. [2]

2.3.4. PAIR PRODUCTION

During the process of pair production o photon converts into an electron – positron pair after interacting with the electric field of a nucleus. A minimum energy, equal to twice the electron rest mass, ie 1.02 MeV, is required in order to achieve the creation of this particle pair. Possible excess energy is splitted equally to the produced particles in the form of kinetic energy. This phenomenon dominates at high energies and its cross section is:

$$\tau = \sigma_{pair} = \frac{7}{9}\frac{A}{N_A\rho}\frac{1}{X_0}$$

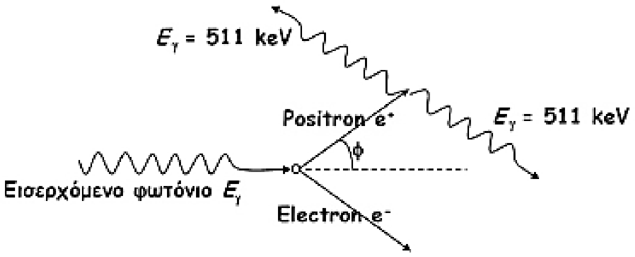

Figure 2.23: A photon of sufficient energy creates an electron - positron pair and then the positron annihilates in a pair of photons with equal energy. [10]

The quantity $\tau = \sigma_{pair}\,(N_A\rho/A) = \frac{7}{9X_0}$, where X_0 the mean radiation length before absorption, as it calculated for the case of braking radiation, gives the possibility of pair production per unit length. Therefore, absorption of photons with pair production is given as:

$$I(x) = I(0)e^{-\tau x} = I(0)e^{-\frac{7}{9}\frac{x}{X_0}}$$

So, mean radiation length X_0 for pair production expresses the $^7/_9$ of mean free path for $e^+ e^-$ production (L_{pair}) by a high energy photon.

The momentum of the produced pair is almost parallel to the momentum of the original photon presenting a minimal deviation. The lateral deflection that the $e^+ e^-$ pair of critical energy acquires, since they travel a distance X_0, is called Moliere radius and is given by the relation:

$$R_M = \frac{21MeV}{E_c} X_0 \approx \frac{7A}{Z} g \cdot cm^{-2}$$

After the pair production the positron loses energy and annihilates after approaching an electron. At higher energies the energy loss of the positron is achieved by ionizing and braking radiation, until it reaches the point where the energy is low enough to annihilate. [10],[11]

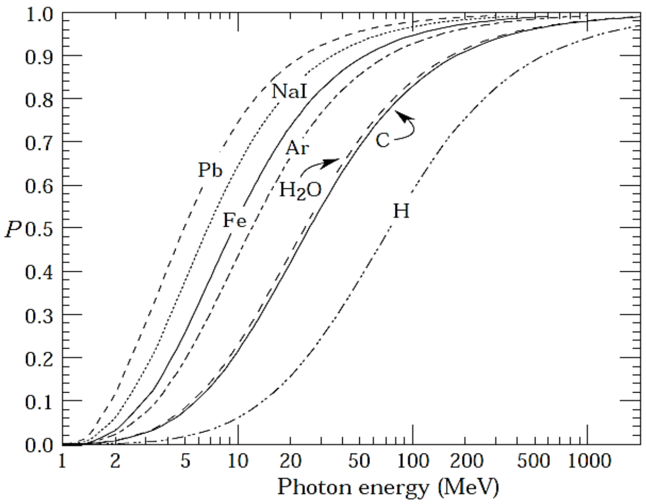

Figure 2.24: Probability P that a photon interaction will lead to e^+ e^- pair production. For photon attenuation length $\lambda = L_{pair}$ the probability that the photon will lead to pair production in an absorber of thickness x is $P[1 - e^{-x/\lambda}]$. [11]

2.4. NEUTRON INTERACTIONS

Neutrons are electrically neutral subatomic particles which together with protons constitute atomic nuclei. The absence of electrical charge makes impossible their acceleration or their focus with magnet system, and also prohibits the direct detection through their ionization track, since they cannot ionize the materials they pass through. However, they can participate in nuclear interactions even at low energies because they can easily penetrate the Coulomb nuclear barrier. [10]

Neutrons outside the nucleus, called free neutrons are unstable and decay into a proton, an electron and an electron antineutrino via the weak interaction:

$$\mathrm{n} \rightarrow \mathrm{p} + e^- + \overline{\nu}_e + \mathrm{Q}$$

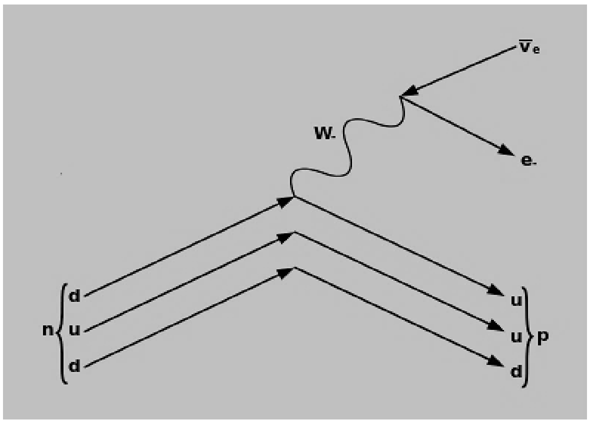

Figure 2.25: Feynman diagram for neutron decay. [14]

The possibility of neutron interactions with certain nuclei depends on the type of the material and the neutron energy. Neutron cross section is very small, so they can travel far enough in matter without any interaction compared to other particles. Neutron energy can determine with some probability the type of reaction that will take place with a certain nucleus. Even for a large energy range, the characteristics of the interaction mechanisms for specific types of nuclei are unchanged. Hence, neutrons can be discriminated into the following categories with respect to their energy:

Thermal	$E \sim kT \sim 1/40$ eV
Cold / Ultracold	$E \sim$ meV / μeV
Epithermal	0.1 eV $< E <$ 100 keV
Fast	100 keV $< E <$ 100 MeV
High energy	$E >$100 MeV

Table 2.2: Categories of neutrons [14]

The main ways of neutron interaction with matter is the scattering and absorption. High energy neutrons are likely to react through scattering, but by reduction of their energy at levels of eV, the probability of absorption increases.

2.4.1. SCATTERING

The energy of neutrons passing through medium is degraded by nuclear collisions (inelastic and elastic collisions). In elastic collisions the colliding nucleus receives a portion of the neutron energy as kinetic. During the non-elastic collisions energy of the incident neutron should be such as to achieve the induction of the nucleus, which occurs in energies in levels of MeV.

- Elastic neutron – nucleus scattering

The elastic scattering is the main mechanism of energy loss for neutrons of MeV energy levels and during this process the energy and momentum of the neutron - nucleus system are conserved. The amount of energy that a neutron transfers to the target nucleus depends on the angle of conflict and their mass difference. One mechanism of elastic scattering is the composite elastic scattering, when the neutron is initially absorbed by the nucleus, resulting in a new nucleus in an excited state, and then the decay of the nucleus, when a neutron is emitted, returning to the initial unexcited state. A second mechanism is the dynamic elastic scattering in which the neutron approximates the nucleus without incorporating by making a sort of elastic collision.

For nucleus with atomic mass number A and neutron scattering angle θ, θ_s expressed in laboratory system and θ_c in center of mass system, E_α neutron energy before scattering E_τ neutron energy after scattering, the general formula for the elastic scattering in laboratory system is:

$$E_\tau = \frac{E_\alpha}{(\mathrm{A}+1)^2}(\cos\theta_s + \sqrt{A^2 - \sin^2\theta_s})^2$$

For energies in laboratory system and the angle θ considered in the center of mass system, the energy relation gives:

$$E_\tau = E_\alpha \frac{(\mathrm{A}^2 + 2\mathrm{A}\cos\theta_c + 1)}{(A+1)^2}$$

If neutron energy is greater than 10 MeV, energy at which neutrons show their wave nature, scattering is independent of angle θ. Each neutron is scattered more than once, so in the second scattering neutrons are not mono – energetic anymore.

The relation between the angles in the center of mass system is the following:

$$cos\theta_s = \frac{Acos\theta_c + 1}{\sqrt{A^2 + 2Acos\theta_c + 1}}$$

For very heavy nuclei (A>200) both laboratory and center of mass systems coincide.

- Inelastic neutron – nucleus scattering

During this process the neutron is instantaneously absorbed by the nucleus and stimulates it. The new nucleus decays partly by the emittance of a lower-energy neutron and then, complete decay is achieved by direct emission of one or more photons. The photon emission requires a minimum energy of the incident neutron, at least as much energy of the first excited level of the nucleus (E_1). In the laboratory system the minimum kinetic energy of the neutron for successful inelastic scattering is calculated by:

$$E_\alpha^{min} = \frac{A+1}{A} \mathrm{E}_1$$

Neutrons after inelastic scattering have less energy and their direction changes considerably.

- Non elastic scattering

The procedure is similar to inelastic scattering, except that the exiting particle isn't a neutron but usually particle alpha. The new nucleus is often stimulated and decays by emission of γ photons. Non elastic scattering is more likely at higher neutron energies, above 5 MeV. [10]

2.4.2. ABSORPTION

In the absorption process, the neutron is captured by the nucleus. During decay the nucleus can emit γ photons, charged particles (protons, alpha particles), or cleaved into two or more fragments.

- Absorption with γ emission (radioactive incorporation)

It is the most common case of absorption, most likely for low kinetic energy neutrons (in the order of keV), where the contested neutron is incorporated in the nucleus, creating an isotope at an excited state. During the decay one or more photons are produced but without particle emission:

$$\mathrm{n} + {}^{A}_{Z}X \rightarrow {}^{A+1}_{Z}X + \gamma$$

- Absorption with charged particle emission

In the case of neutrons of high kinetic energy, the produced composite nucleus during its decay is possible to produce nucleons with frequent examples of the proton emission (n, p), deuterium (n, d) or alpha particle (n, α).

- Absorption with emission of several neutrons

For very high energy neutrons nuclear reactions can lead to emission of two (required energies 7 – 10 MeV) or three neutrons (11 – 30 MeV). In order to produce two neutrons, firstly an inelastic scattering of the neutron with the nucleus is performed, bringing the nucleus at an excited state and then, the now partially excited nucleus decays with emission of one more neutron. For the three neutron producing reaction, firstly the steps for producing two neutrons are performed, as previously described, leaving the nucleus in an excited state, which requires the emission of a third neutron to return to the non-excited state.

- Nuclear fission

The process of fission is likely to occur through the absorption of a neutron or photon of energy beyond the fission energy threshold by a target nucleus. After uptake of neutron or photon the nucleus transits to a non-steady state. Besides emitting daughter nuclei and other fragments, a large amount of energy of about 200 MeV is released.

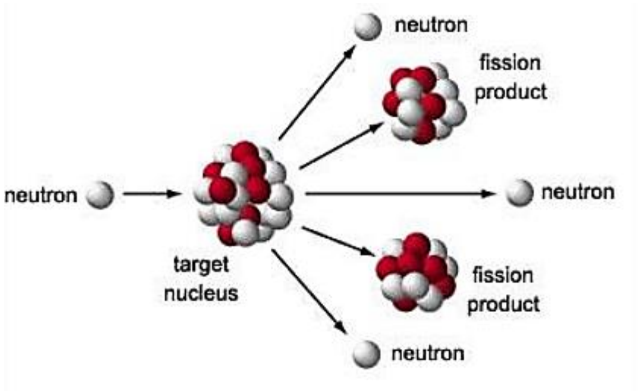

Figure 2.26: Fission process [68]

- Hadron jet production

The nuclear reaction involving neutrons with energy about 100 MeV, which collide with target nuclei, results in the fragmentation of nuclei, i.e. cutting into nucleon complexes in nuclei fragments. The most commonly produced hadrons result in hadron jets. [10]

2.4.3. NEUTRON DECELERATION

The determination of the efficiency of a nucleus for neutron deceleration, the parameter ξ is used, which can estimate the mean number of elastic and isotropic scatterings until a neutron of initial energy E_α decelerates in an energy E_τ by losing energy by a constant percentage per scattering for a particular material. The mean value of energy loss is:

$$\overline{\Delta E} = \overline{E_\alpha - E_\tau} = E_\alpha \frac{1-\alpha}{2}$$

where $\alpha = (\frac{A-1}{A+1})^2$

The mean logarithmic energy loss is given by:

$$\xi = \ln \frac{E_\alpha}{E_\tau} = 1 + \frac{\alpha}{1-\alpha} \ln \alpha$$

ξ takes high values for light nuclei (for hydrogen ξ = 1), while in larger mass numbers is approximated as follows: [18]

$$\xi \approx \frac{2}{A + \frac{2}{3}}$$

The mean value of ln E_τ is reduced by ξ in every impingement και and after n scatterings:

$$lnE_{\tau_n} = lnE_\alpha - n\xi$$

This approach gives good results for a neutron of energy of MeV, but at lower energies, where their speed is comparable with the thermal motions of the target atoms, a statistical model offers a precise description (Maxwell distribution). [14],[17]

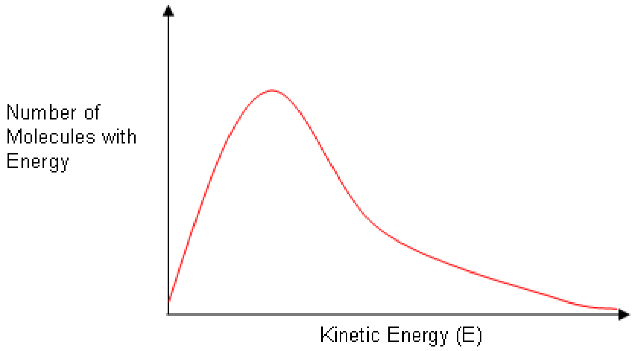

Figure 2.27: Maxwell distribution of neutron energy spectrum with distribution function $f(\upsilon)d\upsilon = 4\pi n(\frac{m}{2\pi kT})^{3/2}\upsilon^2 e^{-m\upsilon^2/2kT}d\upsilon$ [14]

2.5. ELECTROMAGNETIC SHOWERS

A photon or electron of energy higher to a critical energy threshold E_c that enters a material can cause cascade of secondary electrons and photons via braking radiation and pair production. The initial γ photon of energy E_0 produces an e^+ e^- pair, which can produce new photons via braking radiation if they have high enough energy. These new photons can produce again e^+ e^- pairs and particle generation stops when the energy falls below the critical threshold. Then, the particles lose their energy via ionization and excitation. The length into which the production of a new generation of electrons by photons and a new generation of photons by electrons defines the radiation length of the propagation medium X_0.

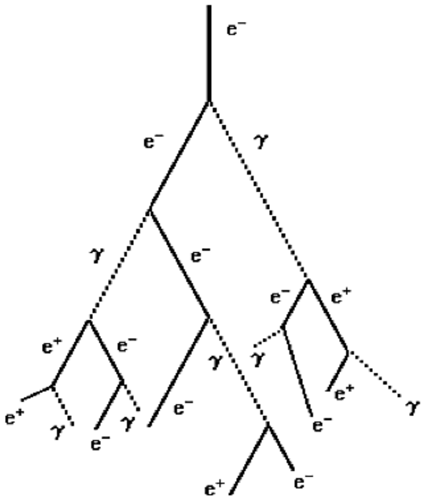

Figure 2.28: Electromagnetic shower [13]

The energy deposition per unit time for an electromagnetic cascade is well described using the Gamma distribution:

$$\frac{dE}{dt} = E_0 b \frac{(bt)^{\alpha-1} e^{-bt}}{\Gamma(\alpha)}$$

- $t = x / X_0$ (distance in units of radiation length),
- $t_{max} = (\alpha - 1) / b = \ln y + C_j$, $j = e, \gamma$,
- $y = E/E_c$ (energy in units of critical energy), where $C_e = -0.5$ for cascades caused by electrons and $C_\gamma = +0.5$ for cascades by photons. [11],[19]

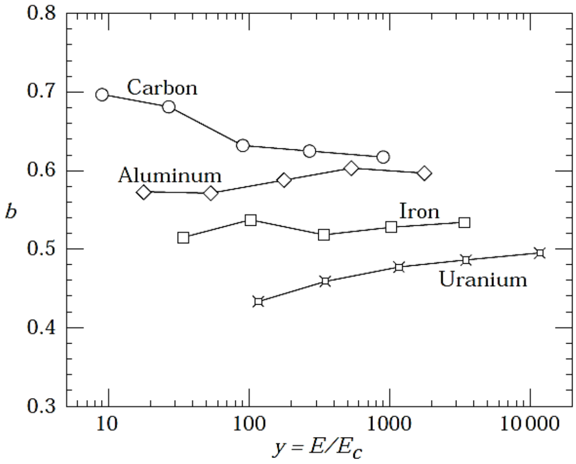

Figure 2.29: Values of the parameter b for the energy depositions of incident electrons of energies $1 \leq E_0 \leq 100$GeV (same for incident photons). Based on the value of b corresponding to each case and the system of equations, the parameter α can also be evaluated. [11]

2.6. HADRONIC SHOWERS

A hadronic shower is generated via the strong interaction of a hadron with the nuclei of the atoms of the material, when the hadron incidents having high energy. At first interaction about half of the energy of the hadron is transferred to secondary particles. During the interactions between nuclei, more than one nucleons participate, resulting in predominantly charged or not pions (π^+,π^-,π^0), in a ratio of about 2:1, followed in importance by nucleons (p,n), strange mesons and baryons (kaons, Λ^0 etc), and photons. The pions have high energies and almost parallel direction to the incident particle. For energies below a certain threshold neutral pions decay into two γ rays ($\pi^0 \rightarrow \gamma + \gamma$), which generate electromagnetic showers. Charged pions have larger decay length and they can be disrupted or interact. If they interact, they produce 2/3 charged pions and 1/3 neutral pions. For very high energies and large decay length they can only interact due to time expansion, while the low-energy pions decay into muons and muon neutrinos ($\pi^+ \rightarrow \mu^+ + \nu_\mu$ και $\pi^- \rightarrow \mu^- + \overline{\nu_\mu}$).

The energy remaining in a secondary nucleon interacts after traveling the mean interaction length, resulting in the production of secondary mesons. Some secondary mesons after their interaction generate additional showers. The process of shower production continues until the point at which the hadron energy becomes lower than the energy threshold. [16],[19]

2.7. MUON ENERGY LOSS AT HIGH ENERGIES

At high energies, the radiation phenomena tend to become greater than the ionization of all charged particles. So, these phenomena are the dominant way for energy loss of energetic muons that exist in cosmic rays or produced by accelerators, having critical energy of hundreds GeV. Such processes are characterized by small cross sections, large energy fluctuations and are related to the creation of cascades. The average rate of muon energy loss can be described by the relation:

$$-\frac{dE}{dx} = \alpha(E) + E \cdot b(E)$$

where α(E) is the energy loss duo to ionization as given by the Bethe – Bloch equation for charged particles and b(E) is the sum of the contributions from the $e^+ e^-$ pair production, the braking radiation and photonuclear procedures. Considering that these slowly changing functions are stable, the mean range x_0 for a muon of initial energy E_0 is given as:

$$x_0 \approx (1/b)\ln(1 + \frac{E_0}{E_{\mu c}})$$

where $E_{\mu c} = \alpha(E_{\mu c}) / b(E_{\mu c})$ expresses the energy at which the loss due to radiation phenomena and ionization is the same. [11]

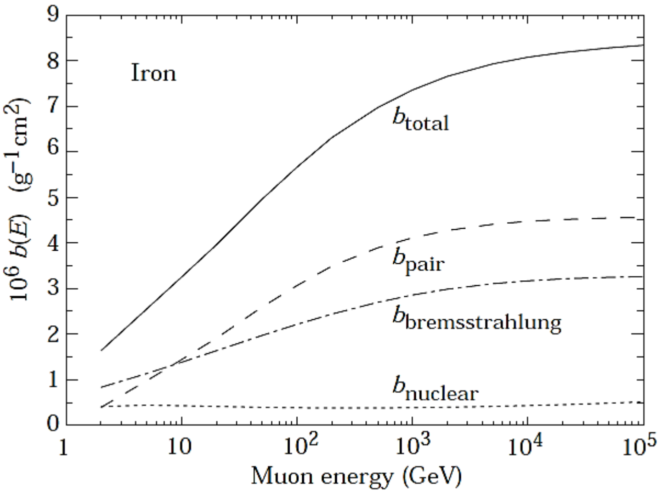

Figure 2.30: Contributions in fractional muon energy loss from the various energy loss phenomena. [11]

3. THE LARGE HADRON COLLIDER

The LHC (Large Hadron Collider) is the world's largest and most powerful particle accelerator and the most complex technological achievement in the field of High Energy Physics and Accelerator technology. The accelerator is located inside a circular underground tunnel having a perimeter of 26.7 km and a depth of 50 - 175 m at frenchswiss borders. This tunnel with a diameter of 3.8 m was constructed between 1984-1989 to host the large electron positron accelerator (Large Electron Positron Collider - LEP), which was in operation until 2000. [21],[53]

Figure 3.1: The LHC tunnel [21]

3.1. LUMINOSITY

The number of collisions is given by the equation $\frac{N}{\Delta t}$ = L [cm^{-2}s^{-1}]σ[cm^{2}], where L is the luminosity and σ the cross-section. Luminosity is considered to be one of the most important parameters of an accelerator, giving the number of collisions that can be produced in a detector per cm^2 and per second. The total cross-section for the proton - proton collision at 7 TeV is 110 mbarn. The absolute luminocity depends on the parameters of the beam and is given by the following equation:

$$L = \frac{n_b f_r n_1 n_2}{2\pi\ \Sigma_x \Sigma_y}$$

fr the rotational frequency in the LHC, n_b the number of packets in the interaction point (IP), n1 and n2 the number of particles each of the two crossing 'packets' contains, $\Sigma_x$and Σ_y is the size of the beam at the interaction point horizontally and vertically. The LHC luminosity does not remain constant during the experiment, but is reduced due to the attenuation of the intensity by beam collisions. At the designed operation of the LHC, the luminosity is about $L = 10^{34}\ cm^{-2}s^{-1}$. [21],[23]

3.2. THE LHC COMPLEX AND PROTON ACCELERATION

The electron - positron accelerators are suitable for strict controls and precise measurements but can not respond to the actions required at the LHC due to the electromagnetic radiation produced when charged particles are accelerated perpendicular to the axis (synchrotron radiation), as in the case of particle accelerators. The hadronic accelerators offer various advantages over the electron accelerators such as the ability to conduct studies on a wide range of energy without the necessary fine-tuning. The hadronic conflicts are the only way to study parton - parton collisions (including gluon - gluon collisions). The nominal LHC energies can achieve the desired values of cross sections of new natural processes.

One of the main goals of the LHC is to accelerate protons and heavy ions. Before entering the LHC ring the beam particles gradually accelerated so as to finally obtain the appropriate energy. Initially protons from hydrogen atoms that have been 'stripped' from their electrons by an electric field application are entering a linear accelerator, the LINAC2, from which protons are extracted with energy of 50 MeV. These protons are directed to the Proton Synchrotron Booster (PSB) where they are accelerated to 1.4 GeV and then they are introduced into the Proton Synchrotron (PS) at which they reach 26 GeV. Finally, they get into the Super Proton Synchrotron (SPS) where they acquire energy of 450 GeV and they end up at the LHC, reaching the maximum energy of 7 TeV per bunch. The required filling time of the accelerator with proton bunches is about 4 minutes and 20 sec, while the time needed to reach the final energy of 7 TeV is 20 min. The bunches are circulated for 10 hours.

The program of the LHC for short periods each year include collisions of heavy ions (lead - Pb) to study plasma quark - gluons. Lead ions are accelerated by the linear accelerator LINAC3 and fed into LEIR (Low Energy Ion Ring) that stores and cools the ions. [7],[21]

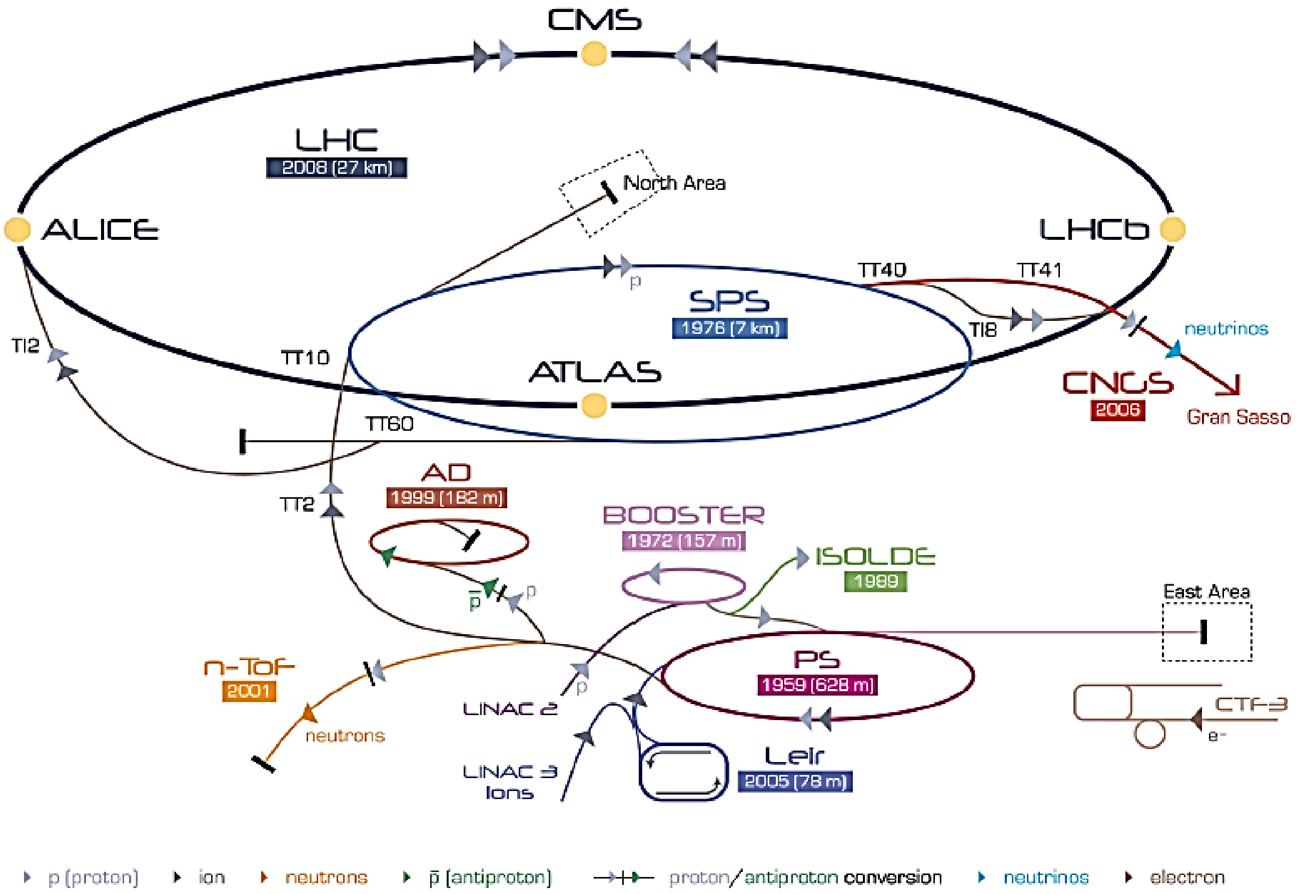

Figure 3.2: The full LHC acceleration complex with the four big experiments. [21]

3.3. LHC P – P COLLISIONS

The LHC produces collisions by crossing two proton beams moving in opposite directions within the ring at four intersection points. The beams are not continuous but are moving into bunches so that interactions between the two beams occur at discrete time intervals. Each beam includes 2808 bunches and each bunch $1.15x10^{11}$ protons. Between each consecutive bunch there will be 7.48 m, resulting in:

26659 / 7.48≈3550 bunches into the total circumference.

It is necessary to be enough space to get a correct sequence of bunches inected into the ring and to be able to insert new bunches when non – useful ones are extracted.

The total energy of the collision is of the order of 14 TeV. In this energy protons will move at 0.999999991c = 299792455 m/s speed, so a proton will take 90 ms to traverse the full perimeter of the accelerator. Each bunch will go around 299792455/26659 = 11245 laps/s, so during the 20 minutes needed to reach the final energy $11245 \cdot 20 \cdot 60 \cdot 26.7 = 3.6 \cdot 10^8$ km. The time between bunches (bunch spacing – BC) is:

t = distance / velocity = 7.48/299792455 = 24.95 ns.

Thus, the interactions between the bunches occur with a time difference of more than 25 ns. Each bunch gets squeezed down using magnetic lenses to 16x16 μm section at an interaction point (IP), where collisions take place. The probability of one particular proton in a bunch hitting a particular proton in the other bunch depends on the rate of the proton size (d^2 with d≈ 1 fm) and the cross sectional size of the bunch (σ2 with σ = 16 microns) in the IP. Then:

Probability = $(d_{proton})^2 / \sigma^2 \Rightarrow$
Probability = $(10^{-15})^2 / (16*10^{-6})^2 \approx 4*10^{-21}$

Therefore, if N is the number of protons per bunch, the number of interactions will be:

Probability $\cdot N^2 = (4 \cdot 10^{-21}) \cdot (1.15x10^{11})^2 \approx 50$ interactions per crossing.

But ust a fraction of these interactions are inelastic scatterings that give rise to particles at sufficient high angles with respect to the beam axis. The total p – p cross section is approximately 110 mbarns, counting the contributions from:

inelastic = 60 mbarn
single diffractive = 12 mbarn
elastic = 40 mbarn

Inelastic event rate at nominal luminosity is:

$N_{event/sec} = L \cdot \sigma_{event} \Rightarrow$
$10^{34} \cdot [(60 \cdot 10^{-3}) \cdot 10^{-24}]$= 600 million/s

With 11245 crosses per second:
11245 · 2808 = 31.6 millions crosses, the average crossing rate.

and so:

600 / 31.6 ≈ 20 inelastic events per crossing, therefore, 20 effective collisions per crossing. Most of the protons that didn’t collide are moving forward. Considering 3550 bunches:

11245 · 3550 = 40 million crosses ⇒ 40 MHz.

In every bunch passing, some of the protons collide at very high energies, giving primary vertices. At maximum luminosity more than 20 primary vertices are expected (pileup vertices). From these primary vertices secondary vertices are created and so on. The less energetic primary vertices are not taken into account. [54],[55],[56]

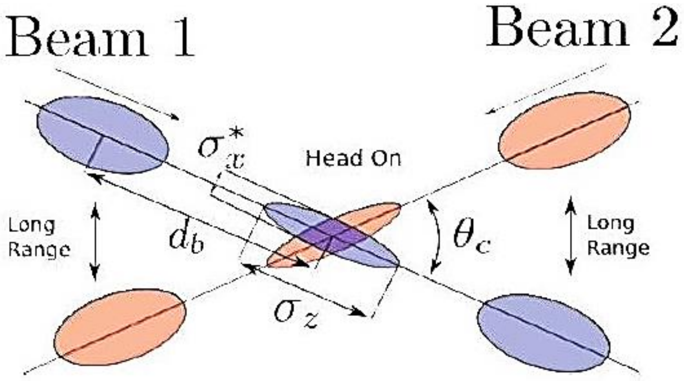

Figure 3.3: The larger is the crossing angle θc, the smaller is the area of overlap and therefore the possibility of collision is smaller. While σz is constant over the machine (~7.5 cm), σx varies and assumes its minimum in the Interaction Points. [54]

3.4. RF CAVITIES

A radiofrequency (RF) cavity is a metallic chamber that contains an electromagnetic field. Its primary purpose is to accelerate charged particles. RF cavities can be structured like beads on a string, where the beads are the cavities and the string is the beam pipe of a particle accelerator, through which particles travel in a vacuum.

To prepare an RF cavity to accelerate particles, an RF power generator supplies an electromagnetic field. The RF cavity is molded to a specific size and shape so that electromagnetic waves become resonant and build up inside the cavity. Charged particles passing through the cavity feel the overall force and direction of the resulting electromagnetic field, which transfers energy to push them forwards along the accelerator.

The field in an RF cavity is made to oscillate (switch direction) at a given frequency, so timing the arrival of particles is important. On the Large Hadron Collider (LHC), each RF cavity is tuned to oscillate at 400 MHz. [69]

Figure 3.4: RF cavities [66]

3.5. MAGNETS

The LHC consists of sophisticated superconducting magnets. Superconductivity is defined as the property of certain materials to conduct electricity with almost no resistance, when in the environment of very low temperature of about 1.9 K. Thus, it becomes possible to pass large amount of current through superconducting wires of relatively small diameter. The basic structural element of the accelerator is the magnetic dipole. Between the poles a toroidal vacuum tube of the dipole containing the bundle is placed. The poles are inclined to each other to reduce the generated field with increasing radius. A series of plates in order to minimize convection composes the electromagnet iron core. Furthermore, a hysteresis loop is required to reduce losses. The required magnetic field is generated by the passage of the core magnetic flux through the gap of the poles. The gap in the iron core is required to compensate the different thermal shrinkage of core and coils during cooling from room temperature to 1.9 K. Each dipole magnet weighs about 35 tons.

We distinguish two crossings of vacuum tubes of the accelerated particles and coils lines of each at the following image. They are surrounded by iron as it is a suitable magnetic flux crossing material to assist in maintaining the forces in the conductors When the coils are oozed by a large amount of power they must be kept under pressure to prevent movement and deformation.

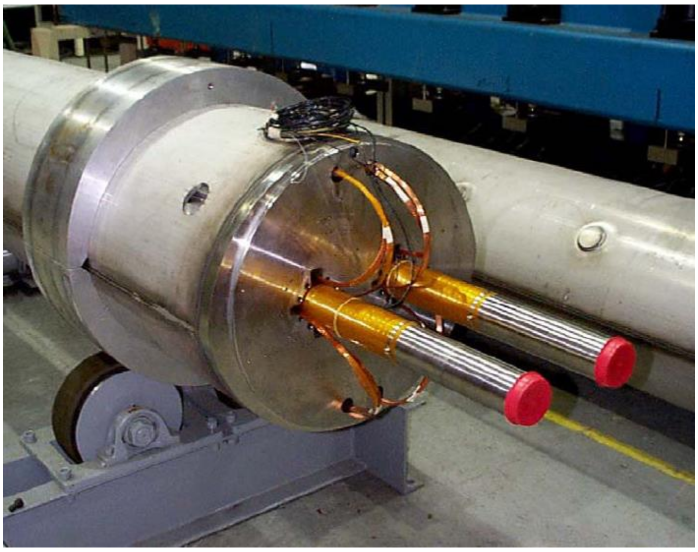

Figure 3.5: Superconducting dipole magnet. The diameter of each coil is 50 mm and the distance of the particle tubings' shafts is180 mm. Each coil is consisted of cells that are oozed by current with growing density. [7]

Another basic element of the LHC is the superconducting magnetic quadrupoles, which show a similar construction to that of the dipoles. A quadrupole magnet acts as a condenser lens in a plane and as decentralized in the other. The two coils of quadrupole share the same core, but its dimensions, as well as developing forces, are smaller. Unlike magnetic dipoles, the coils of quadrupole are oozed by current of variable frequence. The length of the magnetic quadrupole is about twice the length of the dipole magnet because it contains additionally supplementary and magnets of higher polarity (six and eight poles).

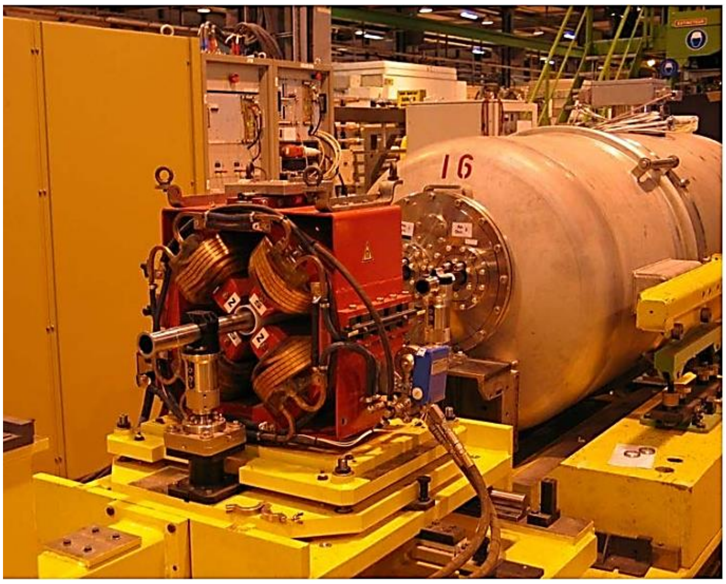

Figure 3.6: Superconducting quadrupole [67]

The system consists of 9593 magnets. 1232 dipole magnets coerces the bundles in a circular orbit and 392 quadrupole magnets ensure that the beams are centralized, increasing the likelihood of particle interaction of the two beams. The acceleration of the beams is controlled by radio frequency cavities (RF cavities) to 400 MHz. Magnets consisting of niobium-titanium coils (Nb - Ti) giving fields as 8.33 T with current 12 kA. [7],[23]

3.6. CRYOGENIC SYSTEM

The existence of a cooling system for maintaining the magnets in the operating temperature of 1.9 K is required. For this purpose five cryogenic islets for cooling the magnets and the linking pipes are manufactured. Cooling is performed using super-fluid helium because of its high thermal conductivity, making the LHC the largest cryogenic system in the world. Totally 120 tons of helium are used, of which 90 tonnes are for magnet cooling and the restof it serves pipe and cryogenic islands cooling.

Cooling is accomplished in three stages. Initially helium (He) is passed to the cooling stations, wherein by channelling 10000 tons of liquid nitrogen its temperature is reduced at 80 K. Thereafter, the helium temperature reaches 4.5K in the cooling stations. 140kW of cooling power is transferred to the ring. At this temperature the helium supplied to the magnets. Finally, the cooling system drops the helium temperature of 1.9 K as desired. [7]

3.7. SUPERCONDUCTING CABLES

The cables consist of 36 strands of superconducting wire, each strand with a diameter of 0.825 mm, and consists of 6300 superconducting filaments made of niobium - titanium alloy (NbTi). Each of the filaments is 0.006 mm thick and has a thin high-purity copper layer around it. In the superconducting state copper behaves as an insulating material (below -263° C), while at non-superconducting state functions as a conductor. Superconducting cables weight 1200 tonnes at a total length of 7600 km. The current flowing through the wires of the dipole magnets is 11700 A. [7]

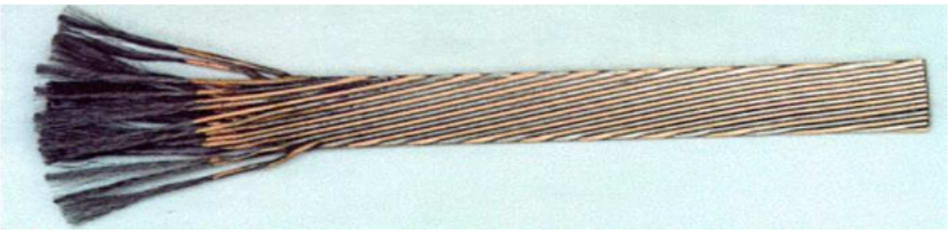

Figure 3.7: Superconducting cables [7]

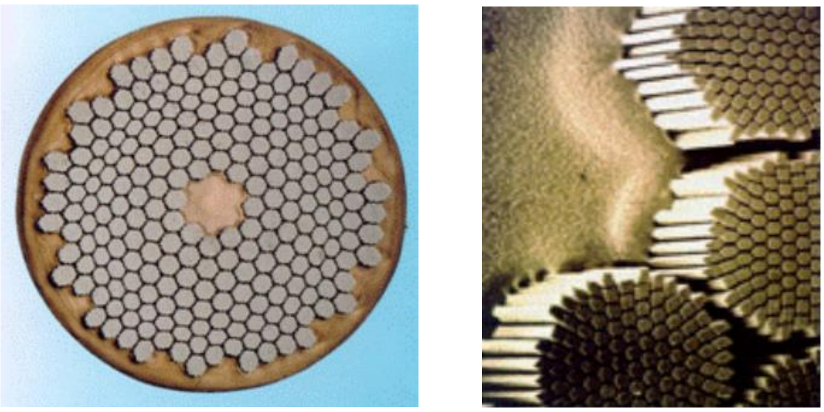

Figure 3.8: Strands (left) and filaments (right). [7]

3.7. LHC EXPERIMENTS

At the meeting points of the beams four detectors are placed. ATLAS (A Toroidal LHC ApparatuS) and CMS (Compact Muon Solenoid) are general purpose detectors designed for a wide range of natural studies, including studies of the Standard Model and the new physics. Both aim at achieving maximum luminosity of $L = 10^{34}\ cm^{-2}s^{-1}$ for proton – proton collisions. The ATLAS experiment will be discussed below. The CMS comprises a detector of 12000 tons based on a big high field superconducting magnet. The ALICE experiment (A Large Ion Collider Experiment) specializes in heavy-ion physics and the study of plasma properties of quark - gluons, which is estimated that existed in the primordial universe, and aims to provide answers in open questions of quantum chromodynamics. The LHCb experiment focuses on the properties of b - quarks and measurements for the violation of CP symmetry. The degree of violation of CP symmetry can not explain the amount of matter in the universe and the source of answers considered to be the study of the possible decay modes of B and D mesons. [7]

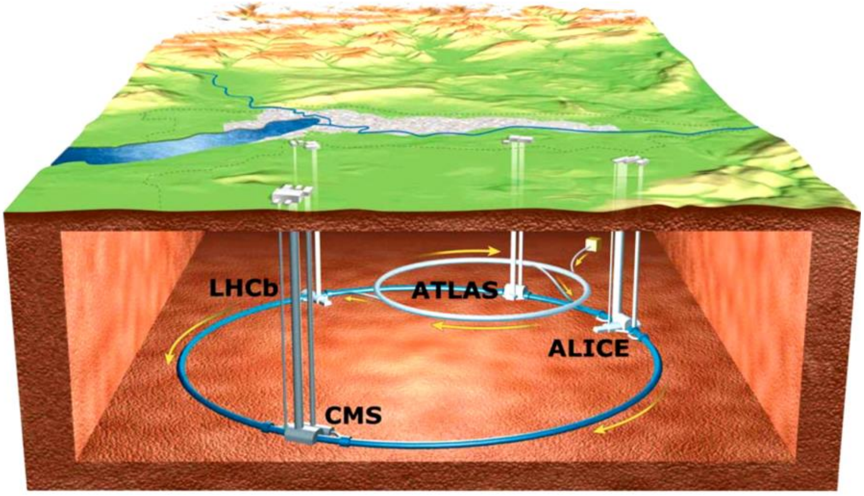

Figure 3.9: Schematic representation of the underground path of the LHC, with an average depth of approximately 100m, with the respective positions of the four experiments. [2]

4. THE ATLAS EXPERIMENT AT THE LHC

The ATLAS detector is the largest detecting apparatus of the LHC program. Its goal is to take measurements on the type, the orbits and energies of particles produced in the collisions. Because the conditions in the LHC, the detectors should have fast and radiation-resistant electronics, satisfactory resolution in momentum of charged particles and efficient track reconstruction, a calorimeter capable of recognizing and measure of photons and electrons, accompanied by a hadronic calorimeter of full coverage, a muon system effective in momentum recognition in a wide range and the ability of accurate identification of muon charge, very efficient triggering a sufficient background deduction and wide acceptability in pseudorapidity of almost full azimuthal angular coverage. The pseudorapidity is a spatial coordinate that describes the angle between the vector of the momentum of a particle with the beam axis, defined as:

$$\eta = -\ln[\tan(2\theta)]$$

where θ the angle between the particle momentum p and the beam axis. [2],[7],[21]

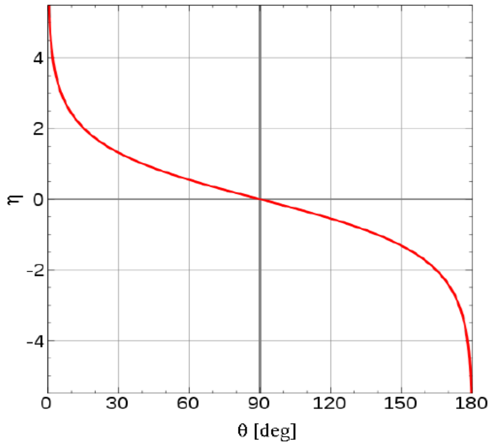

Figure 4.1: Pseudorapidity as a function of the angle θ. [7]

The ATLAS detector is cylindrical, consisting of concentric cylinders with increasing radius, 46 m long, 25 m high and weighs 7000 tons.[24]It is lengthwise symmetrical to the interaction Point (IP). The basic distinction can be made between the cylindrical (barrel) region, where the individual structures form cylindrical layers, and in the area where the detectors form circular discs (end - cap region). The experimental design allows the observation of phenomena associated with massive particles that could not be observed at lower energies. [2],[7]

Figure 4.2: The ATLAS cavern [25] with dimensions 35 x 55 x 40 m [58]

The beams of protons produced at the LHC interact in the center of the detector, allowing the possible production of particles. Any form the resulting physical processes or particles have, ATLAS is able to detect them, and therefore is characterized as a general purpose detecting system. The high energy of the LHC and the increased number of collisions makes the maintenance of mechanical parts in high radiation areas particularly difficult. [2]

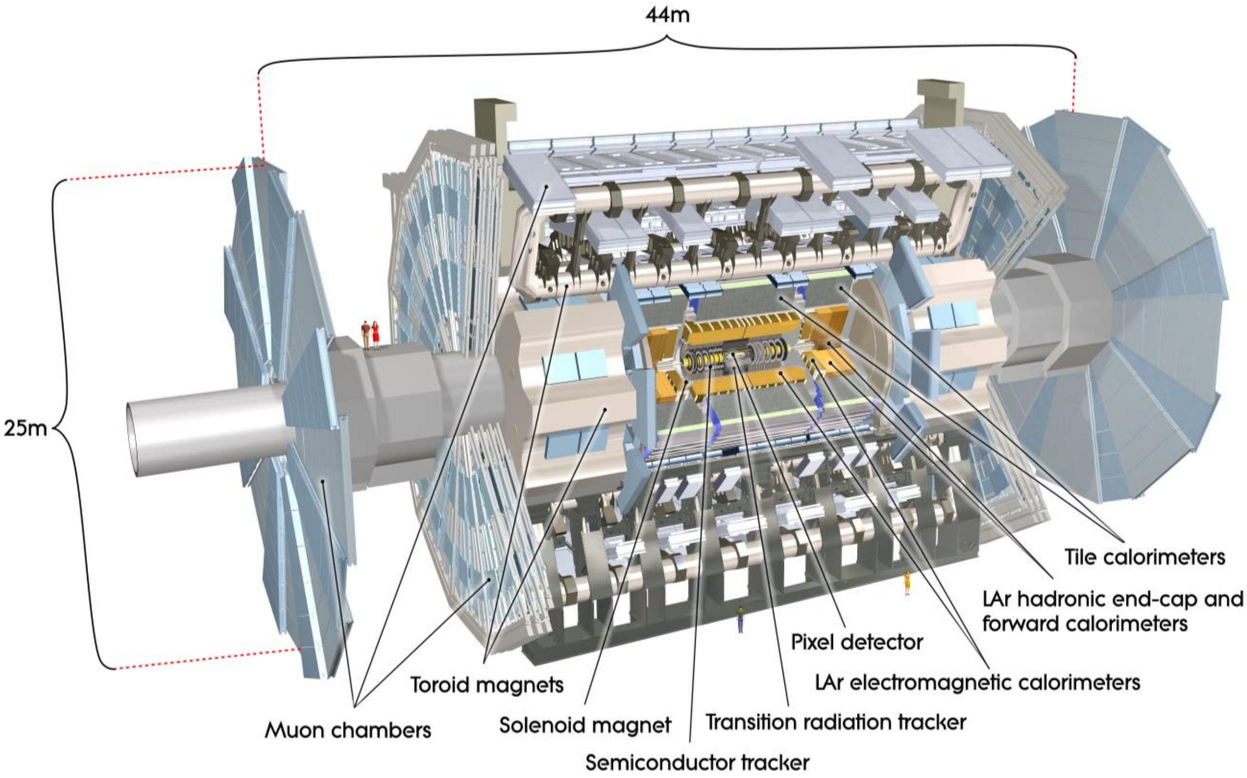

Figure 4.3: The ATLAS experiment. The different parts of the detector are noted. [21]

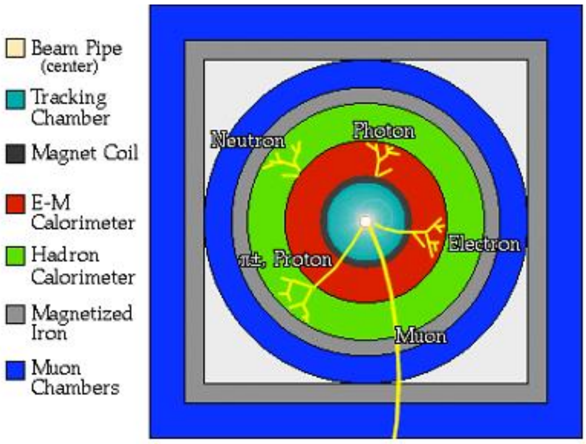

Figure 4.4: ATLAS cross section showing particle paths in each detecting layer. [64]

4.1. Coordination System

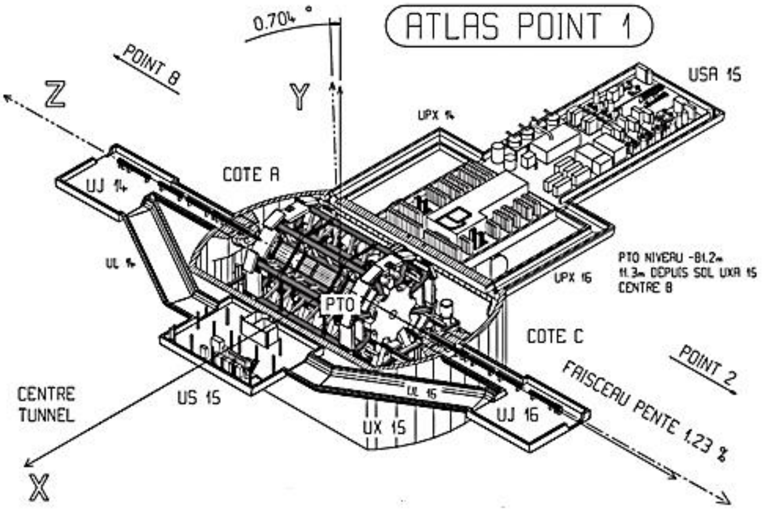

Figure 4.5: The ATLAS right handed coordination system with z in beam direction. [2]

Each measured quantity into the detector is based on this coordinate system: [2]

- The ATLAS coordinate system is right-handed.
- The interaction point (IP) is at the beginning of the coordinate system.
- The z axis is collinear to the beam.
- The x axis points towards the center of the LHC.
- The y-axis points upwards.
- The xy plane (transverse) is perpendicular to the direction of the beam.
- The A/C side of the detector is the side with positive/negative z respectively.
- r is the radial distance to the beam axis.
- φ is the azimuthal angle.
- θ is the polar angle.

- Rapidity is defined as $y = \frac{1}{2} \ln \left(\frac{E+p_z}{E-p_z}\right)$, where E and p_z is the energy and momentum along the z axis.
- In the limit in which the particle is moving near the speed of light, or its mass is almost zero, the pseudorapidity is numerically close to rapidity. Pseudorapidity together with the angle φ determine each position into the detector.
- The ΔR distance on the $\eta\varphi$ plane is defined as $\Delta R = \sqrt{\Delta\eta^2 + \Delta\varphi^2}$, where η and φ are Pseudorapidity and azimuthal angle respectively.

4.2. THE BEAMLINE VACUUM SYSTEM

The beam vacuum system represents the main interface between the ATLAS experiment and the LHC machine. The beampipe in the inner detector region, made of beryllium, runs from the interaction region to about z = ± 355 cm. The wall of this beampipe is 0.8 mm thick, and its inner radius is about 29 mm. At z = ± 355 cm, there is a short 10 cm long aluminum section. The beampipe material then changes to stainless steel. It remains to the previous dimensions until z = ± 1046.5 cm, where it flares to an inner radius of 40 mm and thickness of 1 mm by z = ± 1050.7 cm. At z = ± 1434.2 cm, there is a second flare and the beampipe expands to an inner radius of 60 mm (thickness 1.5 mm), by z = ± 1441.6 cm. The pipe stays this dimension until it nears the front of the TAS absorber, which will be described later, at z = ± 1865 cm. To pass through the small hole in the TAS collimator, by z = ± 1888 cm the beampipe reduces to an inner radius of 17 mm, with a wall thickness of 13 mm, and makes a transition to copper, which is roughly the same material as the TAS collimator itself. [48]

4.3. THE INNER DETECTOR – ID

The Inner Detector of 2.1 m diameter and 6.2 m length, is located in the innermost part of the ATLAS enclosing the beam line a few centimeters away from the axis. Its pseudorapidity occupies the range $|\eta| < 2.5$. Primarily it is required to recognize the kind of particle and the momentum by detecting the interaction with the material at various points, imprinting the pattern of charged particles passing therethrough. The Inner Detector is surrounded by a semi-conducting magnet that causes a magnetic field of 2T in the center of the detector, which curves the trajectory of passing particles, revealing the charge depending on the orientation of the curvature and the momentum by the degree of curvature, and information on the type of particle from the starting point of the track. The Inner Detector systems are mainly based on silicon microstrip detectors.

Three different technologies constitute the Inner Detector given the different particle flow in increasing radii: The Pixel Detector, the Semiconducting Tracker and the Transition Radiation Tracker. These detectors provide accurate measurements of the trajectories; the Pixel detector detects the peaks of the track and the SCT provides accurate measurement of momentum, which results in the provision of track reference points (3 and 4 points respectively). The TRT provides a large number of track points with high accuracy, thereby enhancing pattern recognition and also detects transition radiation photons contributing to particle identification.

Finally, the collisions recorded in the individual segments are combined to reconstruct the path of the charged particles, which is limited by the finite resolution of the detector, the relative positions of detector elements and the presence of the magnetic field and other uncertain contributions. [2],[21],[57]

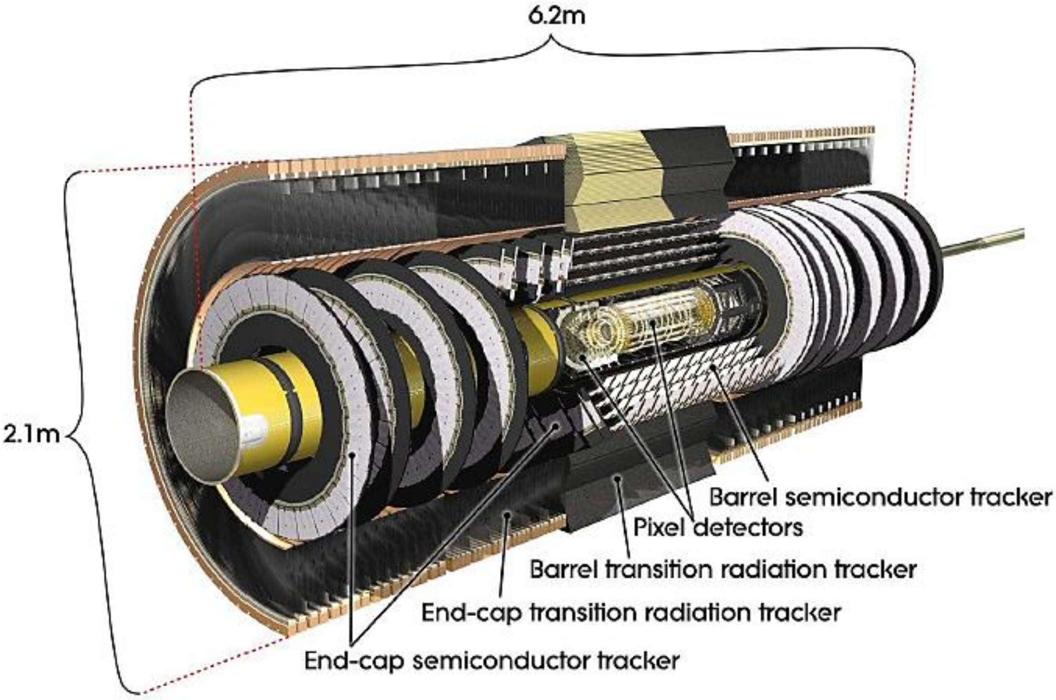

Figure 4.6: The ATLAS Inner Detector with the three subdetectors: the Pixel detector, the Semiconductor tracker and the Transition radiation tracker. [2]

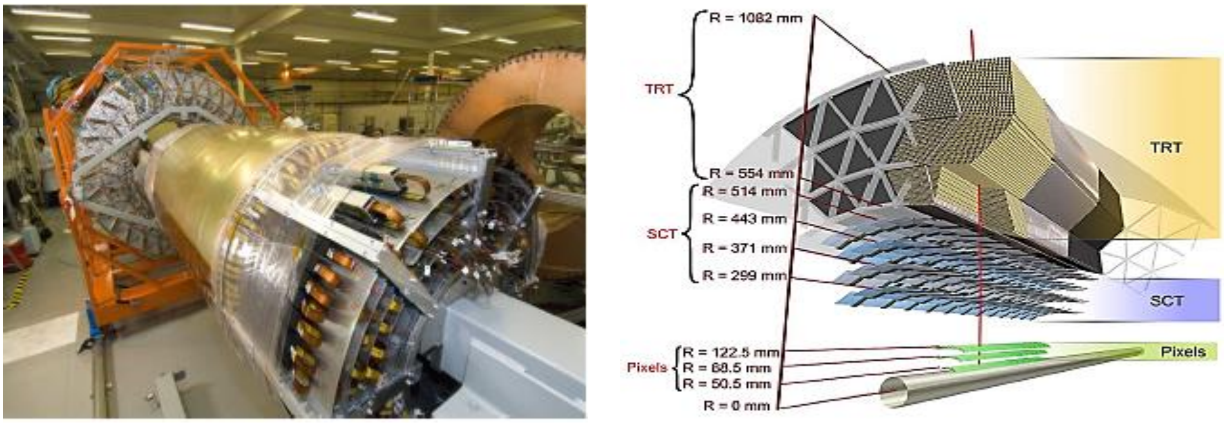

Figure 4.7: Left: The Inner Detector assembly and Right: a representation with the dimensions of the subdetectors. [31]

4.3.1. THE PIXEL DETECTOR

The inner part of the Inner Detector to the beam axis is the Pixel detector, which consists of three identical concentric layers of radii 5.1, 8.9 and 12.3 cm respectively, and plates of azimuthal angle 20°. Each layer has 22, 38 and 52 plates from the inside to the outside and each consists of 13 pixel units. Each unit has 16 front - end readout chips (FE) and a unit control chip (MCC). Each front - end chip contains 160 rows and 18 columns of pixels, in total 2880 pixels per front - end chip and 46080 pixels per detector unit.

Additionally, the Pixel detector consists of three discs at each end - cap and each disc is divided into 8 sections and 6 units per section. Each unit is identical to the cylinder units except from the connecting cables.

In total there are 1744 detectors units with an area of 2x6 cm^2 each and 80 million channels. The dense presence of particles requires good resolution of the silicon pixel detectors of 250 μm thickness, which are the possible unit that can be read having size of 50x400 μm^2 on the Rφ – z plane, with different circuits and electronics each, providing occupancy of 10^{-4} per pixel and per beam.

Each particle that crosses the Pixel detector generates electron - hole pairs that slide towards the readout electrode and if the collected charge exceeds a certain threshold, it can be recorded. The resolution is 10 μm on the Rφ plane and 115 μm in z coordinate. The front – end chips are an important energy source of 0.8 W/cm^2 consuming in the whole detector volume about 15 kW. This heat is removed through integrated cooling channels. The Pixel detector operates at -5° C to -10° C to reduce the wear due to radiation. The requirements for radiation control are more strict because of the proximity to the interaction point. [2],[21],[31]

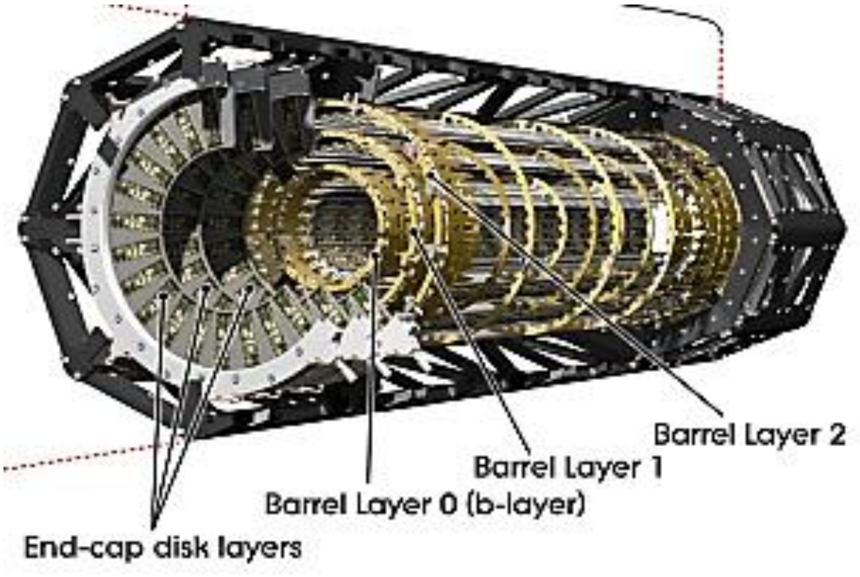

Figure 4.8: The Pixel detector [31]

4.3.2. THE SEMICONDUCTING TRACKER – SCT

The intermediate subdetector system which surrounds the Pixel detector is a silicon strip detector, of size 64.0x63.6 mm and 285 mm thick, which provides high quality track detection at a lower cost compared to the silicon pixels and can follow the traces of the vertical particle trajectories to the beam in a larger area. Its pseudorapidity covers the regions $|\eta| < 1.1 - 1.4$ (29.9-51 cm) and $1.1 - 1.4 < |\eta| < 2.5$ until 56 cm. It has a similar structure and function to the detector Pixel, and similar requirements on the radiation hardness.

In the present, the pixels are replaced by strip detectors of small thickness resulting in easy coverage of a large area. The STC consists of 4088 units of silicon strip detectors in 4 concentric double layer cylinders (2112 units) and two end - caps with nine disks each and 988 units per end - cap. The barrel units have an uniform design, with the strips in an almost parallel direction to the beam axis and the magnetic field, and each unit consists of four rectangular silicon strip sensors, connected in pairs to each side. A second pair of identical sensors is adhered to the previous disposed at a small angle to the z axis (solid angle of 40 mrad) to improve the spatial resolution capability at the z axis.

Essentially eight measurements (four spatial points) are provided for particles produced in the beam interaction region. The expected resolution is 17 μm on the rφ plane and 580 μm at z coordinate. The resulting data are read by 6.2 million readout channels in a total area of 61 m^2.

Each of the end - cap disks consist of not more than 3 unit rings with trapezoidal sensors, that may have five different sizes due to more complex geometry. The direction of the strips is axial, as in the cylinder, attached to angle 40 mrad. **[2],[21],[31],[38]**

4.3.3. THE TRANSITION RADIATION TRACKER – TRT

The transition radiation tracker is the outermost part of the Inner Detector. It uses thin polyimide drift chambers, 4 mm diameter and a length up to 144 cm, to provide about 36 additional measurements per track. This size is the compromise between speed of response and mechanical stability. Besides trajectory determination, particle identification (PID) is also possible, as mentioned above. The TRT consists of a barrel with three layers of 32 units each, with chambers arranged parallel to the beam axis (52,444 in total), occupying radii of 56 - 107 cm and $|z| < 72$ cm, in pseudorapidity range of $|\eta| < 0.7$. It also has two symmetrical end - caps, with 159,744 rooms in each, divided into 18 units (wheels) for 224 chamber layers. It occupies radii 63- 103 cm and $83 < |z| < 340$ cm, in pseudorapidity region of $0.7 < |\eta| < 2.5$. Each chamber behaves as a cathode and is under high negative polarity voltage with the anode grounded. In total, TRT includes 371 932 chambers.

The spatial resolution is about 130 μm, since larger coverage ability and transition radiation detection are necessary. In the center of the chamber a cable of diameter 30 μm is mounted. The chambers contain gas mixture of 70% Xe, 27% CO_2, 3% O_2, which is ionized when a charged particle is passing by. As a result, free electrons are produced which slide towards the anode wire, the signals from all the wires are collected and then they are amplified. The TRT can operate at room temperature.

Between the chambers materials having different refractive indices are inserted, causing the hyper - relativistic particles to emit transition radiation during their passage from the different media, resulting in very strong signals on the cables. The typical photon transition radiation energy deposited in TRT is 8 - 10 keV, while smaller particles that cause ionization, as pions, deposit 2 keV. The electron identification parameter is the number of local energy depositions above a given threshold. [2],[21],[31]

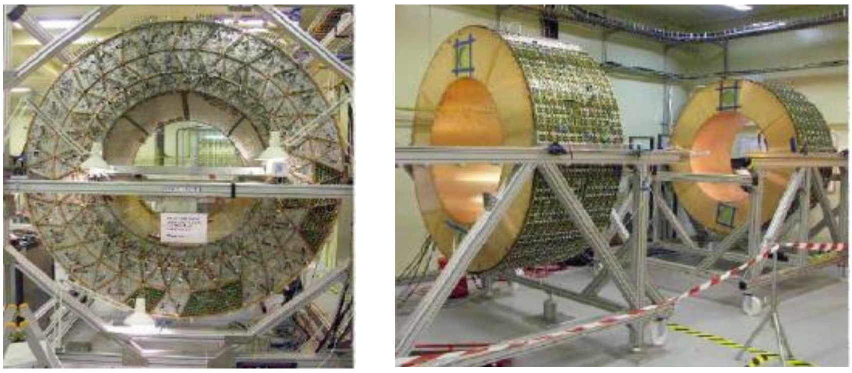

Figure 4.9: Left: The TRT barrel section. Right: end – caps. [33]

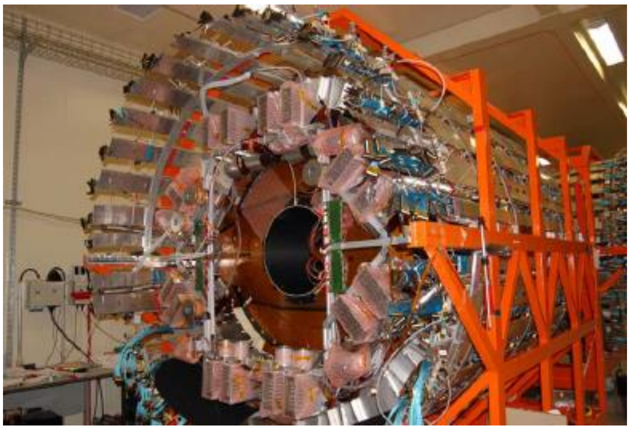

Figure 4.10: TRT and SCT end – caps [33]

Possible geometric disturbances of active detector elements and improper alignment can disturb the resolution of the reconstructed track. For this reason, various alignment algorithms have been developed based on the track to optimize the reconstruction performance of the Inner Detector.

4.4. CALORIMETERS

The calorimeters play a crucial role in the new physics discovery at the LHC, as they measure significant quantities to this direction, such as the reconstruction of the Higgs mass in the $\gamma\gamma$ channel and the observation of significant loss of transverse energy derived from non-interacting supersymmetric particles.

The ATLAS Calorimeter consists of an electromagnetic and a hadronic calorimeter and is located outside the solenoid magnet, between the Inner Detector and the Muon Spectrometer. The calorimeters are required to measure the energy and position of electrons and photons by sampling the deposited energy (10 GeV – 1 TeV), recognize particles, calculate the missing transverse momentum of an event, as well as the energy and direction of jets, and they further contribute to the choice of events to trigger level. At the LHC design luminosity (10^{34} $cm^{-2}s^{-1}$) multiple collisions will occur in every single bunch crossing (BC) every 25 ns, giving rise to the time and space "pileup". So, the calorimeters must be characterized by fast detection response, above 50 ns and detailed granularity. The radiation resistance is a prequisite, given the expected large particle flow in long-term operation. [2],[21],[31], [57]

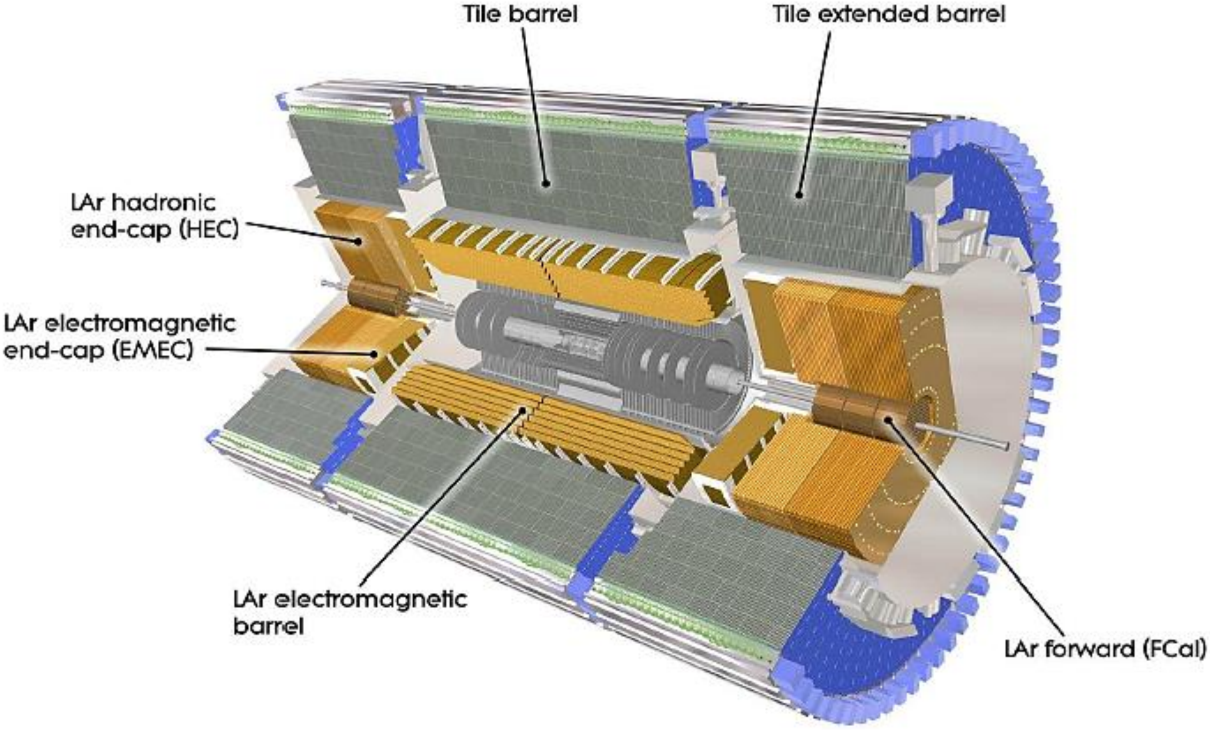

Figure 4.11: The calorimeter system estimates the energy and position of particles by sampling the deposited energy. [2]

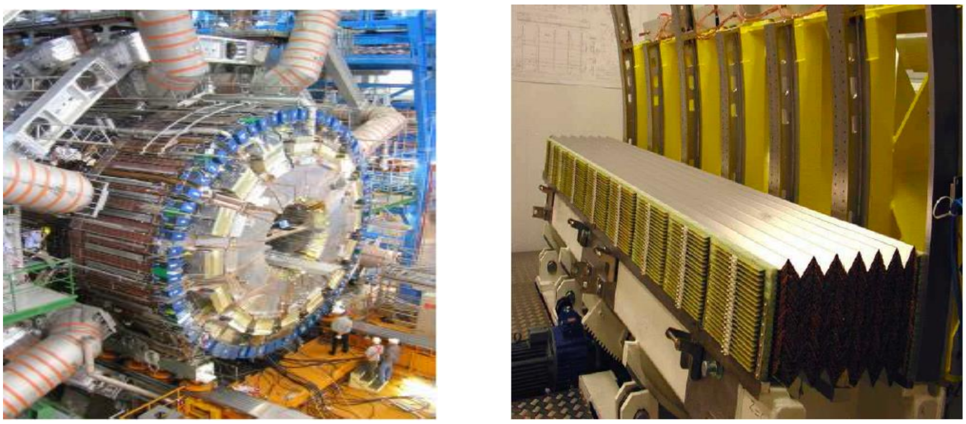

Figure 4.12: Left: The calorimeter integrated into the ATLAS detector. The toroid coils surrounding the calorimeters are also visible. [21] Right: EM “accordion”calorimeter. [31]

4.4.1. THE ELECTROMAGNETIC CALORIMETER – ECAL

The role of EM calorimeter is to absorb energy from particles that interact electromagnetically therewith, i.e., charged particles and photons. The pseudorapidity region that covers is $|\eta| < 3.2$. The ECAL is a liquid argon detector (Lar), wherein the absorbing material is lead (Pb) and the active material is liquid argon. Lead causes particle cascades, so the particles interact with the liquid argon resulting in electron ionization. These electrons can be collected from Kapton accordion shaped electrodes, which provide full coverage at angle φ without azimuthal gaps.

The density of the ECAL is often measured in units of the radiation length X_0. It consists of a barrel (22 X_0), separated into three parts with different granularity and two end - caps (26 X_0). The closest part to the beam (5 X_0) provides accurate measurements on the position of the particles and the deposited energy due to electromagnetic interaction with the material. The intermediate part has the greater granularity and absorbs the majority of the particles. The end - caps are composed of 1024 steel absorbers lined with lead with equal number of electrodes each. The barrel of the ECAL uses the same cryogenic system with magnets, in contrast with to the end – caps, which have their own. [2],[31],[37]

4.4.2. THE HADRONIC CALORIMETER – HCAL

The hadronic calorimeter absorbs energy from particles passing through the ECAL but not interacting via the strong force (mainly hadrons). It consists of a barrel and multiple end – caps, and is separated into two parts of independent technologies, the Tile Calorimeter ($|\eta| < 1.7$), which is placed outside the ECAL barrel, and the Liquid Argon Hadronic Endcap Calorimeter (LArHEC) ($1.5 <|\eta|< 3.2$), placed behind the ECAL end – caps.

The TileCal operates as a sampler of the deposited energy and uses plastic scintillator plates as active material, which generates signals to the photomultipliers.

The absorbent material is steel. It consists of three barrel parts, the central of $|\eta| < 1$ and two external of $0.8 < |\eta| < 1.7$.

The LArHEC uses LAr as active material, and copper (Cu) as an absorber. Each end - cap consists of two wheels, each of which has 32 identical subsystems.

Generally, the hadronic calorimeter is less expensive compared with the ECAL, regarding the positioning of the passing particles and the energy measurement.[2],[21]

Figure 4.13: TileCal Hadronic Calorimeter [65]

2.4.3. THE FORWARD CALORIMETER – FCAL

The pseudorapidity region covered by the FCAL is $3.1 < |\eta| < 4.9$ and it is separated into three parts. The first is made of copper and is used for electromagnetic calorimetry, while the other two parts are made of tungsten (W) in order to measure the energy of hadronic interactions. [2],[31]

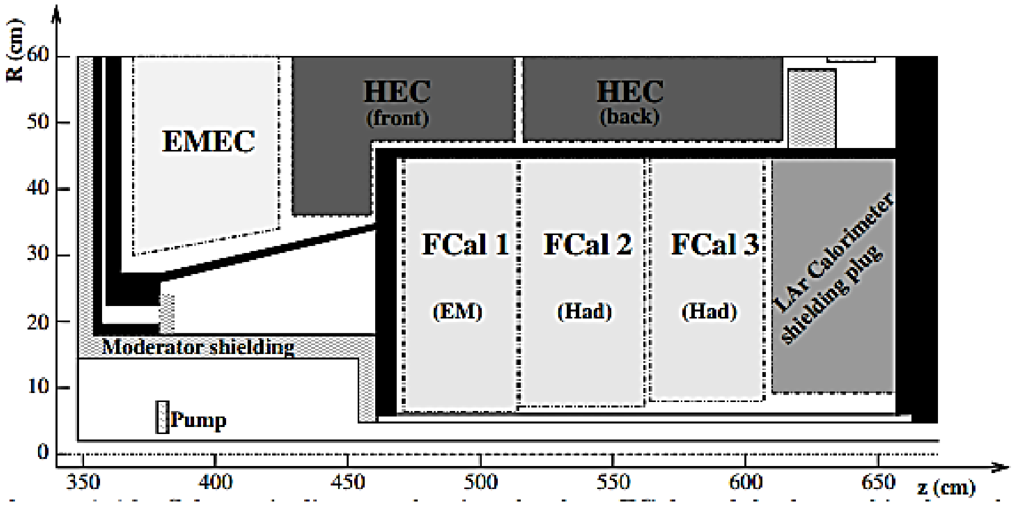

Figure 4.14: Schematic diagram illustrating the three sections of FCal. [31]

4.5. THE MUON SPECTROMETER

The high-energy muons presume interesting physical processes. They appear in standard model measurements at Z^0 and W^- bosons, as well as in studies of the Higgs boson, especially at W^+W^- and Z^0Z^0 decays. Their role is also crucial in the study of supersymmetry. [26]

The muon spectrometer is the outermost part of ATLAS, designed to measure accurately the momentum of muons, which penetrate the previous parts of the detector, hence the large size. It extends from a radius of 4.25 m around the Calorimeter to the outer part of the detector radius (11 m). The muon trajectory is artificially curved so as to measure their momentum with a different arrangement of the magnetic field, slightly reduced accuracy in position measurements and larger volume coverage. Muon momentum can be measured by determining three points in space, and of course, the larger the momentum of a muon, the smaller the curvature of the track by the magnetic field will be. The spectrometer also provides independent muon trigger.

Four different technologies constitute the spectrometer, specifically two subdetectors, the Monitored Drift Tubes - MDT and the Cathode Strip Chambers - CSC, and two triggering technologies, the Resistive Plate Chambers - RPC and the Thin Gap Chambers - TGC, and toroidal magnets in the barrel and the end - caps.

The spectrometer consists of a barrel, which covers a pseudorapidity range of $|\eta| < 1.05$ and two end – caps of $1.05 < |\eta| < 2.7$. In the barrel, the chambers (MDTs) are placed in three concentric cylindrical layers (channels), in radii of 5 m, 7.5 m and 10 m with respect to the z axis, with the two outer layers additionally contain RPCs. In the end - caps the chambers are placed on four disks arranged at 7m distance, 10 m, 14 m, and 21.5 m, with respect to the IP. In the three outer layers MDTs are used, while in the inner section CSCs replace the previous. For triggering TGCs are used instead of RPCs. [2],[21],[31],[57]

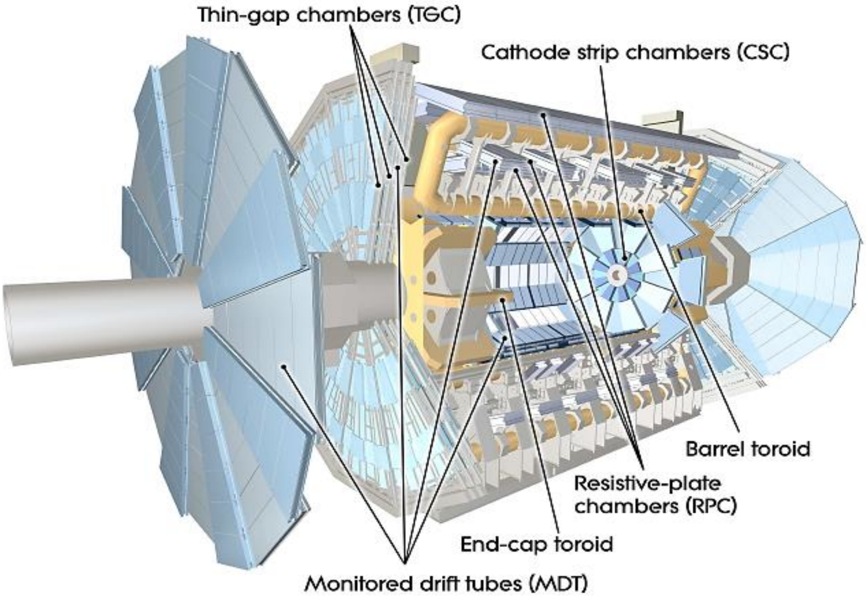

Figure 4.15: The muon spectrometer aimes at identifying, measuring and triggering of muons including four technologies (MDTs, CSCs, RPCs and TGCs). [21]

Each detector station has an error of about 35μm. The parameters of the four technologies are given in the following table:

			Chamber resolution (RMS)			*hits / muon*	
Type	**Function**	**Coverage**	**z/R**	**φ**	**time**	**barrel**	**endcap**
MDT	tracking	$\lvert\eta\rvert < 2.7$	35μm (z)	-	-	20	20
CSC	tracking	$2.0 < \lvert\eta\rvert < 2.7$	40μm (R)	5mm	7ns	-	4
RPC	trigger	$\lvert\eta\rvert < 1.05$	10mm (z)	10mm	1.5ns	6	-
TGC	trigger	$1.05 < \lvert\eta\rvert < 2.7$	2-6mm (R)	3-7mm	4ns	-	9

Table 4.1: The spatial resolution (columns 4 and 5) does not include uncertainties of the alignment of the chambers. The temporal resolution (column 6) does not include contributions from the transmission of signals and the electronics. [26]

A good practical approximation for the determination of a muon trajectory is using sagitta. The maximum deviation of a circle from the line is defined as sagitta, and its accuracy increases when the distance L of the outer measurements also grows. The relation that links sagitta with the transverse muon momentum p_T into a magnetic field of magnetic strength B is as follows:

$$p_T = \frac{BL^2}{8s}$$

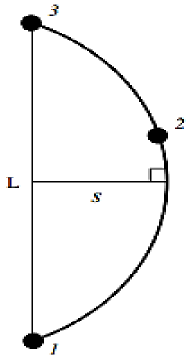

Figure 4.16: Sagitta(s) to three points measurement.[26]

As regarding the end – caps, the momentum measurement is slightly different as there is no magnetic field between internal and external stations, so the track is not curved. Conversely, the direction between the interaction point and the measurement of the inner layer is compared with the direction of the measurements in the middle and the outer layer.

To enable reconstruction, the spectrometer is constructed so that each muon of $|\eta| < 2.7$ will cross at least three detection stations, except maybe some areas. When a particle crosses only two stations, the ID is taken as the third measurement and the momentum is determined by the difference between the angles regarding to the IP. [26]

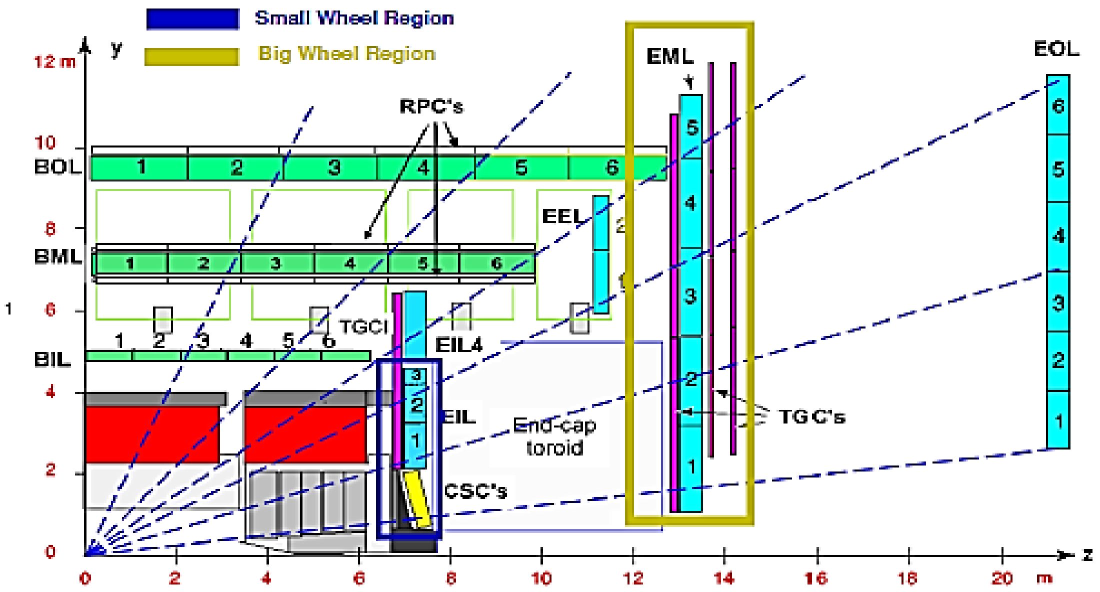

Figure 4.17: Side view of a quarter of the ATLAS muon Spectrometer on z – y plane for angle φ = π/2. The stations (inner, middle, outer) are noted as BI, BM, BO respectively for the barrel and EI, EM, EO for the endcap. With different colors the different chambers are indicated: Endcap MDT (blue), CSC (yellow), barrel MDT (green), RPC (white) and TGC (magenta). [21]

Three different regimes can be identified:

- pT < 30 GeV, for low momenta, the resolution is defined by the fluctuations of the energy loss in the calorimeter;
- 30 < pT < 200 GeV, for intermediate momenta, the resolution is dominated by multiple scattering;
- pT > 200 GeV, for high momenta, the resolution is determined by the intrinsic MDT tube resolution and the alignment of the chambers.

4.5.1. THE MONITORED DRIFT TUBES – MDTS

The MDTs are 3cm diameter aluminum tubes, of 0.4 mm wall thickness and 0.9 m - 6.2 m length and contain Ar 93% and CO2 7% in absolute pressure of 3 bar. They cover almost the entire pseudorapidity range of |η| < 2.7 except for high pseudorapidity region where the CSC are located. They are placed vertically to the beam axis and each chamber comprises of two multilayers of MDT tubes, each of the multilayers composed of three levels (intermediate - external stations) or 4 (internal stations). The operating voltage is 3080V. When a muon is passing through the chamber, the ionized electrons are drifting towards the positive electrode and the positive ions are directed to the cathode. The spatial resolution of a tube is about 80 μm and the overall accuracy of the level across the anode is 40 μm. The MDT detecting system consists of 1150 chambers and contains a total of 354000 drift tubes. [2],[21],[26]

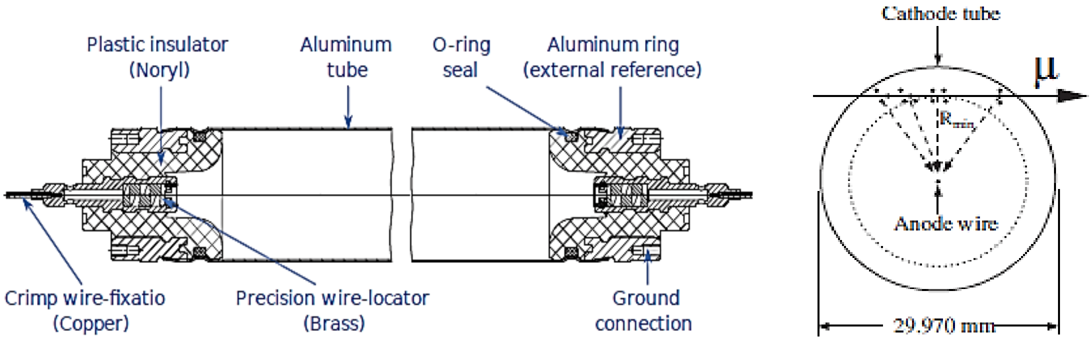

Figure 4.18: Left: Cylindrical aluminum drift tube, the main detector of the MDT chambers. Right: Cross-section of the chamber [2]

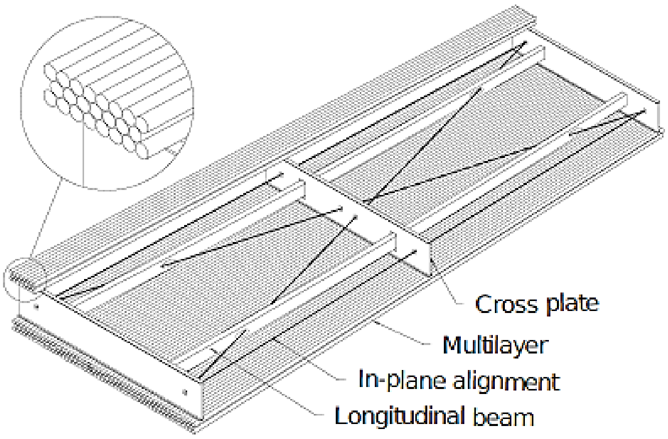

Figure 4.19: Schematic representation of an MDT chamber. [21]

4.5.2. THE CATHODE STRIP CHAMBERS – CSCS

The CSCs are multiwire proportional chambers that occupy a high pseudorapidity region of $2.0 < |\eta| < 2.7$. They are separated to the angle φ into two wheels of eight chambers each. They contain gas mixture of Ar 80% and 20% CO_2 under atmospheric pressure. The accuracy of the coordinates of a passing muon is achieved by measuring the induced charge in the segmented cathode strips by the formed avalanche in the anode wire. Each passing muon gives four independent measurements for both η (resolution of 60 μm) as well as for φ (resolution of 5 mm). The anode wires are oriented towards the radial direction while the cathode strips are placed orthogonally to the anode wires. [2],[21],[26]

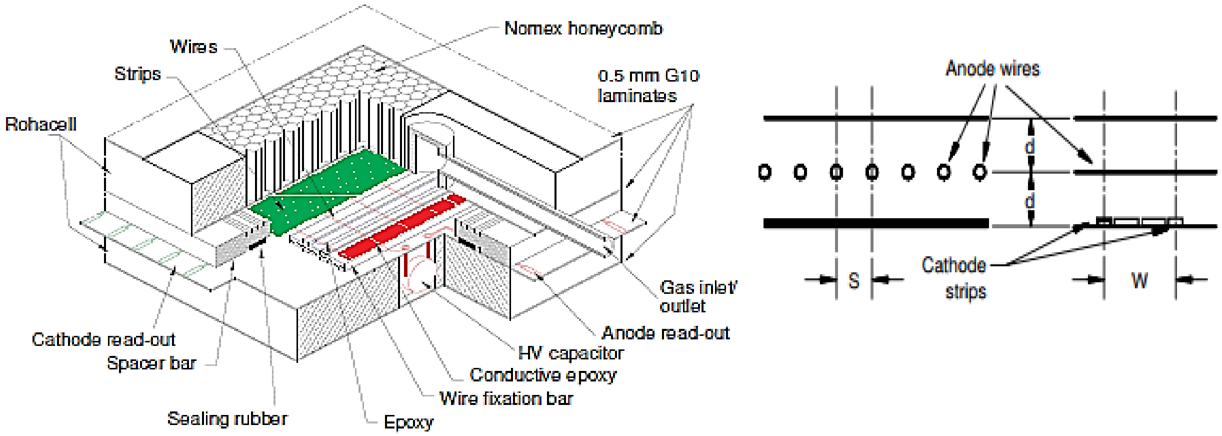

Figure 4.20: Left: Internal CSC structure. [45] Right: Structural CSC diagram showing anode and cathode wires and strips. The spacing of the cables S and anode - cathode distance d is 2.54 mm. [26]

4.5.3. The Resistive Plate Chambers – RPCs

Like MDTs, RPCs are placed on three concentric layers around the beam axis between the eight coils of the toroidal magnets, consisting of two parallel planes which are spaced 2 mm, enclosing a gas mixture of $C_2H_2F_4$ (94.7%), iC_4H_{10} (5%), SF_6 (0.3%). In nominal operation a uniform electric field is flowing through the volume of the chambers, allowing time resolution of 1.5 ns. The readout strips have a typical width of 30 mm and are divided into two planes, orthogonal to each other, for measurements of η and φ. The measure of the φ component has a spatial resolution of 10 mm is of particular importance that the MDT chambers cannot measure this component. The trigger can choose high momentum muons, with thresholds ranging from 9 to 35 GeV. The internal RPC undertakes triggers of lower momentum with thresholds that vary from 6 to 9 GeV. A muon RPC provides six measurements. [2],[21]

4.5.4. Thin Gap Chambers –TGCs

The TGCs are multiwire analog chambers and are placed in four levels around the beam axis. The inner TGC level ($1.05 < |\eta| < 1.92$) is incorporated in the supporting structure of the toroidal coils of the barrel section in $|z| \sim 7$ and is separated into two non-overlapping segments, the forward and the end - cap. Each chamber has a pair of two TGC levels. The remaining 3 TGC levels are located at the wheels outside the intermediate MDT station at $|z| \sim 14$ and they give seven measurements in total, a triplet chamber level (TGC1, $1.05 < |\eta| < 2.7$) and two doublet chambers (TGC2 – TGC3, $1.05 < |\eta| < 2.4$). Cumulatively, there are nine TGC levels. The two cathode graphite levels on the outer surface in are arranged in strips orthogonally placed to the wires. The gas mixture of CO_2 44% n - C_5H_{12} 45% allows operation in high saturation with a time resolution of 4 ns. The measurement to the φ component is conducted by the strips with a spatial resolution of 3 - 7 mm, while the measurement in the r component is carried out by the wires with a spatial resolution of 2 - 6 mm. [2]

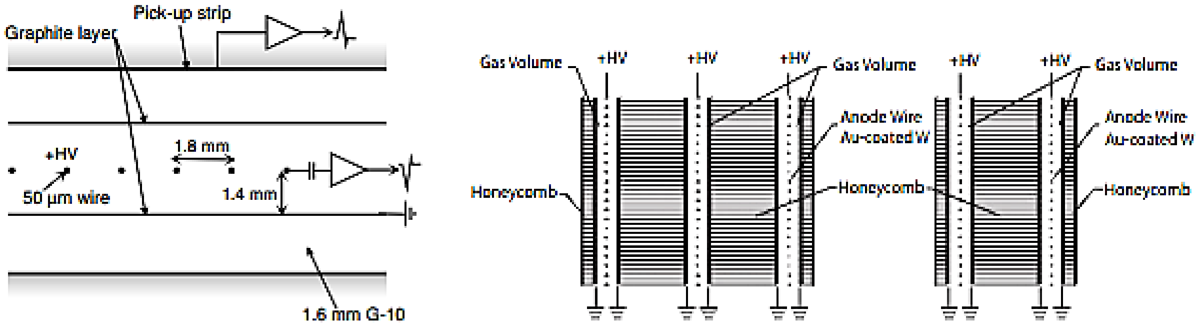

Figure 4.21: Left: The TGC structure in which the anode cables, the cathodes of graphite and a pick - up strip orthogonal to the wires are illustrated.[21] Right: Intersection of a triplet and a doublet TGC unit, with the dimensions of the air gaps have increased with respect to the other elements. [26]

4.6. FORWARD DETECTORS

There are three forward detectors. The main operation of the first two is to identify ATLAS luminosity.

LUCID (Luminosity measurement Using Cerenkov Integrating Detector), which is the main ATLAS online luminosity counter, is located 17 m from the IP, at a radial distance of about 10 cm from the beam-line ($|\eta| \approx 5.8$), and detects non – elastic scatterings in the forward region. It consists of 20 aluminium tubes which surround the beam-pipe. The Cerenkov light emitted by a particle traversing the tube is reflected on average three times before the light is measured by photomultiplier tubes (PMTs). The PMT signal amplitude is used to distinguish the number of particles per tube, and the fast timing response provides unambiguous measurements of individual bunch-crossings. LUCID is situated in a high radiation area and, although the PMTs are radiation hard, their performance is expected to gradually degrade. The Cerenkov light from the detector is transmitted through radiation-hard quartz fibres to a region with low background radiation, in which the fibres are read out with multi-anode PMTs. The 16 electrical signals from the PMT readout are fed into a custom-designed front-end card, containing a fast amplifier and a differential line-driver, and then pass through a discriminator, which registers a hit each time the PMT pulse height is above a preset threshold. A charge-to-digital converter allows offline analysis of the signal amplitudes. One of the digital outputs of the front-end card is fed into a multi-hit time-to-digital converter for offline timing analysis, with a second output going to a custom-designed 9U VME readout card. The readout card houses FPGAs used to calculate the luminosity for each bunch-crossing using different algorithms. After receiving a L1 trigger accept signal, the readout card sends the pattern of hits to the overall readout system, and also provides an independent LUCID trigger. The LUCID readout buffer is sent to the trigger and data acquisition system via the S-link interface for inclusion in the overall event record.

The second Forward Detector, ALFA (Absolute Luminosity For ATLAS), is located 240 m from the IP and it consists of scintillator fibers located inside 'Roman pots', which are designed to approach as close as 1 mm to the beam. The extremely small scattering angles (3 mrad) needed to measure the absolute luminosity, are smaller than the nominal beam divergence, and can therefore only be performed with specially prepared beam conditions.

The third system refers to zero – degree calorimeter (ZDC) which plays dominant role at the determination of collision centrality of heavyweight ions. This system is mounted 140 m from the IP with $|\eta|> 8.3$. Significant backgrounds in hadron-collider experiments are created by beam-gas and beam – halo effects, which can be greatly reduced by requiring a tight coincidence from the two symmetric arms of the ZDCs. The four ZDC modules per arm (one electromagnetic (EM) module and 3 hadronic ones) consist of layers of alternating quartz rods and tungsten plates. [31]

4.7. THE MAGNET SYSTEM

The ATLAS magnet system provides the bending force required for momentum measurements. The system is composed of a central superconducting solenoid, which is aligned along with the beam axis and three superconductive toroidal air-core (a barrel and two end - caps), providing good momentum resolution and ensuring minimal multiple scattering.

The central solenoid is located around the inner detector and gives 2T axial field in the tracker, having an axial length of 5.3 m, 1.2 m radius and operating temperature of 4.5 K using liquid helium around the coils. The same cryogenic system with calorimeter is used to minimize the material. The peak of the field reaches 2.6T at the superconducting windings. The nominal current is 7.6 kA. The coils with the supporting structure and the magnet material must be minimized to avoid particle absorption.

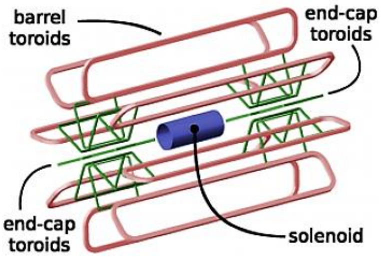

Figure 4.23: Graphical representation of the three main parts of the ATLAS magnet system. The central tube is positioned within the cavity of the liquid argon calorimeter (blue), surrounded by the cylinder (red) and the toroidal coils of the endcap (green). [21]

The toroidal system (air - cored toroid) consists of eight coils which provide non-uniform magnetic field, toroidal and perpendicular to the corresponding field of the solenoid with an average width of 0.5T in the muon spectrometer. A toroidal cylinder with a length of 25.3 m, an internal diameter of 9.4 m and an outer diameter of 20.1 m covers the barrel region. The toroids are electrically connected in series with a nominal current of 20 kA. The magnetic field varies according to pseudorapidity. The peak of the toroidal superconductor is 3.9 T for the barrel region and 4.1 for the end - caps. The end - caps toroid is rotated 22.5° towards the barrel toroid maximizing the bending force to the limit region between the barrel and the end - caps. [2],[21]

Figure 4.24: The cylindrical solenoid magnet enters the surface of the LAr Calorimeter [21]

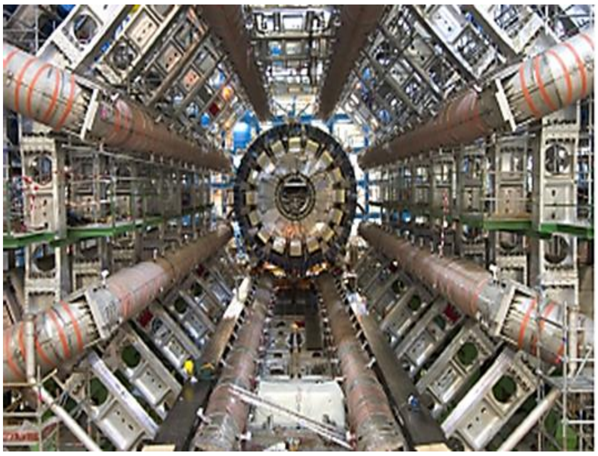

Figure 4.25: The eight ATLAS toroid coils [21]

Figure 4.26: One of the two toroidal magnets in its final position surrounded by the toroidal coils [21]

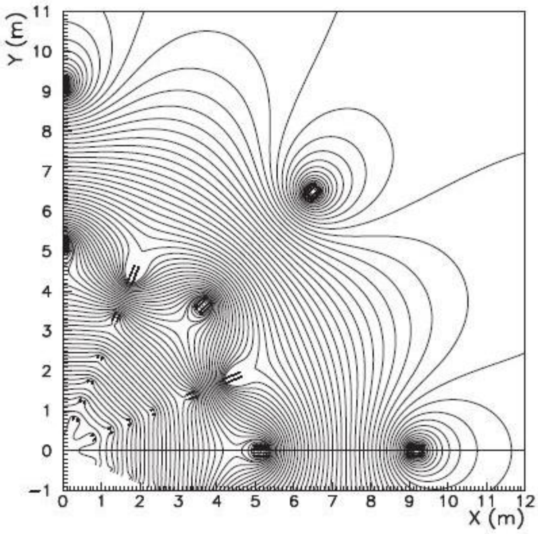

Figure 4.27: The magnetic field in the transverse plane, between barrel and endcap. The coordinate system of the magnetic field is rotated by π/8 with respect to the ATLAS coordinate system. [2]

4.8. THE ATLAS TRIGGER

The current LHC luminosity levels produce 0.2 billion p – p events per second. The mean data size for reading out all fired detector channels belonging to the same bunch crossing (BC) is about 1.5 MB. However, the processing and storage capabilities set an upper bound of about 100 selected events per second. To achieve this enormous reduction factor of the order of 10^7 without losing interest events, the existence of a trigger system is necessary.

The ATLAS trigger system consists of three levels. Each higher level is based on the decisions taken earlier, often introducing additional selection criteria. The Data Acquisition System (DAQ) receives and stores the data of the events of the electronic readout electronics to the rate of the Level 1 trigger. [2]

Level 1

Level 1 (L1) trigger is hardware based by using processors (FPGAs, ASICs), synchronous and based on pipeline logic, having a design which allows decisions within 2.5 μs (75 kHz). L1 searches for signatures from high-pT muons, electrons/photons, jets, and t-leptons decaying into hadrons. It also selects events with large missing transverse energy (E_T^{miss}) and large total transverse energy. The L1 trigger uses reduced-granularity information from a subset of detectors: the Resistive Plate Chambers (RPC) and Thin-Gap Chambers (TGC) for high pT muons, and all the calorimeter sub-systems for electromagnetic clusters, jets, t-leptons, E_T^{miss}, and large total transverse energy. The pipeline logic separates the processing into smaller steps, each of which can be completed in a time equal to the detector response time (25 μs). Thus, many operations can be performed in parallel, if each of them is using different processing unit. The use of the pipeline requires a time contingency of 500 ns to avoid pipeline overflow. The delay of the L1 trigger will be equal to the pipeline length.

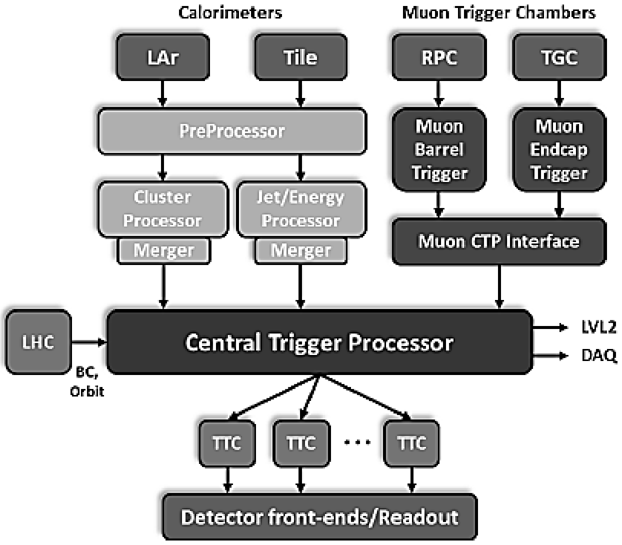

Figure 4.28: ATLAS Level-1 trigger architecture. [39]

The trigger system is in total constituted by the Central Trigger Processor (CTP) which is fed by signals from hardware trigger calorimeter (L1 Calo) and the spectrometer (L1 Muon). [39]

The L1 muon trigger is based on dedicated finely segmented detectors (the RPC's in the barrel and the TGC's in the end-caps, with a sufficient timing accuracy to provide unambiguous identification of the bunch-crossing containing the muon candidate.

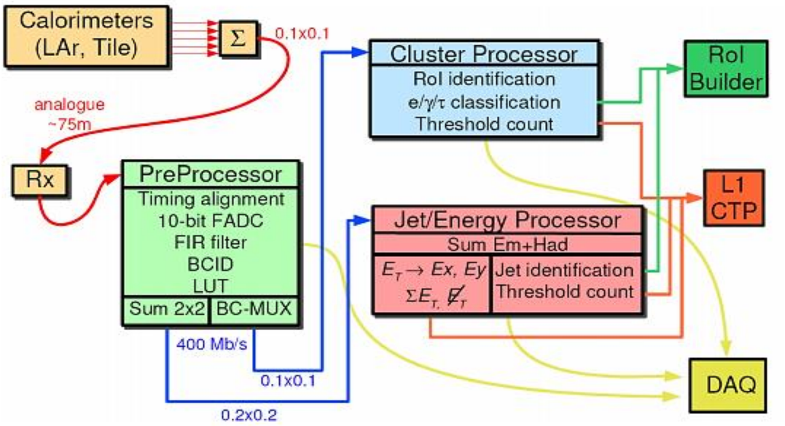

Figure 4.29: Triggering at the Calorimeter [41]

In readout pipeline systems, information from each beam collision for each detector element is maintained during trigger latency. This information can be analog (kept in capacitor), digital (ADC), or binary (hit - no hit). In this case, the output of the trigger system is a single bit "Level -1 Accept" (L1A), which gives a signal to the front - end readout of the detector systems via the Trigger Timing and Control System (TTC) to decide whether to read or not the event information kept in the pipeline of the front - end electronics. The readout of accepted facts can pass to the next trigger stage.

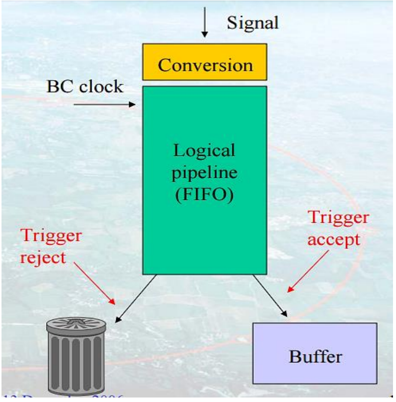

Figure 4.30: L1 triggering Data Flow [42]

The L1 trigger has its own trigger menu (default triggers Level 1), which is read at each data acquisition cycle and contains information about the thresholds from prescaled trigger objects. These objects consist a list of 256 criteria for deciding rejection or not of the event. The technique that ensures the vitality of the trigger system even at high luminosity is called prescaled trigger. Increasing the luminosity, a linear increase of the trigger rate is observed. If a particular trigger is prescaled to a value, then only the number of events that cause trigger equal to this value can be recorded. The trigger menu also includes combinations of trigger objects for use with respect to the decisions to be taken. The area where the detector trigger objects appear, is called Region of Interest (RoI).

The trigger chains in the menu are given names of the form NzXX i, where the various components denote the following:

1. N (optional): The minimum number of objects required.
2. z: The type of selection, including
    - e = electron
    - g = photon (γ)
    - E = total ET , etc.

3: XX The minimum transverse energy required.
4: i An online quality requirement, such as tight, loose etc. This refers to one of many possible sets of criteria depending on the particle type, for example, the shape of the shower produced in the calorimeter.

Each chain is composed of LVL1, LVL2 and EF components. Ordinarily, an event is recorded if it satisfies at least one trigger chain. However, a small fraction of events are recorded in “minimum bias” mode, meaning that they are selected for storage (almost) randomly, regardless of whether or not they satisfied any chain. Similarly, within a single chain, a certain fraction of events are “passed through” one or more components, meaning that they pass regardless of what the trigger’s physics-based decision would have been. On the other hand, some events are rejected at random by a trigger chain, despite the fact that they meet the right criteria to pass. [31],[35],[36],[40],[42]

Level 2

The L2 trigger is software based and uses algorithms that run on multiple computers of multiple processors each, which are connected via a fast network. This level uses a L1 RoI as a seed and performs a partial reconstruction of the event starting from the RoI, and uses full granularity data from all detectors in contrast to the first level. The full computing power is based on complex decision algorithms that reduce trigger frequency at about 3.5 kHz, with a corresponding average processing time of 40 ms, according to the complexity of the event. The events are sent from the readout servers to events constructors for further analysis. [31]

Level 3

The last level (L3) is the event filter and is also software based. It uses the RoIs of the second level and the full granularity of the detector for entire event processing. The rate now reaches 400 Hz with size event of 1.3 Mbyte. The mean processing time is 4 sec. The events of interest for each different physical analysis are separated into streams of events. The events that have finally passed the filter events are stored for further analysis. Level 2 and event filter consist the high level trigger. [31]

Finally, it is noted that during data acquisition multiple conditions are unstable, ie some parts of the detector may malfunction, or be disabled, or changes in beam condition might occur. Therefore, the trigger system should be flexible and robust to manage such changes in real time. [31]

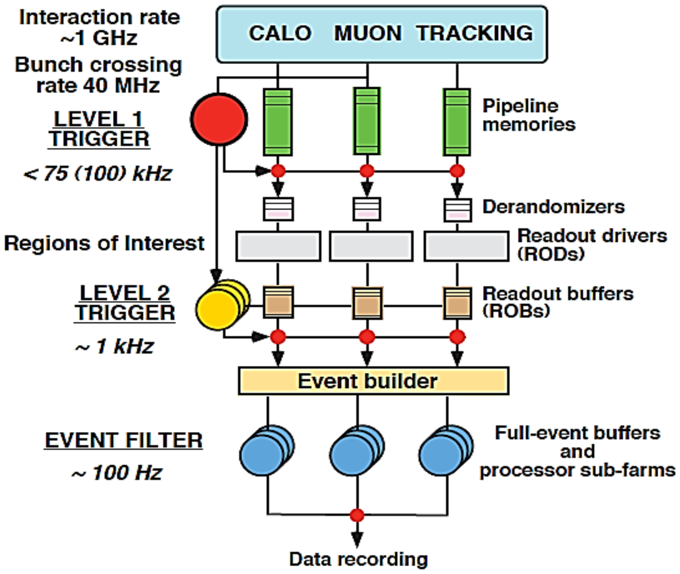

Figure 4.31: Architecture of the ATLAS trigger system with the numbers of the frequency of events at different trigger levels. [2]

Detector	*Channels*	*Frame size (KB)*
Pixels	$1.4*10^8$	60
SCT	$6.2*10^6$	110
TRT	$3.7*10^5$	307
LAr	$1.8*10^5$	576
Tile	10^4	48
MDT	$3.7*10^5$	154
CSC	$6.7*10^4$	256
RPC	$3.5*10^5$	12
TGC	$4.4*10^5$	6
LVL1		28

Table 4.2: Event Size of ATLAS 1.5 MB (140 million channels) [41]

Trigger efficiency

In the case of a trigger chain, the efficiency of the trigger, denoted ε, refers to the probability of a particle passing that particular chain. Efficiency is usually considered with respect to a kinematic variable, such as photon transverse energy, E_T^γ, which generates an efficiency curve, $\varepsilon = \varepsilon\,(E_T^\gamma)$. Conceptually, the efficiency of a photon trigger chain could be measured as follows: for a fixed range of photon E_T, the efficiency is simply the number of photons that passed the chain divided by the total number of photons in the sample. This can be repeated for various bins of E_T^γ and then, a histogram can be constructed, representing the desired efficiency curve. To accomplish this, two histograms should be constructed, the first containing the photons that passed the trigger chain, binned by E_T^{γ}, and the second containing all photons, with the same binning. Dividing the first histogram by the second would yield the desired efficiency curve. The existence of “minimum bias” events make studies such as this one possible. The photons contained in this minimum bias sample can be splitted into energy bins, and for in each bin, the fraction that would have passed the criteria of a trigger chain can be calculated. [35]

4.8.1. MUON TRIGGER ALGORITHMS

The LVL1 muon trigger is based on the measurement of muon trajectories in three different planes (stations). Muons are deflected by the magnetic field generated by the toroids; the angle of deflection depends on their momentum and the field integral along their trajectory. Coulomb scattering in the material traversed, and for low-pT triggers, the energy-loss fluctuation, are also of importance.

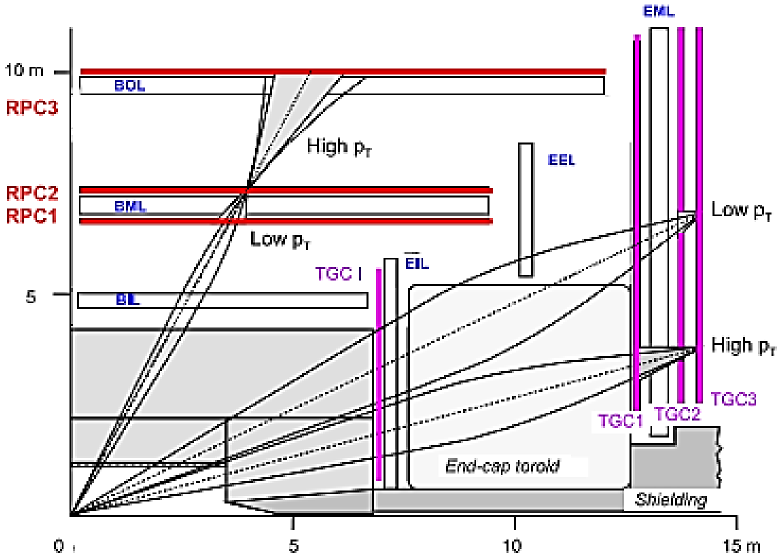

Figure 4.22: Intersection of muon system with reference to the positions of the muon trigger chambers. The differences from a straight-line trajectory of an infinite-momentum track originating at the nominal interaction point are measured using three trigger stations. [34]

The pivot plane is the trigger plane farthest from the IP in the end-cap, and nearest to the IP in the barrel. The two different lever arms from the pivot to the other two trigger planes provide two different measurements of the size of the deflection due to the field. The two different lever arms allow trigger thresholds to cover a wide range of transverse momenta with reasonably good resolution: the shorter lever arm (pivot plane and station 2) covers a lower-momentum range and the longer one (pivot plane and station 1 for the end-cap, pivot plane and station 3 for the barrel), a higher-momentum range.

Each hit found in station RPC1 (TGC3) is extrapolated to station RPC2 (TGC2) along a straight line through the nominal IP. A coincidence window is then defined around this point, where the window size depends upon the required pT threshold. The low-pT trigger condition is then satisfied if, for both projections, there is at least one hit within the coincidence window, and at least one of the two low-pT stations has hits in both trigger planes satisfying the three-out-of-four logic.

A similar procedure is performed for the high-pT trigger, where the planes of RPC3 (TGC1) together with the pivot plane are used. The high-pT trigger is satisfied if the track passes the low-pT criteria, and in the barrel at least one hit in the two trigger planes of RPC3 are in coincidence, and in the end-cap if at least two of the three planes of TGC1 in the h view, and one of the two planes of TGC1 in the r-f view are within the appropriate coincidence window. [34],[44]

4.9. DATA ANALYSIS

The production and analysis of ATLAS data takes place on a series of defined steps. Initially, the raw detector data is generated in bytestreams which are converted to object binary data (Raw Data Objects - RDO). Then the RDO objects are transformed into high energy physics objects (muons, electrons, orbits) and this new form is called Event Summary Data (ESD). As the ESD form contains all the necessary information, including detector collisions and reconstruction algorithms, data size per event is great for data analysis. For this reason, ESDs are converted into Analysis Data Objects (AOD), which retain only the relevant information for data analysis, maintaining a reasonable size per event. [2]

4.10. THE GRID

The large volumes of generated data during LHC operation make impossible the exclusive handling by CERN facilities. Therefore a more sophisticated infrastructure for distribution, processing and storage of data is considered as necessary. This infrastructure consist the worldwide LHC computing grid (WLCG), the world's largest computing grid that distributes the data into four different levels (Tiers), each of which consists of several centers and provides different services. The grid connects thousands of computers and storage systems in over than 170 centers in 41 countries, providing near real-time access to LHC data and clock monitoring in different time zones. [2],[60]

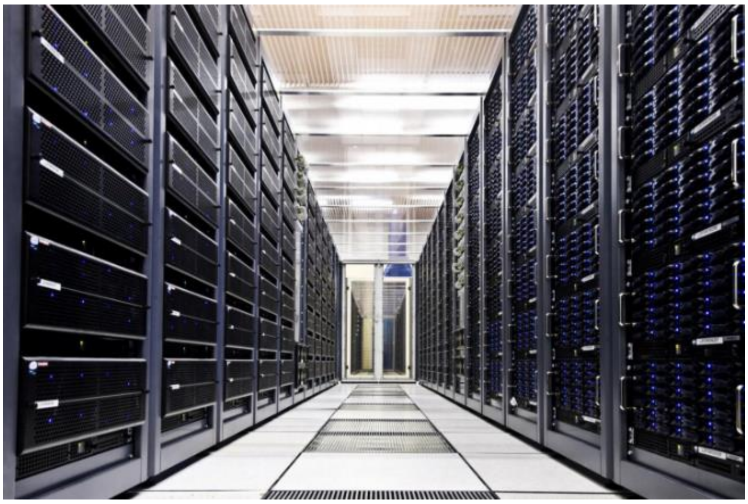

Figure 4.32: Servers in the CERN data center (Tier-0) of the global LHC computing grid. [60]

Tier-0 is the CERN data center, which although is the crossing point of all data coming from the LHC, it provides less than 20% of the total computing capacity of the grid. The purpose of Tier-0 is to keep backup copies (million digital readings from the detectors), to perform the first steps of reconstruction of the raw data into influential data, reprocess the data during LHC pause periods and distribute the data to the next level, Tier-1.

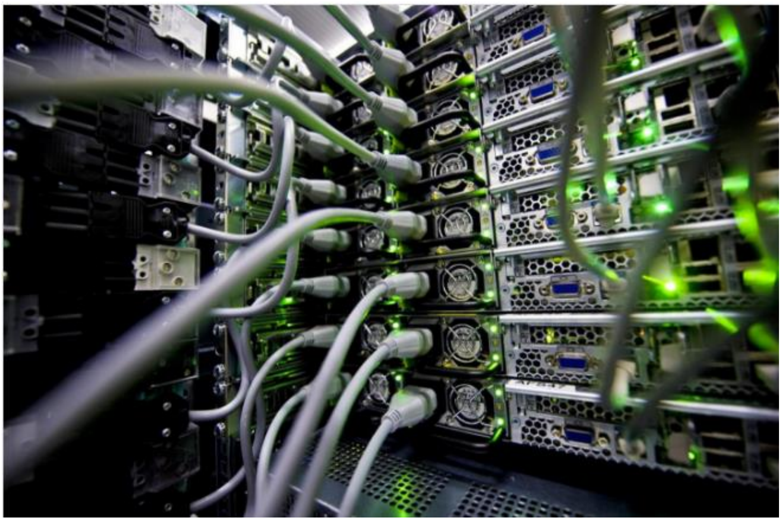

Figure 4.33: Servers at Tier 0 record a copy of primary LHC data, and distribute it to 13 Tier 1 centres around the world. [61]

The Tier-1 centers keep a second copy of raw and reconstructed data and allow the experimental groups to have access to the physical data analysis. It performs high-scale reprocessing and storage of the produced output, distributing data in Tier-2. The Tier-1 consists of 13 data centers large enough to store LHC data. The fiber optic connectors (10 gigabits / second) link CERN to each of the 13 Tier-1 centers worldwide. This high-bandwidth network zone is called LHC Optical Private Network (LHCOPN).

Tier-2 consists of one or more computational facilities and receive data from Tier-1. There are more than 160 Tier-2 centers dedicated to simulation and analysis of the user side. The usually Tier-2 are universities or institutes that can adequately store the data and provide sufficient computing power for specific analysis tasks.

The smaller Tier-3 centers provide local access to individual scientists. [61]

Figure 4.34: A StorageTek machine retrieves server tapes from a stack in the CERN Data Centre. [61]

4.11. THE ATLAS CONTROL SYSTEM

The subdetector systems and the common experimental infrastructure are controlled and monitored by the Detector Control System (DCS) by using a highly distributed system of 140 servers, aiming to a consistent and safe operation of the ATLAS components. Higher levels of control allow automatic control procedures, efficient identification of errors and manipulation, managing communication with external systems, such as the LHC, and provide a synchronization mechanism with the ATLAS data acquisition system. Different databases used for the storage of online parameters of the experiment and storage of system configuration parameters.

The ATLAS control system consists of different front - end systems and the back - end Supervisory Control and Data Acquisition system (SCADA). It is organized into three functional horizontal planes, a Local Control Station (LCS), a Subdetector Control Station (SCS) and a Global Control Station (GCS). This is a flexible hierarchy that reliably models the natural ATLAS subdetecting parts and subsystems.

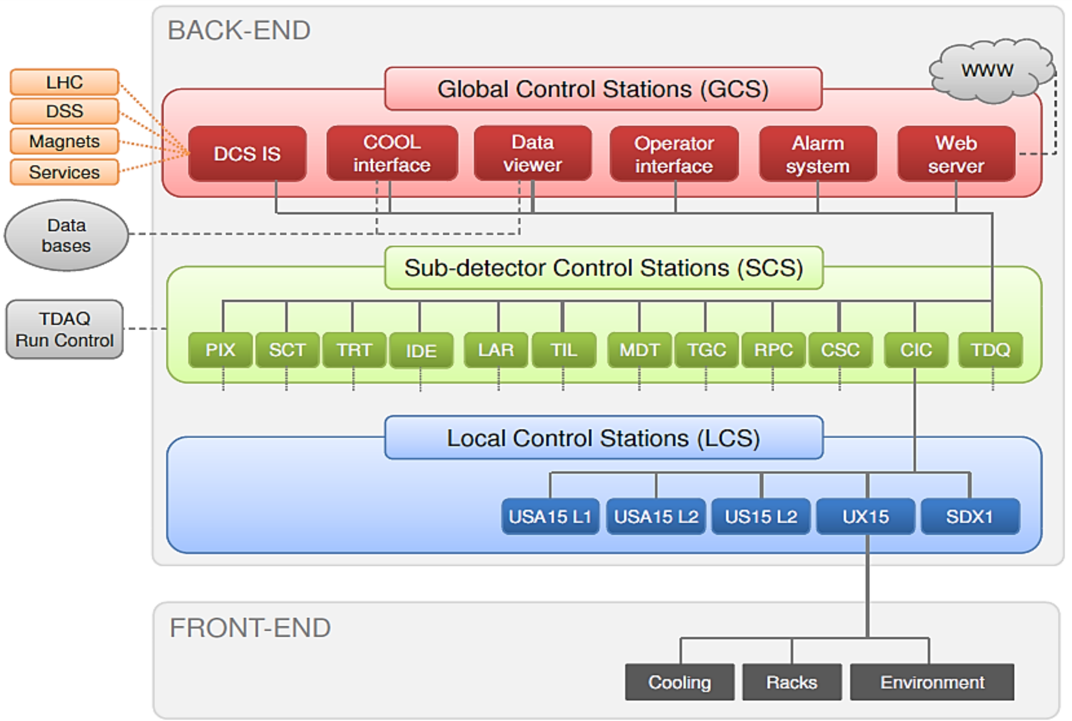

Figure 4.35: The ATLAS Control System. [31]

The LCS layer transmits information regarding the state of subdetectors and subsystems. The LCS may execute orders received from higher hierarchy levels or can perform its own special features. The SCS layer is the middle level of the hierarchy. Each subdetector has its own control station which allows full local control. At this level of the hierarchy the subdetectors are connected to external systems such as the magnet system, the LHC, the detector safety system, and trigger and data acquisition system. The GCS layer forms the upper part of the hierarchy and is responsible for the overall operation of the detector. This level summarizes all the functions of each state of the detectors and subsystems as well as malfunctions (alarms).

The front-end system consists of various parts arranged near the detector or in nearby rooms. It is directly linked with the hardware of the detector, providing reading, digitization and in some cases, signal processing and data transfer to the back-end. On the other hand, it receives and executes instructions from the back-end. The equipment of the front-end consists of sensors, controllers, digitizers, processors and computing systems pf autonomous basis. All the ATLAS front-end equipment has to adapt to different requirements regarding radiation tolerance (radiation levels can reach 100 kGy / year in areas close to the IP), operating under strong magnetic fields (magnetic field amplitude can reach 4 T in the cavern), the long lifetime (because the experiment is planned to operate for more than a decade), and low cost.

The back-end system consists of different software systems which communicate with the front-end providing supervisory control at the detector users. The back-end system, used by the four LHC experiments, carried out using a commercial SCADA package. The SCADA package provides software tools and guidelines ensuring the homogeneity of the back-end in all the different subsystems, their subdetectors and the LHC experiments.

The ATLAS automatic control system archives the important parameters in the ATLAS online database, which is only accessible via the ATLAS control network (ATCN), for security and performance reasons. However, an offline base, which is an exact copy of the online database, serves users within the CERN General Public Network (GPN). Although the operating parameters are of the order of 10^6, the delay of the replication mechanism does not exceed a few sec. [21],[31],[43]

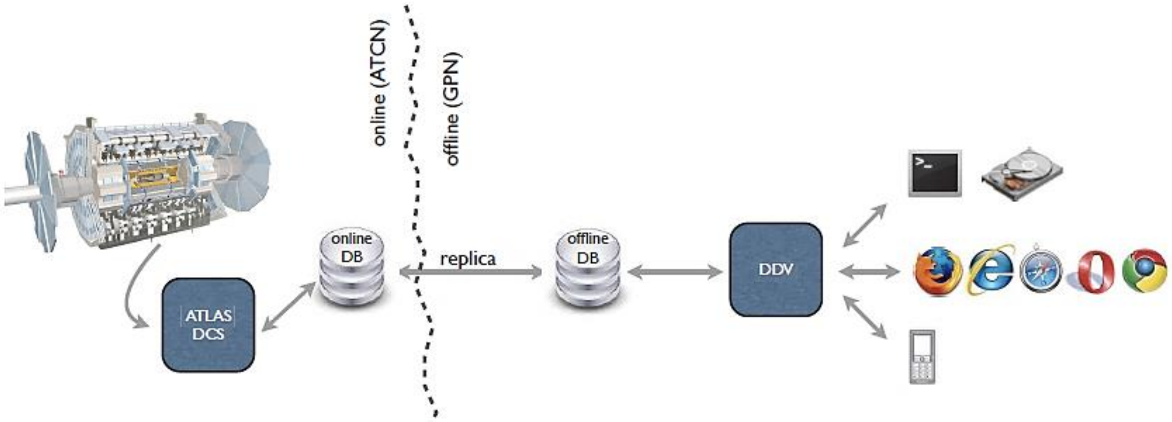

Figure 4.36: Flow of the information. ATLAS sub-detectors write in the online database. DDV reads from the offline database that is a complete replica of the online database. Finally, the user accesses the data through the DDV interface. [2]

4.12. USA15

The ATLAS experimental cavity (UX15) is surrounded by a variety of other caverns and access shafts. The USA 15 cavern, of 20 m width and 62 m length, is designed to accommodate the majority of the electronics that are necessary for carrying out the experiment. It is divided into two floors 1.8 m below and 3.6 m above the beam axis. Access for personnel and work for a long time are necessary conditions, even during operation of the LHC at high luminosity, but without exposing to high radiation levels. From USA15 there are several service tunnels leading to the experimental cavity (ULX16, UPX16, ULX14 and UPX14) and service ducts for cables (TE14 and TE16). Moreover, there is a second cavity US15, in which some of the electronics of the ATLAS are hosted, but access is prohibited during LHC operation. [27]

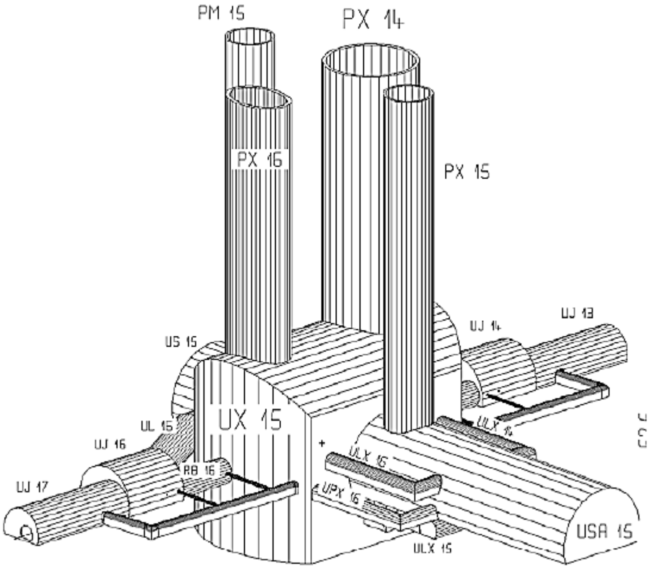

Figure 4.37: The experimental area with its individual cavities, tunnels and access shafts [27]

4.13. BACKGROUND MONITORS

Measurements of particle fluences in ATLAS provide a precise bench-marking of the particle transport codes used in the calculations and also monitor the absorbed doses in the various detectors. For the proper operation of the LHC and the detector experiments, the existence of detectors protection provisions during the proton collisions is necessary, providing fast feedback to the accelerator operations team. [31]

4.13.1. THE ATLAS BEAM CONDITIONS MONITOR AND TAS COLLIMATOR

The protection of the detectors is based on collimators, which absorb particles that deviate from the beam trajectory and may cause damage. A problematic, though rare operating scenario, occurs when multiple proton beams impinge on the collimators. The Beam Condition Monitor (BCM) perceives such events, as well as cases of beam and gas interaction, and aborts LHC operation. Both malfunction scenarios have in common charged particles cascades. By placing two detector channels on both sides of the IP in the z-axis, the particles from cascades hit on the BCM stations with a time difference of $\Delta t = 2z/c$. The stations are suspended from the supporting structure of the beam pipe (BPSS) and take measurements for each beam crossing (BC = 25 ns). The optimum distance of the two channels of four units each is calculated ideally to be about 3.8 m, at points $z = \pm 1.9$ m, resulting in $\Delta t = 12.5$ ns (6.25 ns after a collision). The background particles reach the up - stream station 12.5 ns (1/2 BC) before the particles from collisions and down - stream station at the same time with them. By the use of the out – of - time hits, the background events can be recognized.

Furthermore, BCM provides additional luminance measurements per package to those derived from the main monitor of the ATLAS system, LUCID, by using in – time hits. The measurements are performed with use of synchronous collisions.

The 4 BCM units are located in radius $r \sim 5.5$ cm ($\eta \approx 4.2$) and by angles $\varphi = 0^\circ$, 90°, 180°, 270°, and a deviation of 45° to the beam pipe. [28],[29],[30],[32]

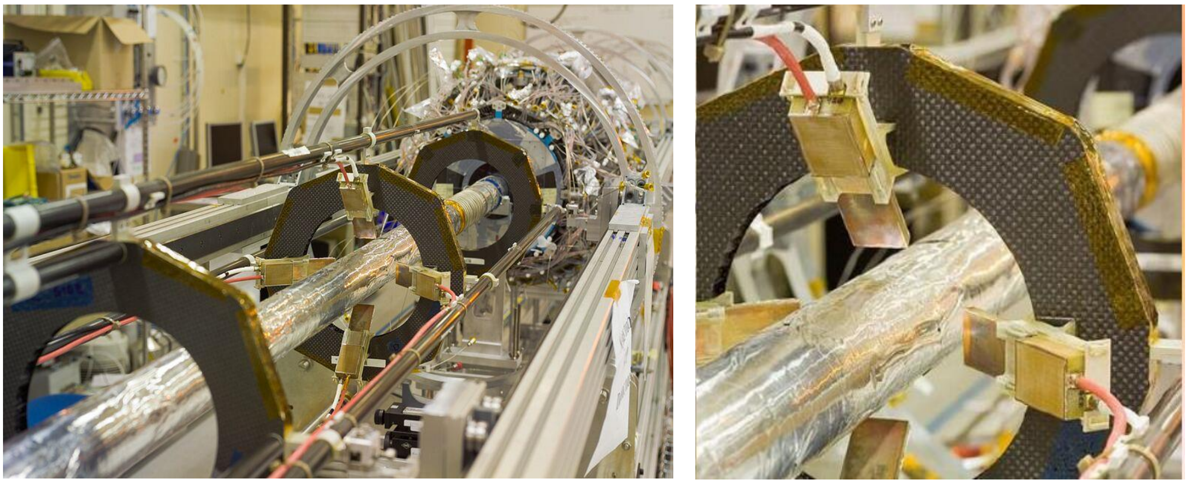

Figure 4.38: BCM onto the supporting unit. [28]

ATLAS additionally is protected by TAS (Target Absorber Secondaries) collimators placed at $z = \pm 18$ m from the IP which protect the inner layer of the cryogenic quadrupole from excess heat due to the collisions. The TAS collimator also protects the Inner Detector by various failures of the beam.

The Beam Interlock System (BIS) includes two optical loops per set which transmit signals BeamPermit, a logic AND of UserPermit signals provided by user systems (like BCM). The logic AND is achieved by using two Beam Interlock Controllers (BIC). User systems connecting to BIS through CIBU user interface (Controls Interlocks Beam User), through which each UserPermit signal is transmitted to the nearest BIC. The beam export is triggered by the BIS and completed within 270 ms after it passed from BICs.

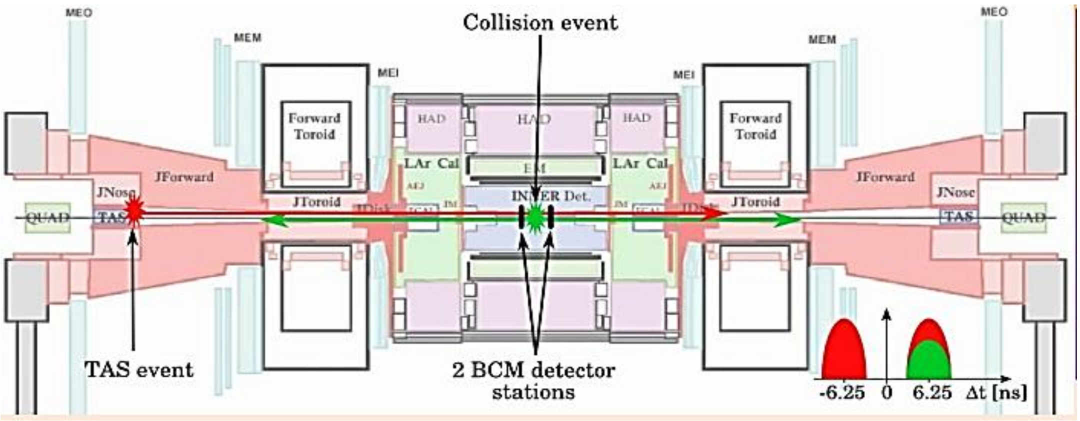

Figure 4.39: Principle of BCM operation. In normal p - p collision at IP (green) secondary particles arrive simultaneously at the 2 BCM. In problematic cases, as during proton impact on the collimator (red), each BCM station will detect secondary particles before the other does. [32]

The BCM detecting units particularly in the region of intense radiation consist of polycrystalline CVD diamond sensors of size 1x1 cm^2. As a charged particle passes (from p - p collisions or secondary proton products that get lost) the crystal lattice of the diamond is ionized, producing a very fast MIP signal with a rise time of less than 1 ns and an width of less than 2 ns. The passing particle leaves a trail of ionization charge of 36 electron - hole pairs per mm at its orbit. A two-stage RF amplifier amplifies the signal and transmits it to an analog format for digitization. For the sensor operation, a bias potential has to be applied to the electrodes to create a drifting field, in which electrons and holes are sliding, inducing current to the electrodes.

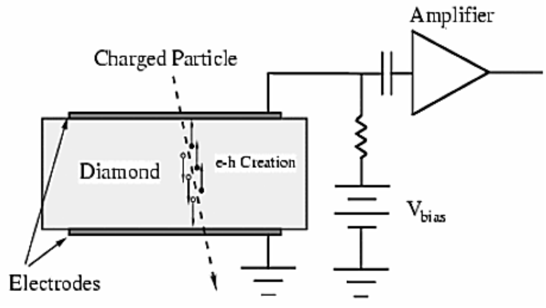

Figure 4.40: Schematic representation of the diamond detector. [30]

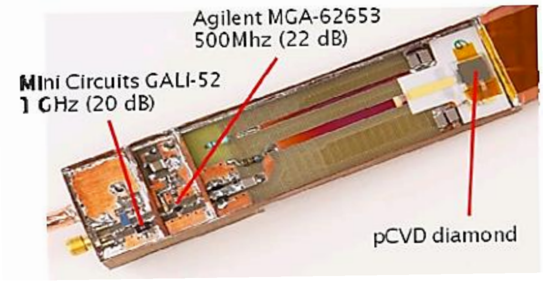

Figure 4.41: BCM unit. The two-stage amplifier consists of the following individuals: 1st stage: Agilent MGA-62653, 500 MHz (22 dB), 2nd stage: Mini Circuit GALI-52, 1 GHz (20 dB). [32]

The BCM has to measure the arrival times of the signals and their time above the threshold (TOT) for each of the 8 units. The analog signals from each BCM unit is routed through high-quality cables behind the calorimeter to lower radiation points and digitized separately for each unit by boards based on NINO chip technology. Before entering NINO, the signals from the BCM are divided into two channels by a voltage divider, in a ratio of 12: 1 to increase the dynamic range. The optimal signal-noise ratio for data and amplifiers requires the adding of a low-pass filter with a bandwidth limit 200-300 MHz of 4th order. The digital outputs of TOT coming from NINO are converted into optical signals, using laser diodes resistant to radiation and through they are transferred through optical fibers to the ATLAS calculation room (USA15), where they are obtained by photodiodes, converted back into electrical signals and fed into a Xilinx Vitrex-4 FPGA chip. The FPGA technology is suitable for the processing of these signals due to the parallel processing capability in high speed.

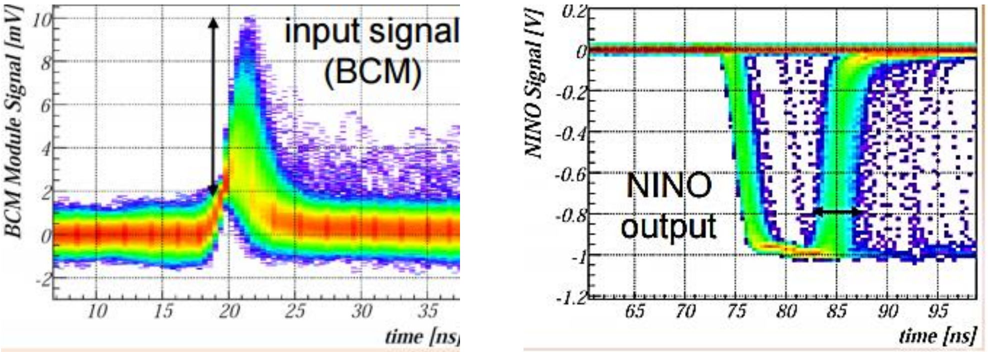

Figure 4.42: Signal before entering NINO (left) and after the exit (right). [28]

The BCM system can be analyzed in the following sections:

LHC Beam abort: Through CIBU system, two signs mark that the conditions in the inner detector have reached the beam abort point, which eventually takes place in a controlled manner.

ATLAS Security System: Four electrical connections exist between the detector safety system (DSS) of the ATLAS, which preserves the experimental equipment and the BCM. The DSS acts preventing losses through interconnections sending warnings and alarms (alarm).

Automatic control system: In less critical situations in conjunction with the hardware based DSS, the DCS is activated, for monitoring the temperature of the detector units and electronics of the Nino board, control voltages and acquire statistical information by signal processing available by connecting a DCS PC via an Ethernet connected to the FPGA. In case of beam abort, the recent information of BCM, which had been stored in the FPGA buffer, is transferred for post mortem treatment.

L1 Trigger: The BCM provides 9 bit information for the level 1 trigger system allowing the triggering of topologically interesting events, as well as real-time information on the luminosity per bundle.

DAQ stream: At each trigger signal from the CTP, the digitized information of the arrival times of the signals and the amplitude of each are sent from the FPGA and stored in a special buffer in the DAQ data flow.

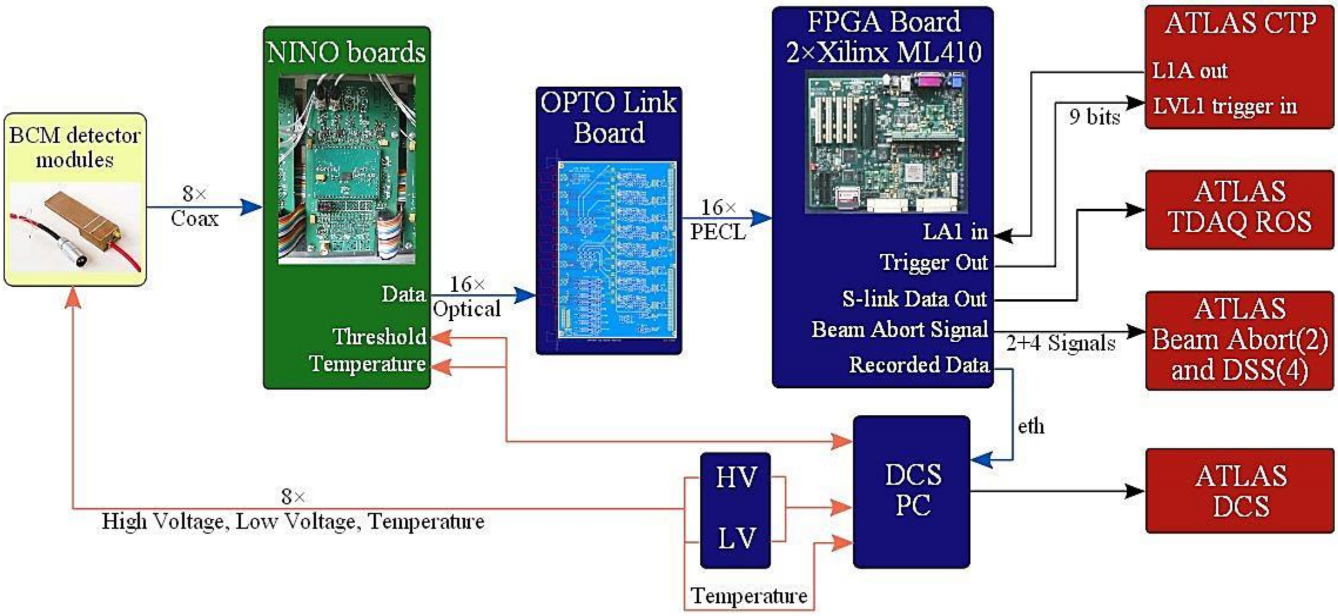

Figure 4.43: BCM system architecture [32]

As a complement of BCM, the beam loss monitoring system (Beam Loss Monitor - BLM) was added, for measuring the ionization current while having a quite simple construction and autonomy. 12 detector units have been placed, six on each side of the IP at points z = ± 3450 mm and a radius of r = 65 mm. The current is converted into a digital signal which is transmitted via optical fibers to the calculations room and recorded by a FPGA. [28],[29],[30],[31],[32]

4.13.2. MONITORS IN THE INNER DETECTOR

The inner detector region of ATLAS contains a set of small detectors, which are sensitive to dose, to the 1MeV neutron equivalent fluence (Fneq), described later, and to thermal neutrons. These detectors consist of Field-effect transistors (RADFET's), which measure the total ionising dose, PIN-diodes, which measure Fneq, and radiation-hardened transistors, which measure thermal neutron fluences.

These detectors measure the integrated doses and fluences in the inner detector and also provide bench-marking estimates of the different contributions (charged particles, neutrons and photons). [31]

4.13.3. MONITORS IN THE MUON SPECTROMETER

Several sets of detectors have been installed in the inner, middle, and outer end-cap muon stations, providing a reliable response to particles in various energy ranges.

Boron-lined proportional tubes with Ar/CO$_2$ gas, insensitive to photons and charged particles, are used for thermal and slow neutrons measurements ($< 10^{-5}$ MeV). Each $n + {}^{10}B \rightarrow Li + a$ interaction sends a slow Li or a- particle into the tube, causing a large ionization pulse, which is used for pulse-height discrimination against Compton electrons and MIPs. Additionally, a Boron-loaded plastic scintillator (BC-454) is sensitive to the neutron interactions and is also used for neutron studies. Detectors with a plastic disk loaded with LiF and coated with a thin layer of ZnS(Ag) scintillator are sensitive to the tritium and a-particles produced in the neutron capture process in lithium.

Another ZnS(Ag) scintillator embedded in plastic is used to study fast neutrons. The plastic is rich in hydrogen, from which incoming neutrons scatter to create recoil protons that produce large ionisation pulses compared to MIPs or low-energy electrons. Pulse-height discrimination schemes provide good rejection against these backgrounds. A liquid scintillator, with pulse-shape discrimination electronics, is used in combination with plastics to measure fast neutrons.

Scintillator detectors with NaI and lutetium oxyorthosilicate (LSO) crystals are used to measure the low-energy photon spectrum (0 - 10 MeV), dominated by photons, but also containing a neutron component, which can be separated out using fitting techniques and detailed simulations.

Finally, small ionisation chambers measure the total ionising dose. [31]

4.13.4. NETWORK OF DETECTORS FOR RADIATION MEASUREMENTS

A system of small silicon pixel detectors, fully capable of delivering real-time images of fluxes and spectral composition of different particle species, has been developed for radiation measurements in the experimental environment. These silicon detectors will be operated via active USB cables and USB-ethernet extenders by a PC placed in the USA15 counting room. The hybrid silicon pixel device consists of a silicon detector chip, 300 mm thick with 256x256 pixels, bonded to a readout chip. Each of the 55 mm x 55 mm pixels is connected to its respective readout chain integrated on the chip. Settings of the pulse height discriminators determine the input energy window and at the same time provide noise suppression. The pixel counter determines the number of interacting quanta of radiation falling within this window. These devices can be used for position and energy sensitive (5 keV – tens of MeV) spectroscopic detection of radiation. They are also capable of counting particle fluxes at rates in excess of GHz/cm^2.

This system can be used in both tracking and counting modes, to record tracks or counts caused by x-rays, gamma-radiation, neutrons, electrons, MIPs and ions. The silicon detectors are partially covered by neutron converters for neutron detection. The tracking mode is based on electronic visualization of tracks and traces of individual radiation quanta in the sensitive silicon volume. In the case of count rates above $5x10^3$ events/cm^2s, the devices are operated in counting mode, in which charge deposition in the pixels is counted at different threshold settings. Calibration of the devices enables the conversion of the individual tracks observed and/or counts measured into fluxes of respective types of radiation and dose rates. These pixel devices will be placed inside ATLAS: four devices on the LAr calorimeter facing the inner detector, four devices on the tile calorimeter, four devices near the muon chambers in the inner end-cap muon station, and two devices near the forward shielding and close to the outer end-cap muon station. [31]

5. MONTE CARLO METHOD AND SIMULATION

5.1. THE MONTE CARLO METHOD

The high complexity of the various natural systems considers their modeling through numerical methods necessary rather than an analytical approach. Simulation techniques take into consideration the speed of modern computer systems, allowing convergence to a valid solution. The Monte Carlo method is a widely used general approach for the numerical modeling of physical systems. It can be used to duplicate theoretically a statistical and is particularly useful for complex problems that cannot be modeled by computer codes that use deterministic methods. Monte Carlo includes a class of computational algorithms that rely on iterative random sampling of distribution functions, which are inputs to the model, and produce as a result the probabilities of different expenses. The distribution functions are normalized in the appropriate range. The individual probabilistic events that comprise a process are simulated sequentially.

The stochastic description of particle interactions is expressed through the statistical quantity of cross-section. When a particle stream impinges on a target, the differential cross-section represents a statistical distribution function.

The Monte Carlo method follows some predefined steps for the simulation of particle interactions. Firstly, a primary particle is generated with predefined fixed initial conditions (position and momentum). The particle travels inside the current medium for a certain distance before it interacts for the first time. The value of the distance is sampled by a random number generator from a probability density function (PDF), which differs for each type of particle and material. Afterwards, all the possible N interactions that can take place are considered, giving a certain probability. The probability of occurrence is assigned to the i^{th} interaction by an internal algorithm depending on the cross sections of the different processes. After sampling another uniformly distributed random number, the type of interaction occurring is decided. Changes of the position and the momentum of the primary particle will be taken into account by the end of the particle step. All active particles (a primary and its secondaries) are placed on the computer stack together with their properties (type, spatial coordinates, momentum, etc). There is also the possibility that a particle is annihilated (undergoes an inelastic process, being absorbed, or transformed, surpasses the geometry's boundaries, or its energy is lower than predefined energy cut-off) or stopped during the interaction and thus, it is no longer taken into account, so it is removed from the stack of tracked particles, after the quantities of interest are recorded. After the first interaction has finished, the primary particle is put on the stack with the others and the steps above are repeated for all given primaries.

Finally, the data obtained from the simulation are exported into data files. Almost all of the CPU time is spent in detecting particle processes. So it is necessary to balance the need for short time consumption and validity of the results. [13]

5.1.1. THE LAW OF LARGE NUMBERS

Let X_1, X_2, …, X_n be independent trials of a finite mean value $\mu = E(X_i)$ and variance $\sigma^2 = V(X_i)$. For every $\varepsilon > 0 \in R$ and $\sum_{i=1}^{n} X_i = S_n$:

$$V(S_n) = n\sigma^2 \Rightarrow V(S_n / n) = \sigma^2 / n$$

$$\text{and } E(S_n / n) = \mu$$

Using the Chebyshev inequality:

$$P\left(\left|\frac{S_n}{n} - \mu\right| \geq \varepsilon\right) \leq \frac{\sigma^2}{n \cdot \varepsilon^2}$$

$$\lim_{n \to \infty} P\left(\left|\frac{S_n}{n} - \mu\right| \geq \varepsilon\right) = 0$$

So, according to the Low of Large Numbers, the average value of the results obtained by the repetition of the same experiment many times is very close to the expected value, which tends to be more accurate when increasing the number of repetitions (n → ∞). It guarantees stable long-term results for the mean values of independent random events. The validity of the Monte Carlo method is based on this principle. [62]

5.1.2. PSEUDO – RANDOM NUMBER GENERATORS

Besides the numerous tests, the validity of the approach is based on the use of uniformly distributed random numbers, which requires the use of a pseudorandom number generator (RNG) to produce large quantities of random numbers for statistical sampling.

In each trial of a Monte Carlo simulation, the random numbers should be generated as if it were just samples of a random variable of a specific PDF. A typical pseudo – random number generation algorithm is used for transforming pseudorandom numbers that follow a uniform distribution, into numbers distributed according to a given distribution. It is a periodic algorithm that has a long period of thousands of cycles and is initialized using a number 'seed'. The pseudorandom numbers can be predicted and they have a deterministic behavior, so they are not really random, but they provide simplicity in practical approach and ensure the reproducibility of the same performance if tested in exactly the same simulation. By using a good algorithm, the pseudorandom numbers show the same statistical properties with truly random numbers. Different executions with the same seed will give the same set of pseudorandom numbers, and even a small variation of the seed provides a completely different set. [13]

5.2. MCNP5 SOFTWARE

The MCNP software which was developed by the Los Alamos National Laboratory, is an internationally recognized software for interaction analysis of neutrons and gamma rays using the Monte Carlo statistical method.

The program uses embedded databases coming from recognized libraries. Its operation is based on the creation of an appropriate simulation by using geometric models of layout design, by the determination of surfaces (surface cards) and the elementary volumes between the surfaces (cells) which are obtained using the intersection, union and complement between surfaces, and the various materials composing the space thanks to their density. [46]

5.2.1. INPUT FILE

The general structure of an MCNP code is as follows:

Message Block {optional}
blank line delimiter {optional}
One Line Problem Title Card
Cell Cards [**Block 1**]
blank line delimiter
Surface Cards [**Block 2**]
blank line delimiter
Data Cards [**Block 3**]
blank line terminator {optional}

The three main parts of the code (cell cards, surface cards, data cards) should be written in the correct order. Each card can be 80 characters at maximum, otherwise the simulation terminates with error occurrence. Within the 5 leftmost card positions the number of the corresponding surface or cell is indicated, but if more than 5 positions are used, the continuation of the previous card is meant. The title card describes the problem to be simulated.

Cell Cards

The cells describe any physical structure of the problem and their description in the code given below:

j m d geom param

- $j \in [0, 99999]$ is the number of the current cell and is different for each cell
- m is the number of the material comprising the cell
- d is the material density, with d> 0 define the atomic density in atoms per cm, while d <0, the density in grams per cubic centimeter is given
- geom is the geometric characterization the cell produces through surface cards
- param is where other parameters are set, such as the importance of each particle, which determines if the particle will be monitored within the cell (imp = 1) or not (imp = 0).

MCNP uses the Cartesian coordinate system and some basic simple geometries:

Mnemonic	***Type***	***Description***	***Equation***	***Card Entries***
P	***plane***	general	$Ax+By+Cz-D=0$	A B C D
PX		normal to x – axis	$x-D=0$	D
PY		normal to y – axis	$y-D=0$	D
PZ		normal to z – axis	$z-D=0$	D
SO	***sphere***	centered at origin	$x^2+y^2+z^2-R^2=0$	R
S		general	$(x-\bar{x})^2+(y-\bar{y})^2+(z-\bar{z})^2-R^2=0$	$\bar{x}\ \bar{y}\ \bar{z}$ R
SX		centered on x – axis	$(x-\bar{x})^2+y^2+z^2-R^2=0$	$\bar{x}$ R
SY		centered on y – axis	$x^2+(y-\bar{y})^2+z^2-R^2=0$	$\bar{y}$ R
SZ		centered on z – axis	$x^2+y^2+(z-\bar{z})^2-R^2=0$	$\bar{z}$ R
C/X	***cylinder***	parallel to x – axis	$(y-\bar{y})^2+(z-\bar{z})^2-R^2=0$	$\bar{y}\ \bar{z}$ R
C/Y		parallel to y – axis	$(x-\bar{x})^2+(z-\bar{z})^2-R^2=0$	$\bar{x}\ \bar{z}$ R
C/Z		parallel to z – axis	$(x-\bar{x})^2+(y-\bar{y})^2-R^2=0$	$\bar{x}\ \bar{y}$ R
CX		on x – axis	$y^2+z^2-R^2=0$	R
CY		on y – axis	$x^2+z^2-R^2=0$	R
CZ		on z – axis	$x^2+y^2-R^2=0$	R
K/X	***cone***	parallel to x – axis	$\sqrt{(y-\bar{y})^2+(z-\bar{z})^2}-t(x-\bar{x})=0$	$\bar{x}\ \bar{y}\ \bar{z}$ t^2 ±1
K/Y		parallel to y – axis	$\sqrt{(x-\bar{x})^2+(z-\bar{z})^2}-t(y-\bar{y})=0$	$\bar{x}\ \bar{y}\ \bar{z}$ t^2 ±1
K/Z		parallel to z – axis	$\sqrt{(x-\bar{x})^2+(y-\bar{y})^2}-t(z-\bar{z})=0$	$\bar{x}\ \bar{y}\ \bar{z}$ t^2 ±1
KX		on x – axis	$\sqrt{y^2+z^2}-t(x-\bar{x})=0$	$\bar{x}$ t^2 ±1
KY		on y – axis	$\sqrt{x^2+z^2}-t(y-\bar{y})=0$	$\bar{y}$ t^2 ±1
KZ		on z – axis	$\sqrt{x^2+y^2}-t(z-\bar{z})=0$	$\bar{z}$ t^2 ±1
SQ	***ellipsoid hyperboloid paraboloid***	axis not parallel to x-, y-, or z- axis	$A(x-\bar{x})^2+B(y-\bar{y})^2+C(z-\bar{z})^2$ $+2D(x-\bar{x})+2E(y-\bar{y})$ $+2F(z-\bar{z})+G=0$	A B C D E F G $\bar{x}\ \bar{y}\ \bar{z}$
GQ	***cylinder cone ellipsoid paraboloid hyperboloid***	axis not parallel to x-, or y-, or z- axis	$Ax^2+By^2+Cz^2+Dxy+Eyz$ $+Fzz+Gz+Hy+Jz+K=0$	A B C D E F G H J K
TX	***elliptical or circular torus. Axis is parallel to x-, y-, or z- axis***		$\frac{(x-\bar{x})^2}{B^2}+\frac{(\sqrt{(y-\bar{y})^2+(z-\bar{z})^2}-A)^2}{C^2}-1=0$	$\bar{x}\ \bar{y}\ \bar{z}$ A B C
TY			$\frac{(y-\bar{y})^2}{B^2}+\frac{(\sqrt{(x-\bar{x})^2+(z-\bar{z})^2}-A)^2}{C^2}-1=0$	$\bar{x}\ \bar{y}\ \bar{z}$ A B C
TZ			$\frac{(z-\bar{z})^2}{B^2}+\frac{(\sqrt{(x-\bar{x})^2+(y-\bar{y})^2}-A)^2}{C^2}-1=0$	$\bar{x}\ \bar{y}\ \bar{z}$ A B C
XYZP	surface defined by points			

Table 5.1: MCNP geometries [46]

By combining the above more complex geometries can arise. Every point in space must belong to either a surface or a cell, so that there are no gaps in geometry.

Surface Card

The structure of the surface card is then:

j a list

- j is the serial number of the surface card and obviously different for each surface
- a is the geometric stereo which can be one of the aforementioned basic geometries is the number that specifies the location (eg plane distance from the origin) or stereo size (eg sphere radius).

There are also surfaces defined by macrobodies. Using a combinatorial-geometry-like macrobody capability is an alternative method of defining cells and surfaces. The macrobodies can be mixed with the standard cells and surfaces. MCNP can use the following macrobody structures: [47]

- BOX—ARBITRARILY ORIENTED ORTHOGONAL BOX
- RPP—RECTANGULAR PARALLELEPIPED
- SPH—SPHERE
- RCC—RIGHT CIRCULAR CYLINDER, CAN
- RHP OR HEX—RIGHT HEXAGONAL PRISM
- REC—RIGHT ELLIPTICAL CYLINDER
- TRC—TRUNCATED RIGHT ANGLE CONE
- ELL—ELLIPSOID
- WED—WEDGE
- ARB—ARBITRARY POLYHEDRON

Afterwards, the cards with the rest of the simulation parameters are filled.

Mode Card

Firstly, mode card is filled followed by one or more of p (photons), e (electrons), n (neutrons), having a blank space between them. This card describes which particles are generated and monitored during the simulation.

Material Cards

Material cards should be also defined. The syntax of the respective card is the following:

mn zaid1 fraction1 zaid2 fraction2

- mn is the material card designated by the letter m followed by the serial number of the material n,
- zaid is the atomic number of the atomic mass of the isotope (often followed by a number that indicates the library in which isotope data are recorded),

- fraction is the fraction of the nuclei content, wherein a positive number indicates atomic density in atoms per cm, and a negative number indicates the nucleus weight fraction.

Source Card

To conduct the simulation it is necessary to place one (or more depending on the study) source, which is determined by the sdef command, followed by other parameters for its determination. The main parameters used in the majority of simulations are:

- pos to determine its position in three-dimensional space
- erg for the source energy
- par for the particle type
- dir for the direction of the particle emission

Details are given in the following table:

Variable	***Meaning***	***Default***
CEL	cell	determined from XXX, YYY, ZZZ and possibly UUU, VVV, WWW
SUR	surface	0 (means cell source)
ERG	energy (MeV)	14 MeV
DIR	μ, the cosine of the angle between VEC and UUU, VVV, WWW. The azimuthal angle is always sampled uniformly in [0, 2π]	Volume case: μ is sampled uniformly in [-1, 1] (isotropic). Surface case: p(μ) = 2μ for μ∈[0, 1] (cosine distribution)
VEC	reference vector for VEC	Volume case: required unless isotropic. Surface case vector normal to the surface with sign determined by NRM.
NRM	sign of the surface normal	+1
POS	reference point for positioning sampling	0, 0, 0
RAD	radial distance of the position from POS or AXS	0
EXT	Cell case: distance from POS along AXS. Surface case: cosine of angle from AXS.	0
AXS	reference vector for EXT and RAD	no direction
X	x – coordinate of position	no X
Y	y – coordinate of position	no Y
Z	z – coordinate of position	no Z
CCC	cookie – cutter cell	no cookie – cutter cell
ARA	area of surface (required only for direct contributions to point detectors from a plane surface source)	none
WGT	particle weight	1
EFF	reference efficiency criterion for positon sampling	0.01
PAR	type of particle source emits	=1(neutron) if MODE ***N*** or ***P*** or ***N P E***, =2 (photon) if MODE ***P***, =3 (electron) if MODE ***E***

Table 5.2: Source parameters for the SDEF command [46]

The parameter values can be described in 3 levels: (1) Direct value assignment (πχ ERG=1.25), (2) using distribution number (πχ ERG=d5) and (3) as a function of another variable (πχ ERG=Fpos). In cases 2 and 3, three additional cards required:

- SI (source information)
- SP (source probabilities)
- SB (source bias)

Tally Cards

For taking measurements, which will appear in the output file, tally cards are used. The structure of the card is:

Fn:p1 S1 (S2 … S3) S6S7

where n is the number whose last digit identifies the tally as given in the table below:

Mneumonic	*Tally Type*	*Particles pl*	*Fn Units*	**Fn Units*
F1:pl	surface current	N or P or N,P or E	#	MeV
F2:pl	average surface flux	N or P or N,P or E	#/cm^2	MeV/cm^2
F4:pl	average flux in a cell	N or P or N,P or E	#/cm^2	MeV/cm^2
FMESH4:pl	track – length tally over 3D mesh	N or P or E	#/cm^2	MeV/cm^2
F5a:pl	flux at a point or ring	N or P	#/cm^2	MeV/cm^2
FIP5:pl	pin – hole flux image	N or P	#/cm^2	MeV/cm^2
FIR5:pl	planar radiograph flux image	N or P	#/cm^2	MeV/cm^2
FIC5:pl	cylindrical radiograph flux image	N or P	#/cm^2	MeV/cm^2
F6:pl	energy deposition	N or P or N,P	MeV/g	jerks/g
F7:pl	fission energy deposition in a cell	N	MeV/g	jerks/g
F8:pl	pulse height distribution in a cell	P or N,P or E	pulses	MeV

Table 5.3: MCNP5 tally types. The type of the tallied particle is noted as pl. [46]

- p1 the particle type the user wishes to measure (p, e, n or a combination separated with ,)
- Si is the surface number or cell number of measurement

Energy bins

In order to take measurements, the energy spectrum of the source has to be separated into narrower energy regions (energy bins). The given output is referred to every energy bin, as well as to the whole spectrum, by adding each contribution within each energy bin.

Time or History Cards

Finally, the run time of the code until satisfactory results occur should be defined. The usual method for limiting how long MCNP runs is to specify either the maximum number of source particle histories or the maximum execution time. The maximum number of histories N is specified on the card nps N, where N defines the maximum number of events of source particles that get lost. In addition, or as an option, the computing-time cutoff T, in minutes of computer time, may be specified by the card ctme T.

Variance reduction

MCNP offers a variety of variance reduction techniques based on different nonanalog simulations. The art of using MCNP to solve difficult problems is to use these program features to obtain both precise and computationally efficient results.

- Geometry Splitting

In geometry splitting, importances are assigned to each cell in the problem. When a particle leaves a cell with importance I_1 and enters a cell of importance I_2, the particle is split/rouletted according to the ratio I_2/I_1. This technique of geometry splitting with Russian roulette is very reliable since, if no other biasing techniques are used, all the particles in a cell will have the same weight regardless of the paths taken to reach the cell.

- Weight Windows

The weight-window variance reduction technique adjusts the weights of particles as they change energy and move through the various cells in the problem geometry. In each cell, a lower weight bound and an upper bound, defined as a multiple of the lower bound, are specified. If a particle entering a cell or a particle created in the cell has a weight above the upper bound, the particle is split such that all split particles are within the weight window. Similarly, if a particle has a weight below the lower bound, Russian roulette is used to increase the particle’s weight until it lies within the window or until it is killed.

- Exponential Transform

The exponential transform artificially changes the distance to the next collision. In this technique, particles can be moved preferentially towards the tally region and inhibited from moving away from it. The exponential transform stretches the path length between collisions in a preferred direction by adjusting the total cross section.

- Energy Splitting/Russian Roulette

When such a particle is created, the ESPLT command can be used to split the particle into more daughter particles of the same type. Also, when a particle of energy outside the energy region of interest is created, Russian roulette is used to eliminated some of these particles.

- Forced Collisions

The forced collision biasing method increases the sampling of collisions in specified cells. This method splits particles into collided and uncollided parts. The collided part is forced to interact within the current cell while the uncollided particle exits the cell without collision.

- Source Biasing

One of the easiest nonanalog techniques to implement is source biasing. In MCNP any of the SDEF variables can be biased. For example, source particles can be started with enhanced weights, with preferred energies, and in regions closer to the detector. One of the most useful source biasing techniques is to start particles in preferred directions, generally towards tally regions.

5.2.2. OUTPUT FILE

The output file contains the statistical results that came from the execution of the code depending on the tallies which were defined in the input file. By default only a small portion of all the possible output is produced. Always output are (1) input file listing, (2) summary of particle loss/creation, (3) summary of KCODE cycles (if KCODE is used), (4) tallies (if used), and (5) tally fluctuations charts. The results are given per source particle, analytically for each energy bin accompanied with the respective error, and also cumulatively with the total error.

By using various techniques of variance reduction it is possible to produce tally results that are very precise, given the small relative error, but not very accurate. Technically, precision is the uncertainty (as measured by the tally variance) in the tally mean x caused by the statistical fluctuations in the individual scores xi of the simulated histories. By contrast, accuracy is a measure of how close the tally mean x is to the true physical quantity being estimated. The difference between the true value and the expectation value of the simulation tally is called the systematic error, an important quantity but one that is seldom known.

Statistical checks are used for the evaluation of the results. [46]

Relative error

The relative error is the fractional 1-sigma estimated uncertainty in the tally mean, i.e., R $\equiv S_{\bar{x}} / \bar{x}$, the ratio of the standard deviation of the tally mean to the mean.

Range of R	***Quality of Tally***
> 0.5	Meaningless
0.2 to 0.5	Factor of a few
< 0.1	Reliable (except for point/ring detectors)
<0.05	Reliable even for point/ring detectors

Table 5.4: Interpretation of the reactive error R. [46]

Figure of merit

Another important statistic generated by MCNP is the figure of merit (FOM), defined as

$$FOM = \frac{1}{R^2 T}$$

where T is the run time. Since T varies with the computer, the same simulation performed on different machines produces different FOMs. FOM should remain relatively constant except for fluctuations early in the simulation. For different variance reduction techniques, the one with the largest FOM is preferred.

Variance of the Variance

To indicate the accuracy of the relative error R, MCNP estimates the relative variance of R, i.e. a variance of a variance (VOV). The VOV is defined as

$$VOV = \frac{S^2(S_{\bar{x}}^2)}{(S_{\bar{x}}^2)} = \frac{\sum_{i=1}^{N}(x_i - \bar{x})^4}{[\sum_{i=1}^{N}(x_i - \bar{x})^2]^2} - \frac{1}{N}$$

where is the variance of $(S_{\bar{x}}^2)$.

The Empirical PDF for the Tally

MCNP also constructs the tally PDF f(x) to help assess the quality of the confidence interval estimates for the tally mean. Examination of the high-end tail of this distribution is very important for problems involving infrequent events with very high score.

Confidence Intervals

From the relative error R, MCNP estimates the confidence interval for the tally. Because the estimated mean and estimated uncertainty in the mean are correlated, the mid-point of the confidence interval needs to be shifted slightly from the mean. The amount of this midpoint shift, SHIFT, is proportional to the third central moment, and should decrease as 1/N. MCNP calculates this refinement for the confidence interval.

A Conservative Tally Estimate

Sometimes a user wishes to make a conservative tally estimate, just in case rare high-tally events may not be completely considered. In the output, MCNP shows what would happen to the mean, R, VOV, confidence interval, etc., if the next history (N + 1) were the same as the largest scoring history encountered in the simulation of N histories. If large changes occur, then be very suspicious of the result.

The Ten Statistical Tests

The most valuable tool provided by MCNP is the suite of 10 statistical tests it performs on the tally. Considering N as the number of the events that have been carried out, the ten tests are listed below.

- Tally mean:

1.The mean must exhibit, for the last half of the problem, only random fluctuations as N increases. No up or down trends must be exhibited.

- Relative error, R:
    2. R must be less than 0.1 (0.05 for point/ring detectors).
    3. R must decrease monotonically with N for the last half of the problem.
    4. R must decrease as $1/\sqrt{N}$ for the last half of the problem.
- Variance of variance
    5. The magnitude of the VOV must be less than 0.1 for all types of tallies.
    6. VOV must decrease monotonically for the last half of the problem.
    7. VOV must decrease as $1/\sqrt{N}$ for the last half of the problem.

- Figure of Merit, FOM:
    8. FOM must remain statistically constant for the last half of the problem.
    9. FOM must exhibit no monotonic up or down trends in the last half of the problem.
- Tally PDF, f(x):
    10. The SLOPE determined from the 201 largest scoring events must be greater than 3.

6. THE ATLAS RADIATION BACKGROUND

At the LHC the dominant primary source of background radiation is collisions at the interaction point. The very high energies and collision rate means that the levels of low-energy neutron, high-energy hadron and photon radiation are at an extremely high level in the ATLAS experiment. This causes several problems such as radiation damage to silicon detectors and electronics, increased detector occupancy, background signals resulting in spurious triggers in some of the detector systems and creation of residual radionuclides that will lead to radiological hazards that impact access and maintenance scenarios.

Radiation in the LHC underground areas and in the accelerator tunnel is produced when protons interact with the nuclei of the residual gas atoms (beam gas interactions) or with the nuclei of the atoms of every other material surrounding the beams such as beam screens collimators, magnets, cables, cryostats or the beam dump (point losses). When there are circulating beams in the LHC there is a small but continuous loss of protons along the ring. These lost protons will interact with the material that is closed to the beams. These primary interactions produce secondary particles (neutrons, pions, kaons, other protons), with some of them having sufficient energy to interact again and cause the production of tertiary particles and so on, resulting in a hadronic cascade. The fragments of the struck nuclei produced in the hadronic cascade are radioactive and decay in a timescale between a fraction of a second and many days. The accelerator thus continues to produce radioactivity even though there are no more circulating beams.

The secondary charged hadrons in the Inner Detector dominate the background at small radii. At larger radii the backgrounds of other particles, such as neutrons, become more important. The purpose of the shielding in ATLAS is to reduce the number of background particles in regions that the radiation background is more intense, such as near the beampipe and specifically at the Inner Detector and the Muon spectrometer, to a manageable level and to protect people working in the electronics cavern (USA15). [31], [48]

6.1. RADIATION ESTIMATORS

The “primary” estimators, obtained directly from transport codes, are determined by the tracking models of the transport code and are rarely modified by the user. Estimators derived from these quantities can be considered “secondary” quantities, which are obtained in the user “post processing” step by multiplying or convolving the primary quantities with conversion factors.

Particle fluence Φ is defined as the number dN of particles incident on a sphere of cross-sectional area da, irrespective of their direction and it is a necessary to describe and quantify radiation side effects:

$$\Phi = {dN}/{d\alpha} \qquad (\mathrm{kHz/cm^2})$$

Also, fluence can be described as the time integral of fluence rate (flux).

Particle current is a measure of the net number of particles crossing a surface with a well-defined orientation. In a directed radiation field fluence and current are the same only for normal incidence to the surface.

The 1 MeV neutron equivalent fluence (F_{neq}) is obtained by convoluting the various particle energy spectra and fluences with silicon displacement damage functions, normalized using the non-ionising energy loss (NIEL) cross-sections to the expected damage of 1 MeV neutrons. As a result, a comparison of damage effects for different radiation fields is feasible.

The absorbed dose is a measure of the energy deposited in a medium by ionizing radiation per unit mass, taking into account all energy loss mechanisms and its unit of measure is Joules/kg (Gray – Gy). The ionising dose is defined as the integrated dE/dx energy loss in the detector material from charged particles, excluding ionisation energy loss from nuclear recoils. It is given in units of Gy/y, where one year corresponds to 8×10^{15} inelastic p – p collisions, assuming an inelastic cross-section of 80 mb, a luminosity of 10^{34} $\mathrm{cm^{-2}\ s^{-1}}$ and a data-taking period of 10^{7} s. Ionising dose is responsible for surface or interface effects in silicon devices, as well as inducing gas detector aging effects.

Single event effects (SEE) include Single Event Upsets (SEU) in electronic circuits, which are recoverable, and Single Event Damage (SED), which may lead to the destruction of electronic components. The SEE rate is calculated by summing the rates of charged hadrons and neutrons with kinetic energies greater than 20MeV.

Muon single plane counting rate ($\mathrm{kHz/cm^2}$) is the estimator for the rate at which Muon Drift Tubes and similar detectors in the muon system will count in response to the background particle rates.

Muon penetrating particle rate ($\mathrm{kHz/cm^2}$) is the estimator for the muon level-1 trigger rate from background particle rates.

Star density ($\mathrm{N/cm^3}$) represents the density of hadronic inelastic interactions with energy above 50MeV. [48]

6.2. SHIELDING STRATEGIES AND MATERIALS

High energy particles from the IP initiate showers, as they encounter the materials of the detector. Ideally, the shielding materials should be thick enough to absorb all charged particles. ATLAS has almost 2825 tons of shielding (1887 tons of metal, 920 tons of concrete, and 18 tons of plastic) in order to limit the hazards of background radiation. Since different types of radiation require different types of shielding materials, a multi-layered shielding approach is used.

The inner layer needs to be as dense as possible in order to stop high energy hadrons and secondaries, so it is built from materials that give a large number of interaction lengths into a limited volume, such as copper and iron. In the case of iron, a minimum carbon content of a few percent is advantageous, since it efficiently moderates the neutron energies down to lower values.

The remaining neutrals are mostly neutrons, which can travel long distances, losing their energy gradually. The second layer is consisting of doped polyethylene, which is used to moderate the neutron radiation escaping from the first layer. The low energy neutrons are then captured by a dopant (either boron or lithium).

Photon radiation is created during the neutron capture process. The third shielding layer, which consists of steel or lead, is made to stop these photons. Lead is more effective in stopping photons but it has the disadvantage of giving off more neutron radiation than steel.

In ATLAS, most of the energy from the primary particles is dumped into the TAS collimators, and the Forward Calorimeters (FCal) which are among the strongest sources of secondary radiation and are somewhat self-shielding. Since they are compact, they have been further shielded with layers of dense material and cladding. Although self-shielding, the FCal sits inside the endcap calorimeters, and is not far from the first forward muon station, so there is relatively little space for shielding in this “corner” of the detector, and many design iterations have been done to optimize the shielding shapes and materials in this region.

Shower lengths will be determined by the material-dependent radiation lengths for electrons and photons, and hadronic interaction lengths for hadrons. Shower lengths increase logarithmically with particle energy so, as the energy increases, shower maximum moves deeper into the material and leakage out the back of the shielding increases. [48]

Material	***ρ (g/cm^3)***	***λ(cm)***	***X_0 (cm)***	***Comment***
Pure Cu	8.9	17.5	1.45	expensive
Cu Alloy	8.6 – 8.8	18.0 – 18.4	1.4 – 1.35	machinable
Pure Fe	7.9	19.1	1.8	n resonances
Steel	7.8	19.2	1.8	low carbon
Caste Fe	7.2	20.4	2	3% carbon
Pb	11.4	18.9	0.56	γ filter
Pure W	19.3	10.3	0.35	elemental
W Alloy	18.2	11.2	0.38	expensive
Concrete	2.4	46.9	10.9	walls
C	2.3	50.0	18.8	moderator
Al	2.7	37.2	8.9	structural
Polyethylene	0.94	92.4	47.0	moderator

Table 6.1: Radiation lengths and interaction lengths for the materials more commonly used in the shielding. The graphic comparison of some of these materials is presented in Appendix 1. [48]

6.3. ATLAS SHIELDING REGIONS

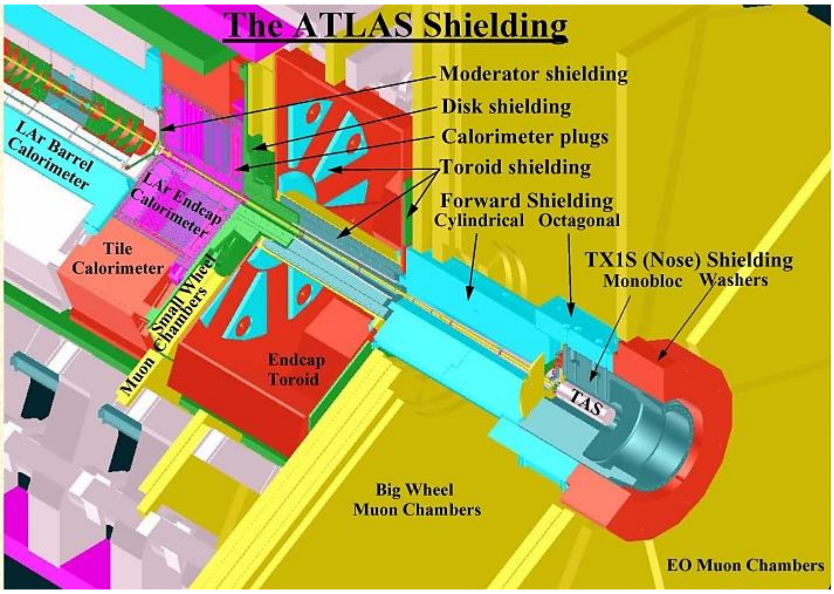

Figure 6.1: The shielding in ATLAS is divided up in six subprojects. [31]

6.3.1. JF - THE FORWARD SHIELDING

The purpose of the two Forward Shielding assemblies is to protect the middle and outer end – cap muon stations from background particles created in secondary interactions in the beampipe, the calorimeters and the TAS collimators. This shielding is removable and will be stored in the surface building during maintenance of ATLAS. The JF shielding consists of 2x387=775 tons of cast iron, 2x24=48 tons of steel plates and 2x5.5=11 tons of polyethylene for a total weight of 2x418=836 tons.

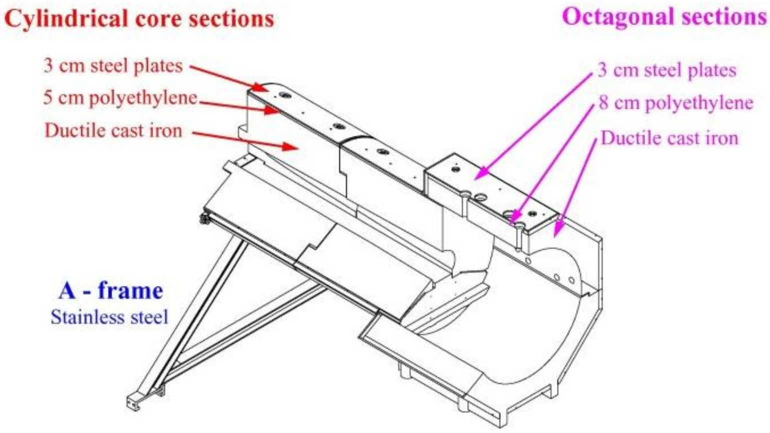

Figure 6.2: JF shielding [31]

The shielding consists of two parts: The cylindrical core, which is enclosed in a 5 cm polyethylene layer and the octagonal back that is surrounded by a thick layer of 8 cm. Three pieces called JFC1 ("the bridge"), JFC2 and JFC3 are used for the core and two pieces called "JFS3 upper" and "JFS3 lower" for the octagonal back. All pieces are made of cast ductile iron, which has a large carbon content useful as a moderator of neutron radiation and they are surrounded by a layer of polyethylene doped with boron in the form of H_3BO_3 and followed by a 3 cm thick steel layer. These polyethylene layers are made of 10000 bricks of three different shapes. [31],[63]

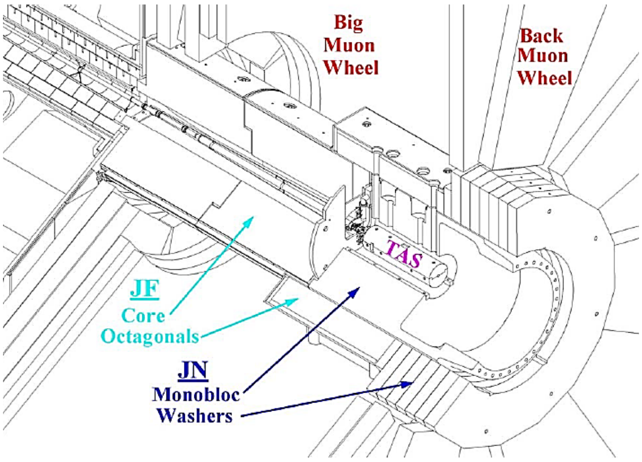

Figure 6.3: The massive shielding in the forward region (JF, JN) and TAS collimator. [48]

6.3.2. JD - THE DISK SHIELDING

The Disk shielding (JD) has a diameter of 872 cm and a total weight of 2x87=174 tons and serves a threefold purpose. Firstly, it supports the muon chambers in the first end-cap muon station (Small Wheel). Secondly, it shields these chambers from background radiation emerging from the calorimeters. Also, it provides a well-defined way for the magnetic field flux return from the solenoid magnet. The bulk of this shielding disk, which supports end – cap muon trigger chambers, consists of a vertical steel disk with a diameter of 872 cm. Three such disks are used for the 8 cm thick “large disc”. Two disks of diameter of 540 cm are used for the 5 cm thick “small disk”. Two cast iron ribs of 1.6 tons attached to the large disk are used to increase the mechanical stability of the JD.

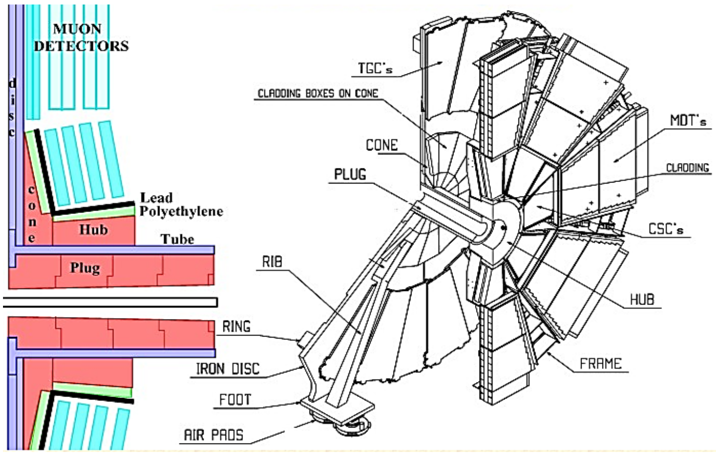

Figure 6.4: JD shielding [31]

The magnetic field is lead back through the electronic boxes of the Tile calorimeter by using 31 ring segments, with a weight of 161 kg each, attached to the large disk.

At the center of the large disk and surrounding the beam-pipe is a stainless steel tube of length 208 cm, weight 5.4 tons and diameter 106 cm stainless steel tube containing a set of cylindrical shielding pieces made of leaded red brass (85% Cu, 5% Pb, 5% Sn, 5% Zn), which also supports Cathode Strip Chambers (CSCs) and Monitored Drift Tubes (MDTs).

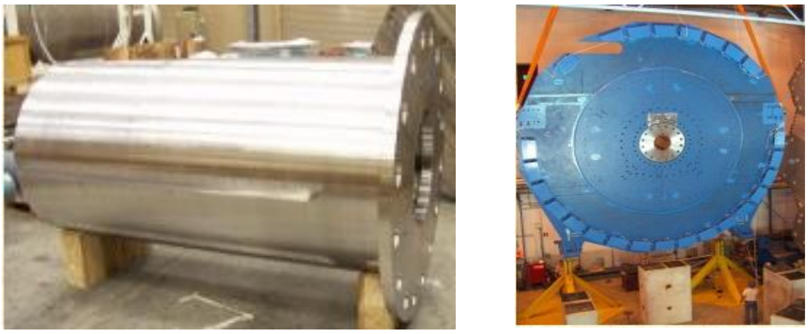

Figure 6.5: Left: The stainless steel tube. Right: The front of the JD shielding (IP side). [63]

The total weight of the muon chambers is about 13 tons (SW 12 tons and TGCs 1 tone) which brings the total weight of one JD/SW assembly to 98 tons. [31], [63]

6.3.3. JT - THE TOROID SHIELDING

The toroid shielding consists of two parts: JTT which is outside the toroid and surrounds the beampipe, and JTV which is neutron shielding situated inside the endcap toroid cryostat.

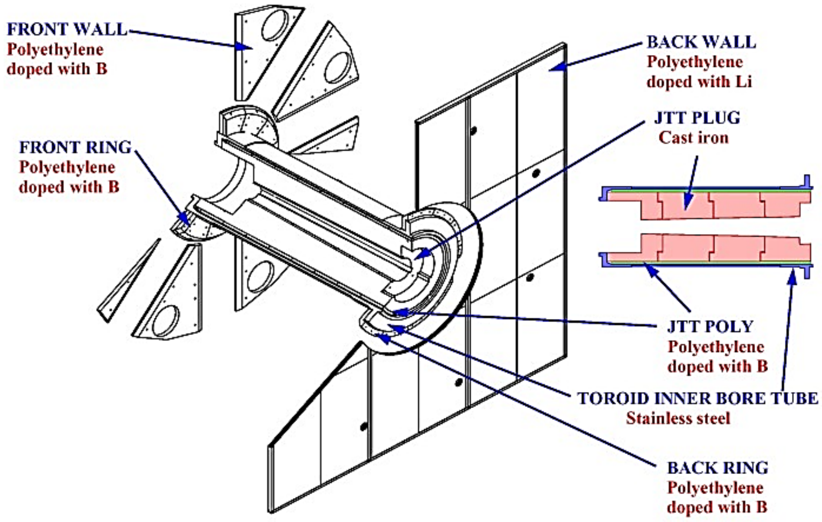

Figure 6.6: JT shielding [31]

The JTT is a cylindrical structure made of ductile cast iron of overall length about 473.6 cm, which surrounds the beampipe on the inside of the two end-cap toroid cryostats. The shielding consists of four plug pieces numbered (1 – 4) from the back. The front piece has a large hole in the center, into which the stainless steel tube of the JD fits. On the outside of the cast iron is a polyethylene layer doped with B_2O_3 (5%) that is used for neutron shielding. The photons created in the polyethylene layer are stopped by the stainless-steel ECT bore tube, which supports the shielding in the end-cap toroid. The JTT shielding consist of 2x55=110 tons of cast iron and 2x1.3=2.6 tons of polyethylene for a total weight of 113 tons.

Figure 6.7: The JTT is installed in the hole in the center of the ECT cryostat which is illustrated left. The final JTT ductile iron core pieces are shown at the picture right. [63]

The JTV consists of various polyethylene structures, which are located in the vacuum of the end-cap toroid cryostats and its purpose is to moderate neutron radiation and stop the low – energy neutrons by absorption in the boron. In particular, it consists of the front wall (petals) which are 8 cm thick plates and a front and back ring, all made of polyethylene. The polyethylene is doped with boron carbide B_4C (5%), which causes fewer out-gassing problems than other dopants. The front ring covers the radius 93 to 142 cm and it has a weight of 432 kg, while the back ring covers the radius 96.5 to 134.3 cm and has a weight of 220 kg. Photons created when the neutrons are absorbed by the boron are stopped by the aluminium of the cryostat itself. [31], [63]

Figure 6.8: Left: Installation of JTV petals on the endcap toroid endplate. Right: A JTV petal segment in the front wall. [63]

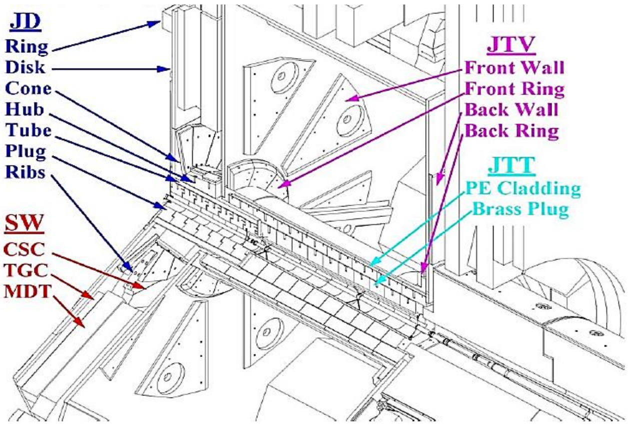

Figure 6.9: Various pieces of the disk shield (JD) and toroid shield (JTT and JTV). The location of the muon chambers in the Small Wheel (SW) are also indicated. [48]

6.3.4. JM - THE MODERATOR SHIELDING

The moderator shielding (JM) on the front face of each of the endcap and forward liquid argon calorimeters reduces the neutron fluences and protects the inner detector from back-splash of neutrons from the calorimeter. Its mass that is as small as possible and the total weight of this shielding is only 2x168 kg. It is made of polyethylene, doped with (5%) boron carbide (B_4C). This dopant results in a plastic that is more radiation hard than if other boron dopants were used. This is important since the shielding in front of the forward calorimeter is exposed to a very large dose of radiation during the ATLAS lifetime.

JM shielding consists of two parts: The 2m diameter disc of 90 kg on the front face of the endcap liquid argon calorimeter and the tube and plug of 52 kg which lines the alcove in front of the forward calorimeter. The tube cover has water pipes on the inside for cooling during beampipe bake-out. [31], [63]

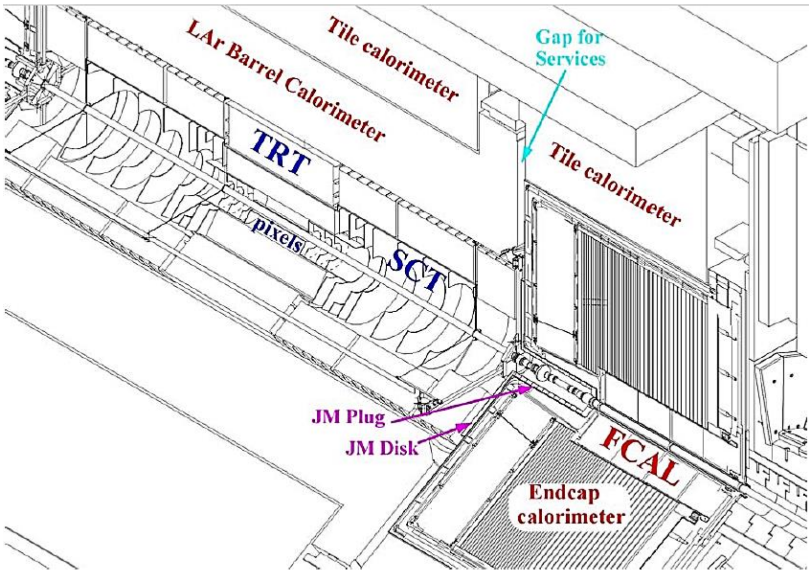

Figure 6.10: Inner detector region and JM shielding [48]

Figure 6.11: Left: The JM after installation on the endcap calorimeter. Right: Installation of scintillators on top of the JM disc. [63]

6.3.5. JN - THE NOSE SHIELDING

The nose (JN or TX1S) shielding supports the TAS collimator and protects ATLAS from the radiation created in the TAS, which is designed to prevent the first LHC quadrupole from quenching due to the energy deposited by the particles emerging from the interactions in ATLAS. The nose shielding is permanently installed in ATLAS and cannot be removed during shutdowns.

The main part of this shielding is the cylindrical 117 tone heavy monobloc made of cast iron with outer diameter of 295 cm. It is supported by a tube that is anchored in a 460 tone concrete structure. This cast iron tube has a weight of 51 tons and it has an inner diameter of 257 cm and an outer diameter of 297 cm.

The 2x200 tone heavy "washers", which are located around the support tube, surround the tube and the monobloc and increase the radial thickness of the iron shielding by 112 cm in a region where the monobloc is thin. [31], [63]

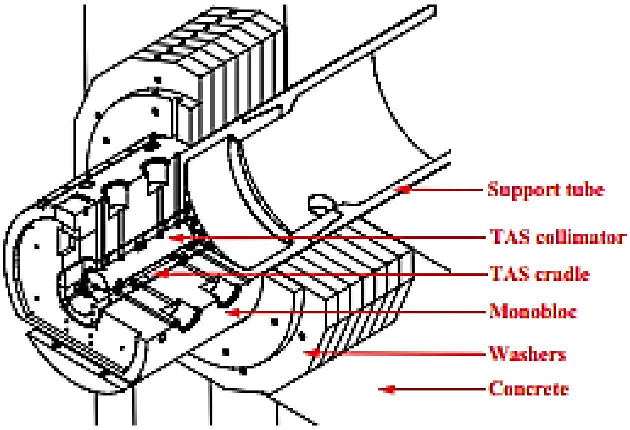

Figure 6.12: Schematic view of JN [31]

Figure 6.13: Left: The monobloc after installation. Right: Front view of the TAS collimator and the remotely controlled beampipe flange. [63]

6.3.6. Plugs in the LAr calorimeter

There are three brass shielding elements inside each of the end-cap calorimeter cryostats, located directly behind the calorimeters. The largest one of outer diameter 387 cm, inner diameter of 118.2 cm and weight of 12 tons is attached to the rear endplate of the cryostats. Closer to the beam-line are two other shielding plugs. Plug 2 is a smaller ring shaped shielding with a weight of 0.9 tons, an inner diameter of 95 cm and an outer diameter of 135 cm. Plug 3 is a cylindrically-shaped extension of the forward calorimeters. The main purpose of these shielding elements is to protect the end-cap inner muon stations from the background radiation. [31], [63]

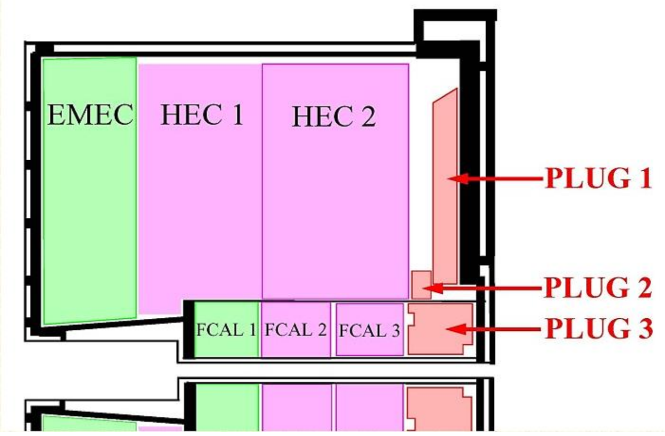

Figure 6.14: LAr calorimeter shielding plugs [31]

6.4. Measurements, Predictions and Radiation impact

The largest impact from background radiation is of course to be expected close to the beampipe, in particular in the region of the inner detector and the forward Calorimeters. The secondary sources leading to background radiation in the outer regions of the detector depend on the locations where the most energy is deposited by primary particles. The three hottest sources in order of importance are (1) the core of the TAS collimator at 19.5 meters, (2) the core of the forward calorimeter at 5.2 meters, and (3) the beamline, from 5.2 meters to about 14 meters. Projected radiation levels in key areas of the detector are described below. The energy deposited in each TAS collimator is of the order of 2.3 TeV. Each FCAL calorimeter absorbs about 0.45 TeV while about 50 GeV are deposited in the beam pipe. [31]

6.4.1. PREDICTIONS FOR THE INNER DETECTOR

The inner detector sees the primary particle production coming from the interaction point, along with albedo particles with their largest number coming from the face of the endcap calorimeter. Charged hadrons, dominated by charged pions originating from the p-p collisions, constitute the most serious background for the innermost layers of the inner detector. The charged hadron fluence contours run parallel to the beamline, which is a consequence of the flatness of the charged particle rapidity plateau of minimum bias events. Hadrons above 10 MeV are less numerous, but are also important.

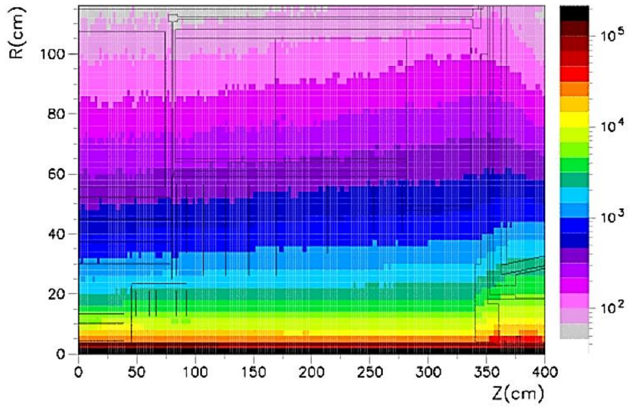

Figure 6.15: Charged hadron fluence rates in the inner detector. [48]

The variation in fluence levels is much less for neutrons than for charged hadrons. Most of the neutrons in the inner detector are the result of albedo (back-splash from the calorimeters).

Considering photons, the fluence contours are similar to those of neutrons away from the beamline, indicating that most of the photons are being produced from neutron capture. Photons are also produced copiously from interactions in the beamline equipment and the minimization of the material it is important in this region. Another source of photons is from π^0 decay, which dominates the fluences at high energies. [31], [48]

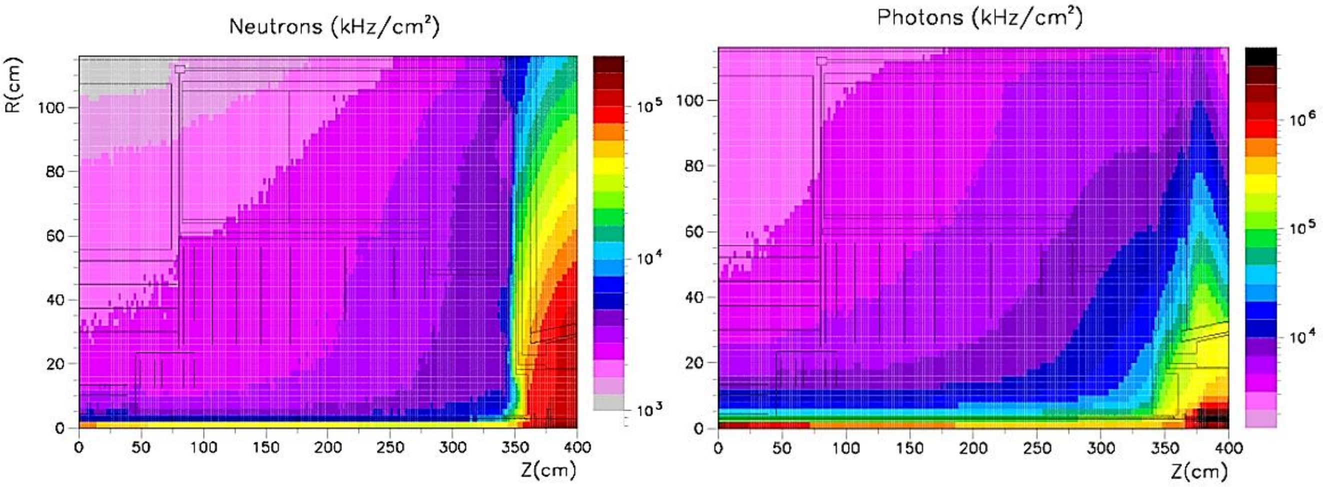

Figure 6.16: Left: Total neutron fluence in the Inner detector. Right: Proton fluence rates in the Inner detector [48]

6.4.2. RADIATION IMPACT ON THE INNER DETECTOR

Ionizing energy loss in the surface layers results in damage to silicon devices. Electrons resulting from ionization in semiconductor oxide layers quickly drift from the oxide layer, driven by the bias voltage. The low mobility holes that are left behind slowly drift towards the Si-SiO_2 interface, where they accumulate as a charged layer, modifying the operating characteristics of the device.

Another effect is bulk (or displacement) damage which dominates the damage to “minority carrier” devices (silicon detectors, bipolar electronics etc.). Damage effects by energetic particles in the bulk of any material can be described as being proportional to the displacement damage cross section D, which depends on the particle type and energy.

Silicon detectors, and other detector components, are also subject to damage by ionizing radiation, also referred as “ionising dose” damage (Gy/y). The character of the damage due to this ionisation energy loss is quite different from displacement damage, in that it typically involves only the surface layers of detectors, since the low energy electrons and positrons responsible for the majority of the damage have little penetrating power in silicon.

Charged particles will induce ionization at an energy dependent rate, dE/dX, given by Bethe-Bloch formula, and photon backgrounds can be important since they interact readily to produce charged particles. [31], [48]

6.4.3. PREDICTIONS FOR THE CALORIMETER

The forward calorimeters will be exposed to up to 160 kGy/y, whereas the end-cap electromagnetic calorimeters are exposed to up to 30 kGy/y, numbers which lead to very large integrated doses over the full lifetime of the experiment. This is one reason why only the LAr technology with its intrinsically high resistance to radiation is used in the end-cap and forward regions. The tile calorimeter, with its scintillator samplings read out by wavelength-shifting fibres, is protected by the LAr electromagnetic calorimeter and is exposed to less than 30 Gy/y.

The photon map shows an electromagnetic shower development at around z = ± 4.9 m. The neutron map emphasizes the hadronic shower maximum at z = ± 5.1 m. [31], [48]

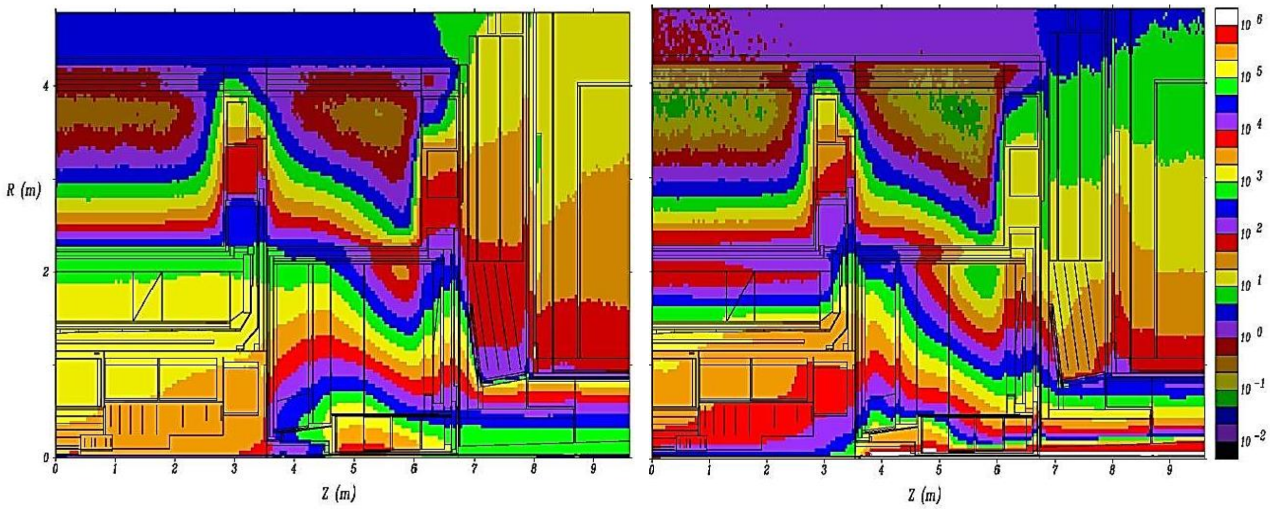

Figure 6.17: Total neutron flux and Photon flux in the calorimeter region (GCALOR) [48]

6.4.4. IMPACT ON THE CALORIMETER

The TileCal consists of steel absorber material, impervious to radiation damage and scintillating plates read out by wavelength shifting (WLS) fibers. TileCal irradiation tests for possible damage to the scintillator and WLS fibers concluded that these elements can have their light yields reduced by ionizing radiation, including the ionization induced by interacting background neutrons.

The TileCal photomultiplier tubes (PMTs) and front end electronics are in ‘drawers’ positioned between structural steel support girders at the back of the TileCal modules. In both the barrel and endcap, this region is well shielded by the total depth of the ATLAS calorimeters. The most exposed regions are at the ends of the drawers, where there are gaps for inner detector services and electronics.

As for the LAr calorimeters, the argon itself is not susceptible to radiation damage, either short or long term. However, the radiation rates in the ATLAS FCAL region are exceptionally high, and there was concern that activation of the argon might lead to signal or safety problems. The absorber and structural materials used in the ATLAS LArg calorimeters are primarily metals known to be radiation resistant and ‘stable’, meaning that they do not release potential poisons into the argon. [48]

6.4.5. PREDICTIONS FOR THE MUON SPECTROMETER

The main source of the background recorded in the active elements is from particles produced in the interactions of primary hadrons from p - p collisions with the material of the detector, especially the calorimeters and the toroid structures, and with machine elements such as the collimators and the beam pipe. The particles are neutrons, low-energy photons originating from neutron capture, and charged particles. The neutrons mostly have thermal energies, while the photons are concentrated in the 200 keV to 2 MeV energy range. The interaction of these photons with the detector material (aluminium in the case of the precision chambers, bakelite or G10 in the case of the trigger detectors) produces a signal in the sensitive volume of the chamber via the Compton effect with a probability of about 10^{-2}. Neutrons have a much lower probability to produce a direct signal in the muon detectors, but are directly responsible for the photon flux. The charged-particle background consists mainly of muons, charged pions, protons, electrons and positrons. The muons and pions are produced mostly in K^0 decays, while the protons emerge from neutron spallation processes. Hadrons and muons have a typical momentum of 100 MeV.

The CSC’s in the inner end-cap stations will be exposed to the highest ionizing dose (3 - 20 Gy/y). The chambers closest to the beam-line in the middle end-cap stations are expected to receive at most 10 Gy/y. Most of the muon spectrometer will, however, be exposed to less than 1 Gy/y. [31], [48]

6.4.6. CONSEQUENCES OF THE BACKGROUND AT THE MUON SYSTEM

High particles fluxes in the muon system have a major impact on the spectrometer design. The most important consequences of this background are the high occupancy of the muon detectors, especially in the inner stations at large $|\eta|$, space-charge effects, and the reduced lifetime of the muon detectors. These effects are mainly determined by the intensity of the photon flux, and indirectly by the intensity of the neutron flux. The highest fluxes are expected in the innermost end-cap muon stations, in particular in the CSC’s, which will have to cope with a large background counting rate, although the estimation of this rate is subject to systematic uncertainties. Fluxes tend to be isotropic in the barrel, while in the end-cap a substantial fraction of the particles originates from the interaction region and from the beam-pipe in the region of the end-cap toroids, which is the main local source of secondary radiation. The physics performance of the Muon System begins to be degraded if the background level becomes larger than ten times the one presently estimated by muon track reconstruction studies. Moreover, a high fake LVL1 muon trigger rate occurs due to charged particles with a momentum around 100 MeV. [31]

6.4.7. FAKE MUON TRIGGERS

They are two broad classes of background hits: primary collision products, such as prompt muons from heavy particle decays and hadronic debris of calorimeter showers; very low-energy secondaries from radiation background. The ATLAS muon instrumentation has been designed to offer the rate capability and robustness to the high occupancies required for running at nominal luminosity. The LVL1 trigger system is based on dedicated, fast and finely segmented detectors. The accidental trigger rate should remain below the rate expected from prompt muons including safety factors in predicted background rates.

The radiation background affects the muon system by generating uncorrelated noise hits and by producing penetrating particles. A large background flux is expected in the experimental cavern at the LHC from the interactions of hadrons produced in p-p collisions with the forward elements of the ATLAS detector, the shielding system and machine elements. The particles produced in such secondary interactions and their decay products can induce high counting rates in the muon trigger system and may significantly reduce the muon track-finding efficiency.

The muon-detector counting rate depends strongly on the muon station position and pseudorapidity. Typically, in the barrel chambers at high luminosity, the nominal rate in the first station is ~10 Hz/cm^2, and increases to 100 Hz/cm^2 around $|\eta|= 0.7$. For the end-cap chambers, the counting rate in the inner stations increases up to ~1 kHz/cm^2. The counting rate in all the other stations is significantly lower, with values in the range between 10 and 30 Hz/cm^2, and depends weakly on pseudorapidity. The dominant contribution to this rate comes from the photon flux, whereas charged particles contribute a rate of only a few Hz/cm^2. The MDT chambers have been designed to handle up to 5 times counting rates of about 10 Hz/cm2 in the middle of the barrel and up to about 100 Hz at Pseudorapidity ~2, while CSCs are designed for rates above 200 Hz/cm2 and are to be used in the most critical forward location. RPCs and TGCs provide transverse measurements used by the trigger to reject muons with pT below a given threshold. The sensitivities of the chambers to the neutron and photon background for estimation of the trigger rates are given below:

Chamber type	***Neutron sensitivity***	***Photon sensitivity***
MDT	$\sim5*10^{-4}$	$\sim8*10^{-3}$
CSC	$\sim10^{-4}$	$\sim5*10^{-3}$
RPC/TGC	$\sim10^{-4}$	$\sim5*10^{-3}$

Table 6.2: Average sensitivity of muon chambers to neutron and photon background used in trigger rate estimates. [48]

Particles of low energy (up to 10 MeV) include mainly soft Compton electrons and neutron-induced soft protons. Such particles produce hits in a single trigger counter (no correlation between trigger planes). This incoherent background was produces triggers at rates much below those expected from p-p collision products. The dominant contribution to the fake low-pT trigger rate in both barrel and end-cap arises from the coincidence of a pair of hits from a penetrating particle in one of the low-pT stations, with one or more hits deposited by any other particle. The fake high-pT trigger rate is dominated by a low-pT trigger in coincidence with any other hits (or track) in the high-pT station of the barrel or end-cap.

Harder particles that (momenta above 10 MeV) can give rise to hits in more than one plane of trigger detectors, and thus fake a muon trigger. The majority of such triggers are due to muons of momentum around 100 MeV, arising directly or indirectly from the decay of neutral kaons ($K_L^0 \rightarrow \mu\pi\nu$). This background is therefore called the '100 MeV background'. The K_L^0 flux is produced by interactions of secondaries with the material of the detector, and the forward shielding.

The counting rates have been evaluated as:

$$\textit{Single plane counting rate} = n \cdot \varepsilon_n + \gamma \cdot \varepsilon_\gamma + (p + \pi + \mu + 0.25e)$$
$$\textit{Penetrating particle rate} = 0.1 \cdot \gamma \cdot \varepsilon_\gamma + (p + \pi + \mu + 0.25e)$$

where "n" and "γ" stand for neutron and photon particle fluences respectively,"ε_n" and "ε_γ" are the corresponding average neutron and photon chamber sensitivities. For charged particles, p, π, μ, and e, stand for currents instead of fluences. Fluence is proportional to the track length in a given volume and is appropriate for hits resulting from neutral particle interactions in the chamber while particle current gives a better estimate of the counting rate induced by charged particles crossing a chamber. The efficiency for charged particles to produce a hit in a chamber is taken as 100%. Electron currents are multiplied by a factor 0.25 to avoid double counting of electrons produced in photon interactions in neighbouring material. The factor 0.1 multiplying the photon fluence in the penetrating particle rate is a rough estimate of the fraction of photon interactions that result in a coincidence of two adjacent planes.

Single chamber counting rate is dominated by the photons at ~80%, while neutrons contribute at the 10% level. In the inner barrel, the contribution from punchthrough muons raises to about 15% and from pions to a few %. In the forward region, photons contribute somewhat less to the counting rate. Penetrating particle rates are shared between charged particles and photons in the forward region and dominated by photons and electrons in the barrel. Photons and protons account for about 70% of the rate while muons and electrons share the remaining 30% and pions are negligible.

MDT Inner Forward	*single*	12% **n**	64% γ	8% p	7% μ	9% e
	penetrating		21% γ	27% p	24% μ	28% e
MDT Outer Forward	*single*	12% **n**	74% γ	4% p	1% μ	7% e
	penetrating		35% γ	17% p	7% μ	41% e

Table 6.3: Relative contributions from different particle species to the single plane and penetrating particle counting rates. The "MDT Inner Forward" set of data, corresponds to the Small Wheel MDT chamber closest to the beam, while the MDT Outer Barrel, corresponds to MDT chambers of the outer barrel. [48]

6.4.7.1. PARTICLE EFFICIENCIES

The chamber efficiencies for neutrons, photons and electrons have been calculated for each type of chamber with the detailed Geant3 geometry taking into account the angular distribution of the particles.

GCALOR							
	neutron	*single-plane photons*	*double-plane photons*	*double-compton*			*fraction of electron rate*
				3/4	*2/3*	3/4*2/3	
MDT (BA)	$3.0*10^{-4}$	$5.0*10^{-3}$					5%
MDT (EC)	$3.0*10^{-4}$	4.7/5.2 10^{-3}					10%
CSC	$1.2*10^{-4}$	$7.4*10^{-3}$					10%
RPC	$2.0*10^{-4}$	$6.5*10^{-3}$	$5.0*10^{-4}$	$3.5*10^{-7}$			5%
TGC	$5.0*10^{-4}$	4.4/5.1/6.7 10^{-3}	2.0/3.5/5.7 10^{-4}	1.2/2.4/4.0 10^{-6}	4.9/9.5/16. 10^{-5}	2.7/4.4/7.2 10^{-8}	10%
FLUKA							
	neutron	*single-plane photons*	*double-plane photons*	*double-compton*			*fraction of electron rate*
				3/4	*2/3*	3/4*2/3	
MDT (BA)		$5.5*10^{-3}$					5%
MDT (EC)		5.7/5.6 10^{-3}					10%
CSC		$6.0*10^{-3}$					10%
RPC		$5.4*10^{-3}$	$2.2*10^{-4}$	$1.9*10^{-7}$			5%
TGC		5.7/5.5/5.5 10^{-3}	3.8/3.6/3.7 10^{-4}	3.5/2.6/2.6 10^{-6}	9.6/9.5/10. 10^{-5}	22./8.9/10.4 10^{-8}	10%

Table 6.5: Summary of average efficiencies obtained by folding efficiency curves with the GCALOR spectra and the FLUKA spectra. In the endcap the values are given for high/mid/low η values respectively. [48]

Efficiency for neutrons

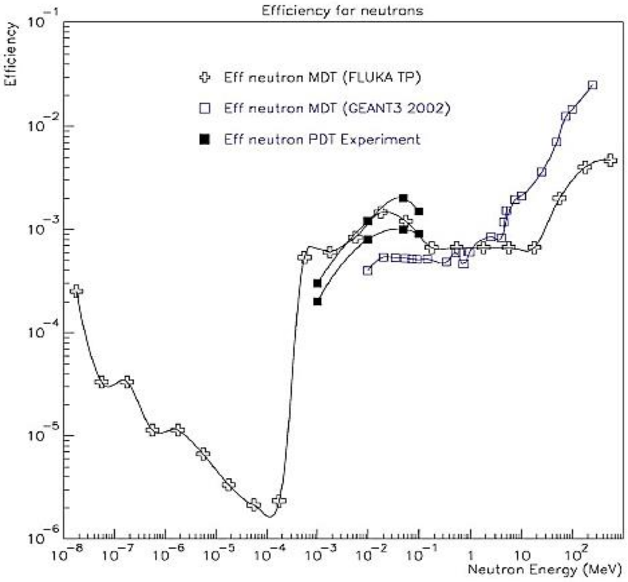

Figure 6.18: MDT Efficiency for neutrons [48]

There are three components that contribute to the efficiency. Neutron capture, most probable for thermal neutrons, with subsequent gamma emission and interaction are responsible for the efficiency up to approximately 0.1 keV. Then, from the chamber signal detection threshold (~ 1 keV) up to 10 MeV, it is the recoil of gas nuclei with its associated ionization that produces the signal. At higher energies, charged secondaries, mainly protons from quasi-elastic neutron scattering in the chamber wall or surrounding material, are the source of the signal.

The average efficiencies have been calculated for the different chambers and different locations.

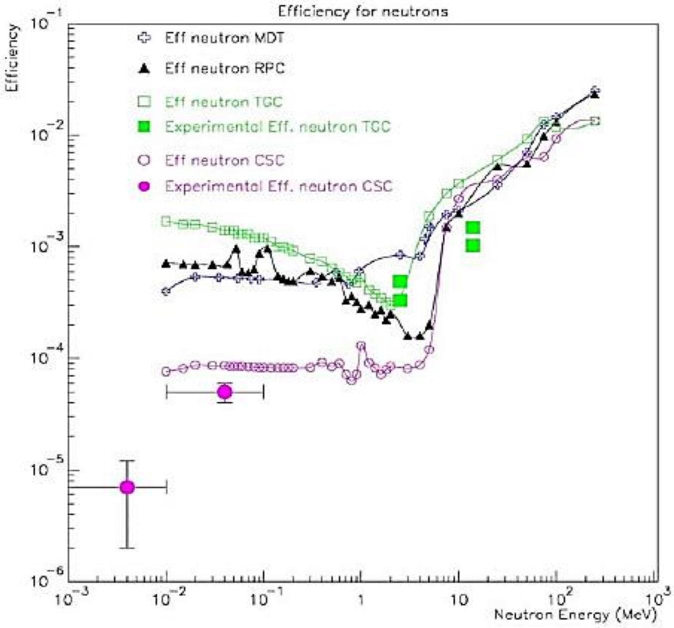

Figure 6.19: Efficiency for neutrons for the different chamber types as calculated with Geant3. Experimental measurements are shown for CSC and TGC. [48]

Efficiency for photons

The single plane efficiency for photons in the MDT chambers is shown above:

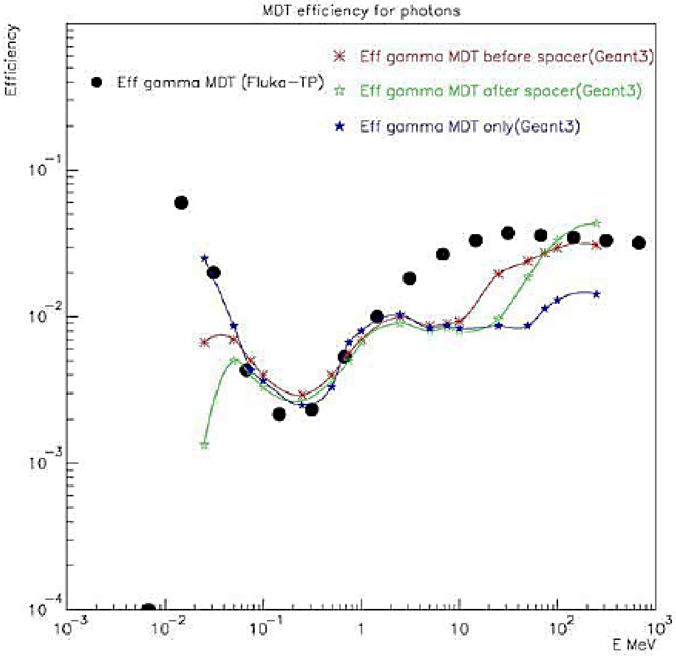

Figure 6.20: Efficiency for photons in MDT chambers as calculated with Geant3 (coloured stars) and as calculated with FLUKA (black circles). [48]

The efficiency below 100 keV is due to photo-electric effect in the gas, while the raising curve in the 1 MeV region is due to Compton scattering in the tube wall. Around 10 MeV, pair production becomes important and interactions in the material surrounding the chamber do play a role. The calculation was done for an isotropic photon flux and for a set of three MDTs without the surrounding RPCs and chambers support. The curves are similar in the region where Compton scattering in the wall dominates. At low energy differences can be expected due to the different gas composition and sensitivity to surrounding material. At high energies, the latter has also an influence.

The single plane efficiency for RPC is shown below. Photon absorption is relatively less important in this case.

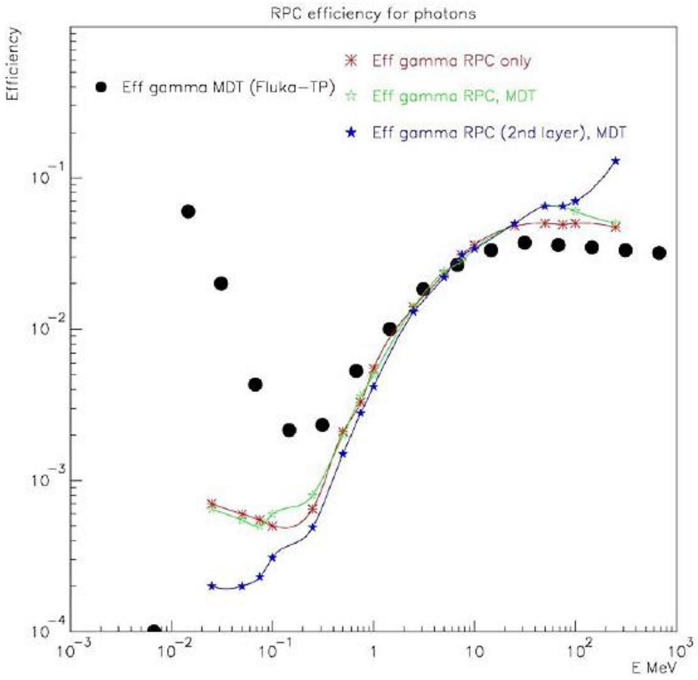

Figure 6.21: Single plane efficiency for photons in RPC chambers as calculated with Geant 3. [48]

The efficiency for firing a single plane in a TGC triplet is shown in the figure below. The efficiency has been measured experimentally with collimated sources of photons impinging perpendicularly to the chamber surface. The energy range covered was 20 keV to 1.8 MeV. The Geant3 simulated efficiency is in quite good agreement with the experimental data.

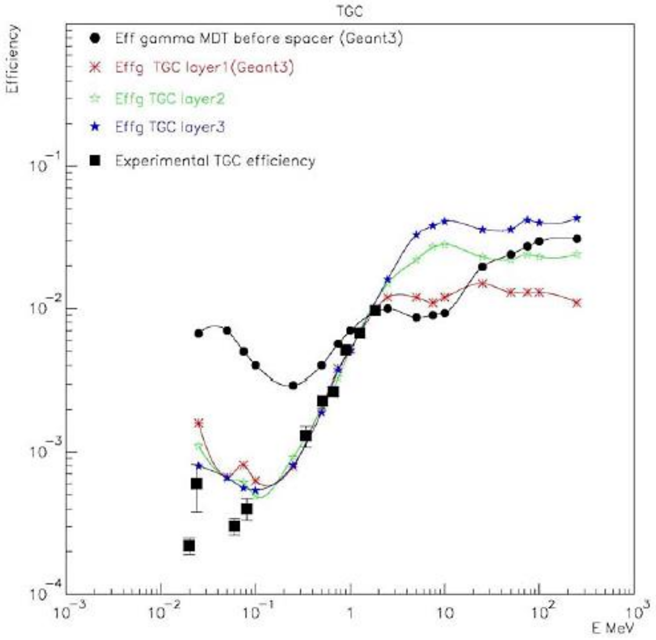

Figure 6.22: Efficiency for firing a single plane in a TGC triplet as simulated with Geant3. Experimental data are also represented. [48]

The efficiency for CSC is shown below. Good agreement is seen in the region dominated by Compton effect. Differences in the details of the chambers geometry and in the gas used in the simulation and in the experiment may explain the higher experimental efficiency below 100 keV.

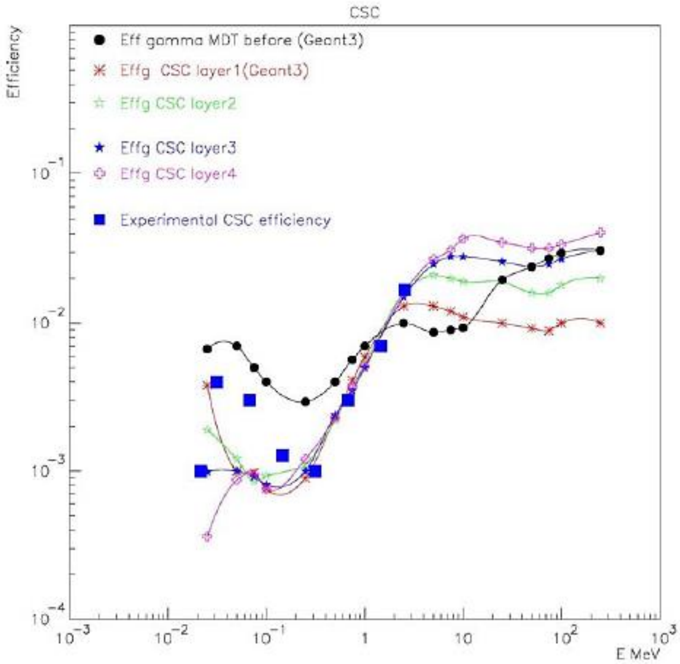

Figure 6.23: Efficiency for firing one the CSC plane. Experimental values are also available. [48]

The average MDT and RPC photon efficiency have been calculated with the GCalor energy spectrum and the AV16 FLUKA spectrum by folding the spectra with the efficiency. The RPC single plane efficiency folded spectra are shown:

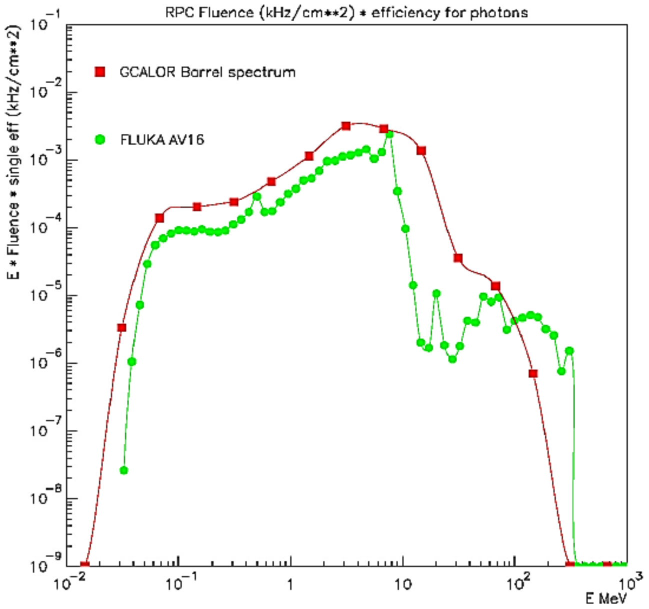

Figure 6.24: Photon energy spectra folded with the efficiency for firing a single RPC plane. [48]

An important characteristic of the RPCs is the probability for a photon to fire a couple of planes inside a station. So far it was assumed that 10% of the photons would be able to satisfy the coincidence. The efficiency for satisfying the coincidence has been calculated: the coincidence window is 3 strips, (-1,0,+1) in strip number.

The probability that a photon fires two planes as a function of the energy of the photon is shown in the picture below. It is a sharply raising curve around a few MeV.

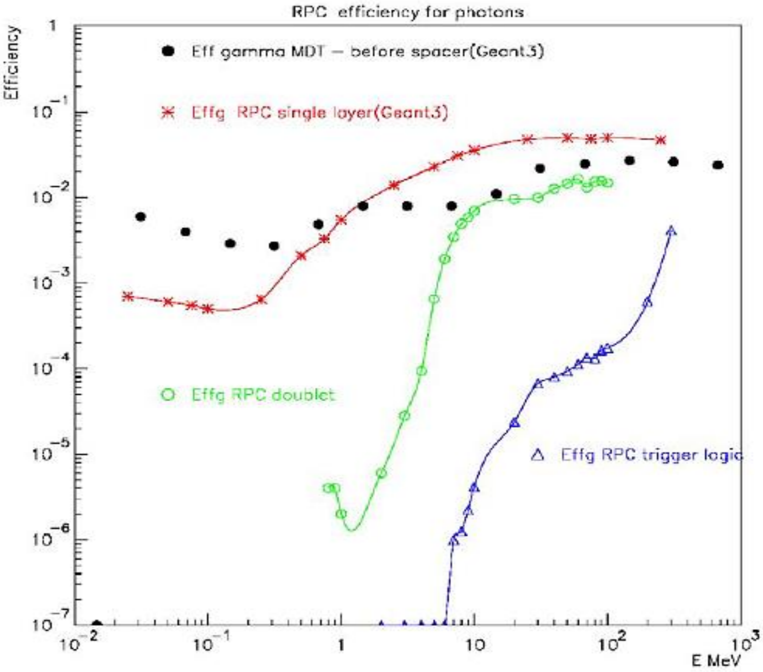

Figure 6.25: Gamma efficiency for RPC: stars for a single layer, open circles for firing a doublet, open triangles for fulfilling the trigger logic. The single plane efficiency of TP MDT is given for comparison (full dots). [48]

The probability that the photon interaction fulfils the muon trigger logic in the eta projection is also shown in the figure. At these energies, the photons mainly undergo Compton scattering, producing sometime energetic electrons able to cross two planes. But, in addition, the scattered photon may continue, unhampered by the magnetic field, reach the next station and produce a second electron (“Double-Compton”).

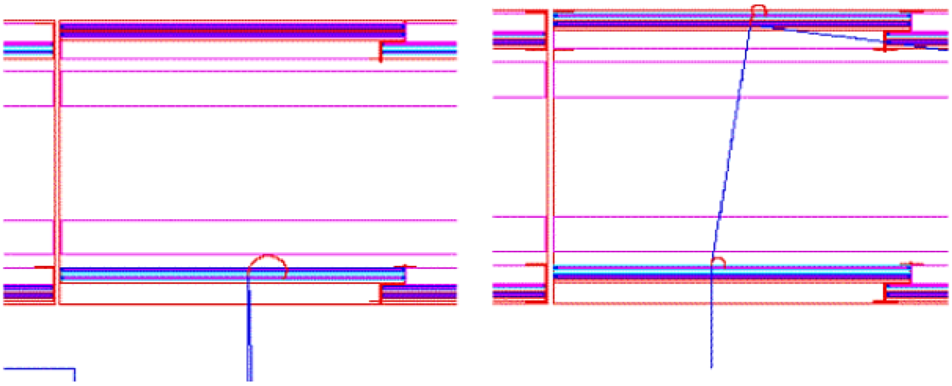

Figure 6.26: Example of 10 MeV photon that triggers two planes (left) and 3 planes (right). [48]

The following table summarizes the efficiencies and expected counting rates.

	Average efficiency	*Counting rate at low luminosity*
Single plane (GCalor)	$6.5*10^{-3}$	0.7-1 Hz/cm^2
Single plane (FLUKA)	5.4*10-3	1.2-2.2 Hz/cm^2
Doublet (GCalor)	5.0*10-4	$5\text{-}7*10^{-2}$ Hz/cm^2
Doublet (FLUKA)	2.2*10-4	$5\text{-}9*10^{-2}$ Hz/cm^2
Low pt Trigger (GCalor)	3.5*10-7	340-490 Hz (barrel)
Low pt Trigger (FLUKA)	1.9*10-9	420-790 Hz (barrel)

Table 6.6: Averaged efficiency for firing a single RPC plane, a doublet of RPC and fulfilling the low pt trigger logic in the barrel. Counting rate are given fr low luminosity. The range in rates corresponds to low and high Z, respectively. The counting rates for the barrel are calculated for a surface of 10^7 cm^2. [48]

For the TGCs examples of photons firing 3 out 4 planes in a TGC doublet and fulfilling the full endcap trigger logic are shown:

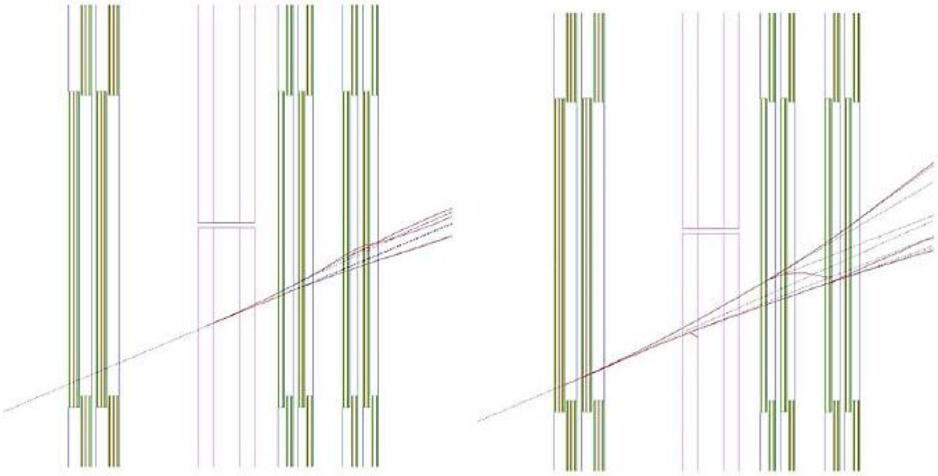

Figure 6.27: Example of 200 MeV photon that triggers 3 out of 4 planes (left) and the full trigger logic 3-out-4 and 2-out-3 (right). [48]

The probability of firing 3 out of 4 planes in a TGC doublet is about an order of magnitude higher than in a RPC doublet, due to the different angular distribution of the photons and the lower magnetic field.

- Efficiency for charged hadrons

Protons and pions are rather energetic, having energies above 20 MeV. They fire a plane or a couple of RPC planes with 100% probability.

- Efficiency for electrons

In the case of electrons, most of the e± background is produced locally in the muon chamber material, and is therefore accounted for in the photon sensitivity functions. What is relevant for the trigger is the fraction of electrons that is able to fire a RPC or a TGC doublet. The figure below shows that probability as a function of the electron energy as simulated with Geant3. [48]

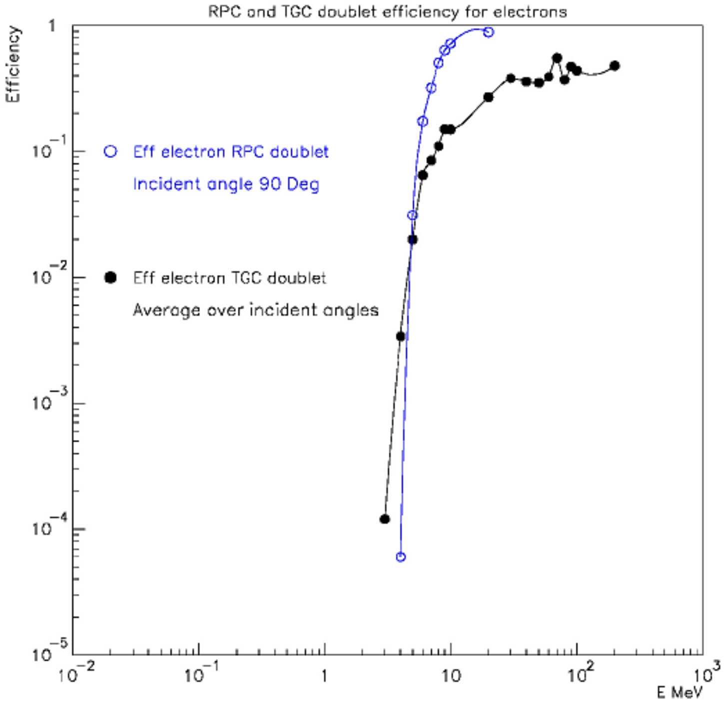

Figure 6.28: Probability for an electron to fire a RPC doublet and to fire a TGC doublet. [48]

6.4.8. IMPACT ON ELECTRONICS

The high radiation levels in ATLAS can affect electronic components by one or both of the following routes: (1) the slow accumulation of radiation damage over long periods of time as the experiment runs, leading to signal degradation or destruction of components, or (2) individual interactions of background particles (mostly high energy hadrons) with electronic components, causing large local ionization deposits that corrupt data (“single event upsets”) or destroy components (“single event damage”). In principle, these effects extend to all components in the trigger and data acquisition system, both analog and digital: preamps and front-ends, pipelines and processors, optical and wire data links, monitoring electronics, voltage regulators and power supplies, etc. And because the inner detector silicon microstrip and pixel detectors are essentially electronic devices, these are vulnerable to the same classes of damage as the data acquisition system. [48]

7. SIMULATIONS AND MEASUREMENTS

7.1. METHODOLOGY OF THE SIMULATION

Simulations using simple geometries like sphere and cube where conducted in order to verify the validity of more complex geometries (Appendix 1).

7.1.1. CYLINDRICAL GEOMETRIES

A Co-60 source is chosen for the first simulations. It is placed initially at (0,0,0) which is the center of any simulated geometry. Co-60 decays into two photons with energies 1.173 MeV and 1.332 MeV respectively.

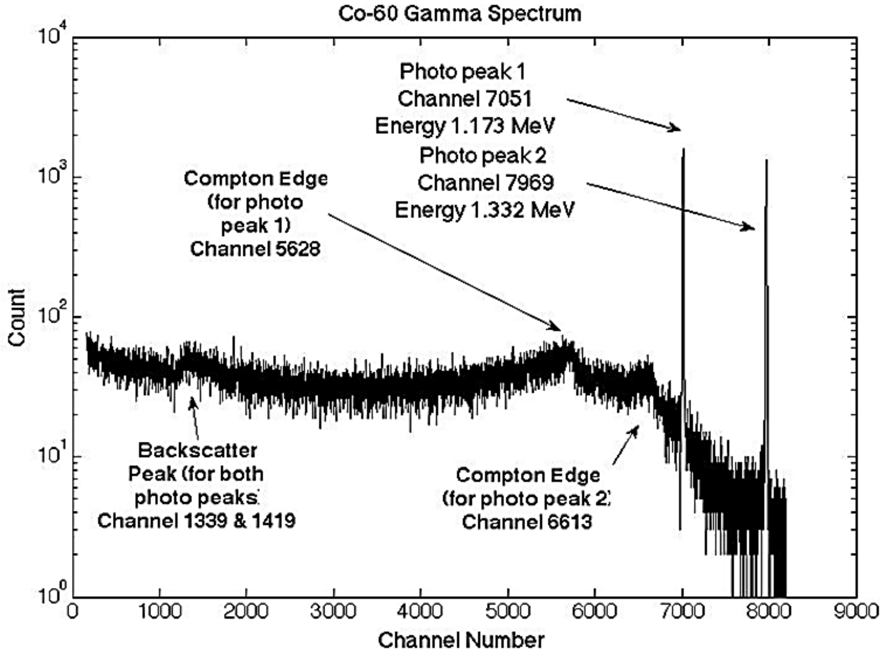

Figure 7.1: Co-60 spectrum

Simple Cylindrical modules can be combined to give a satisfactory representation of the ATLAS detector and its cavern. A Right Circular Cylinder (RCC) macrobody of 50 m long on the x-axis with a radius of 12.5 m, the Co-60 source in the center and filled with air is used. This dimensions can roughly represent the ATLAS barrel, without any elements inside. The simulation runs for 1 minute of computer time.

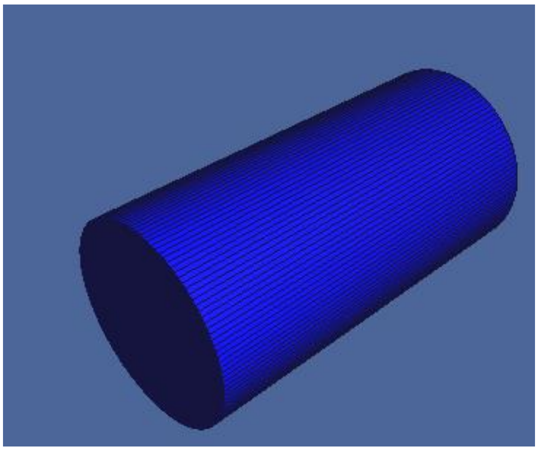

Figure 7.2: Simulated cylinder with MCNP (3D plot). [Vised]

The total average cell photon flux within the cylinder is 13.89822 E-08 particles/cm^2 (relative error 0.0005). For the surface flux:

Surface	***Flux per source particle (#/cm^2)***	***Total flux for 2 source particles(#/cm^2)***	***Relative error***
Cylinder	2.87071 E-08	5.74142 E-08	0.0008
Right base	1.12482 E-08	2.24964 E-08	0.0070
Left base	1.15430 E-08	2.3086 E-08	0.0068

Table 7.1: Photon flux in a cylinder simulated by MCNP.

7.1.2. SOURCE TRIALS

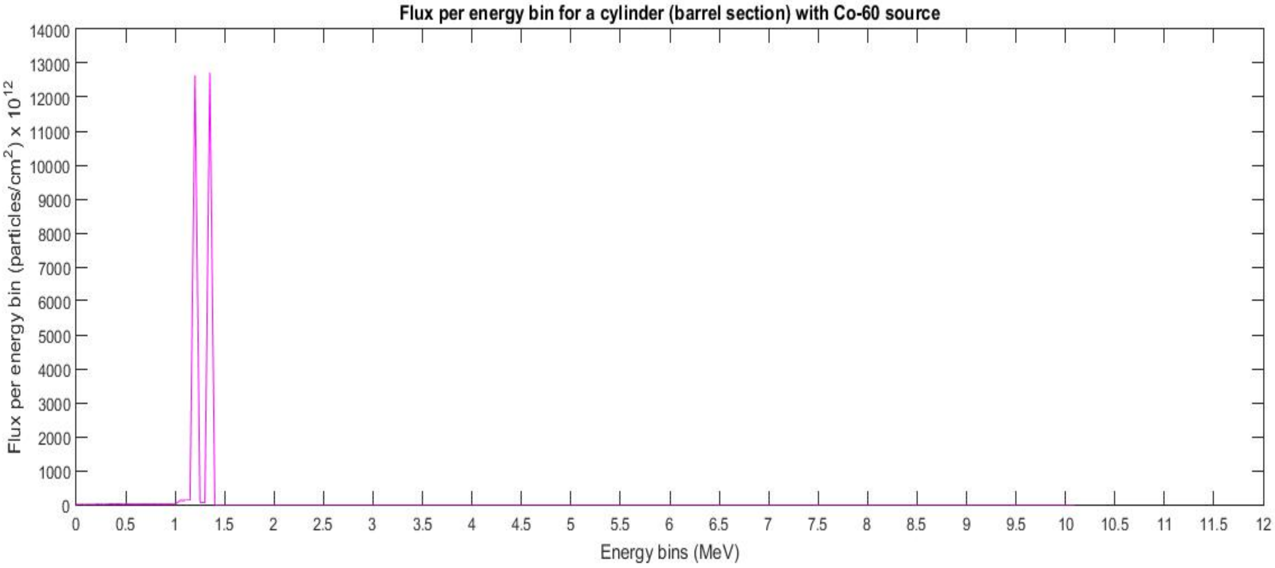

Figure 7.3: Surface flux spectra of the Co-60 source (for the barrel section) when it is placed at (0,0,0). [Matlab]

Different photon sources into the cylinder simulated above are compared.

- Relocation of the Co-60 source:

Co-60 source at x=-1m		
Surface	***Surface Flux (#/cm^2)***	***Relative error***
Cylinder	5.73676 E-08	0.0008
Right base	2.09388 E-08	0.0073
Left base	2.49846 E-08	0.0067
Co-60 source at x=-10m		
Cylinder	5.44194 E-08	0.0009
Right base	1.17560 E-08	0.0099
Left base	5.49392 E-08	0.0044
Co-60 source at x=-20m		
Cylinder	4.30708 E-08	0.0012
Right base	0.70113 E-08	0.0117
Left base	20.4134 E-08	0.0023
Co-60 source at y=1m		
Cylinder	5.75696 E-08	0.0008
Right base	2.25316 E-08	0.0071
Left base	2.30094 E-08	0.0069
Co-60 source at y=10m		
Cylinder	7.91262 E-08	0.0008
Right base	2.00498 E-08	0.0068
Left base	2.00644 E-08	0.0067

Table 7.2: Photon flux measurements after the relocation of the source.

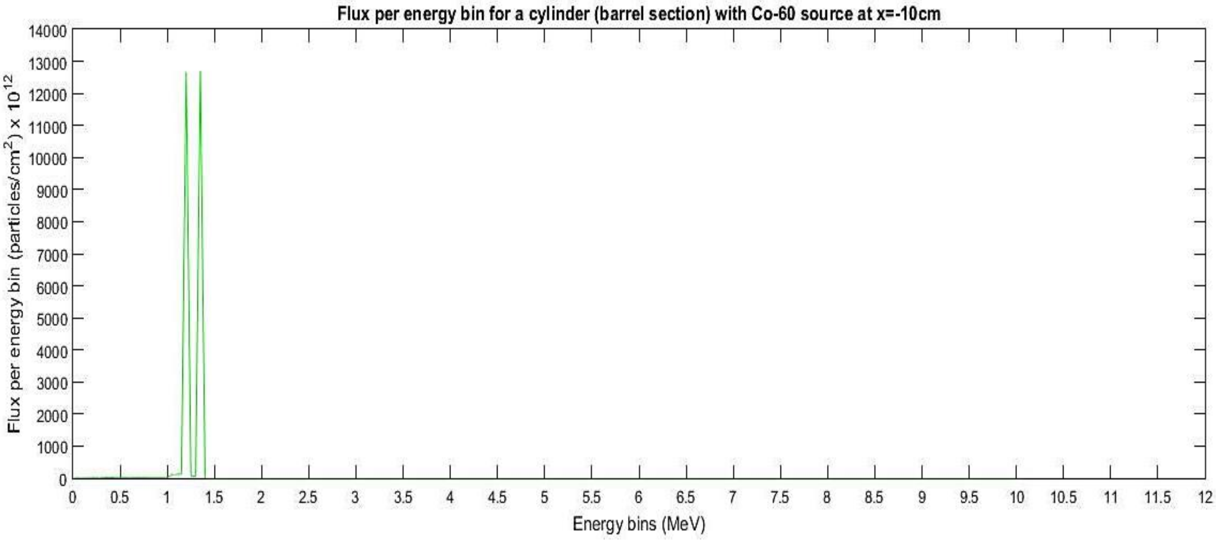

Figure 7.4: Surface flux spectrum when the Co-60 source is relocated at x=-10cm. It can be observed that it remains exactly the same. [Matlab]

- More Co-60 sources:

Two Co-60 sources at x=-1m and x=1m		
Surface	***Surface Flux (#/cm^2)***	***Relative error***
Cylinder	11.4854 E-08	0.0008
Right base	4.57448 E-08	0.0071
Left base	4.55412 E-08	0.0069
Three Co-60 sources at x=-1m, x=0 m and x=1m		
Cylinder	17.2298 E-08	0.0008

Right base	6.83652 E-08	0.0071
Left base	6.83994 E-08	0.0069
Three Co-60 sources at x=-10m, x=0 m and x=10m		
Cylinder	16.6367 E-08	0.0008
Right base	8.9236 E-08	0.0061
Left base	8.9922 E-08	0.0060

Table 7.3: Photon flux measurements when an extra sources are used.

- Other sources:

Source at (0,0,0) that emmits one photon of energy 1.332+1.173=2.505 MeV		
Surface	***Total Surface Flux (#/cm^2)***	***Relative error***
Cylinder	2.86875 E-08	0.0008
Right base	1.14596 E-08	0.0081
Left base	1.14364 E-08	0.0078
Source at (0,0,0) that emmits one photon of energy 5 MeV		
Cylinder	2.87121 E-08	0.0009
Right base	1.15031 E-08	0.0080
Left base	1.15612 E-08	0.0079

Table 7.4: Fluxes when other sources are used

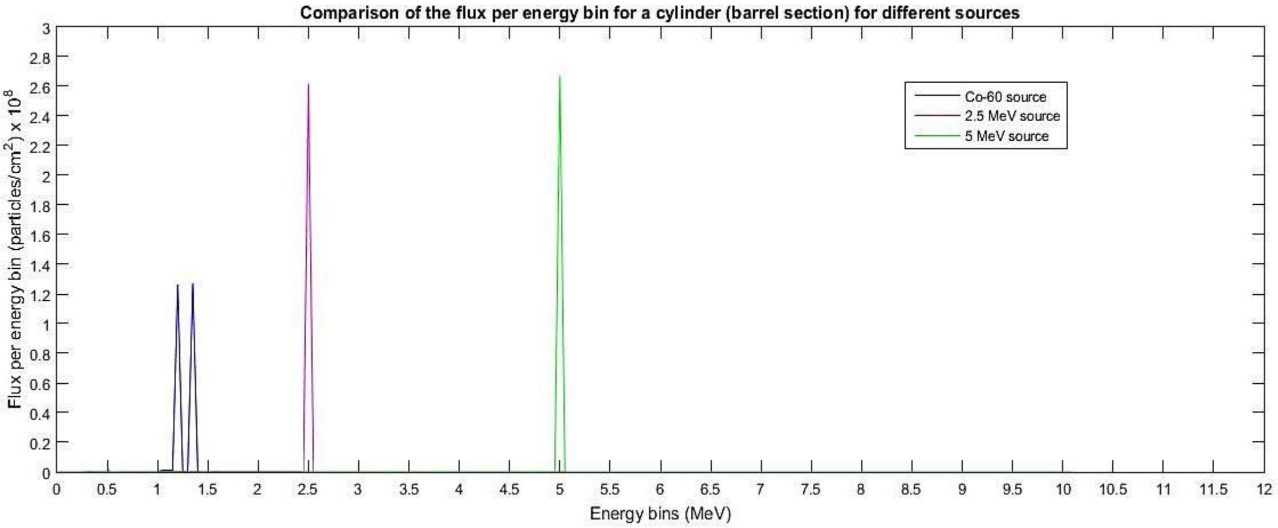

Figure 7.5: Comparison of the flux spectra per energy bin for the Co-60 source, the 2.5 MeV source and the 5 MeV source. Obviously, peaks are expected at the energies of the source particles and practically, the spectrum is relocated, when the energy of the source particles increases. [Matlab]

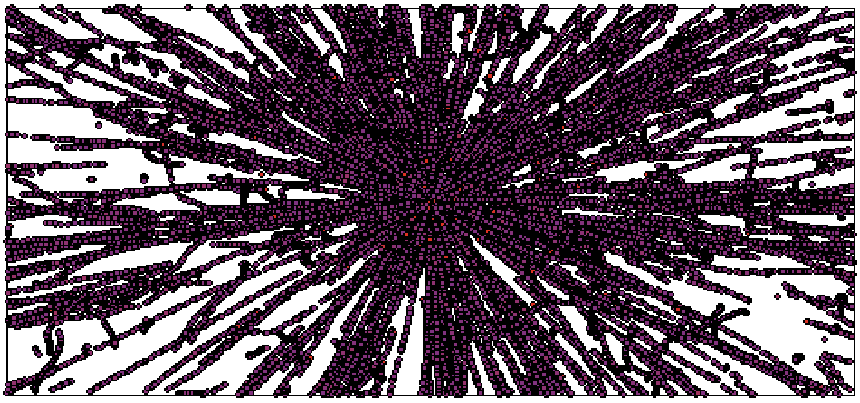

Figure 7.6: Particle tracks from a 30 MeV source placed at (0,0,0) and their tracks after collision. 73468 points were plotted. minimum energy used = 0.1000E-08 maximum energy used = 0.1000E+04, minimum energy found >1.e-9=0.1000E-02, maximum energy found = 0.3000E+02, blue for minimum, red for maximum. [Vised]

Figure 7.7: Particle tracks from a 10 MeV source placed at (2000,0,0) and their tracks after collision. 58522 points were plotted. [Vised]

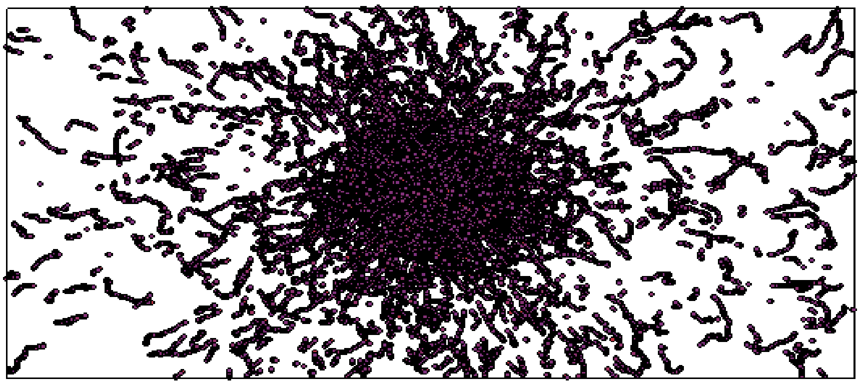

Figure 7.8: Particle tracks from three Co-60 sources placed at (-20,0,0), (0,0,0),(20,0,0) respectively and their tracks after collision. 85403 were points plotted. [Vised]

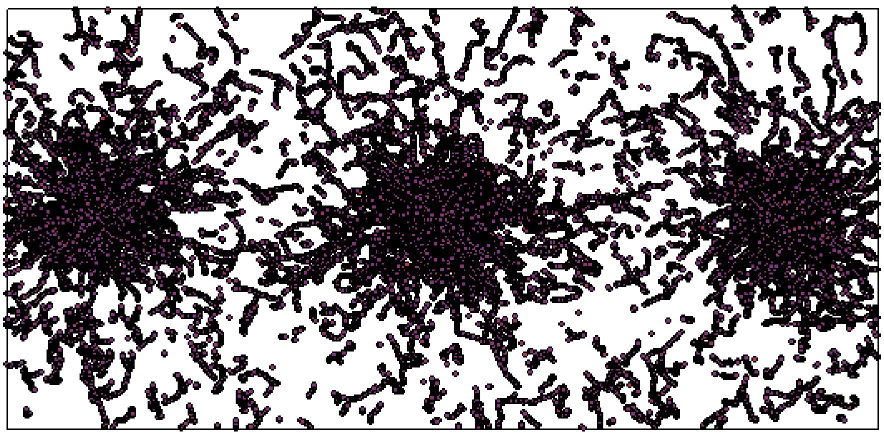

Figure 7.9: Particle tracks from three Co-60 sources placed at (-2000,0,0), (0,0,0),(2000,0,0) respectively and their tracks after collision. 84568 points were plotted. [Vised]

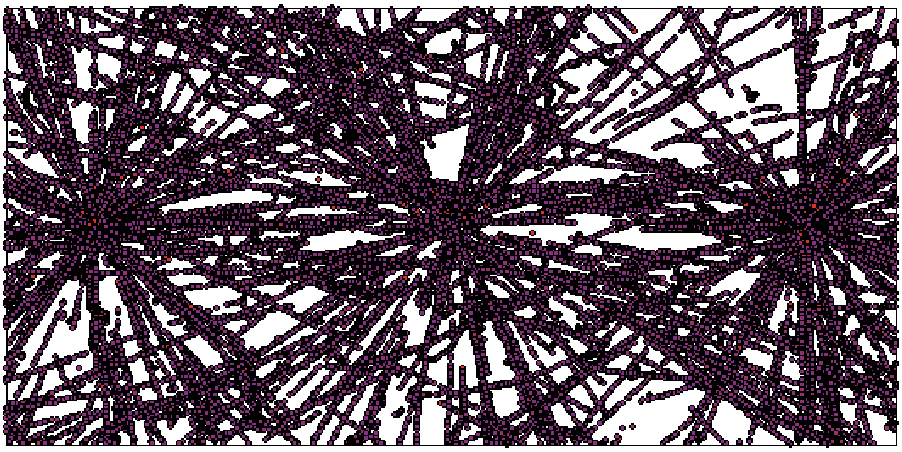

Figure 7.10: Particle tracks from three 30 MeV sources placed at (-2000,0,0), (0,0,0), (2000,0,0) respectively and their tracks after collisions. 75097 points were plotted. [Vised]

If we consider sources placed closely on the x-axis, a line source occurs. The total flux depends of the total number of source particles, given that each source emmits one photon of energy 5 MeV. So, the resulting flux depends on how many sources it is supposed to be placed in order to obtain approximately a continuous line and the total flux is multiplied accordingly. This line source can represent a beam on the cylinder axis.

Line source of energy 5 MeV from x=-25m to x=25m (uniform probability)		
Surface	***Surface Flux per source particle(#/cm^2)***	***Relative error***
Cylinder	2.50906 E-08	0.0011
Right base	3.69682 E-08	0.0071
Left base	3.71622 E-08	0.0069

Table 7.5: Flux when a line source is used

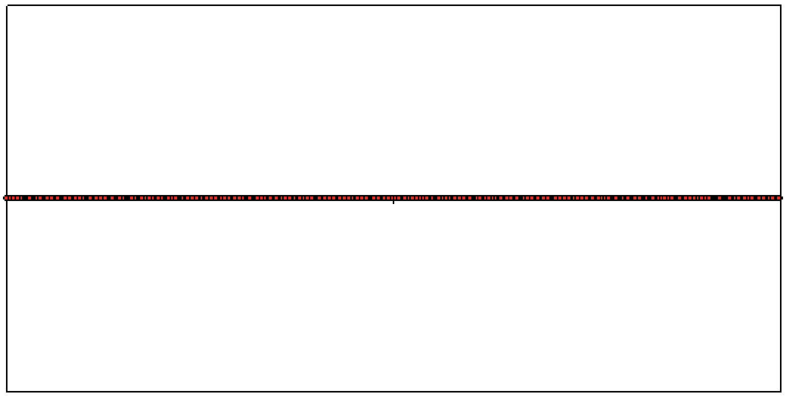

Figure 7.11: Line source of energy 5 MeV. The even distribution of the source can be confirmed. [Vised]

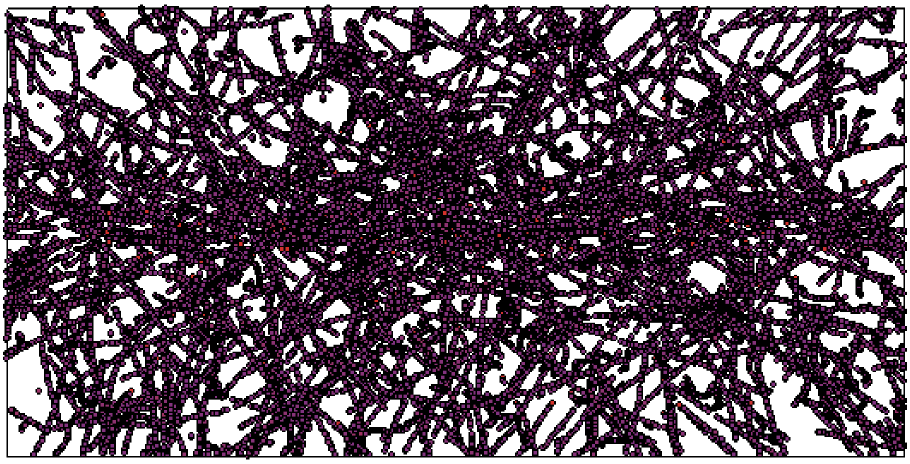

Figure 7.12: Tracks after collisions from particles emmited from a line source of energy 5 MeV. [Vised]

Moreover, a volume source equal to the volume of the cylinder (radius 12.5m , length 50 m) was used. Photons emit following uniform probability. According to the previous case, the total flux depends on how many sources are placed into the cylindrical volume.

Cylindrical source of energy 5 MeV length 50m, radius 12.5 m		
Surface	***Surface Flux per source particle(#/cm^2)***	***Relative error***
Cylinder	3.60612 E-08	0.0016
Right base	3.09944 E-08	0.0072
Left base	3.07619 E-08	0.0071

Table 7.6: Flux when a cylindrical source is used

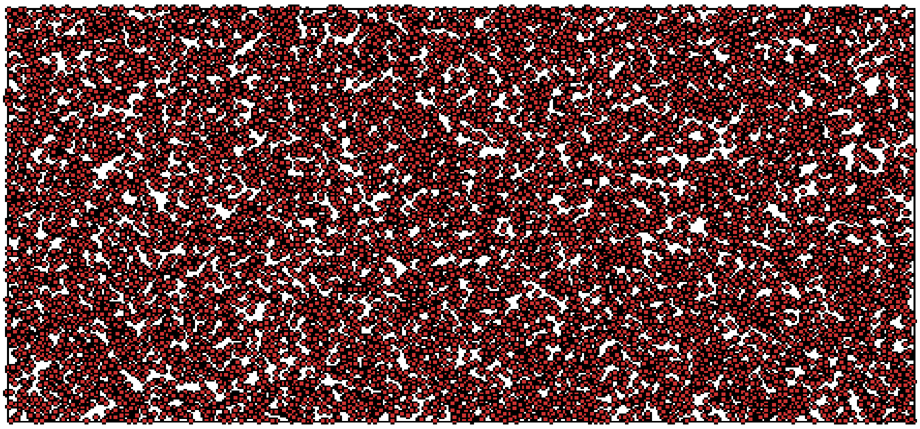

Figure 7.13: Distribution of source particles emmited from the cylindrical source. 16363 points plotted, minimum energy used = 0.1000E-08 maximum energy used = 0.1000E+04 minimum energy found >1.E-9 = 0.5000E+01, maximum energy found = 0.5000E+01, blue for minimum, red for maximum. The even distribution of the source can be confirmed. [Vised]

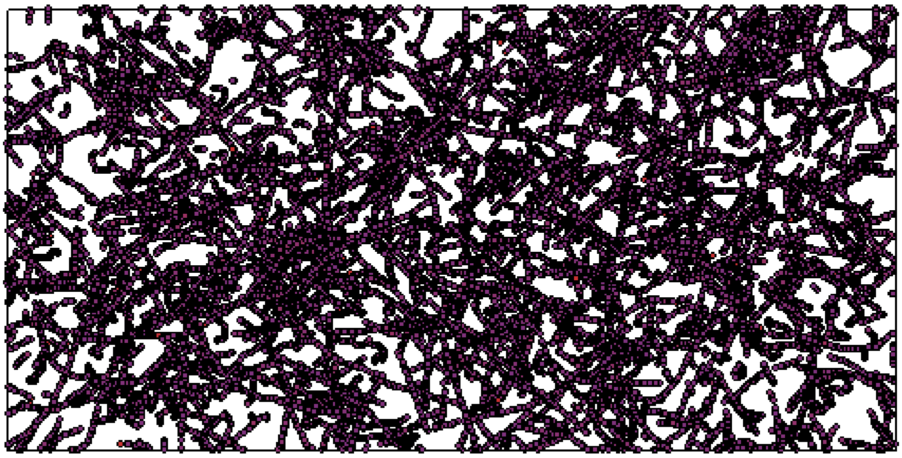

Figure 7.14: Particle tracks (collisions) for the aforementioned source. 60176 points were plotted. [Vised]

Considering all the above, the flux on each surface, when simulating a cylinder filled with air, depends strongly on the number of emmited source particles and not on the energy of these particles, which relocates the flux spectrum. Regarding the energy of the source particles, it is also observed that more energetic particles form straighter tracks and they can travel further. The number of the existing sources can be a very influencing factor, when the relocation of the source can influence slightly only the fluxes on the the approaching surfaces.

In different materials the energy of the source influences the induced flux on surfaces.

7.2. ATLAS DESIGN AND SIMULATION

The simulated ATLAS geometry was based mainly on the following geometry consisted of coaxial cylinders.

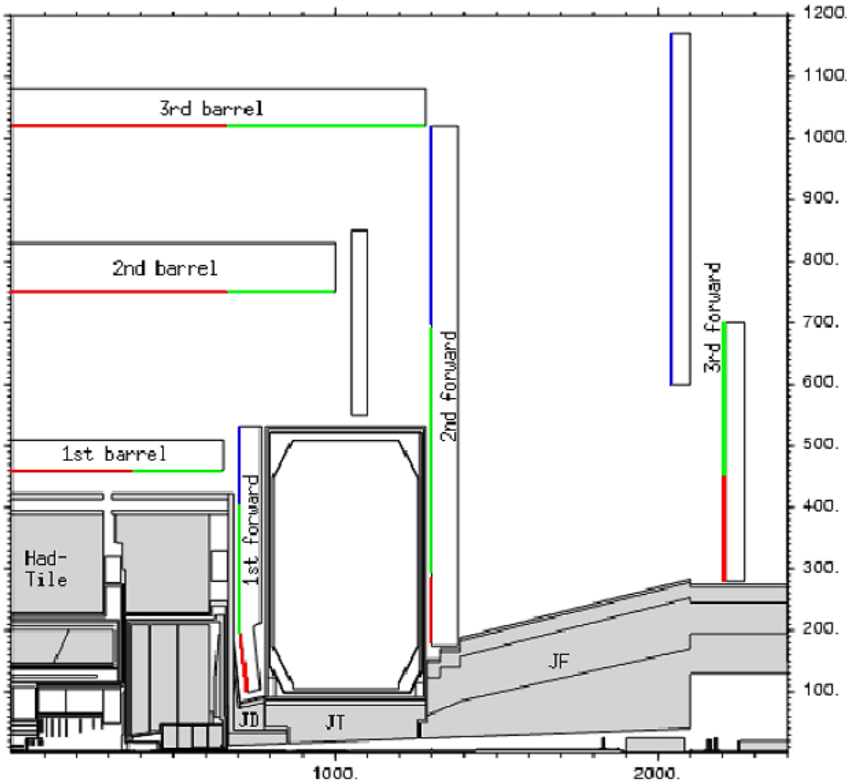

Figure 7.15: One quadrant of the ATLAS detector [48]

The use of cylindrical MCNP macrobodies considered to be the most suitable and easiest choice to represent this geometry.

7.2.1. DIMENSIONS OF THE ATLAS GEOMETRY

- ***Beampipe***:
    - **Region1:** z=[-355, 355]cm , r=2.9 cm, wall = 2.98 cm (beryllium).
    - **Region2:** z= [-1046.5,-355]cm & z=[355, 1046.5] cm, r=2.9 cm, wall = 2.98 cm (stainless steel).
    - **Region 3:** z= [-1050.7,- 1046.5]cm & z=[1046.5, 1050.7] cm, r = 4cm, wall = 4.1 cm (stainless steel).
    - **Region 4:** z= [-1441.6,- 1050.7]cm & z=[1050.7, 1441.6] cm, r = 6 cm, wall = 6.15 cm (stainless steel).
    - **Region 5:** z= [-1888, -1441.6] cm & z = [1441.6, 1888] cm, r=1.7 cm wall = 3 cm (copper).

- ***Inner Detector***: z=[-309.2, 309.2] cm, r=110.6 cm.

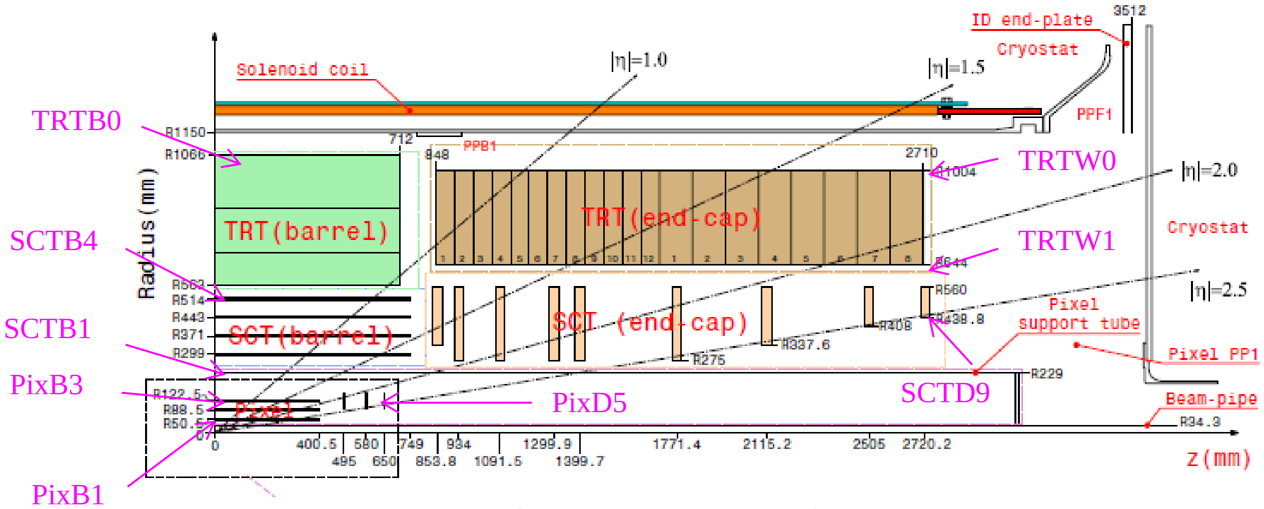

Figure 7.16: Cross section of a detailed geometry of the ID. The various areas in the ID where fluxes have been measured are also indicated. [31]

Envelopes	*Z (cm)*	*R (cm)*
Pixel	309.2	4.55-24.2
SCT barrel	80.5	25.5-54.9
SCT end – cap	81-279.7	25.1-61
TRT barrel	78	55.4-108.2
TRT end - cap	82.7-274.4	61.7-110.6

Table 7.7: Dimensions of the different areas of the Inner Detector [31]

- ***EM Calorimeter (Barrel):*** z=[-309.2, 309.2] cm, r=200 cm around the ID.
- ***Forward Calorimeter***: z=[500,600] cm and symmetrically for z<0, r=25 cm.
- ***EM-Had Calorimeter***: z=[350, 650] cm and symmetrically for z<0, r=200 cm around the FCal.
- ***Hadronic Calorimeter Barrel***: z=[-309.2,309.2] cm, r=400 cm around EM Cal.
- ***Hadronic Calorimeter End-cups***: z=[350,650] cm and symmetrically for z<0, r=400 cm around EM-Had.

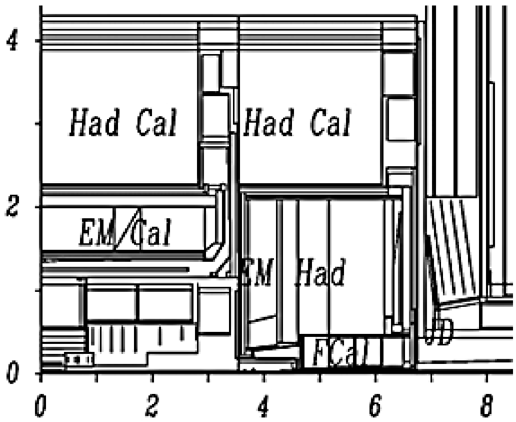

Figure 7.17: Geometry of the Calorimeters around the ID. [48]

- ***Shielding Regions, TAS and Magnets***:
- ***JT Cu Shielding***: z=[800, 1300] cm and symmetrically for z<0, r=50 cm.
- ***JD Shielding***: z=[650, 800] cm and symmetrically for z<0, r=50 cm.
- ***JF Iron Shielding 1***:z=[1300, 1800] cm, r=100 cm.
- ***TAS***: z=[1888, 2188] cm, r=20 cm
- ***Quadrupole:*** z=[2200, 2400] cm, r=20 cm
- ***JF Iron Shielding 2***: z=[1800, 2188] cm, r=200 cm around TAS.
- ***JF Iron Shielding 3***:z=[2188, 2400] cm, r=100 cm.
- ***JN Shielding 1***: z=[2188, 2300] cm, r=250 cm around JF.
- ***JN Shielding 2***: z=[2388, 2400] cm, r=300 cm around JF.
- ***Superconducting Magnet***: z=[800, 1300] cm and symmetrically for z<0, r=500 cm around JT Cu Shielding.

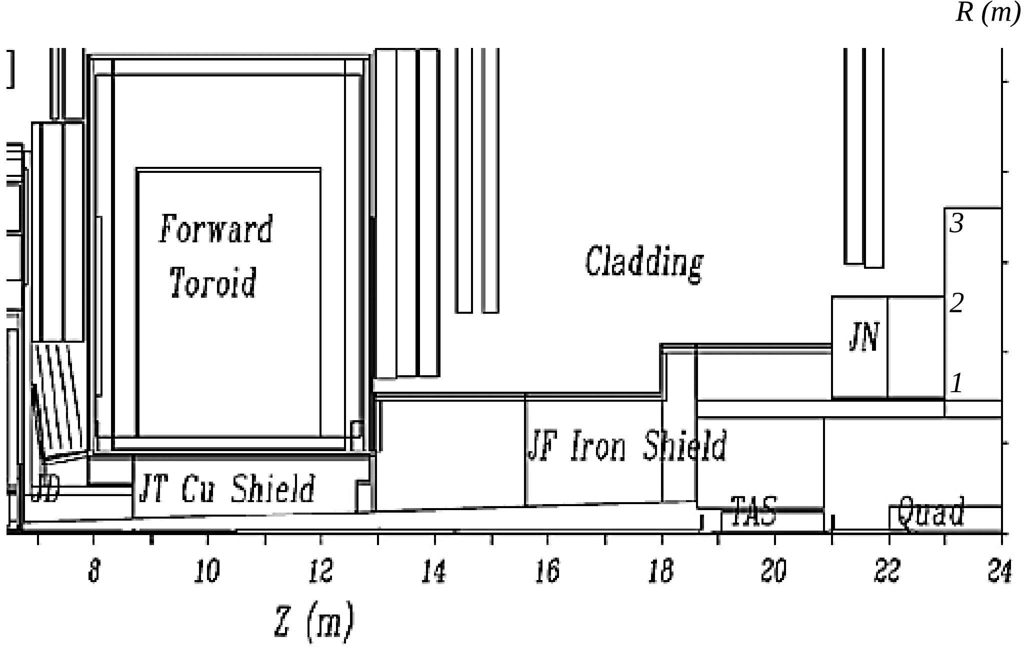

Figure 7.18: Geometry of the shielding, the TAS collimator, the Forward Toroid and the quadrupole. [48]

- ***Muon Spectrometer***

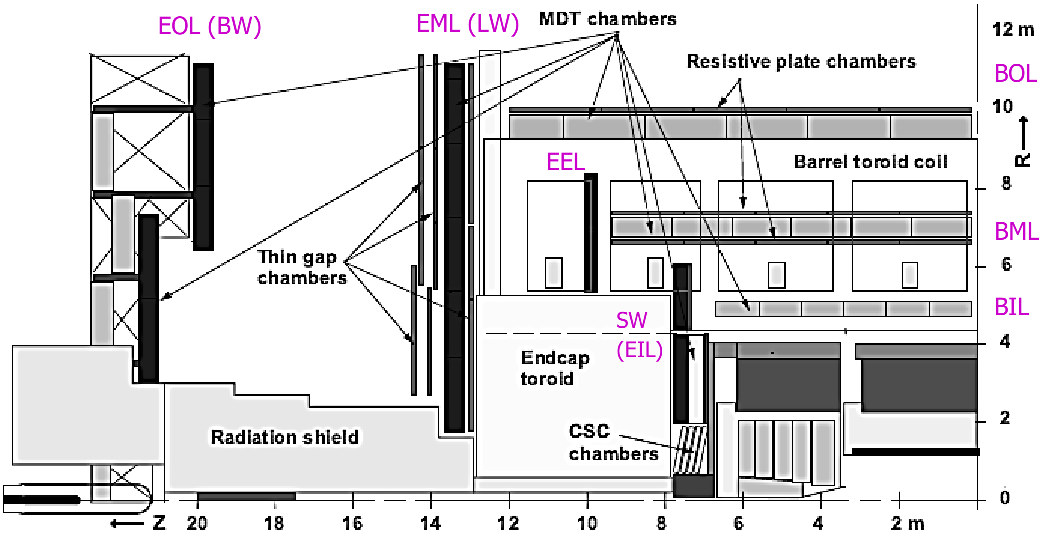

Figure 7.19: Detailed geometry of the muon spectrometer [26]

- ***CSCs***: z=[650, 800] cm, r=[50, 200] cm around JD Shileding.
- ***Small Wheel (EIL)***: z=[650, 800] cm and symmetrically for z<0, r=600 cm around CSCs.
- ***Muon Inner Barrel (BIL):*** z=[-650, 650] cm, r=[500, 550] cm, wall 0.04 cm.
- ***Muon Medium Barrel (BML):*** z=[-900, 900] cm, r=[700, 750] cm, MDTs as above.
- ***RPCs (outside BML):*** z=[-900, 900] cm, r=[680, 770] cm around BML
- ***Muon Outer Barrel (BOL):*** z=[-1200, 1200] cm, r=[920, 970] cm.
- ***RPCs (BOL):*** z=[-1200, 1200] cm, r=[920, 990] cm.
- ***Muon End Cap (EEL):*** z=[1000, 1075] cm, r=[600, 900] cm.
- ***Muon Medium End Cap (EML):*** z=[1300, 1380] cm, r=[120, 1100] cm.
- ***TGCs 1 (EML):*** z=[1390, 1400] cm, r=[200, 1200] cm.
- ***TGCs 2 (EML):***z=[1410, 1420] cm, r=[200, 1200] cm.
- ***Muon Outer End Cap 1 (EOL):***z=[1800, 1850] cm, r=[600, 1200] cm.
- ***Muon Outer End Cap 2 (EOL):***z=[2100, 2150] cm, r=[250, 500] cm.
- ***ATLAS cylinder***: z=[-2400, 2400] cm, r=1250 cm.
- ***ATLAS cavern***: Rectangular parallelepiped (3500 x 5500 x 4000 cm)

7.2.2. SELECTION OF THE MATERIALS

The *materials* used for each subsystem are listed below: [49]

- ***Beampipe***
  - ***Inner Beampipe:*** Vacuum
  - ***Beampipe Walls***:

1. Beryllium Be-4, (4000, weight fraction 1), Density (g/cm^3) =1.848000

2. Stainless steel 202: Density (g/cm^3) =7.860000

Element	**Photon ZA**	**Neutron ZA**	**Weight Fraction**	**Atom Fraction**	**Atom Density**
C	6000	6000	-0.000750	0.003405	0.000296
N	7000	7014	-0.001250	0.004866	0.000422
Si	14000	14000	-0.005000	0.009708	0.000843
P	15000	15031	-0.000300	0.000528	0.000046
S	16000	16000	-0.000150	0.000255	0.000022
Cr	24000	24000	-0.180000	0.188773	0.016386
Mn	25000	25055	-0.087500	0.086851	0.007539
Fe	26000	26000	-0.675050	0.659160	0.057217
Ni	28000	28000	-0.050000	0.046454	0.004032

Table 7.8: Composition of the Stainless Steel 202 [49]

3. Copper Cu-29 (29000 weight fraction 1), Density (g/cm^3) = 8.960000

- ***Inner Detector***:
    - ***Pixel***: silicon Si-14,(14000, weight fraction 1), Density (g/cm^3) =2.330000
    - ***SCT:*** silicon Si-14,(14000, weight fraction 1), Density (g/cm^3) =2.330000
    - ***TRT***: xenon Xe-54, (54000, weight fraction 1),Density (g/cm^3) = 0.005485
- ***EM calorimeter***: lead Pb-82 (82000, weight fraction 1), Density (g/cm^3) =11.350000
- ***Hadronic Calorimeter:*** Stainless Steel
- ***CSCs:*** Argon Ar-18 (18000, weight fraction 1), Density (g/cm^3) = 0.001662
- ***Muon Spectrometer***: aluminium wall Al-13, for photons (13000,weght fraction 1), for neutrons (13027,weght fraction 1), Density (g/cm^3) = 2.698900
- ***MDTs (BIL)***: Argon Ar-18
- ***RPCs***: 1,1,1,2 tetrafluroethane
- ***CSCs***: Argon Ar-18
- ***TGCs***: Co_2 , for photons C (6000, weight fraction 0.272912), O (8000, weight fraction 0.727088), for neutrons C (6000, weight fraction 0.272912), O (8016, weight fraction 0.727088), Density (g/cm^3) = 0.001842
- ***Superconducting Magnets***: Titanium Alloy Grade 5, (simulating the actual Nb-Ti alloy), Density (g/cm^3) = 4.430000

Element	**Photon ZA**	**Neutron ZA**	**Weight Fraction**	**Atom Fraction**	**Atom Density**
H	1000	1001	-0.000110	0.004953	0.000291
C	6000	6000	-0.000570	0.002154	0.000127
N	7000	7014	-0.000210	0.000680	0.000040
O	8000	8016	-0.001410	0.004000	0.000235
Al	13000	13027	-0.061250	0.103023	0.006056
Ti	22000	22000	-0.893630	0.847256	0.049805
V	23000	23000	-0.040000	0.035635	0.002095
Fe	26000	26000	-0.002830	0.002300	0.000135

Table 7.9: Composition of the Titanium Alloy [49]

- ***TAS collimator***: Copper Cu-29 (29000 weight fraction 1), Density (g/cm^3) = 8.960000
- ***Quadrupole***: Titanium Alloy Grade 5, (simulating the actual Nb-Ti alloy), Density (g/cm^3) = 4.430000
- ***JD Shielding***: Stainless Steel 202
- ***JF Shielding***: Iron Fe-26 (26000 weight fraction 1), Density (g/cm^3) = 7.874
- ***JT Shielding***: Copper Cu-29
- ***JN Shielding***: Cast Iron, Density (g/cm^3) = 7.150000

Element	***Photon ZA***	***Neutron ZA***	***Weight Fraction***	***Atom Fraction***	***Atom Density***
C	6000	6000	-0.034000	0.137104	0.012189
Si	14000	14000	-0.026000	0.044836	0.003986
P	15000	15031	-0.003000	0.004691	0.000417
S	16000	16000	-0.001000	0.001510	0.000134
Mn	25000	25055	-0.006500	0.005730	0.000509
Fe	26000	26000	-0.929500	0.806128	0.071667

Table 7.10: Composition of the Cast Iron. [49]

7.2.3. PHOTON FLUXES ON SURFACES

Photon fluence rates (flux rates per second) for various regions of the ATLAS detector have been collected by FLUKA AV16 and GCALOR simulations.

- Inner Detector:

Region	***R(cm)***	***Z(cm)***	***Flux (#/cm^2)>30keV (FLUKA)***	***Flux (#/cm^2) (GCALOR)***	***FLUKA/GCALOR***
PixB1	4.2	0-40.7	45764 E+03	309 E+05	1.48
PixB3	12.7	0-40.7	9147 E+03	963 E+04	0.95
PixD5	9.9-16	77	8329 E+03	129 E+05	0.65
SCTB1	30	0-75	4403 E+03	458 E+04	0.96
SCTB4	52	0-75	3905 E+03	375 E+04	1.04
SCTD9	44-56	272	7582 E+03	772 E+04	0.98
TRTW1	48	324-332	12596 E+03	105 E+05	1.20
TRTW0	104	324-332	5651 E+03	43 E+05	1.31
TRTB0	108	0-76	243 E+04	241 E+04	1.01

Table 7.11: Fluxes in the various regions of the Inner Detector. Statistical uncertainties are typically less than 10%. [48]

- Calorimeters:

Given that an LHC year = 120 days = 10.368.000 sec.

Region	***Fluence/cm^2/year***	***Flux (#/cm^2) (GCALOR)***
Lar Barrel	0.378E+11	3645.83
Lar End - Cap	0.384E+10	370.37
Tile Low z region	0.226E+09	2.18
Tile mid z region	0.615E+10	593.17
Tile Cal	0.545E+10	525.66

Table 7.12: Fluxes in the various regions of the Calorimeters. [48]

- Muon Spectrometer:

Region	***Photon flux (#/cm^2)***	***Average flux per region***
Muon Barrel		
Inner Barrel		
MDT IN low-z	1.00E+03	1.1E+03
MDT IN mid-z	1.10E+03	
MDT IN high-z	1.20E+03	
Middle Barrel		
RPC MID low-z	1.00E+03	1.17E+03
RPC MID mid-z	1.10E+03	
RPC MID high-z	1.40E+03	
Outer Barrel		
RPC OUTER low-z	1.10E+03	1.30E+03
RPC OUTER mid-z	1.30E+03	
RPC OUTER high-z	1.50E+03	
Muon End - Cap		
Small Wheel Region		
SW MDT OUT	2.40E+03	10.76E+03
SW MDT MID	5.40E+03	
SW MDT IN	11.00E+03	
SW TGC	10.00E+03	
SW CSC	25.00E+03	
Large Wheel Region		
LW MDT OUT	1.70E+03	5.7E+03
LW MDT MID	4.40E+03	
LW MDT IN	11.00E+03	
Back Wheel Region		
BW MDT OUT	0.80E+03	1.17E+03
BW MDT MID	1.20E+03	
BW MDT IN	1.50E+03	

Table 7.13: Fluxes in the various regions of the Muon Spectrometer [48]

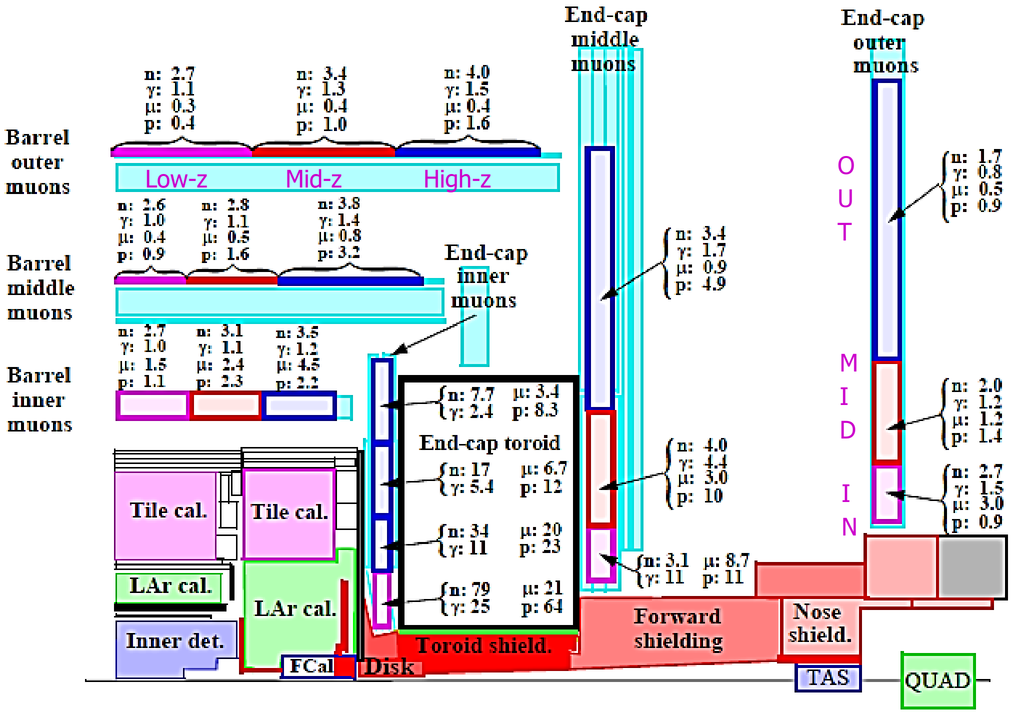

Figure 7.20: Particle fluxes in the various muon spectrometer stations at high luminosity 10^{34} $cm^{-2}\,s^{-1}$. Neutron and photon fluxes in units of kHz/cm^2, muon and proton fluxes in Hz/cm^2. [GCALOR]. [48]

7.2.4. SIMULATION RESULTS FOR THE ATLAS DETECTOR

Geometry

Every geometry is depictured via the MCNP Visual Editor (Vised). Vised uses a different color for each material. The design process begins with the beampipe:

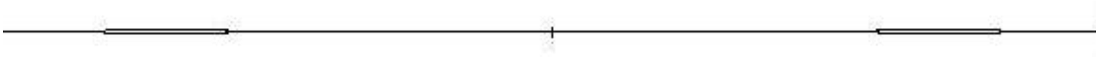

Figure 7.21: Design of the ATLAS beampipe

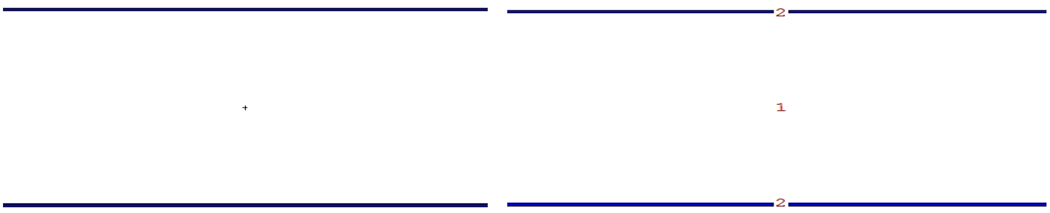

Figure 7.22: Zoom towards the IP. The material of the wall (beryllium) is indicated with blue color. Vacuum in the inside is indicated with white. The numbers of cells can be shown on the right.

The simulation continues by designing the ID subsystems around the beampipe. Vised uses dark pink for air, light blue for silicon and orange for xenon:

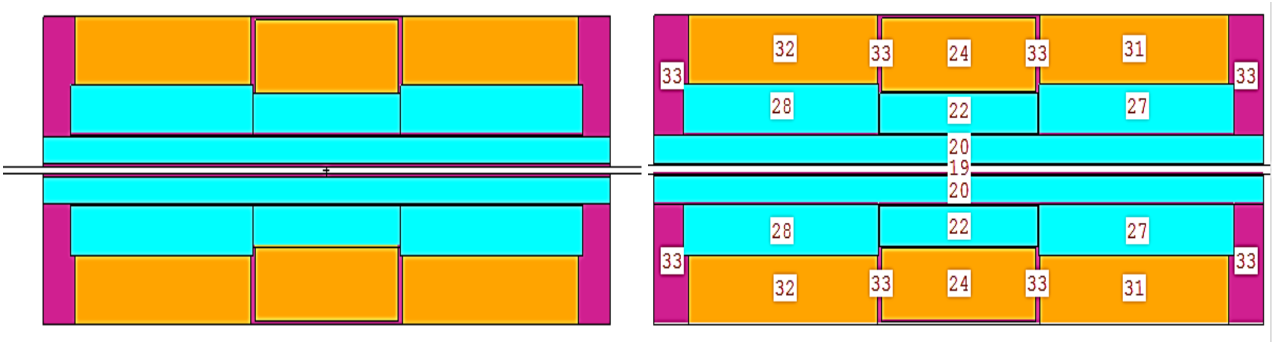

Figure 7.23: Design of the Inner detector subsystems.

Around the ID, the Calorimeters are designed:

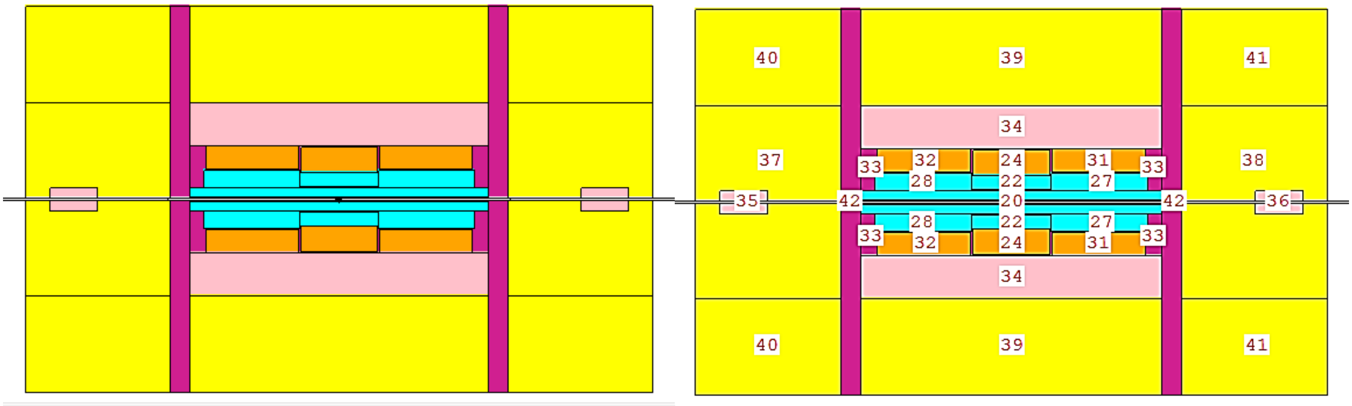

Figure 7.24: Design of the Calorimeters. Light pink is used for the lead and yellow for the stainless steel.

Afterwards, the easiest element to be applied is the shielding. JD shielding is indicated by yellow color, as it is made of stainless steel. Vised uses light green for the copper (JT, TAS), purple for the iron, dark red for the cast iron and grey for the alloy.

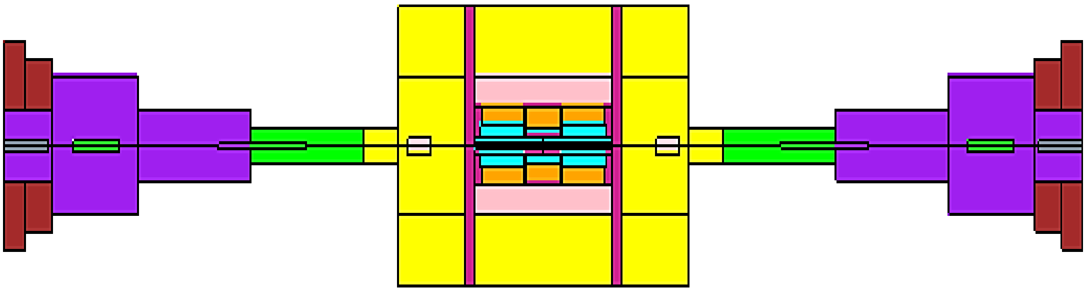

Figure 7.25: ATLAS beampipe, ID, Calorimeters and Shielding.

The muon subsystems can be added now. The first barrel station contains MDTs ,which are simulated as below:

Figure 7.26: MDTs for the BIL.

MDTs consist mainly of argon, which Vised represents with this light grey color. The walls of the MDTs can be discriminated if the picture is zoomed:

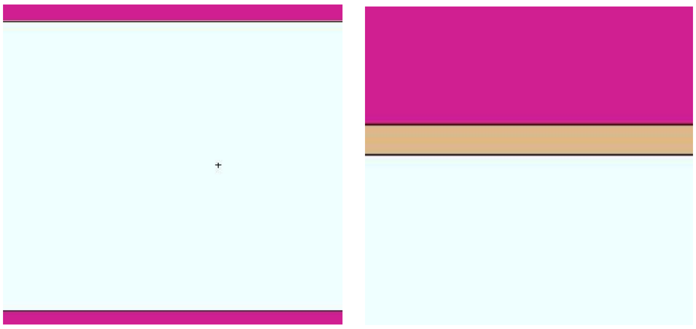

Figure 7.27: Zoomed aspect of the BIL station. The wall of the MDTs made of aluminium is represented by light brown.

The second station BML contains also RPCs around the MDTs. RPCs, made of tetrafluroethane, are indicated by light green:

Figure 7.28: RPCs and MDTs for the BML.

Muon barrel stations, as well as the small wheels and the muon end caps (EEL) are shown in the following picture:

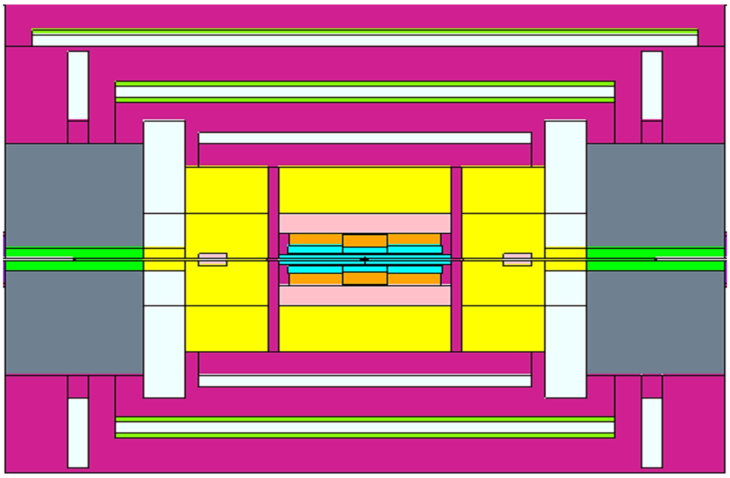

Figure 7.29: Muon barrel stations, SW and EEL.

The end – cap stations are also designed. TGCs in the EML, containing mainly Co_2 , are represented by pink:

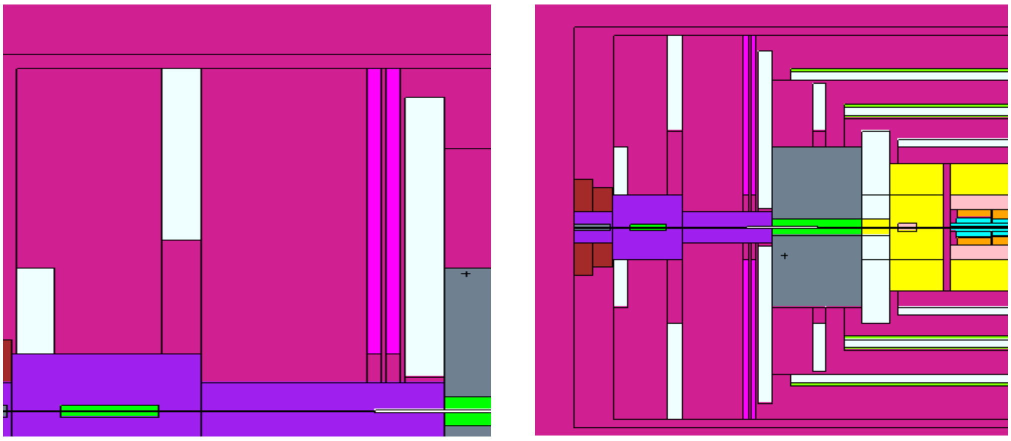

Figure 7.30: Left: Muon end – cap stations. Right: half of the ATLAS detector, where all the muon stations are shown.

Finally, the whole of the ATLAS detector with its cavern is designed:

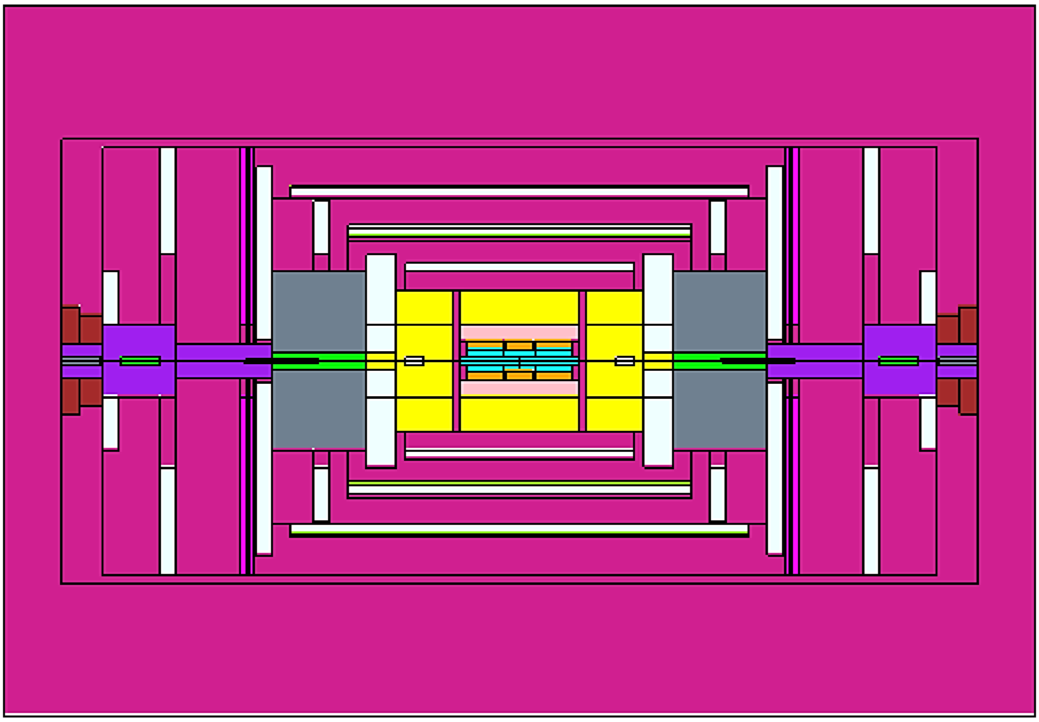

Figure 7.31: The ATLAS detector with its cavern.

7.2.5. ANALOG SIMULATION

Sources

An analog simulation can be conducted by placing simple sources within the ATLAS geometry. Particularly, two simulations with different sources were carried out; a point source of 100 MeV and a cylindrical source extended from -2500 cm to 2500 cm with a radius of 2.9 cm and energy 100 MeV, both emmiting photons were used. These simulations used 30 minutes of CPU time.

- **Simulation 1:** 100 MeV point photon source

Following the logic of simulating particles emmiting from a p-p interaction as a solid source placed at the origin. The energy of the source is set at 100 MeV, which is the upper energy limit that MCNP allows and represents the highest possible energy of background particles.

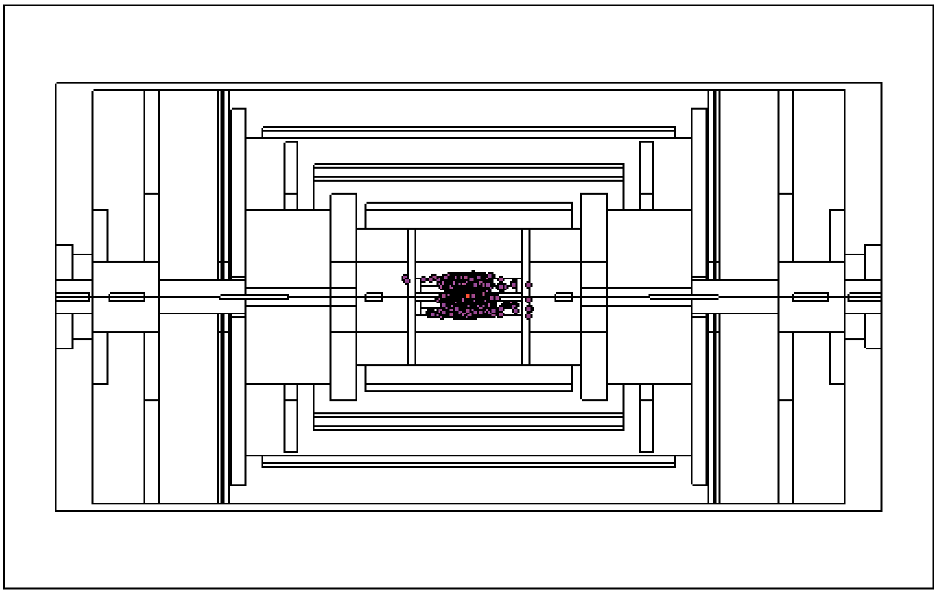

Figure 7.32: Particles after collision (purple) are observed in the regions of the Inner Detector and slightly in Calorimeter regions. No particles are observed further.

The number of particles after collision decreases dramatically when moving outwardly, due to the larger distances they have to travel without undergoing attenuation processes and also because of the absorbing capacities of the materials. Although the result of the simulation can be considered as logical, a different approach ought to be used in order to get more precise results.

- **Simulation 2:** 100 MeV cylindrical photon source

A different approach includes the placement of a cylindrical source imitating beamlike background particles in the beampipe.

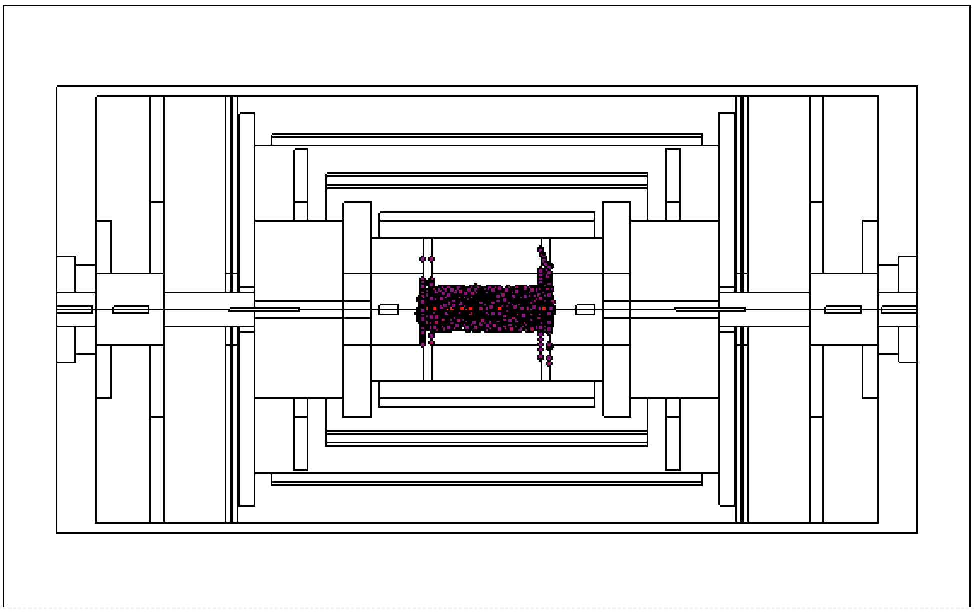

Figure 7.33: Particles after collision (purple) are observed in the regions of the Inner Detector and slightly in Calorimeter regions. No particles are observed further. The distribution of the particles is very similar as above.

The low number of particle histories prevents a more accurate simulation, so a different running period must be chosen.

Tallies

A large quantity of source particles is considered.

- ***F2 tallies:*** F2 tallies were placed on certain critical surfaces. The simulations were run for 24 hours (1440 minutes) in order to minimize the statistical errors. 10E+11 source particles were counted. All cell importances were set to 1.

	Regions	***Photon flux on surface Cylindrical source***	***Ratio (GCALOR/MCNP)***
1	Pixel PixB1	50156 E+03	0.912
2	Pixel PixB3	23018 E+03	0.397
3	SCT SCTB1	24414 E+03	0.18
4	SCT SCTB4	7919 E+03	0.49
5	TRT TRTB0	5444 E+03	0.446
6	SCT SCTD9	9705.6 E+03	0.78
7	TRT TRTW1	6648.3 E+03	1.89
8	LAr Barrel	314.222 E+03	0.012
9	LAr End-cap	1.0456 E+03	0.35
10	Tile Cal	12.1426 E+03	0.04
11	MDT IN	8.7912 E+03	0.125
12	MDT MID	4.0772 E+03	0.29
13	RPC OUT	2.3325 E+03	0.557
14	Small Wheel	1.3571 E+03	7.923

15	End-cap middle	2.6213 E+03	2.17
16	End-cap outer	0.9639 E+03	1.21

Table 7.14: Photon fluxes on various surfaces of the ATLAS detector in comparison with measurements.

- **F4 tallies:** Cell flux tallies were placed in critical areas of the ATLAS geometry. Symmetrical regions were ignored, as well as areas filled with air, which represent gaps between the various components of the detector or cells for geometry simplification. 1440 minutes of CPU time were used.

No	***Cell Number (MCNP code)***	***Cell***	***Flux in cell***
1	1	Beampipe 1	23111900
2	2	Wall 1	23367800
3	3	Beampipe 2	756148
4	5	Wall 2	771706
5	7	Beampipe 3	0
6	9	Wall 3	0
7	11	Beampipe 4	0
8	13	Wall 4	0
9	15	Beampipe 5	0
10	17	Wall 5	0
11	20	Pixel Detector	16825600
12	22	SCT barrel	7226700
13	24	TRT barrel	3457780
14	27	SCT end - caps	6290040
15	31	TRT end - caps	3084020
16	34	EM Calorimeter Barrel	172794
17	35	Forward Calorimeter	1309
18	37	EM-Had Calorimeter	215067
19	39	Hadronic Calorimeter Barrel	56939
20	40	Hadronic Calorimeter End-caps	15122
21	43	JD shielding	43
22	45	JT Cu Shielding	11
23	47	JF Iron Shielding -1-	2.5
24	49	TAS collimator	0
25	51	Quad	0
26	53	JF Iron Shielding -2-	10.1
27	55	JF Iron Shielding -3-	0
28	57	JN Shielding -1-	7.14
29	59	JN Shielding -2-	9.2
30	61	Superconducting Magnet	43
31	63	CSC	194.6
32	65	Small Wheel (EIL)-MDT	609
33	66	Small Wheel (EIL)-inside	6030
34	67	Small Wheel (EIL)-MDT	674

35	72	Muon Inner Barrel (BIL)-MDT	5054
36	73	Muon Inner Barrel (BIL)-inside	4512
37	74	Muon Inner Barrel (BIL)-MDT	4407
38	76	RPCs (BML)	2414
39	77	Muon Medium Barrel (BML)-MDT	2374
40	78	Muon Medium Barrel (BML)-inside	2230
41	79	Muon Medium Barrel (BML)-MDT	2217
42	80	RPCs (BML)	2074
43	82	Muon Outer Barrel 1 (BOL)-MDT	1374
44	83	Muon Outer Barrel 1 (BOL)-inside	1272
45	84	Muon Outer Barrel 1 (BOL)-MDT	1323
46	85	RPCs (BOL)	1209
47	88	Muon End Cap (EEL) -MDT	449.6
48	89	Muon End Cap (EEL)-inside	342
49	90	Muon End Cap (EEL) –MDT	320
50	96	Muon Medium End Cap (EML)-MDT	167
51	97	Muon Medium End Cap (EML)-inside	156
52	98	Muon Medium End Cap (EML)-MDT	162
53	104	TGCs (EML) 1	159
54	108	TGCs (EML) 2	148
55	113	Muon Outer End Cap 1 (EOL) –MDT	80.7
56	114	Muon Outer End Cap 1 (EOL)-inside	72
57	115	Muon Outer End Cap 1 (EOL) –MDT	73.5
58	120	Muon Outer End Cap 2 (EOL)	22.7
59	121	Muon Outer End Cap 2 (EOL)	25
60	122	Muon Outer End Cap 2 (EOL)	31.6
61	150	ATLAS Cylinder	260

Table 7.15: Photon fluxes in various cells of the ATLAS detector.

7.2.6. NON ANALOG TECHNIQUES

For many deep penetration problems, such as the analysis of the ATLAS radiation background, a direct simulation (analog MCNP) would require far too many histories to achieve acceptable results with the computer time available. It is observed that very few of the source particles reach the detector or region used for the tally, i.e., most particles produce a zero score. For such cases, “tricks” must be employed to reduce the relative error of a tally or its variance for a fixed computing time, or to reduce the computing time to achieve the same relative error.

The number of particles reaching the tally region can often be dramatically increased by abandoning a strict analog simulation without changing the value of the tally. The solution is to assign each particle a weight, and, as the particle is artificially forced towards the scoring region, the particle weight is decreased in a manner such that the average of the particle weights reaching the detector is the same as the expected tally in a true analog simulation. Thus, if we make a certain event in a particle history m times more likely, we must multiply the particle's weight by 1/m to avoid biasing the tally expectation. [46]

7.2.6.1. GEOMETRY SPLITTING

In geometry splitting, importances are assigned to each cell in the problem. Typically, source cells should have an importance of unit and cells closer to the tally regions should have larger importances, so the cell importances should be adjusted so as to keep the population of particles in the cells relatively constant as one moves from the source region to the tally region. First, a short run of 10 minutes CPU time with all photon importances set to unity is performed, and the "cell population" was examined. Then, the cell importances can be estimated by the ratio of cell populations P in adjacent cells, i.e. $I_n \approx P_{n-1}/P_n$, P_{n-1} the inner cell.[46] A simple approach is used; the importance of each cell is calculated depending on only one previous neighbouring cell. The cells in which the ratio P_{n-1}/P_n <1, the importance is set to 1. The importance is zero only outside the ATLAS cavern. The reference cell 1 has importance=1.

Cell	*Population*	*Importances*			*Cell*	*Population*	*Importances*		
1	128			1	65	3	$I_{65} \approx P_{63}/P_{65}$	2.3333	2
2	133	$I_2 \approx P_1/P_2$	1.0391	1	66	4	$I_{66} \approx P_{63}/P_{66}$	1.7500	2
3	7	$I_3 \approx P_1/P_3$	18.2857	18	67	4	$I_{67} \approx P_{63}/P_{67}$	1.7500	2
4	4	$I_4 \approx P_1/P_4$	32	32	68	1	$I_{68} \approx P_{64}/P_{68}$	7	7
5	7	$I_5 \approx P_3/P_5$	1	1	69	1	$I_{69} \approx P_{64}/P_{69}$	7	7
6	4	$I_6 \approx P_4/P_6$	1	1	70	0	$I_{70} \approx P_{64}/P_{70}$	-	7
7	0	$I_7 \approx P_3/P_7$	-	18	71	26	$I_{71} \approx P_{39}/P_{71}$	515.308	515
8	0	$I_8 \approx P_4/P_8$	-	32	72	27	$I_{72} \approx P_{71}/P_{72}$	0.9630	1
9	0	$I_9 \approx P_7/P_9$	-	18	73	26	$I_{73} \approx P_{72}/P_{73}$	1.0385	1
10	0	$I_{10} \approx P_8/P_{10}$	-	32	74	26	$I_{74} \approx P_{73}/P_{74}$	1	1
11	0	$I_{11} \approx P_7/P_{11}$	-	18	75	27	$I_{75} \approx P_{74}/P_{75}$	0.9630	1
12	0	$I_{12} \approx P_8/P_{12}$	-	32	76	27	$I_{76} \approx P_{75}/P_{76}$	1	1
13	0	$I_{13} \approx P_{11}/P_{13}$	-	18	77	26	$I_{77} \approx P_{76}/P_{77}$	1.0385	1
14	0	$I_{14} \approx P_{12}/P_{14}$	-	32	78	27	$I_{78} \approx P_{77}/P_{78}$	0.9630	1
15	0	$I_{15} \approx P_{11}/P_{15}$	-	18	79	27	$I_{79} \approx P_{78}/P_{79}$	1	1
16	0	$I_{16} \approx P_{12}/P_{16}$	-	32	80	25	$I_{80} \approx P_{79}/P_{80}$	1.0800	1
17	0	$I_{17} \approx P_{15}/P_{17}$	-	18	81	30	$I_{81} \approx P_{80}/P_{81}$	0.8333	1
18	0	$I_{18} \approx P_{16}/P_{18}$	-	32	82	27	$I_{82} \approx P_{81}/P_{82}$	1.1111	1
19	175	$I_{19} \approx P_2/P_{19}$	1.3158	1	83	26	$I_{83} \approx P_{82}/P_{83}$	1.0385	1
20	3243	$I_{20} \approx P_{19}/P_{20}$	0.0540	1	84	27	$I_{84} \approx P_{83}/P_{84}$	0.9630	1
21	224	$I_{21} \approx P_{20}/P_{21}$	14.4777	14	85	26	$I_{85} \approx P_{84}/P_{85}$	1.0385	1
22	1481	$I_{22} \approx P_{21}/P_{22}$	0.1512	1	86	0	$I_{86} \approx P_{61}/P_{86}$	-	5
23	161	$I_{23} \approx P_{22}/P_{23}$	9.1988	9	87	1	$I_{87} \approx P_{62}/P_{87}$	4	4
24	390	$I_{24} \approx P_{23}/P_{24}$	2.4224	2	88	1	$I_{88} \approx P_{86}/P_{88}$	-	5
25	297	$I_{25} \approx P_{20}/P_{25}$	10.9192	11	89	1	$I_{89} \approx P_{86}/P_{89}$	-	5
26	255	$I_{26} \approx P_{20}/P_{26}$	12.7176	13	90	1	$I_{90} \approx P_{86}/P_{90}$	-	5
27	2196	$I_{27} \approx P_{25}/P_{27}$	0.1352	1	91	2	$I_{91} \approx P_{87}/P_{91}$	4	4

28	1799	$I_{28} \approx P_{26}/P_{28}$	0.1417	1	92	2	$I_{92} \approx P_{87}/P_{92}$	4	4
29	232	$I_{29} \approx P_{27}/P_{29}$	9.4655	9	93	1	$I_{93} \approx P_{87}/P_{93}$	4	4
30	189	$I_{30} \approx P_{28}/P_{30}$	9.5185	10	94	0	$I_{94} \approx P_{47}/P_{94}$	-	18
31	478	$I_{31} \approx P_{29}/P_{31}$	0.5335	1	95	0	$I_{95} \approx P_{48}/P_{95}$	-	32
32	409	$I_{32} \approx P_{30}/P_{32}$	0.4621	1	96	1	$I_{96} \approx P_{94}/P_{96}$	-	18
33	755	$I_{33} \approx P_{24}/P_{33}$	0.5166	1	97	1	$I_{97} \approx P_{94}/P_{97}$	-	18
34	37838	$I_{34} \approx P_{33}/P_{34}$	0.0200	1	98	0	$I_{98} \approx P_{94}/P_{98}$	-	18
35	0	$I_{35} \approx P_{5}/P_{35}$	-	7	99	5	$I_{99} \approx P_{95}/P_{99}$	-	32
36	0	$I_{36} \approx P_{6}/P_{36}$	-	4	100	5	$I_{100} \approx P_{95}/P_{100}$	-	32
37	6789	$I_{37} \approx P_{35}/P_{37}$	-	7	101	5	$I_{101} \approx P_{95}/P_{101}$	-	32
38	7320	$I_{38} \approx P_{36}/P_{38}$	-	4	102	0	$I_{102} \approx P_{47}/P_{102}$	-	18
39	13398	$I_{39} \approx P_{34}/P_{39}$	2.8242	3	103	0	$I_{103} \approx P_{48}/P_{103}$	-	32
40	1701	$I_{40} \approx P_{37}/P_{40}$	3.9912	4	104	1	$I_{104} \approx P_{102}/P_{104}$	-	18
41	1525	$I_{41} \approx P_{38}/P_{41}$	4.8000	5	105	2	$I_{105} \approx P_{103}/P_{105}$	-	32
42	734	$I_{42} \approx P_{34}/P_{42}$	51.5504	52	106	0	$I_{106} \approx P_{47}/P_{106}$	-	18
43	0	$I_{43} \approx P_{5}/P_{43}$	-	7	107	0	$I_{107} \approx P_{48}/P_{107}$	-	32
44	0	$I_{44} \approx P_{5}/P_{44}$	-	7	108	1	$I_{108} \approx P_{106}/P_{108}$	-	18
45	0	$I_{45} \approx P_{9}/P_{45}$	-	18	109	2	$I_{109} \approx P_{107}/P_{109}$	-	32
46	0	$I_{46} \approx P_{10}/P_{46}$	-	32	110	29	$I_{110} \approx P_{85}/P_{110}$	0.8966	1
47	0	$I_{47} \approx P_{17}/P_{47}$	-	18	111	0	$I_{111} \approx P_{53}/P_{111}$	-	18
48	0	$I_{48} \approx P_{18}/P_{48}$	-	32	112	0	$I_{112} \approx P_{54}/P_{112}$	-	32
49	0	$I_{49} \approx P_{17}/P_{49}$	-	18	113	0	$I_{113} \approx P_{111}/P_{113}$	-	18
50	0	$I_{50} \approx P_{18}/P_{50}$	-	32	114	0	$I_{114} \approx P_{111}/P_{114}$	-	18
51	0	$I_{51} \approx P_{17}/P_{51}$	-	18	115	0	$I_{115} \approx P_{111}/P_{115}$	-	18
52	0	$I_{52} \approx P_{18}/P_{52}$	-	32	116	0	$I_{116} \approx P_{112}/P_{116}$	-	32
53	0	$I_{53} \approx P_{17}/P_{53}$	-	18	117	0	$I_{117} \approx P_{112}/P_{117}$	-	32
54	0	$I_{54} \approx P_{18}/P_{54}$	-	32	118	0	$I_{118} \approx P_{112}/P_{118}$	-	32
55	0	$I_{55} \approx P_{51}/P_{55}$	-	18	119	0	$I_{119} \approx P_{110}/P_{119}$	-	1
56	0	$I_{56} \approx P_{52}/P_{56}$	-	32	120	0	$I_{120} \approx P_{53}/P_{120}$	-	18
57	0	$I_{57} \approx P_{55}/P_{57}$	-	18	121	0	$I_{121} \approx P_{53}/P_{121}$	-	18
58	21	$I_{58} \approx P_{56}/P_{58}$	1.5238	2	122	0	$I_{122} \approx P_{53}/P_{122}$	-	18
59	0	$I_{59} \approx P_{55}/P_{59}$	-	18	123	0	$I_{123} \approx P_{54}/P_{123}$	-	32
60	1	$I_{60} \approx P_{56}/P_{60}$	32	32	124	0	$I_{124} \approx P_{54}/P_{124}$	-	32
61	6	$I_{61} \approx P_{45}/P_{61}$	5.3333	5	125	0	$I_{125} \approx P_{54}/P_{125}$	-	32
62	8	$I_{62} \approx P_{46}/P_{62}$	4	4	126	0	$I_{126} \approx P_{119}/P_{126}$	-	1
63	0	$I_{63} \approx P_{43}/P_{63}$	-	7	127	29	$I_{127} \approx P_{126}/P_{127}$	-	1
64	0	$I_{64} \approx P_{44}/P_{64}$	-	7	128	29	$I_{128} \approx P_{127}/P_{128}$	1	1

Table 7.16: Calculation of the importance in each cell based on the cell populations

Tallies

- ***F2 tallies:*** This non-analog simulation is using the same cylindrical source as before and is running for 1440 minutes.

No	*Regions*	*Photon flux on surface (#/cm^2)*		*Ratio (Analog/Non Analog)*	*Ratio (GCALOR/MCNP)*
		Analog	*Non Analog*		
1	Pixel PixB1	50156 E+03	25440.8 E+03	1.97	1.797
2	Pixel PixB3	23018 E+03	11580.2 E+03	1.98	0.79
3	SCT SCTB1	24414 E+03	12337.5 E+03	1.97	0.36
4	SCT SCTB4	7919 E+03	3901.78 E+03	2.03	0.99
5	TRT TRTB0	5444 E+03	2703.63 E+03	2.01	0.898
6	SCT SCTD9	9705.6 E+03	5025.34 E+03	1.9	1.5
7	TRT TRTW1	6648.3 E+03	3332.64 E+03	2	3.77
8	LAr Barrel	314.222 E+03	157.119 E+03	2	0.024
9	LAr End-cap	1.0456 E+03	0.502 E+03	2.08	0.73
10	Tile Cal	12.1426 E+03	5.826 E+03	2.08	0.083
11	MDT IN	8.7912 E+03	4.529 E+03	1.94	0.242
12	MDT MID	4.0772 E+03	2.067 E+03	1.97	0.57
13	RPC OUT	2.3325 E+03	1.184 E+03	1.97	1.09
14	Small Wheel	1.3571 E+03	0.503 E+03	2.7	21.3
15	End-cap middle	2.6213 E+03	0.119 E+03	22	47.80
16	End-cap outer	0.9639 E+03	0.121 E+03	7.96	9.6

Table 7.17: Photon fluxes from the non-analog simulation and the ratio comparing with the analog simulation fluxes and the GCALOR values. It is indicated when the ratio is improved (pink), and when the divergence is very large (blue).

It is observed that the fluxes of the outermost regions decline much more from the CGALOR values than those of the analog simulation, while the ratio at many innermost regions has improved.

- **F4 tallies**

Fluxes in various cells for the simulation using geometry splitting. The source and the running time (1440 minutes) are the same as before:

No	*Cell Number (MCNP code)*	*Cell*	*Flux in cell*	*Ratio (Analog/Non Analog)*
1	1	Beampipe 1	23381600	0.988
2	2	Wall 1	23441700	0.9968
3	3	Beampipe 2	800118	0.945
4	5	Wall 2	758418	1.018
5	7	Beampipe 3	0	NaN
6	9	Wall 3	0	NaN
7	11	Beampipe 4	0	NaN

8	13	Wall 4	0	NaN
9	15	Beampipe 5	0	NaN
10	17	Wall 5	0	NaN
11	20	Pixel Detector	16768400	1.003
12	22	SCT barrel	7237960	0.998
13	24	TRT barrel	3468160	0.997
14	27	SCT end - caps	6324200	0.995
15	31	TRT end - caps	3091460	0.998
16	34	EM Calorimeter Barrel	172636	1.0009
17	35	Forward Calorimeter	1089.8	1.2
18	37	EM-Had Calorimeter	214540	1.002
19	39	Hadronic Calorimeter Barrel	56822	1.002
20	40	Hadronic Calorimeter End-caps	14957.5	1.01
21	43	JD shielding	66.4	0.65
22	45	JT Cu Shielding	0	Inf
23	47	JF Iron Shielding -1-	7	0.359
24	49	TAS collimator	0	NaN
25	51	Quad	0	NaN
26	53	JF Iron Shielding -2-	4.5	2.2
27	55	JF Iron Shielding -3-	0	NaN
28	57	JN Shielding -1-	2.9	2.49
29	59	JN Shielding -2-	9	1.009
30	61	Superconducting Magnet	38.8	1.11
31	63	CSC	214.7	0.906
32	65	Small Wheel (EIL)-MDT	485	1.26
33	66	Small Wheel (EIL)-inside	466	1.29
34	67	Small Wheel (EIL)-MDT	395	1.7
35	72	Muon Inner Barrel (BIL)-MDT	5324	0.949
36	73	Muon Inner Barrel (BIL)-inside	4652	0.9698
37	74	Muon Inner Barrel (BIL)-MDT	4443	0.99
38	76	RPCs (BML)	2447	0.987
39	77	Muon Medium Barrel (BML)-MDT	2470	0.96
40	78	Muon Medium Barrel (BML)-inside	2195	1.02
41	79	Muon Medium Barrel (BML)-MDT	2202.8	1.006
42	80	RPCs (BML)	2138.7	0.9697
43	82	Muon Outer Barrel 1 (BOL)-MDT	1383	0.993
44	83	Muon Outer Barrel 1 (BOL)-inside	1253.5	1.016
45	84	Muon Outer Barrel 1 (BOL)-MDT	1224.5	1.08
46	85	RPCs (BOL)	1191	1.015
47	88	Muon End Cap (EEL) -MDT	291	1.5
48	89	Muon End Cap (EEL)-inside	281	1.22
49	90	Muon End Cap (EEL) –MDT	296	1.08
50	96	Muon Medium End Cap (EML)-MDT	136	1.23
51	97	Muon Medium End Cap (EML)-inside	130.8	1.19
52	98	Muon Medium End Cap (EML)-MDT	127	1.28
53	104	TGCs (EML) 1	157	1.017
54	108	TGCs (EML) 2	150	0.989
55	113	Muon Outer End Cap 1 (EOL) –MDT	113	0.71

56	114	Muon Outer End Cap 1 (EOL)-inside	99	0.73
57	115	Muon Outer End Cap 1 (EOL) –MDT	96	0.765
58	120	Muon Outer End Cap 2 (EOL)	73.7	0.308
59	121	Muon Outer End Cap 2 (EOL)	71	0.353
60	122	Muon Outer End Cap 2 (EOL)	55.5	0.57
61	150	ATLAS Cylinder	249	1.04

Table 7.18: Fluxes in cells of the ATLAS geometry

It can be observed that the fluxes when using geometry splitting are close enough to the analog ones. The non – analog simulation has not proven much more precise. This probably depends on the function of defining cell populations for the non – analog simulation; a most accurate function should take into account more than one neighbouring cells, resulting in a more realistic new cell population.

7.2.7. FURTHER SIMULATIONS

Simulations for neutron fluxes on critical surfaces were also carried out. The cylindrical source, as in the case of photons, was used here, and the running time was set at 1440 minutes. The results for 10E+11 source particles are presented below.

No	*Regions*	*Neutron flux on surface (#/cm^2) Cylindrical source*
1	Pixel PixB1	243978000
2	Pixel PixB3	148010000
3	SCT SCTB1	168359000
4	SCT SCTB4	151782000
5	TRT TRTB0	127549000
6	SCT SCTD9	90193600
7	TRT TRTW1	128770000
8	LAr Barrel	5139490
9	LAr End-cap	7687
10	Tile Cal	998661
11	MDT IN	70309.8
12	MDT MID	35974.6
13	RPC OUT	21491
14	Small Wheel	7661.5
15	End-cap middle	2874
16	End-cap outer	2751

Table 7.19: Neutron fluxes on critical surfaces of the ATLAS geometry.

8. CONCLUSION AND FUTURE PROSPECTS

The previous simulations seem to give results close enough to those predicted by demanding simulations conducted by ATLAS collaboration. Of course, in the future, more techniques for variance reduction can be tested, as well as improvement can occur if a more complex function for cell populations of the geometry splitting technique is used. The accuracy of the results, as in the case of those by ATLAS collaboration, demands highly time – consuming simulations. MCNP code introduces some restrictions, concerning the choice of materials and the composition of mixtures, which prevents a more accurate approach of the real material constitution of the ATLAS detector. Furthermore, another restriction refers to the inability of multithreading in this edition; this service would enable MCNP code to run faster, but it will be included in future editions. Despite these disadvantages, the results can be rendered satisfying regarding the level of this work, in the terms of a diploma thesis, the time available for the design of the geometry, the selection of the materials and processing and mainly the results. As a future work, a more detailed design can be used and simulations can be carried out for neutrons and electrons.

APPENDICES

APPENDIX 1: SIMPLE MCNP GEOMETRIES AS A BASE FOR THE MORE COMPLEX SIMULATIONS

Spherical Geometries

Some simple trials must be conducted in order to ground on the final simulations of the ATLAS detector, where more complex geometries are used. Firstly, a comparison between treoretical values and simulated ones was conducted.

Photon flux on a surface is defined as:

$$\text{Flux} = \frac{\#photons}{surface}$$

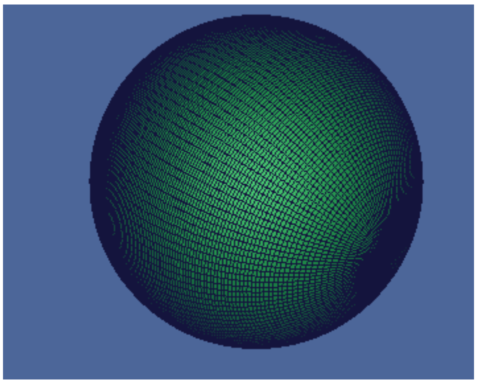

Simulated Sphere with MCNP (3D plot). [Vised]

A cobalt-60 source was used in the common center of spheres. The simulation contains concentric spheres with radii from 1m to 25 m with step of 1 m, filled with air and radioactivities from 1 Beq to 10 Beq for the Co-60 source. For better graphical representation a smaller sphere of radius 1 cm is included. The simulation carries out 10^6 scenarios. This running time is sufficient as air is not an absorbent material, so, the relative errors are negligible.

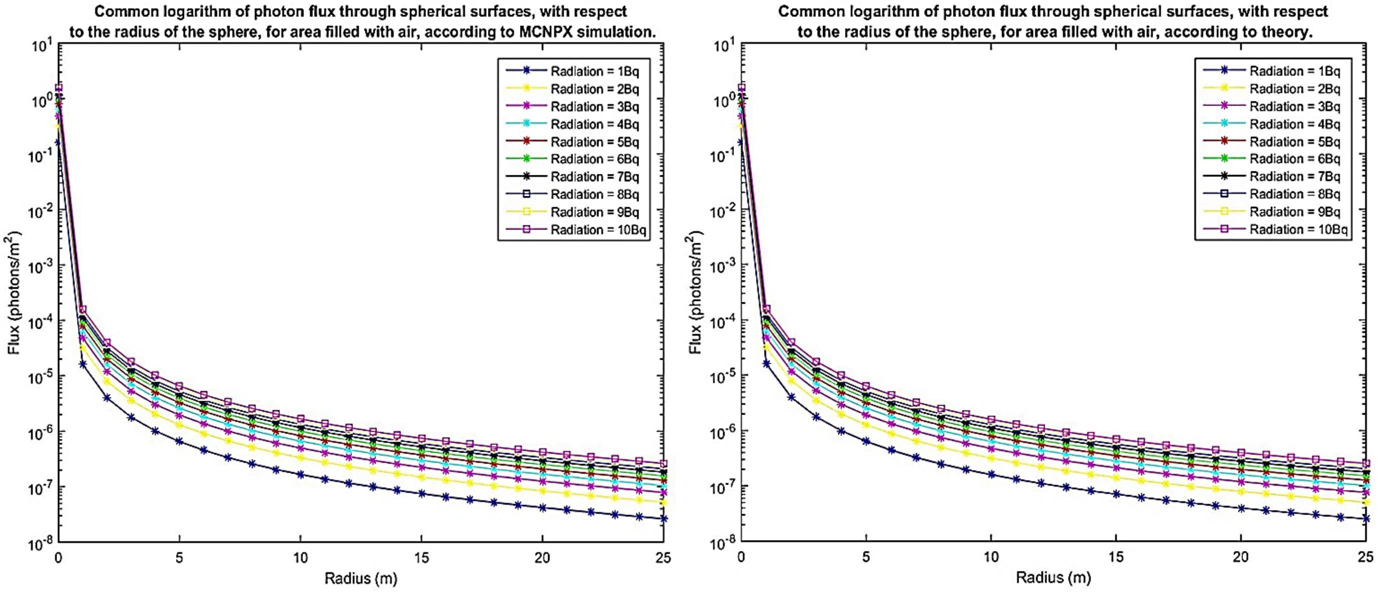

MCNP simulation and theoretical results. For radioactivities 1-10 Bequerel and for each radius the two representations are the same. Additionally, both representations have the same form regadless of the radioactivity (semilogarithmic plots). [Matlab]

It can be assumed that the chosen representation is correct, and more complex geometries can be based on this.

If the source is relocated from the point (0,0,0) to (10,0,0) the mean flux for the spheres of radii 2-15m is the same regadless of the source relocation. A difference can occur when in the first case the source is inside the sphere and in the second case is outside.

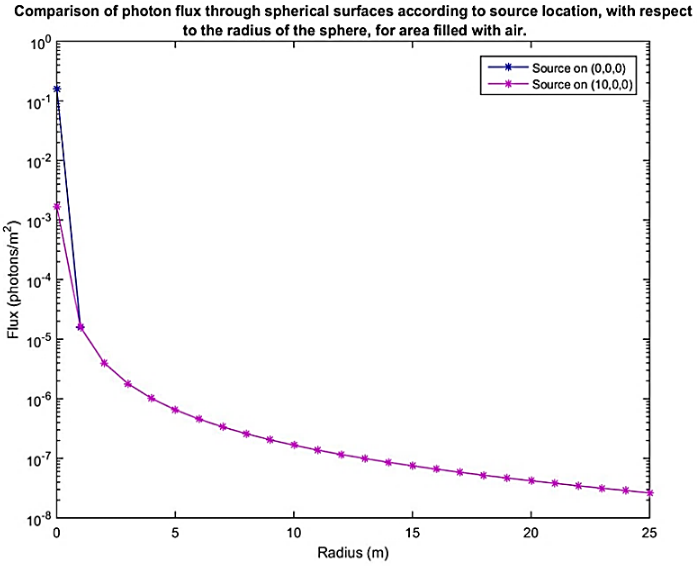

Relocation of the Co-60 source at (10,0,0). [Matlab]

Two identical Co-60 sources are located at (-10,0,0) and (10,0,0) and measurements are obtained for a sphere of radius 25 m filled with air. Every Co-60 source emmits two photons per second, so for the two sources, 4 photons per secont will be produced. Thus, the results form the output file will be multiplied 4 times.

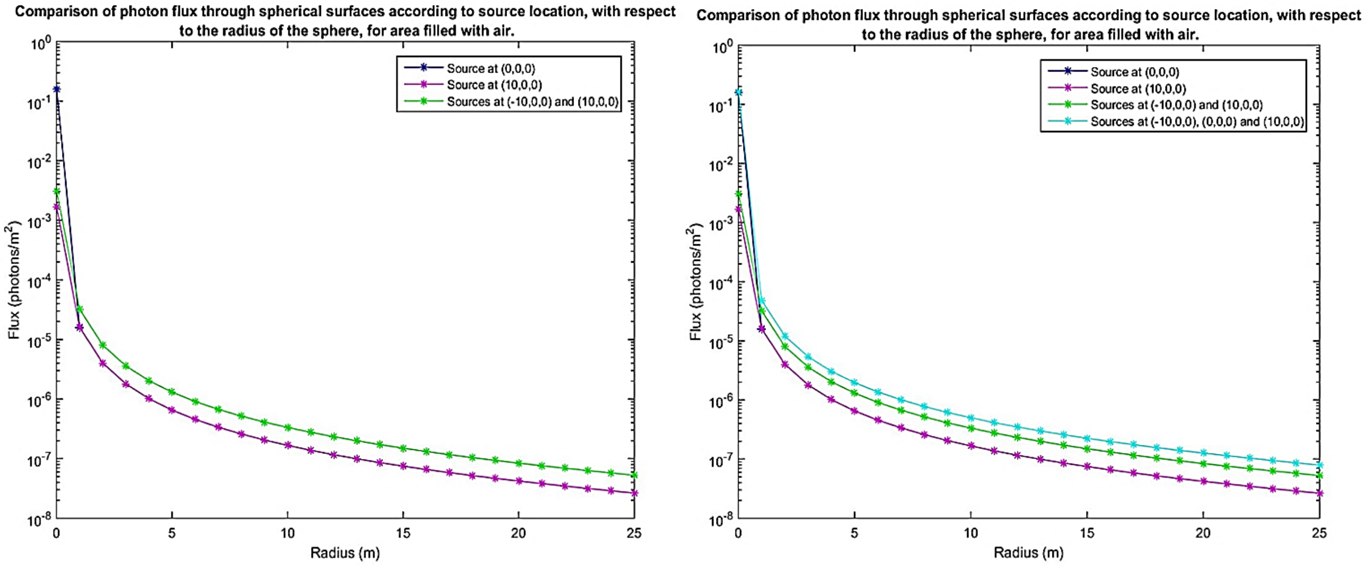

Left: Flux if two sources are deposited (green) comparing to the single one (pink). Right: Flux comparison between one source (pink and blue), two sources (green), three sources (light blue). [Matlab]

It can be observed that the mean photon flux is increased when an extra identical source is added.

Spherical geometries are notably important for this study because they are suitable for measurements regardless direction, as they are symmetrical towards x,y and z axis.

Cubic and Rectangular parallelepiped geometries

A cube (25m x 25m x 25m) using plane intersections is simulated

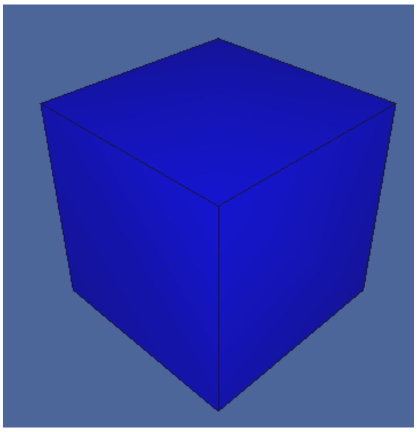

Simulated cube with MCNP (3D plot). [Vised]

The average surface photon flux on each surface is:

Surface	***Flux per source particle (#/cm^2)***	***Total Flux for 2 source particles (#/cm^2)***	***Relative error***
plane perpendicular to x-axis at x=25 m	8.43991 E-09	16.8798 E-09	0.0053
plane perpendicular to x-axis at x=-25 m	8.51725 E-09	17.0345 E-09	0.0052
plane perpendicular to y-axis at y=25 m	8.43859 E-09	16.8772 E-09	0.0053
plane perpendicular to y-axis at y=-25 m	8.39849 E-09	16.7970 E-09	0.0052
plane perpendicular to z-axis at z=25 m	8.47317 E-09	16.9463 E-09	0.0051
plane perpendicular to z-axis at z=-25 m	8.38113 E-09	16.7623 E-09	0.0052

It becomes easily observed that the average photon flux is almost the same on each surface. Also, the average photon flux in the volume of the cube is 2.56918E-08 #/cm^2 (0.0005). When using a macrobody cube, the average flux in the volume of the cube and each of the surfaces gives almost the same values with those above. The simplicity of the macrobody structure makes it the best choice for a cubic or rectangular parallepiped geometry.

Materials

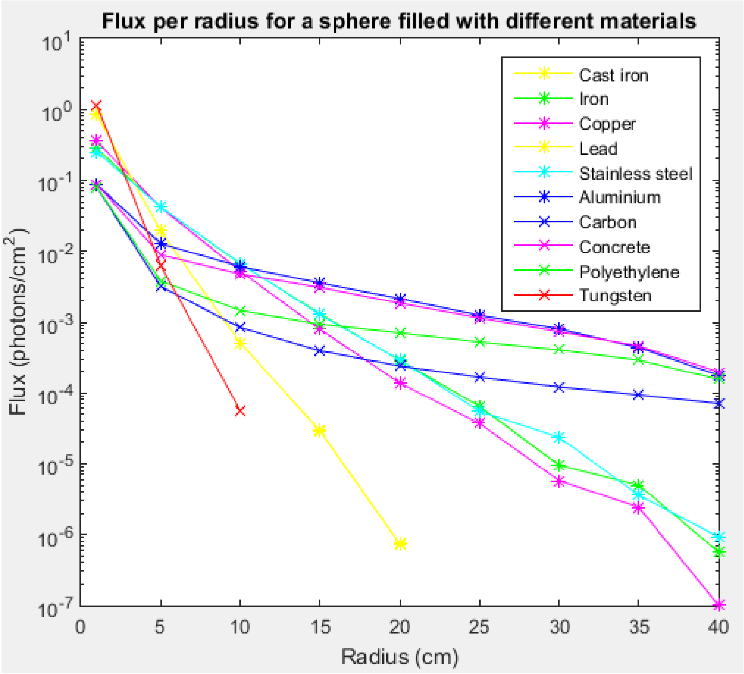

Comparison of some commonly used shielding materials from Table 6.1. The curve of the cast iron is the same as the one of the lead. [Matlab]

The ATLAS shielding is based on the use of different materials, which are compared below. Measurements are taken every 5 cm in a sphere of total radius of 40 cm.

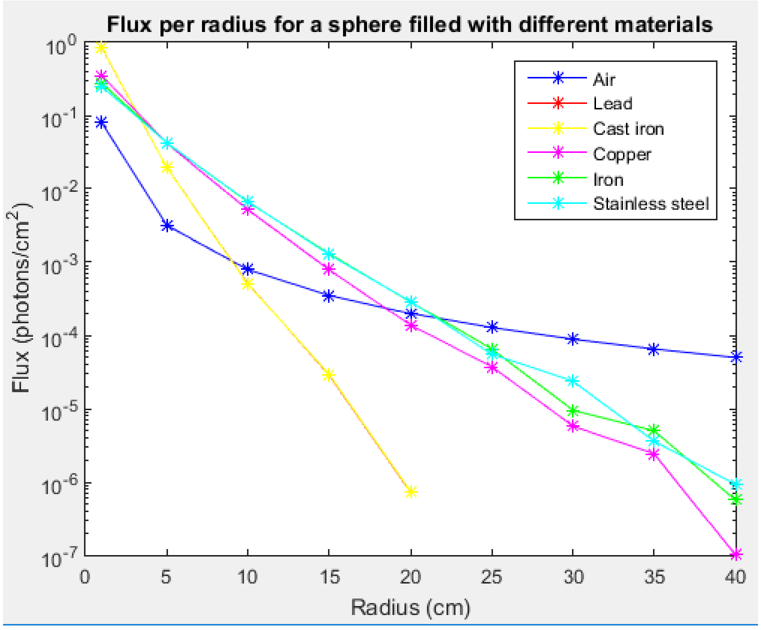

Comparison of the attenuation of photon fluxes in ATLAS shielding materials. The curve of the cast iron is the same as the one of the lead. [Matlab]

The curves of the flux attenuation in some ATLAS materials depending on the distance from the source are fitted to the power curve (ax^b) using the method of non - linear least squares. In this way, it is observed that the attenuation in the sphere follows approximately the same function, which matches the theory of the exponential attenuation.

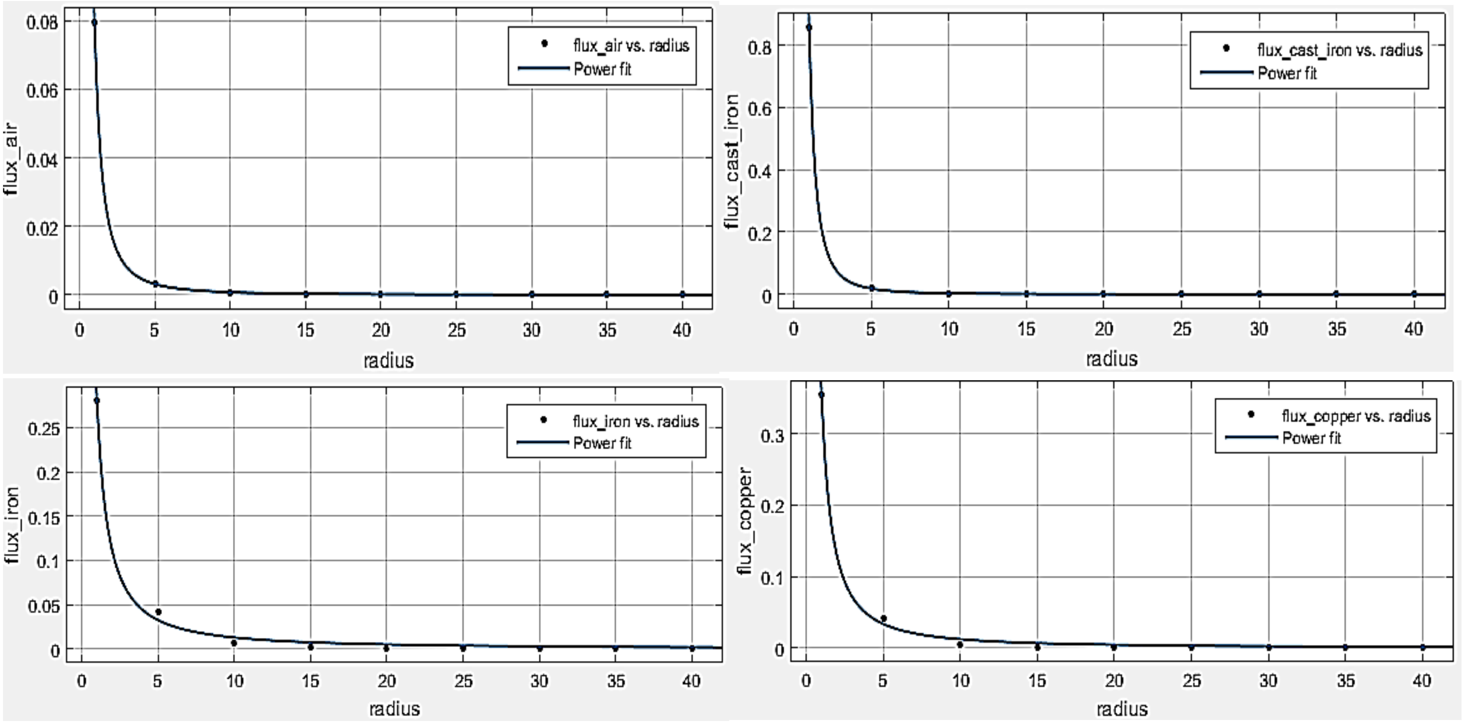

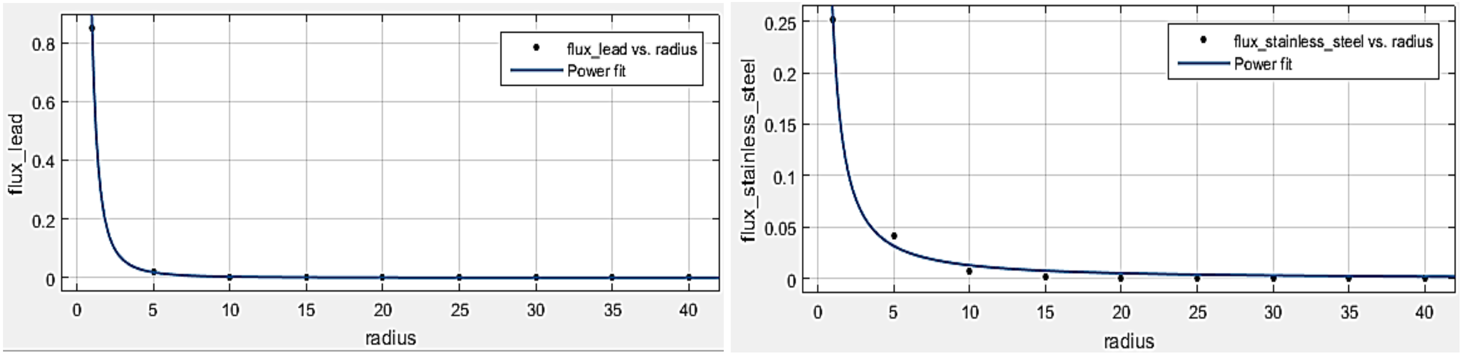

General model Power1: f(x) = ax^b. [Matlab]

The coefficients a,b for the materials that follow the general power distribution are presented:

Material	***a***	***b***	***Confidence interval (95%) for a***	***Confidence interval (95%) for b***
air	0.07958	-2	(0.07958, 0.07958)	(-2, -2)
Copper	0.3555	-1.467	(0.3433, 0.3677)	(-1.651, -1.282)
Lead	0.8508	-2.387	(0.8477, 0.854)	(-2.489, -2.285)
Stainless steel	0.2525	-1.286	(0.2383, 0.2667)	(-1.497, -1.076)
Iron	0.2814	-1.339	(0.2682, 0.2947)	(-1.536, -1.143)
Cast iron	0.8576	-2.392	(0.8544, 0.8607)	(-2.494, -2.29)

Source energies

The influence due to the energy of the point source at (0,0,0) was tested for different materials. Sources of energies 1, 5, 10, 20, 50, 70 and 100 MeV were placed into concentric spheres at the origin and the measurements below were taken on the surface of the sphere with radius 5 cm:

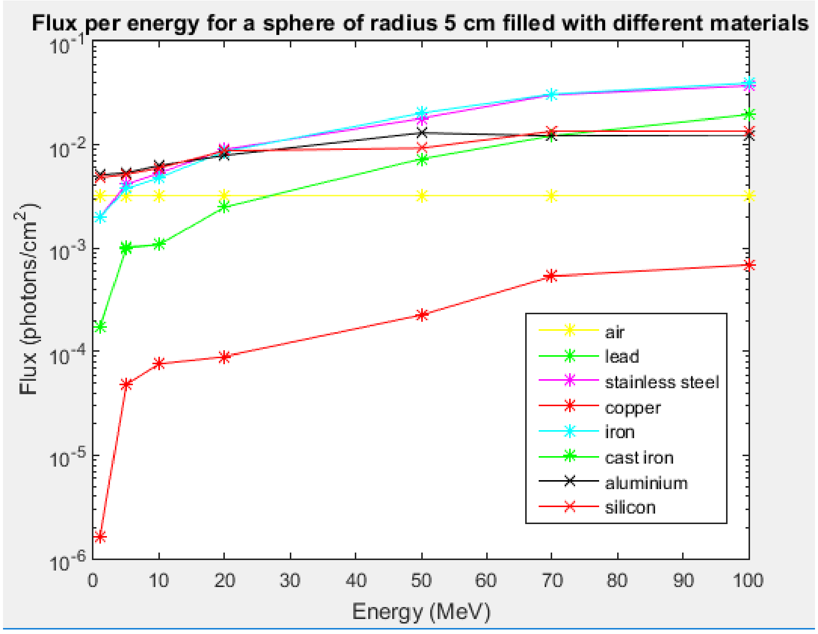

Photon flux for different materials and sources of increasing energy.

The flux in air remains almost constant despite the increase. The flux in the other materials is increasing following different rates as it can better be seen when their fitting curves are taken. The curves of the flux in some ATLAS materials depending of the energy of the source are fitted to the power curve (ax^b) using the method of non - linear least squares.

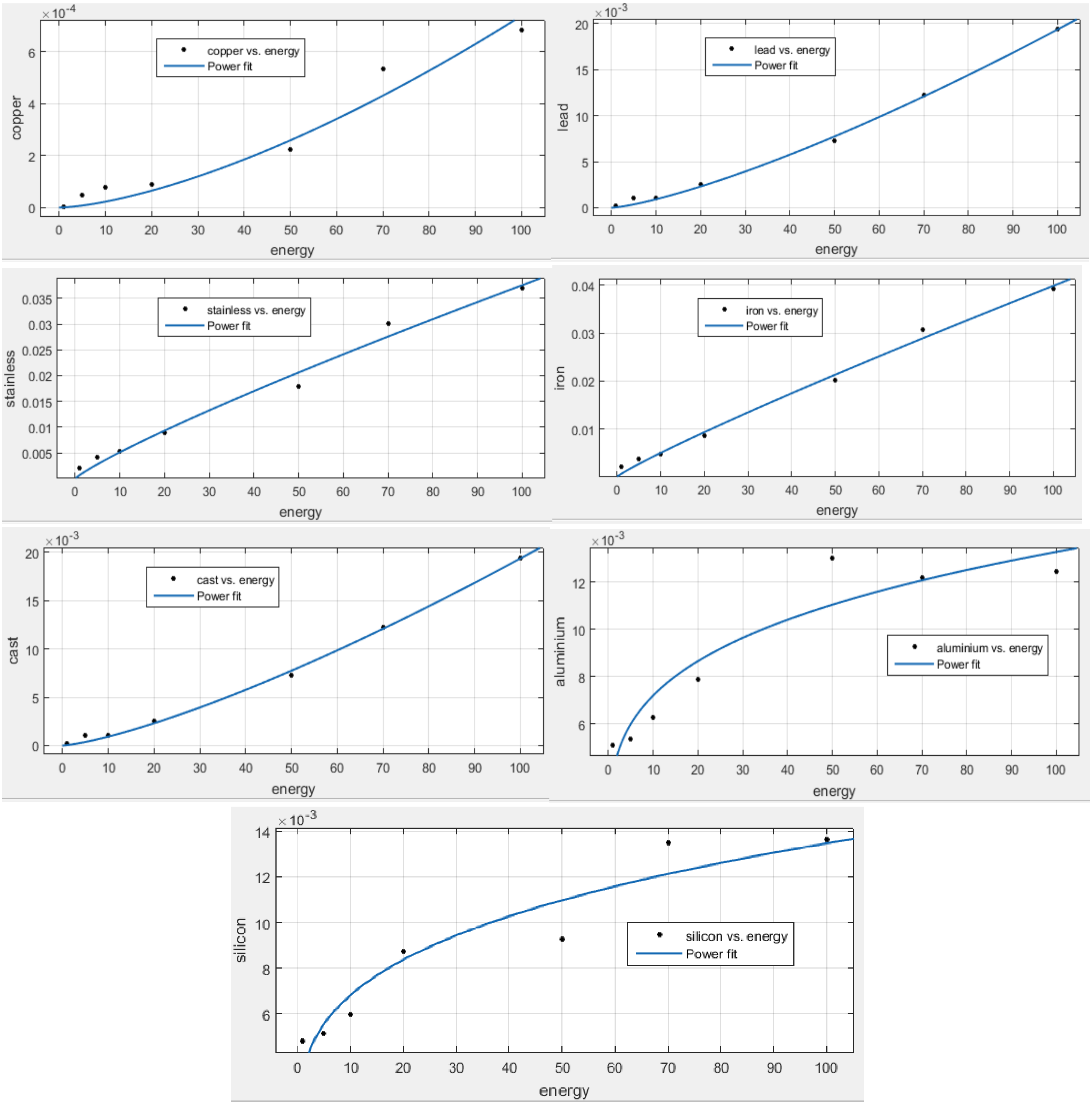

Fitting curves following the General model Power 1: f(x) = ax^b. [Matlab]

The coefficients a, b for each material are:

Material	***a***	***b***	***Confidence interval (95%) for a***	***Confidence interval (95%) for b***
Copper	7.023e-07	1.511	(-1.536e-06, 2.941e-06)	(0.7967, 2.225)
Lead	4.402e-05	1.322	(1.659e-05, 7.145e-05)	(1.181, 1.462)
Stainless steel	0.0007	0.8647	(4.953e-05, 0.00135)	(0.6504, 1.079)
Iron	0.0006206	0.9041	(0.0002164, 0.001025)	(0.7543, 1.054)
Cast iron	4.406e-05	1.322	(1.613e-05, 7.199e-05)	(1.179, 1.464)
Aluminium	0.003897	0.2662	(0.002055, 0.00574)	(0.1439, 0.3886)
Silicon	0.00345	0.2958	(0.001718, 0.005183)	(0.1674, 0.4242)

APPENDIX 2: THE FINAL MCNP CODE FOR THE ATLAS DETECTOR

I. Blocks 1&2: Cells and surfaces

```
1    0        -1
2    2  -1.848 -2 1
3    0        -3
4    0        -4
5    3   -7.86 -5 3
6    3   -7.86 -6 4
7    0        -7
8    0        -8
9    3   -7.86 -9 7
10    3   -7.86 -10 8
11    0        -11
12    0        -12
13    3   -7.86 -13 11
14    3   -7.86 -14 12
15    0        -15
16    0        -16
17    4   -8.96 -17 15
18    4   -8.96 -18 16
19    1 -0.001225 -19 2
20    5   -2.33 -20 19
21    1 -0.001225 -21 20
22    5   -2.33 -22 21
23    1 -0.001225 -23 22
24    6 -0.005485 -24 23
25    1 -0.001225 -25 20
26    1 -0.001225 -26 20
27    5   -2.33 -27 25
28    5   -2.33 -28 26
29    1 -0.001225 -29 27
30    1 -0.001225 -30 28
31    6 -0.005485 -31 29
32    6 -0.005485 -32 30
33    1 -0.001225 -33 20 22 24 27 28 31 32
34    7  -11.35 -34 33
35    7  -11.35 -35 5
36    7  -11.35 -36 6
37    3   -7.86 -37 35 5 2
38    3   -7.86 -38 36 6 2
39    3   -7.86 -39 34
40    3   -7.86 -40 37
41    3   -7.86 -41 38
42    1 -0.001225 -42 2 39 40 41
43    3   -7.86 -43 5
44    3   -7.86 -44 6
45    4   -8.96 -45 13 9 5
46    4   -8.96 -46 14 10 6
47    8  -7.874 -47 13 17
48    8  -7.874 -48 14 18
```

```
 49     4   -8.96 -49 17
 50     4   -8.96 -50 18
 51    10   -4.43 -51 17
 52    10   -4.43 -52 18
 53     8  -7.874 -53 49 17
 54     8  -7.874 -54 50 18
 55     8  -7.874 -55 51 17
 56     8  -7.874 -56 52 18
 57     9   -7.15 -57 55
 58     9   -7.15 -58 56
 59     9   -7.15 -59 55
 60     9   -7.15 -60 56
 61    10   -4.43 -61 45
 62    10   -4.43 -62 46
 63    11 -0.001662 -63 43
 64    11 -0.001662 -64 44
 65    12 -2.6989 -65 63
 66    11 -0.001662 -66 63
 67    12 -2.6989 -67 63
 68    12 -2.6989 -68 64
 69    11 -0.001662 -69 64
 70    12 -2.6989 -70 64
 71     1 -0.001225 -71 42
 72    12 -2.6989 -72 71
 73    11 -0.001662 -73 72
 74    12 -2.6989 -74 73
 75     1 -0.001225 -75 61 62 65 66 67 68 69 70 71 72 70 74 42
 76    13 -0.00425 -76 75
 77    12 -2.6989 -77 76
 78    11 -0.001662 -78 77
 79    12 -2.6989 -79 78
 80    13 -0.00425 -80 79
 81     1 -0.001225 -81 80 61 62 88 89 90 91 92 93
 82    12 -2.6989 -82 81
 83    11 -0.001662 -83 82
 84    12 -2.6989 -84 83
 85    13 -0.00425 -85 84
 86     1 -0.001225 -86 61
 87     1 -0.001225 -87 62
 88    12 -2.6989 -88 86
 89    11 -0.001662 -89 86
 90    12 -2.6989 -90 86
 91    12 -2.6989 -91 87
 92    11 -0.001662 -92 87
 93    12 -2.6989 -93 87
 94     1 -0.001225 -94 47
 95     1 -0.001225 -95 48
 96    12 -2.6989 -96 94
 97    11 -0.001662 -97 94
 98    12 -2.6989 -98 94
 99    12 -2.6989 -99 95
100     11 -0.001662 -100 95
```

```
  101    12 -2.6989 -101 95
  102     1 -0.001225 -102 47
  103     1 -0.001225 -103 48
  104    14 -0.001842 -104 102
  105    14 -0.001842 -105 103
  106     1 -0.001225 -106 47
  107     1 -0.001225 -107 48
  108    14 -0.001842 -108 106
  109    14 -0.001842 -109 107
  110     1 -0.001225 -110 47 48 81 85 96 97 98 99 108 109 100 101 104 105
  111     1 -0.001225 -111 53
  112     1 -0.001225 -112 54
  113    12 -2.6989 -113 111
  114    11 -0.001662 -114 111
  115    12 -2.6989 -115 111
  116    12 -2.6989 -116 112
  117    11 -0.001662 -117 112
  118    12 -2.6989 -118 112
  119     1 -0.001225 -119 110 113 114 115 116 117 118
  120    12 -2.6989 -120 53
  121    11 -0.001662 -121 53
  122    12 -2.6989 -122 53
  123    12 -2.6989 -123 54
  124    11 -0.001662 -124 54
  125    12 -2.6989 -125 54
  126     1 -0.001225 -126 53 54 119 120 121 122 123 124 125
  150     1 -0.001225 -150 126 53 54 57 59 60 58
  151     1 -0.001225 -151 150
  200     0         151

c     ************************************************************************
c    Detector Subsystems
c     ************************************************************************
c    --- Beampipe ---
    1       rcc -355 0 0 710 0 0 2.9
c    wall
    2       rcc -355 0 0 710 0 0 2.98
c    ----------------
    3       rcc -355 0 0 -691.5 0 0 2.9
    4       rcc 355 0 0 691.5 0 0 2.9
c    wall
    5       rcc -355 0 0 -691.5 0 0 2.98
    6       rcc 355 0 0 691.5 0 0 2.98
c    ----------------
    7       rcc -1046.5 0 0 -4.2 0 0 4
    8       rcc 1046.5 0 0 4.2 0 0 4
c    wall
    9       rcc -1046.5 0 0 -4.2 0 0 4.1
   10        rcc 1046.5 0 0 4.2 0 0 4.1
c    ----------------
   11        rcc -1050.7 0 0 -390.9 0 0 6
   12        rcc 1050.7 0 0 390.9 0 0 6
```

```
c   wall
  13      rcc -1050.7 0 0 -390.9 0 0 6.15
  14      rcc 1050.7 0 0 390.9 0 0 6.15
c   ----------------
  15      rcc -1441.6 0 0 -958.4 0 0 1.7
  16      rcc 1441.6 0 0 958.4 0 0 1.7
c   wall
  17      rcc -1441.6 0 0 -958.4 0 0 3
  18      rcc 1441.6 0 0 958.4 0 0 3
c   ********************************************
c   air between beampipe and pixel
  19      rcc -309.2 0 0 618.4 0 0 4.55
c   Pixel
  20      rcc -309.2 0 0 618.4 0 0 24.2
c   air between SCT barrel and Pixel
  21      rcc -80.5 0 0 161 0 0 25.5
c   SCT barrel
  22      rcc -80.5 0 0 161 0 0 54.9
c   air between SCT barrel and TRT barrel
  23      rcc -78 0 0 156 0 0 55.4
c   TRT barrel
  24      rcc -78 0 0 156 0 0 108.2
c   air for SCT end - caps
  25      rcc 81 0 0 198.7 0 0 25.1
  26      rcc -279.7 0 0 198.7 0 0 25.1
c   SCT end - caps
  27      rcc 81 0 0 198.7 0 0 61
  28      rcc -279.7 0 0 198.7 0 0 61
c   air for TRT end - caps
  29      rcc 82.7 0 0 191.7 0 0 61.7
  30      rcc -274.4 0 0 191.7 0 0 61.7
c   TRT end - caps
  31      rcc 82.7 0 0 191.7 0 0 110.6
  32      rcc -274.4 0 0 191.7 0 0 110.6
c   Inner Detector
  33      rcc -309.2 0 0 618.4 0 0 110.6
c   ********************************************
c   EM Calorimeter (Barrel)
  34      rcc -309.2 0 0 618.4 0 0 200
c   Forward Calorimeter
  35      rcc -500 0 0 -100 0 0 25
  36      rcc 500 0 0 100 0 0 25
c   EM-Had Calorimeter
  37      rcc -350 0 0 -300 0 0 200
  38      rcc 350 0 0 300 0 0 200
c   Hadronic Calorimeter Barrel
  39      rcc -309.2 0 0 618.4 0 0 400
c   Hadronic Calorimeter End-cups
  40      rcc -350 0 0 -300 0 0 400
  41      rcc 350 0 0 300 0 0 400
c   Calorimeter
  42      rcc -650 0 0 1300 0 0 400
```

```
c    *********************************************
c    Shielding Regions
c    JD shielding
  43       rcc -650 0 0 -150 0 0 50
  44       rcc 650 0 0 150 0 0 50
c    JT Cu Shielding
  45       rcc -800 0 0 -500 0 0 50
  46       rcc 800 0 0 500 0 0 50
c    JF Iron Shielding -1-
  47       rcc -1300 0 0 -500 0 0 100
  48       rcc 1300 0 0 500 0 0 100
c    TAS collimator
  49       rcc -1888 0 0 -200 0 0 20
  50       rcc 1888 0 0 200 0 0 20
c    Quad
  51       rcc -2200 0 0 -200 0 0 20
  52       rcc 2200 0 0 200 0 0 20
c    JF Iron Shielding -2-
  53       rcc -1800 0 0 -388 0 0 200
  54       rcc 1800 0 0 388 0 0 200
c    JF Iron Shielding -3-
  55       rcc -2188 0 0 -212 0 0 100
  56       rcc 2188 0 0 212 0 0 100
c    JN Shielding -1-
  57       rcc -2188 0 0 -112 0 0 250
  58       rcc 2188 0 0 112 0 0 250
c    JN Shielding -2-
  59       rcc -2300 0 0 -100 0 0 300
  60       rcc 2300 0 0 100 0 0 300
c    *********************************************
c    Superconducting Magnet
  61       rcc -800 0 0 -500 0 0 500
  62       rcc 800 0 0 500 0 0 500
c    *********************************************
c    Muon Stations
c    CSC
  63       rcc -650 0 0 -150 0 0 200
  64       rcc 650 0 0 150 0 0 200
c    Small Wheel (EIL)
  65       rcc -650 0 0 -0.05 0 0 600
  66       rcc -650.05 0 0 -149.9 0 0 600
  67       rcc -799.95 0 0 -0.05 0 0 600
c
  68       rcc 650 0 0 0.05 0 0 600
  69       rcc 650.05 0 0 149.9 0 0 600
  70       rcc 799.95 0 0 0.05 0 0 600
c    Air before Muon Inner Barrel (BIL)
  71       rcc -600 0 0 1200 0 0 500
c    Muon Inner Barrel (BIL)
  72       rcc -600 0 0 1200 0 0 500.05          $MDT
  73       rcc -600 0 0 1200 0 0 549.95
  74       rcc -600 0 0 1200 0 0 550
```

```
c    Air between Muon layers 1 and 2
   75        rcc -900 0 0 1800 0 0 680
c    RPCs (BML)
   76        rcc -900 0 0 1800 0 0 700
c    Muon Medium Barrel (BML)
   77        rcc -900 0 0 1800 0 0 700.05         $MDT
   78        rcc -900 0 0 1800 0 0 749.95
   79        rcc -900 0 0 1800 0 0 750
c    RPCs (BML)
   80        rcc -900 0 0 1800 0 0 770
c    Air Between BML an BOL
   81        rcc -1300 0 0 2600 0 0 920
c    Muon Outer Barrel 1 (BOL)
   82        rcc -1200 0 0 2400 0 0 920.05       $MDT
   83        rcc -1200 0 0 2400 0 0 969.95
   84        rcc -1200 0 0 2400 0 0 970
c    RPCs (BOL)
   85        rcc -1200 0 0 2400 0 0 990
c    Air for EEL
   86        rcc -1000 0 0 -75 0 0 600
   87        rcc 1000 0 0 75 0 0 600
c    Muon End Cap (EEL)
   88        rcc -1000 0 0 -0.05 0 0 900
   89        rcc -1000.05 0 0 -74.9 0 0 900
   90        rcc -1074.95 0 0 -0.05 0 0 900
c
   91        rcc 1000 0 0 0.05 0 0 900
   92        rcc 1000.05 0 0 74.9 0 0 900
   93        rcc 1074.95 0 0 0.05 0 0 900
c    Air between Shielding and EML
   94        rcc -1300 0 0 -80 0 0 120
   95        rcc 1300 0 0 80 0 0 120
c    Muon Medium End Cap (EML)
   96        rcc -1300 0 0 -0.05 0 0 1100         $MDT
   97        rcc -1300.05 0 0 -79.9 0 0 1100
   98        rcc -1379.95 0 0 -0.05 0 0 1100
c
   99        rcc 1300 0 0 0.05 0 0 1100
  100        rcc 1300.05 0 0 79.9 0 0 1100
  101        rcc 1379.95 0 0 0.05 0 0 1100
c    Air between Shielding and TGCs 1
  102        rcc -1390 0 0 -30 0 0 200
  103        rcc 1390 0 0 30 0 0 200
c    TGCs (EML) 1
  104        rcc -1390 0 0 -30 0 0 1200
  105        rcc 1390 0 0 30 0 0 1200
c    Air between Shielding and TGCs 2
  106        rcc -1430 0 0 -30 0 0 200
  107        rcc 1430 0 0 30 0 0 200
c    TGCs (EML) 2
  108        rcc -1430 0 0 -30 0 0 1200
  109        rcc 1430 0 0 30 0 0 1200
```

```
c    Air for geometry simplification
  110       rcc -1800 0 0 3600 0 0 1200
c    Air between shielding and EOL
  111       rcc -1800 0 0 -80 0 0 600
  112       rcc 1800 0 0 80 0 0 600
c    Muon Outer End Cap 1 (EOL)
  113       rcc -1800 0 0 -0.05 0 0 1200          $MDT
  114       rcc -1800.05 0 0 -79.9 0 0 1200
  115       rcc -1879.95 0 0 -0.05 0 0 1200
c
  116       rcc 1800 0 0 0.05 0 0 1200
  117       rcc 1800.05 0 0 79.9 0 0 1200
  118       rcc 1879.95 0 0 0.05 0 0 1200
c    Simplification
  119       rcc -1880 0 0 3760 0 0 1200
c    Muon Outer End Cap 2 (EOL)
  120       rcc -2100 0 0 -0.05 0 0 500           $MDT
  121       rcc -2100.05 0 0 -79.9 0 0 500
  122       rcc -2179.95 0 0 -0.05 0 0 500
c
  123       rcc 2100 0 0 0.05 0 0 500
  124       rcc 2100.05 0 0 79.9 0 0 500
  125       rcc 2179.95 0 0 0.05 0 0 500
c    Simplification
  126       rcc -2180 0 0 4360 0 0 1200
c    ********************************************
c    ATLAS Cylinder
  150       rcc -2400 0 0 4800 0 0 1250
c    ATLAS Cavern
  151       rpp -2700 2700 -1700 1700 -2000 2000
```

II. Block 3: Data specification - Materials

```
c    ************************************************************************
c              Materials Specification
c    ************************************************************************
m1   7014.      -0.755636                       $ air
     8016.      -0.231475 18000.     -0.012889
m2   4000.           -1                         $beryllium
m3   6000.       -0.00075                       $stainless steel 202
     7000.       -0.00125 14000.       -0.005 15000.      -0.0003
     16000.      -0.00015 24000.        -0.18 25000.      -0.0875
     26000.      -0.67505 28000.        -0.05
m4   29000.          -1                         $Copper
m5   14028.          -1                         $silicon
m6   54000.          -1                         $Xenon
m7   82000.          -1                         $lead
m8   26000.          -1                         $Iron
m9   6000.         -0.034                       $Cast Iron
     14000.        -0.026 15000.       -0.003 16000.      -0.001
     25000.       -0.0065 26000.      -0.9295
m10   1000.      -0.00011                       $Titanium Alloy
      6000.      -0.00057 7000.      -0.00021 8000.      -0.00141
      13000.     -0.06125 22000.     -0.89363 23000.        -0.04
      26000.     -0.00283
m11   18000.         -1                         $Argon
```

```
m12   13000.          -1                              $Aluminium
m13   6000.         -0.25                             $tetrafluroethane
      1000.         -0.25 9000.       -0.5
m14   6000.       -0.272912                           $Carbon Dioxide
      8000.       -0.727088
```

III. Block 3: Data specification - Sources

- **Source emmiting a photon of energy 100 MeV**

```
c    ************************************************************************
c                 Source Specification
c    ************************************************************************
sdef pos=d1 erg=d2 par=2
si1 L 0 0 0
sp1 1
c    Energies
si2 L 100
sp2    1
```

- **Cylindrical source of energy 100 MeV**

```
c    ************************************************************************
c                 Source Specification
c    ************************************************************************
c    Cylindrical source
sdef ERG=100 CEL d1 AXS=1 0 0 POS 0 0 0 RAD d2 EXT d5
si1 L 1
sp1 1
si2 0 2.9            $ radius of cylinder containing cell
si5 -2500 2500       $ axial range of cylinder containing src cells
```

IV. Block 3: Data specification - Tallies

Type F4: The Average Cell Flux Tally   Type F2 : The Average Surface Flux Tally

```
c            ************************************************************************    c
Tallies
c    ************************************************************************
                f14:p 1                        f12:p 20.1 $Pixel
                f24:p 2                        f22:p 22.1 $SCT barrel
                f34:p 3                        f32:p 24.1 $TRT barrel
                f44:p 5                        f42:p 27.1 $SCT-TRT ec cylindrical section
                f54:p 7                        f52:p 29.1 $SCT-TRT ec cylindrical section
                f64:p 9                        f62:p 25.2 $SCT right ec outer
                f74:p 11                       f72:p 25.3 $SCT right ec inner
                f84:p 13                       f82:p 26.2 $SCT left ec inner
                f94:p 15                       f92:p 26.3 $SCT left ec outer
                f104:p 17                      f102:p 29.2 $TRT right ec outer
                f114:p 20                      f112:p 29.3 $TRT right ec inner
                f124:p 22                      f122:p 30.2 $TRT left ec inner
                f134:p 24                      f132:p 30.3 $TRT left ec outer
                f144:p 27                      f142:p 31.1 $ID layout
```

```
f154:p 31
f164:p 34
f174:p 35
f184:p 37
f194:p 39
f204:p 40
f214:p 43
f224:p 45
f234:p 47
f244:p 49
f254:p 51
f264:p 53
f274:p 55
f284:p 57
f294:p 59
f304:p 61
f314:p 63
f324:p 65
f334:p 66
f344:p 67
f354:p 72
f364:p 73
f374:p 74
f384:p 76
f394:p 77
f404:p 78
f414:p 79
f424:p 80
f434:p 82
f444:p 83
f454:p 84
f464:p 85
f474:p 88
f484:p 89
f494:p 90
f504:p 96
f514:p 97
f524:p 98
f534:p 104
f544:p 108
f554:p 113
f564:p 114
f574:p 115
f584:p 120
f594:p 121
f604:p 122
f614:p 150
```

```
f152:p 34.1 $EM cal barrel
f162:p 35.1 $Right Forward cal barrel
f172:p 39.1 $Had cal barrel
f182:p 38.2 $Had cal right ec outer
f192:p 37.2 $Had cal right ec outer
f202:p 37.3 $Had cal left ec outer
f212:p 61.1 $Muon BIL lower MDT wall
f222:p 72.1 $Muon BIL lower in
f232:p 73.1 $Muon BIL upper MDT wall
f242:p 74.1 $Muon BIL upper in
f252:p 75.1 $Muon BML lower RPC
f262:p 76.1 $Muon BML lower MDT wall
f272:p 77.1 $Muon BML lower MDT in
f282:p 78.1 $Muon BML upper in
f292:p 79.1 $Muon BML upper MDT wall
f302:p 80.1 $Muon BML upper RPC
f312:p 81.1 $Muon BOL lower wall
f322:p 82.1 $Muon BOL lower in
f332:p 83.1 $Muon BOL upper in
f342:p 84.1 $Muon BOL upper MDT wall
f352:p 85.1 $Muon BOL upper RPC
f362:p 65.2 $Muon left SW inner
f372:p 66.2 $Muon left SW outer
f382:p 86.3 $Muon left EEL inner MDT wall
f392:p 86.2 $Muon left EEL outer MDT in
f402:p 88.2 $Muon left EEL inner MDT in
f412:p 86.2 $Muon left EEL outer MDT wall
f422:p 45.2 $Muon left EML inner MDT wall
f432:p 96.2 $Muon left EML inner MDT in
f442:p 94.2 $Muon left EML outer MDT wall
f452:p 97.2 $Muon left EML inner MDT in
f462:p 102.3 $Muon left EML inner TGC1
f472:p 102.2 $Muon left EML outer TGC1
f482:p 106.3 $Muon left EML inner TGC2
f492:p 106.2 $Muon left EML outer TGC2
f502:p 47.2 $Muon left EOL1 inner MDT wall
f512:p 113.2 $Muon left EOL1 inner MDT in
f522:p 111.2 $Muon left EOL1 outer MDT in
f532:p 114.2 $Muon left EOL1 outer MDT wall
f542:p 120.2 $Muon left EOL2 inner MDT wall
f552:p 120.3 $Muon left EOL2 inner MDT in
f562:p 121.2 $Muon left EOL2 outer MDT in
f572:p 122.2 $Muon left EOL2 outer MDT wall
```

V. Cards for Optional Tally Features: The Tally Energy Card

```
c    ***********************************************************************
c                    Energy Bins (MeV)
c    ***********************************************************************
e0    0 100i 100
```

VI. Miscellaneous Data Specifications: The Mode Card

```
mode  n p e
```

APPENDIX 3: ERROR ANALYSIS FOR THE ATLAS DETECTOR

Cylindrical source towards beam axis. Run for 24 hours CPU time.

1. **Photons-Analog simulation:** Tally fluctuation for tallies 1-4:

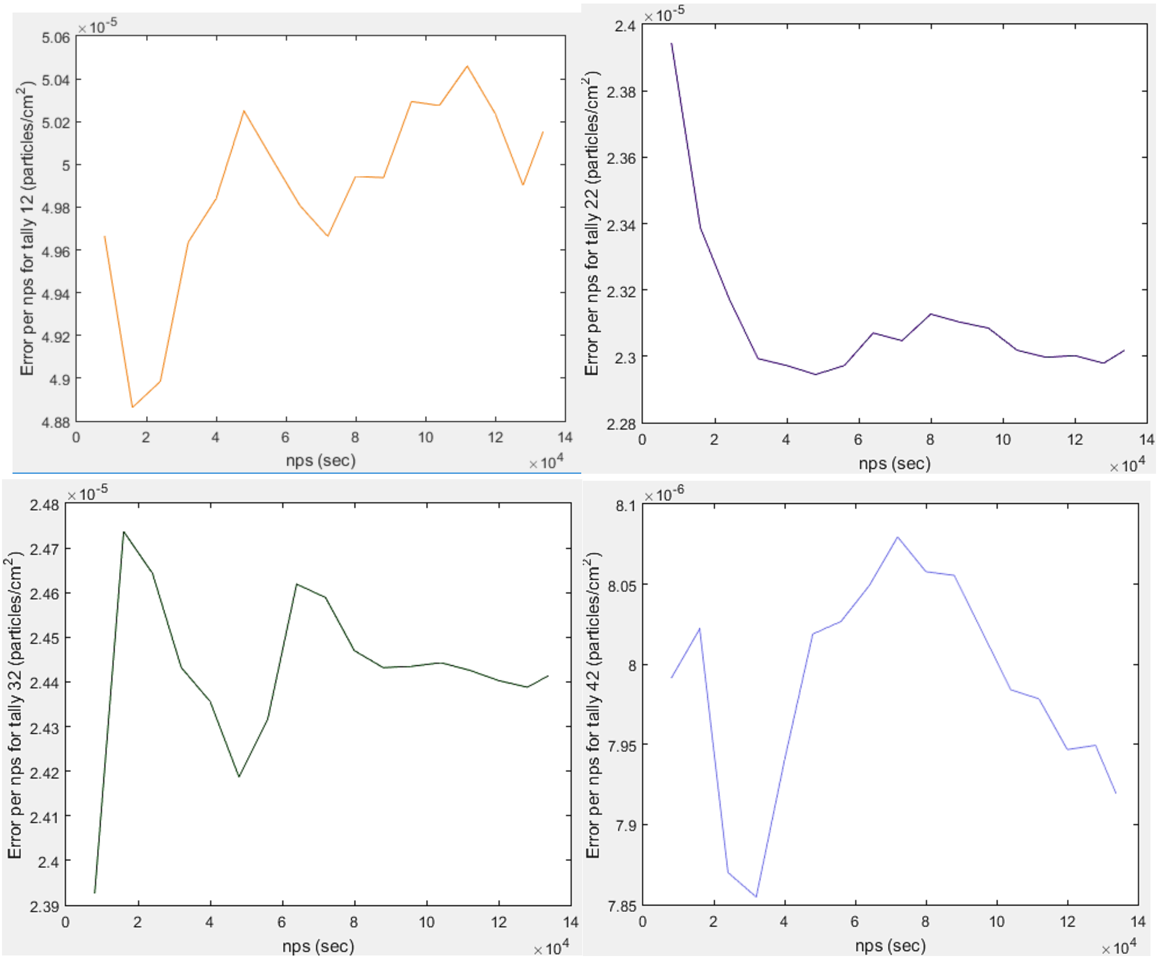

Photons-Analog simulation: Error fluctuation for tallies 1-4:

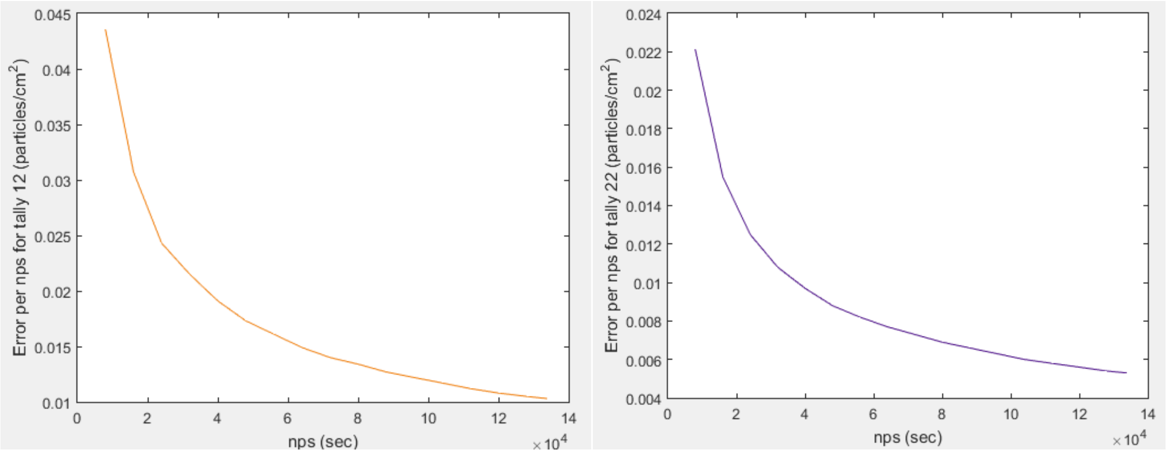

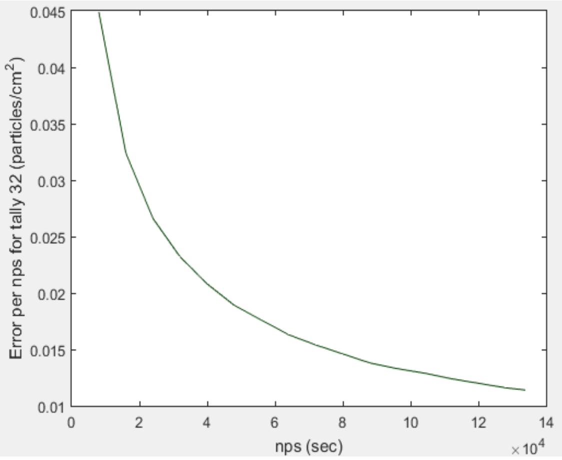

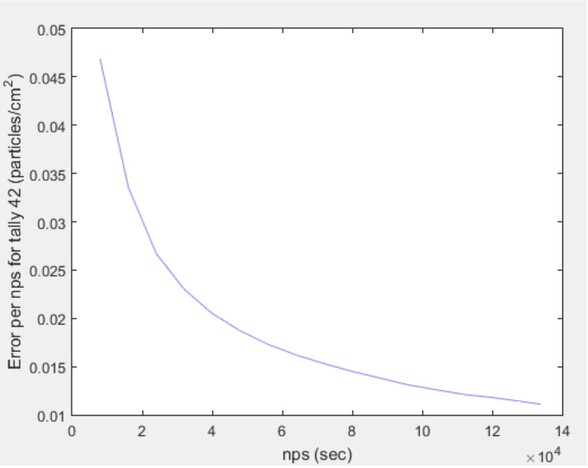

2. **Neutrons:** Tally fluctuation for tallies 1-4

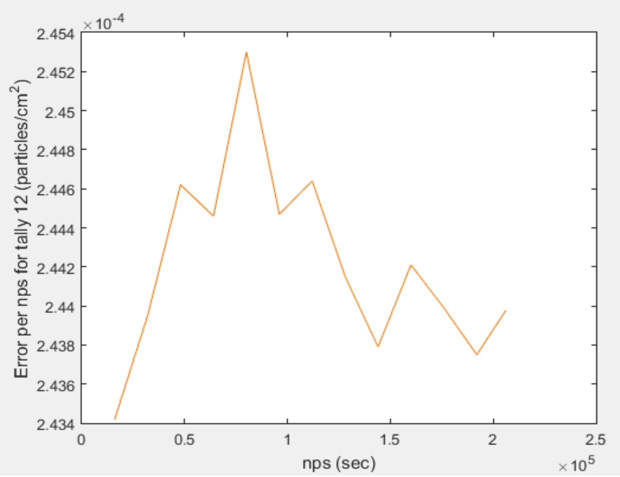

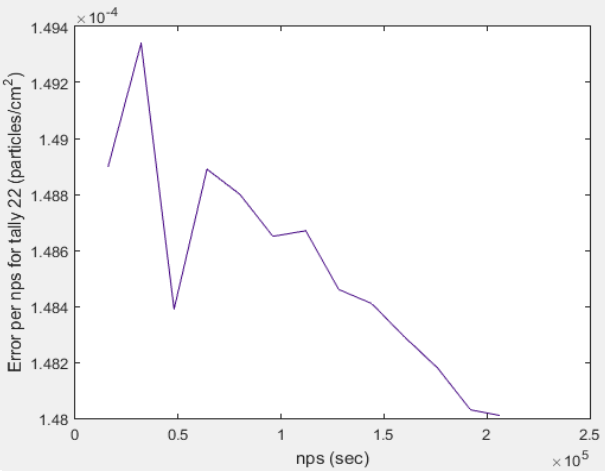

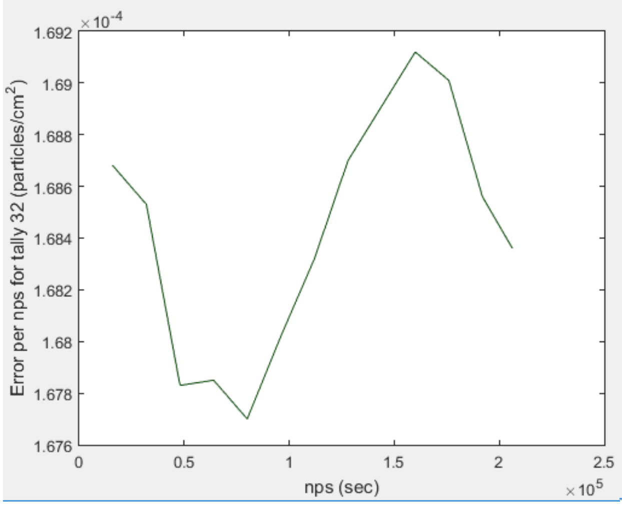

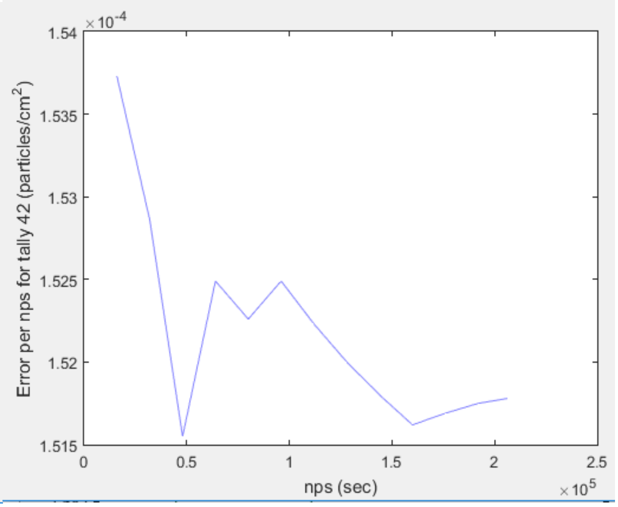

Neutrons: Error fluctuation for tallies 1-4:

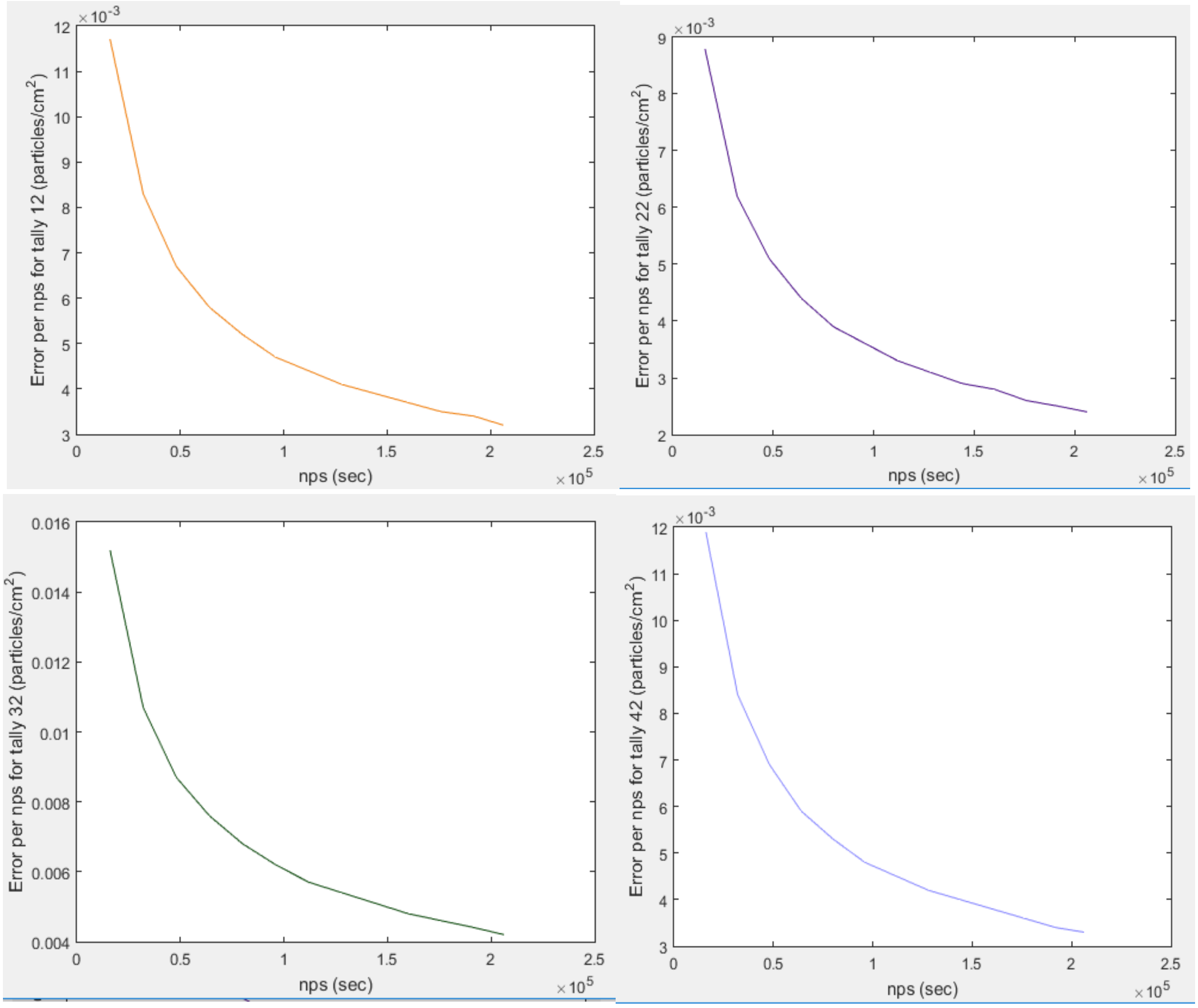

REFERENCES

[1] Διδακτορική διατριβή, ‘Αναζήτηση του μποζονίου Higgs του Καθιερωμένου Προτύπου με τον ανιχνευτή ATLAS στον LHC με αποτέλεσμα την παρατήρηση ενός νέου σωματιδίου συμβατού με το μποζόνιο Higgs’, Ελένη Κ. Μουντριχα, Αθήνα, Σεπτέμβριος 2012.

[2] A dissertation by Charilaos Tsarouchas to The Department of Physics for the degree of Doctor of Philosophy in the subject of Physics, ‘Study of Rare Decays of B Hadrons and Development of a Data Viewer Application of the Detector Control System in the ATLAS Detector’, National Technical University of Athens, April 2012.

[3] LHC Higgs Cross Section Working Group; Dittmaier, Mariotti, Passarino, Tanaka, Alekhin, Alwall, Bagnaschi, Banfi: ‘Handbook of LHC Higgs Cross Sections: 2. Differential Distributions’. CERN Report 2 (Tables A.1 – A.20), 2012.

[4] Journal of High Energy Physics. 1103 (3): 055. arXiv:1012.0530, ‘Higgs production at the LHC’, Baglio, Julien, Djouadi, Abdelhak, 2011.

[5] Baglio, Julien; Djouadi, Abdelhak (2010). "Predictions for Higgs production at the Tevatron and the associated uncertainties". Journal of High Energy Physics. 1010 (10): 063. arXiv:1003.4266 . Bibcode:2010JHEP...10..064B. doi:10.1007/JHEP10(2010)064.

[6] Teixeira-Dias (LEP Higgs working group), P. (2008). "Higgs boson searches at LEP". Journal of Physics: Conference Series. 110 (4): 042030. arXiv:0804.4146 . Bibcode:2008JPhCS.110d2030T. doi:10.1088/1742-6596/110/4/042030

[7] Diploma Thesis, Κιλιντάρη Σοφία,’ Micromegas Detector for ATLAS upgrade for SUPERLHC’, Thessaloniki 2012

[8] Μεταπτυχιακή διπλωματική εργασία, ‘Μελέτη σε δέσμες σωματιδίων ενός ανιχνευτή MICROMEGAS 1x1 m^2, για το αδρονικό θερμιδόμετρο του ILC’, Τσιγαρίδας Α. Στέργιος.

[9] Μεταπτυχιακή διπλωματική εργασία, Κωνσταντίνος Ντέκας, Αθήνα, ‘Μελέτη ανιχνευτή Micromegas σε δοκιμαστική δέσμη πιονίων ορμής 120 GeV/c στο H6/SPS/CERN’, Σεπτέμβριος 2012.

[10] Εθνικό Μετσόβιο Πολυτεχνείο, Σχολή Εφαρμοσμένων Μαθηματικών και Φυσικών επιστημών, Τομέας Φυσικής, ΔΠΜΣ Φυσική και Τεχνολογικές εφαρμογές, ΕΜΠ/ΕΚΕΦΕ Δημόκριτος, ‘Μελέτη του ανιχνευτή Micromegas σε πηγές νετρονίων και φωτονίων με τη χρήση του προγράμματος Geant4’, Καστριώτου Μαρία.

[11] ‘Passage of particles through matter’, Revised September 2005 by H. Bichsel (University of Washington), D.E. Groom (LBNL), and S.R. Klein (LBNL).

[12] Μεταπτυχιακή διπλωματική εργασία, ΣΕΜΦΕ-ΕΜΠ, Κωνσταντίνος Ανδρέα Μακρομάλλης, ‘Ηλεκτρονική Μελέτη Ανιχνευτών Micromegas Διπλών Λωρίδων’

[13] Diploma Thesis, Orfanelli S. Styliani, Athens, 25th of November 2011, ‘Monte Carlo simulations to estimate the damage potential of electron beam and tests of beam loss detector based on quartz Cherenkov radiator read out by a silicon photomultiplier on CLIC Test Facility 3(CTF3)’.

[14] Διπλωματική εργασία, Χαρίτου Γεώργιος, Αθήνα, Σεπτέμβριος 2010, ‘Μελέτη και Σχεδιασμός θωράκισης του επιταχυντή PAPAP του Ι.Π.Φ του Ε.Κ.Ε.Φ.Ε Δημόκριτος μέσω προσομοιώσεων με τη χρησιμοποίηση του λογισμικού MCNP5’.

[15] Zur Erlangung des Grades eines Doktors der Naturwissenschaften,’ Search for Solar Axions with the MICROMEGAS Detector in CAST’, Theopisti Dafni, Echnischen Universitat Darmstadt.

[16] Μεταπτυχιακό Υπολογιστικής φυσικής, Διπλωματική εργασία, ‘Καταιγισμοί κοσμικής ακτινοβολίας’, Ατρείδης Γιώργος.

[17] Διπλωματική εργασία, Αριστοτέλειο Πανεπιστήμιο Θεσσαλονίκης, ‘Δοσιμετρία νετρονίων στο περιβάλλον του υποκρίσιμου πυρηνικού αντιδραστήρα’, Ταχτσίδης Θεόδωρος, Θεσσαλονίκη, Σεπτέμβριος 2010

[18] Διδακτορική Διατριβή, Χρίστος Λαμπούδης, Αριστοτέλειο Πανεπιστήμιο Θεσσαλονίκης, Ιανουάριος 2007, ‘Μελέτη των χαρακτηριστικών της δέσμης νετρονίων και προσδιορισμός παραμέτρων συντονισμού της σύλληψης νετρονίων στο 234U με την μέθοδο της ολικής απορρόφησης, στην πειραματική διάταξη n_TOF του CERN’.

[19] Κοσμικά σωματίδια υψηλών ενεργειών, Αναστάσιος Λιόλιος, Αστεροσκοπείο, Α.Π.Θ.,20 Μαΐου 2008

[20] Generation and Use of Coherent Transition Radiation from Short Electron Bunches, Chitrlada Settakorn, Stanford Linear Accelerator Center, Stanford University, August 2001

[21] To The Department of Physics for the degree of Doctor of Philosophy, Konstantinos A. Ntekas, ‘Performance characterization of the Micromegas detector for the New Small Wheel upgrade and Development and improvement of the Muon Spectrometer Detector Control System in the ATLAS experiment’, January 2016.

[22] To The Department of Physics for the degree of Doctor of Philosophy, Georgios A. Iakovidis, October 2014, ‘Research and Development in Micromegas Detector for the ATLAS Upgrade’.

[23] Greek NTP programme, CERN, Μιχάλης Κορατζίνος, ‘Ο μεγάλος Αδρονικός Επιταχυντής LHC’

[24] Ο ανιχνευτής ATLAS Για το LHC, Ειρήνη Βήχου, University of Illinois at Urbana, CERN 24 Ιουλίου 2008

[25] ΠΕΙΡΑΜΑΤΙΚΕΣ ΔΙΑΤΑΞΕΙΣ ΣΤΗ ΦΥΕ II, Ευάγγελος Ν. Γαζής, Καθηγητής ΕΜΠ, Βενέτης Πολυχρονάκος, Ερευνητής BNL ‘Ανιχνευτές και Μεθοδολογία’, Ιούνιος 2008.

[26] PROEFSCHRIFT ter verkrijging van de graad van doctor aan de Universiteit Twente, Jochem Snuverink, ‘The ATLAS muon Spectrometer: Commissioning and tracking’.

[27] ‘Radiation in the USA15 cavern in ATLAS’, ATLAS Document No: ATL-COM-TECH-2004-001, Created: 18/03/04, Ian Dawson, Vincent Hedberg.

[28] The ATLAS Beam Condition Monitor Commissioning A. Gorišek, J. Stefan Institute, Jamova 39, 1000 Ljubljana, Slovenia b for the ATLAS BCM collaboration.

[29] The ATLAS Beam Condition Monitor Commissioning, Andrej Gorišek , J. Stefan Institute,Ljubljana, Slovenia, TWEPP, Naxos, Greece, 15-19 September 2008.

[30] PUBLISHED BY INSTITUTE OF PHYSICS PUBLISHING AND SISSA, February 2008 'The ATLAS Beam Conditions Monitor', V. Cindro, D. Dobos, I. Dolenc, H. Frais-Kölbl, A. Gorišek, E. Griesmayer, H. Kagan, G. Kramberger, B. Maček, I. Mandić, M. Mikuž, M. Niegl, H. Pernegger, D. Tardif, W. Trischuk, P. Weilhammer and M. Zavrtanik

[31] PUBLISHED BY INSTITUTE OF PHYSICS PUBLISHING AND SISSA , The CERN Large Hadron Collider: Accelerator and experiments, 'The ATLAS Experiment at the CERN Large Hadron Collider', published: August 14, 2008

[32] RD09 –9th International Conference on Large Scale Applications and Radiation Hardness of Semiconductor Detectors, BoštjanMaček,J. Stefan Institute, 'The ATLAS Beam Conditions and Beam Loss Monitors', 30 September -2 October 2009, Florence, Italy

[33] Laura Jeanty, 15 August 2007, NEPPSR 2007, 'The ATLAS Transition Radiation Tracker'.

[34] 20th International Conference on Computing in High Energy and Nuclear Physics (CHEP2013) IOP Publishing, Journal of Physics: Conference Series 513 (2014) 012040, 'Performance of the ATLAS muon trigger in pp collisions at $\sqrt{s} = 8$ TeV'.

[35] Department of Physics, McGill University, David Layden, Honours Mathematical Physics, University of Waterloo, August 22, 2013, 'Measuring 2012 Photon Trigger Efficiency in the ATLAS Experiment'

[36] International Conference on Computing in High Energy and Nuclear Physics 2012 (CHEP2012) IOP Publishing Journal of Physics: Conference Series 396 (2012) 012010, 'The ATLAS Level-1 Trigger System'

[37] XIII International Conference on Calorimetry in High Energy Physics (CALOR 2008) IOP Publishing Journal of Physics: Conference Series 160 (2009) 012043, 'The ATLAS Liquid Argon Calorimeter: an overview'.

[38] PUBLISHED BY IOP PUBLISHING FOR SISSA MEDIALAB ,'Operation and performance of the ATLAS semiconductor tracker'.

[39] TOPICAL WORKSHOP ON ELECTRONICS FOR PARTICLE PHYSICS 2012, 17–21 SEPTEMBER 2012, OXFORD, U.K., 'The upgrade of the ATLAS Level-1 Central Trigger Processor'.

[40] PUBLISHED BY INSTITUTE OF PHYSICS PUBLISHING AND SISSA, 'The ATLAS central level-1 trigger logic and TTC system'.

[41] 'The ATLAS Trigger System',Martin zur Nedden, Humboldt-University of Belrin, Graduate School 1504, Autumn Block Course October 2011

[42] 'Overview of the ATLAS Trigger/DAQ System', A. J. Lankford, UC Irvine May 4, 2007

[43] International Conference on Computing in High Energy and Nuclear Physics 2012 (CHEP2012) IOP Publishing Journal of Physics: Conference Series 396 (2012) 012028, 'The ATLAS Detector Control System'.

[44] ATLAS DETECTOR AND PHYSICS PERFORMANCE, Technical Design Report, Volume 1, Created: 25 May 1999, Prepared By: ATLAS Collaboration

[45] To The Department of Physics for the degree of Doctor of Philosophy, Georgios A. Iakovidis, October 2014, 'Research and Development in Micromegas Detector for the ATLAS Upgrade'.

[46] AN MCNP PRIMER, J. K. Shultis, R. E. Faw, Dept. of Mechanical and Nuclear Engineering Kansas State University Manhattan, KS 66506.

[47] MCNPX^{TM} USER'S MANUAL, Version 2.5.0, LA-CP-05-0369 Denise B. Pelowitz, editor, April 2005.

[48] Atlas Radiation Background Task Force Summary Document, Reported by S.Baranov, M.Bosman, I.Dawson, V.Hedberg, A.Nisati, M.Shupe, 'Estimation of Radiation Background, Impact on Detectors, Activation and Shielding Optimization in ATLAS'.

[49] Prepared for the U.S. Department of Homeland Security U.S. Customs and Border Protection and Domestic Nuclear Detection Office under U.S. Department of Energy Contract DE-AC05-76RL01830, 'RADIATION PORTAL MONITOR PROJECT', Compendium of Material Composition Data for Radiation Transport Modeling, Revision 1, RJ McConn Jr, CJ Gesh, RT Pagh, RA Rucker, RG Williams III, March 4, 2011.

[50] https://home.cern/about/physics/heavy-ions-and-quark-gluon-plasma

[51] https://home.cern/topics/antimatter/matter-antimatter-asymmetry-problem

[52] https://home.cern/about/physics/supersymmetry

[53] https://home.cern/new-technologies-high-luminosity-lhc

[54] http://www.lhc-closer.es/taking_a_closer_look_at_lhc/0.lhc_p_collisions

[55] http://www.lhc-closer.es/taking_a_closer_look_at_lhc/0.cross_section

[56] http://www.lhc-closer.es/taking_a_closer_look_at_lhc/0.simple_movement

[57] http://atlas.web.cern.ch/Atlas/TP/NEW/HTML/tp9new/node1.html

[58] https://timeline.web.cern.ch/atlas-cavern-inaugurated

[59] http://physicslab.eap.gr/thesis/tsirigotis/Chapter04_MuonDetection.pdf

[60] https://home.cern/about/computing/worldwide-lhc-computing-grid

[61] https://home.cern/about/computing/grid-software-middleware-hardware

[62] https://www.dartmouth.edu/~chance/teaching_aids/books_articles/probability_book/Chapter8.pdf

[63] http://atlas.web.cern.ch/Atlas/GROUPS/Shielding/shielding.htm#

[64] https://www.nevis.columbia.edu/~parsons/ATLASdetector.pdf

[65] http://www.pa.msu.edu/hep/quarknet/news01.html

[66] http://iopscience.iop.org/article/10.1088/1367-2630/9/9/335/pdf

[67] http://lhc-machine-outreach.web.cern.ch/lhc-machine-outreach/photogallery/SM18/index.html

[68] http://www.atomicarchive.com/Fission/Fission1.shtml

[69] https://home.cern/about/engineering/radiofrequency-cavities